

NANOSTRUCTURED HYBRID ELECTROLYTES FOR LITHIUM  
BATTERIES

A Dissertation

Presented to the Faculty of the Graduate School

of Cornell University

in Partial Fulfillment of the Requirements for the Degree of

Doctor of Philosophy

by

Jennifer Lyn Schaefer

January 2014

© 2014 Jennifer Lyn Schaefer

# NANOSTRUCTURED HYBRID ELECTROLYTES FOR LITHIUM BATTERIES

Jennifer Lyn Schaefer, Ph.D.

Cornell University 2014

It has long been recognized that secondary batteries containing lithium metal anodes have some of the highest theoretical energy densities of known battery chemistries, due to the light weight and low deposition potential of lithium metal. Lithium metal batteries have several roadblocks to effective, wide-spread implementation: lithium metal is reactive with many lithium-ion electrolytes causing low coulombic efficiency and it electrodeposits unevenly upon recharge, creating a safety hazard due to potential short-circuit. Polymer electrolytes have been under investigation for several years due to their relatively low reactivity with lithium metal and potential to electrodeposit more uniformly, due to their higher mechanical strength. This dissertation researches polymer-ceramic hybrid electrolytes with several goals: improving room temperature ionic conductivity of the electrolytes while maintaining chemical stability and mechanical integrity, allowing tunability of mechanical properties, improving lithium-ion transference number of the electrolyte, and studying the lithium metal dendrite growth as a function of electrolyte properties. It is found that constraint of the polymer chain by tethering to a nanoparticle improves ambient temperature ionic conductivity by mitigating matrix crystallization. Immobilization of anionic ligands onto the nanoparticle is found to be a facile way to synthesize nanometric lithium salts with improved transference numbers; importantly, the chemistry of the suspending solvent is found to have a significant impact on ionic conductivity. It is found that polyether-based electrolytes with and without hybrid nanoparticle fillers exhibit the same lithium metal battery lifetime regardless of mechanical properties or ionic conductivity. Surprisingly, certain copolymer electrolytes are found to provide for exceeding longer lifetimes.

## BIOGRAPHICAL SKETCH

Jennifer Lyn Schaefer was born November 29, 1986 to Harold and Shirley Hubbell. She was a 2004 graduate of Deposit Central School in Deposit, N.Y. Jennifer attended Widener University in Chester, P.A. from 2004-2008 where she completed degrees in Chemical Engineering (B.S., M.Eng.) and Chemistry (B.S.). During her Master's thesis work at Widener, Jennifer took an interest in materials research. She came to Cornell in 2008 to pursue her Ph.D. in Chemical Engineering and chose to research hybrid materials and their applications as electrolytes in lithium batteries under the advisement of Prof. Lynden Archer. Jennifer is the wife of Andrew Schaefer and mother to Matthew and Zalea.

Dedicated to the Almighty God: omnipotent, omnipresent, and omniscient.

## ACKNOWLEDGEMENTS

I would like to thank my advisor, Prof. Lynden Archer, for his unfailing support and wise guidance over the past 5+ years. And I will thank him in advance for any desperate phone calls that I may make to him in the future as I am unable to stop by the office on a whim.

Thank you to my committee for their comments and criticisms.

Thank you to the entire Archer Research Group and to my undergraduate research assistants, including Dennis Yanga, Orbi Ish-Shalom, and Brianna DeRooy.

Thank you to the CCMR and KAUST-CU facility staff, including Brenda Fisher and David Jung.

Thank you to the Olin Hall staff, including Breana Soule and Shelby Clark-Shevalier.

## TABLE OF CONTENTS

BIOGRAPHICAL SKETCH	iii
DEDICATION	iv
ACKNOWLEDGEMENTS	v
CHAPTER 1. Introduction	1
CHAPTER 2. Electrolytes for high energy density lithium batteries	14
CHAPTER 3. Application of electrolytes in lithium battery electrolytes	76
CHAPTER 4. Nanoscale organic hybrid electrolytes	106
CHAPTER 5. Nanoporous hybrid electrolytes	127
CHAPTER 6. Short-circuit behavior of lithium metal coin cells containing tunable nanoscale, hybrid electrolytes	159
CHAPTER 7. Studies on crosslinked copolymer electrolytes	176
CHAPTER 8. High lithium transference electrolytes via creation of 3-dimensional, charged, networks of dense functionalized nanoparticle composites	207
CHAPTER 9. Covalently cofunctionalized hybrid nanoparticle salts and the effect of solvent type on ion dissociation	232

## **CHAPTER 1.**

### **INTRODUCTION**

This dissertation outlines my work on nanostructured hybrid electrolytes for applications in lithium metal batteries. The goal of my studies was to determine the viability of a hybrid electrolyte platform for use in lithium-based batteries, utilize the platform to obtain electrolytes with improved transport properties, and further utilize the platform to perform studies to advance the understanding of lithium dendrite growth in secondary lithium metal batteries upon recharge.

The body of literature on electrolytes for lithium-based batteries is summarized in Chapters 2 and 3, published reviews which discuss electrolytes for high energy battery platforms and nanocomposite electrolytes, respectively. Figure 1.1 summarizes the classes of electrolytes discussed in Chapters 2 and 3: liquids, polymers, ceramics, and combinations thereof. The nanostructured, hybrid electrolyte platforms of interest in this work are thoroughly outlined in Chapters 4-9. Previous work on related hybrid materials should be referred to regarding their fundamental structure and rheological properties.<sup>[1-4]</sup> In addition, for broader understanding of the electrolyte platform, parallel studies on ionic-liquid hybrid electrolytes should be referred to.<sup>[5-8]</sup> Therefore, this introduction will be limited to the discussion of challenges related to lithium metal batteries, specifically.

Lithium metal batteries were the first lithium-based battery platform, discovered and patented by M. Stanley Whittingham in the 1970s while at Exxon Research and Engineering Company.<sup>[9,10]</sup> Early in this research, the challenge of dendritic growth upon recharge of lithium metal batteries became apparent, resulting in numerous fires at the Exxon research laboratory in Linden, New

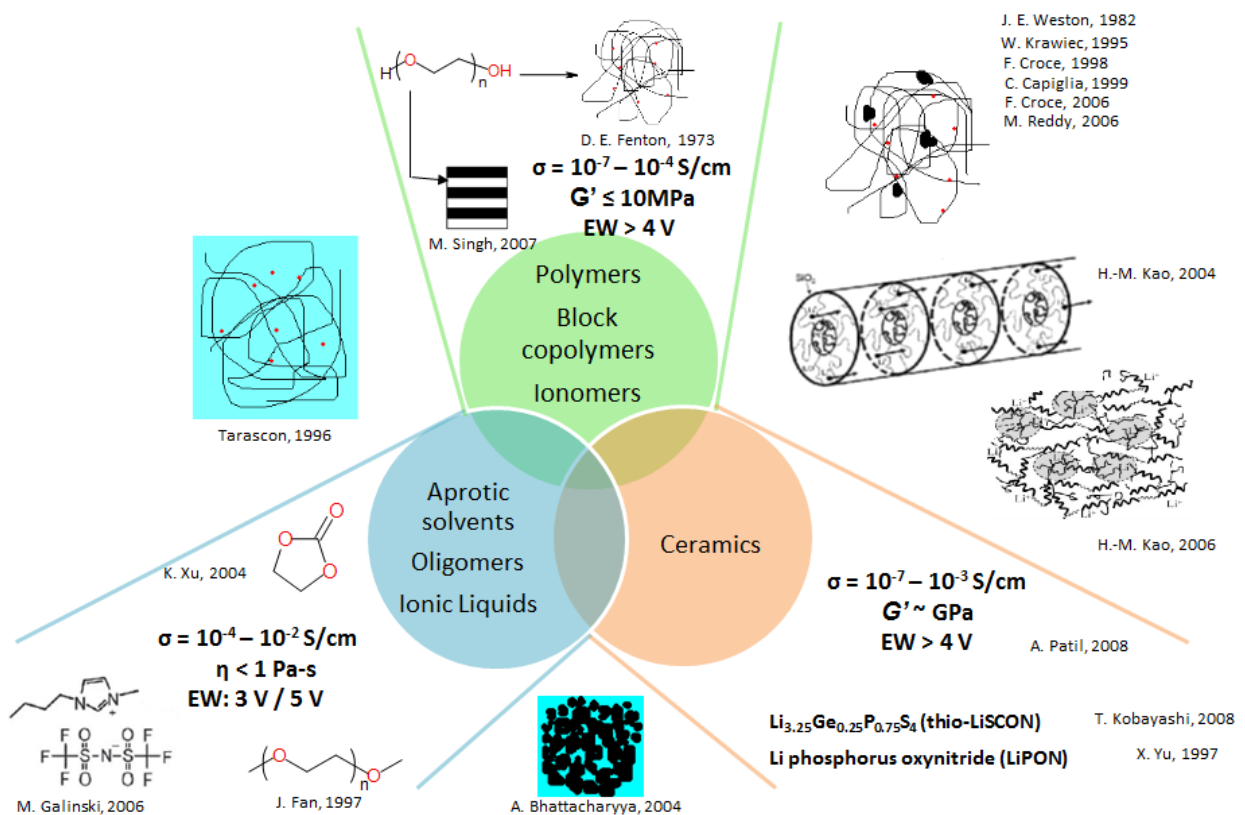


**Figure 1.1** Summary of the classes of materials investigated as electrolytes for lithium-based batteries. Further description provided in Chapters 2 and 3.

Jersey. When lithium-ion intercalation compounds were discovered a few years later that led to lithium-ion battery technologies with energy densities far exceeding those of other rechargeable batteries already on the market, unsafe lithium metal battery technology went out of focus. The current need for energy densities exceeding that available by lithium-ion technologies has led to a renewed interest in lithium metal battery technology. Three major challenges have hindered lithium metal battery technology thus far: cycling efficiency, charge/discharge rate capability, and safety.<sup>[11-14]</sup>

Lithium is a highly reactive metal, unstable in the presence of water, oxygen, and nitrogen. It is generally accepted that all electrolytes react with a clean lithium metal electrode, creating an interfacial layer termed the solid-electrolyte-interface (SEI). Reaction of the lithium metal electrode to form the interface consumes the electrode, resulting in diminished active material, diminished electrolyte, and thus diminished capacity. This reaction is known to be quite severe with electrolytes commonly used in lithium-ion batteries (ex. LiPF<sub>6</sub> in ethylene carbonate/dimethyl carbonate, EC/DMC), where the SEI is unable to protect the lithium metal electrode from continued reaction upon cycling.<sup>[15]</sup> More recently, several additives such as lithium nitride have been proposed for their propensity to form a stable SEI at lithium, thus preventing its further reaction and improving cycling efficiency with liquid electrolytes. An alternative, a polymer electrolyte, is known to have improved cycling efficiencies without interface additives relative to commonly employed liquids.

Batteries with polymer electrolytes suffer from low maximum charge-discharge rates at ambient temperatures and below due to crystallization of the polymer matrix. These issues are thoroughly discussed in Chapters 2 and 3. Strategies that have been investigated for improving the ionic conductivity of polymer electrolytes include lowering of the polymer glass transition

temperature,  $T_g$ , and melting temperature,  $T_m$ , by the use of plasticizers in the form of particles, oligomers, liquids, or large salts, changes in the chemistry of the polymer backbone, and constraining of the polymer segments. More recently, it has been suggested that an operating temperature of 60°C is acceptable for electric vehicle applications, so the absolute need for high ambient ionic conductivity has been relaxed.<sup>[16]</sup>

Safety issues of lithium metal batteries are arguably the largest hurdles for their successful widespread implementation. Replacement of the flammable, aprotic liquid electrolyte with a polymer electrolyte does not eliminate safety concerns in the event of battery failure by short-circuit. This is evidenced by fires in large-scale lithium metal polymer batteries used in AT&T broadband cable equipment cabinets. These events led to failure of the start-up battery company Avestor. Short-circuiting in lithium metal batteries is nearly always caused by dendritic lithium growth upon repetitive battery recharge, a phenomenon that will be more thoroughly discussed here.

Many metals undergo dendritic growth during electrodeposition, including zinc, copper, silver, and gold. Metallic protrusions that are commonly called whiskers, but sometimes referred to as dendrites, are known to form from the surface of many different metals while sitting statically, due to compressive internal stress. While literature suggests that this form of dendrites has also been observed on lithium metal electrodes,<sup>[17]</sup> the overwhelmingly common lithium dendrite is formed upon electrodeposition and this phenomenon is what this dissertation will consider. Electrodeposited dendrites differ in structure depending on the deposition conditions, including the applied current density, the chemistry of the electrolyte, and the mechanical properties of the electrolyte.<sup>[18-22]</sup> It is accepted that dendrite propagation is a simple result of amplified ion flux to a protrusion relative to that of the flat interface. The nucleation of the lithium dendrite as well

as the propagation of the dendrite in the presence of a complex electrolyte are more controversial topics.

In 1990, Chazalviel considered the problem of uneven metallic electrodeposition at high rate.<sup>[23]</sup> He modeled the 1-dimensional ion concentrations and voltage profile in a non-dimensionalized cell containing a dilute, binary, monovalent salt with a cation that will electrodeposit at a blocking electrode, and no additional salt. He considered the effects of diffusion and migration; convection was ignored. He predicted that at steady-state, two regimes exist within the electrolyte: Region 1, where the cation and anion concentrations are nearly equal, and Region 2, near to the electrode, where the anion concentration has been depleted. This non-electroneutral region is termed the space-charge region, and it is over this length that most of the voltage gradient exists. This voltage gradient is deemed the instability that causes the dendrite nucleation. The timescale for the space-charge region to form was found to be that of Sand's transition time:

$$\tau_s = \pi D \left( \frac{eC_0}{2Jt_a} \right)^2$$

where  $D$  is the ambipolar diffusion coefficient,  $C_0$  is the ion concentration,  $J$  is the applied current density, and  $t_a$  is the anion transference number, the ratio of the mobility of the anion to the sum of the mobilities of both ions.

In further analysis, the dendrite growth rate is predicted to be equal to the velocity of the retreating anion. The dendrite is hence “chasing” the anions to the counter-electrode, and the dendrite growth time is predicted as:

$$t_g = \frac{\sigma L}{\mu_a J}$$

where  $\sigma$  is the electrolyte ionic conductivity,  $L$  is the interelectrode distance, and  $\mu_a$  is the anion mobility.

Experimental support has been found for the Chazalviel model in both the high current density regime where it was designed, as well as below the crossover current density,  $J^*$ , in the low current density regime,<sup>[24,25]</sup> where

$$J^* = \frac{2eC_0D}{t_aL}.$$

Using optical microscopy, optical index gradients are visible at the electrode-electrolyte interface and suggest an anion depletion zone in the vicinity of the dendrite.<sup>[26]</sup> Galvanostatic polarization measurements on symmetric lithium cells containing the solid polymer electrolyte polyethylene oxide with a lithium salt have indicated that dendrites are formed at high current densities at the divergence in the potential that corresponds to Sand's time. When cells were galvanostatically polarized at low current densities, battery short-circuit times,  $t_{sc}$ , were found to be close to Sand's time with  $t_{sc} \sim J^{-2}$  (Figure 1.2). In these studies, the characteristics of the electrolyte were such that the predicted dendrite growth time  $t_g$  was small.<sup>[25]</sup> The low current density result was attributed by the authors as due to local areas of anion deficiency that form laterally along the electrode, as opposed to a space-charge region across the entire electrode as predicted to occur at high current density.

It is important to note that not all experimental results fit the predictions of the Chazalviel model. Liu et. al. have multiple reports of  $t_{sc} \sim J^{-1.3}$  when employing polyethylene oxide-based electrolytes (Figure 1.3).<sup>[27-29]</sup> The short-circuit times achieved by this group also vary in

magnitude with longer lifetimes than that predicted by the Chazalviel model. The discrepancy between the published results is unknown and is also ignored by the majority of the literature in this field.

Dendrite propagation in elastic media has been modeled by Monroe and Newman.<sup>[30]</sup> In this work, a sinusoidal perturbation was imposed at the polymer electrolyte - lithium metal electrode interface, and a stability analysis was performed to determine if the nucleus would grow. Considering surface tension, deformation, and compressive forces, the perturbation was found to be unstable, and the dendrite growth mitigated, when the shear storage modulus of the polymer electrolyte was greater than 1.8 times the modulus of lithium metal, 4.2 GPa at 25°C. Thus, they predict that a very hard polymer electrolyte is required to prevent dendrite growth.

Experimental support for the result by Monroe and Newman was published recently, in 2012, by Balsara, et. al.<sup>[31]</sup> In galvanostatic cycling of lithium metal cells employing the block copolymer polystyrene-polyethylene oxide with lithium salt electrolytes, they find that the inverse of the charge passed through the cell until short-circuit ( $C_d = t_{sc} \times J$ ) extrapolates to zero – infinite lifetime – when the electrolyte modulus is  $10^9$ - $10^{10}$  Pa (Figure 1.4).

This dissertation adds to the knowledge of lithium metal battery lifetimes as a function of electrolyte properties. Hybrid electrolytes with tunable mechanical properties are reported in Chapters 4 and 5. The short-circuit properties of lithium metal batteries containing these hybrid electrolytes are reported in Chapter 6. Studies of electrolyte characterization and short-circuit properties of lithium metal cells containing novel copolymer electrolytes are reported in Chapter 7. Finally, properties of hybrid electrolytes with tethered anions ( $t_a \rightarrow 0$ ) and the short-circuit properties of cells containing these electrolytes are reported in Chapters 8 and 9.

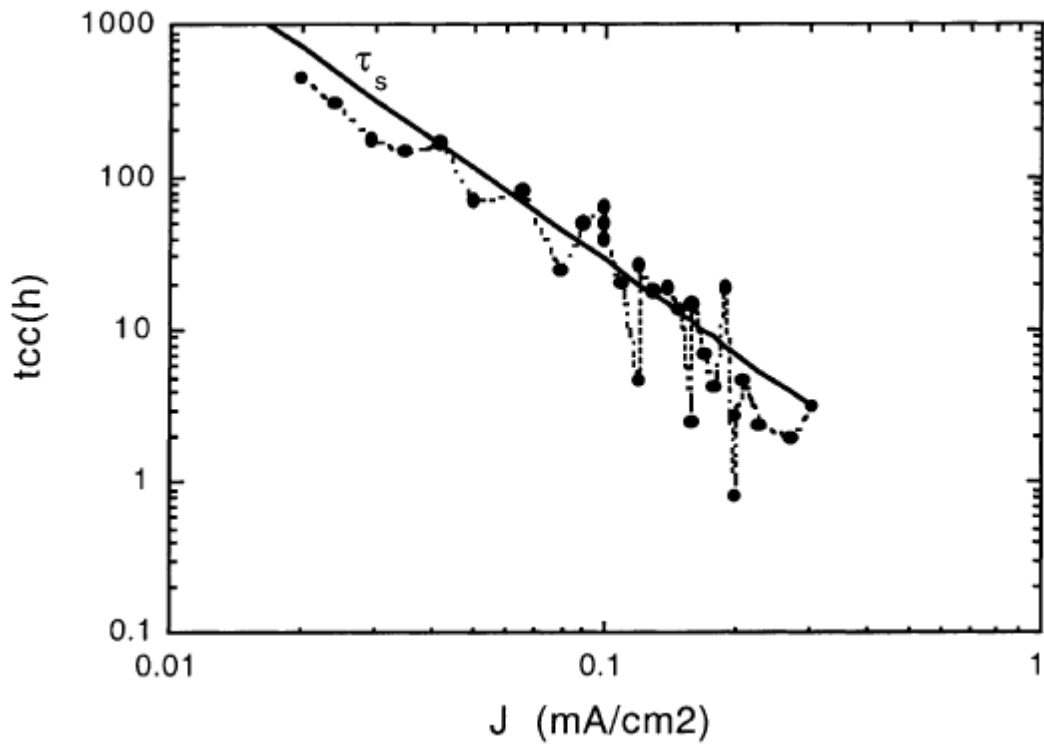


**Figure 1.2** Variation of the short-circuit time of Li/PEO/Li cells at 90°C undergoing galvanostatic polarization as a function of operating current density. The line shows Sand's time  $\tau_s$  with a  $J^2$  dependence. Reproduced with permission from [25].

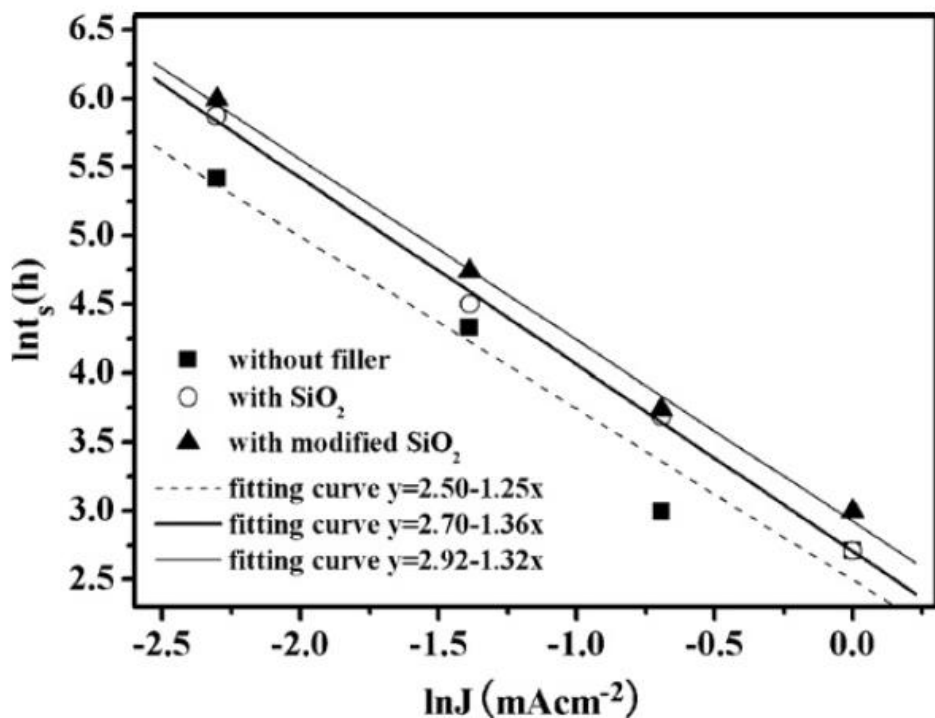


**Figure 1.3** Variation of the short-circuit time as a function of current density of Li/PEO/Li and Li/PEO+SiO<sub>2</sub>/Li visualization cells undergoing galvanostatic polarization at 60°C. Reproduced with permission from [27].

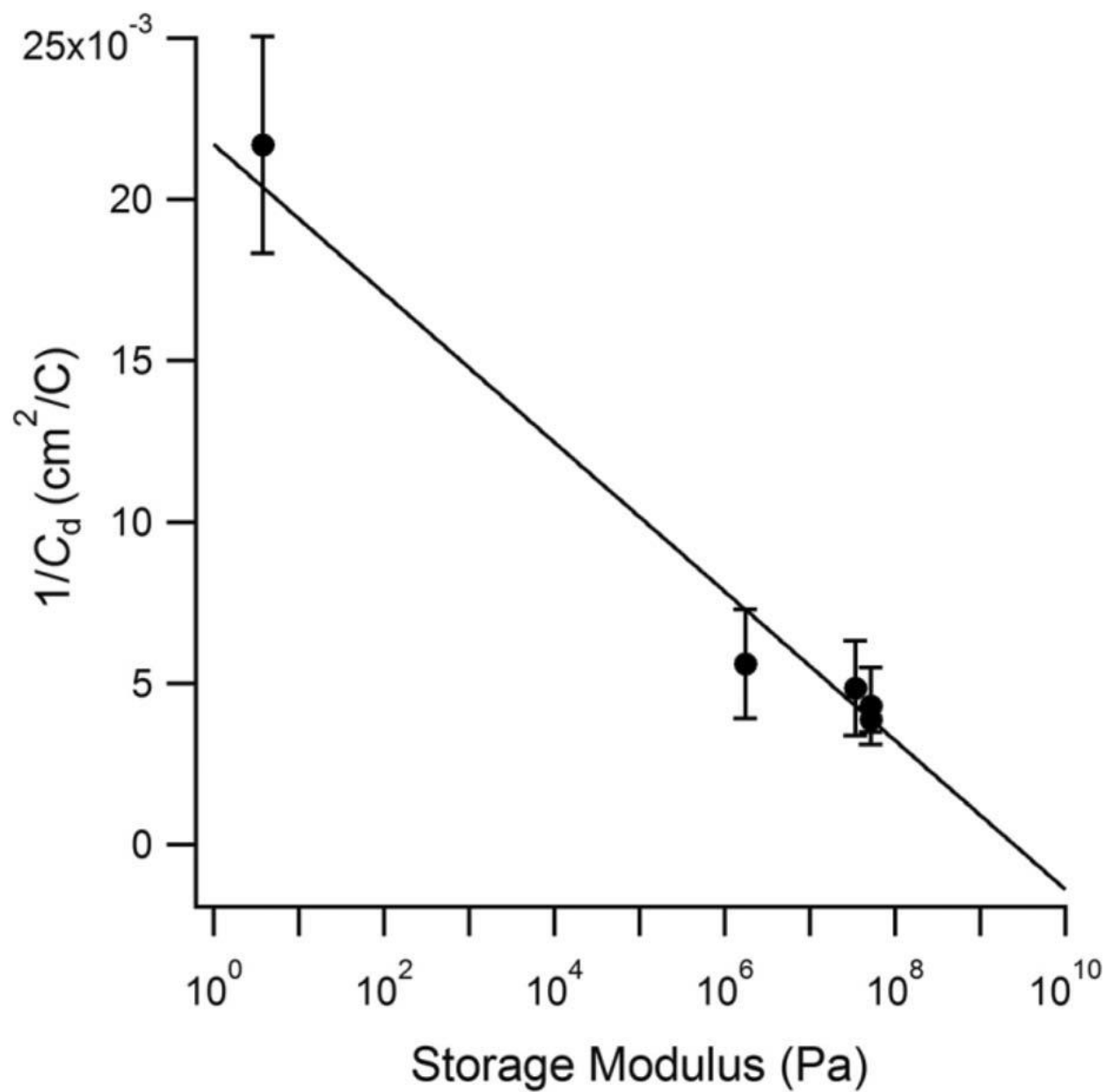


**Figure 1.4** Variation of the inverse of the charge passed until short-circuit ( $C_d = t_{sc} \times J$ ) of Li/SEO/Li coin cells at 90°C undergoing galvanostatic cycling as a function of electrolyte shear storage modulus. Reproduced with permission from [31].

## References

- [1] P. Agarwal, H. Qi, L. A. Archer, *Nano letters* 2010, 10, 111.
- [2] S. Srivastava, J. H. Shin, L. A. Archer, *Soft Matter* 2012, 8, 4097.
- [3] S. Srivastava, L. A. Archer, S. Narayanan, *Physical Review Letters* 2013, 110, 148302.
- [4] P. Agarwal, S. A. Kim, L. A. Archer, *Physical Review Letters* 2012, 109.
- [5] S. S. Moganty, N. Jayaprakash, J. L. Nugent, J. Shen, L. A. Archer, *Angew. Chem. Int. Ed.* 2010, 49, 9158.
- [6] S. S. Moganty, S. Srivastava, Y. Lu, J. L. Schaefer, S. A. Rizvi, L. A. Archer, *Chemistry of Materials* 2012, 24, 1386.
- [7] Y. Lu, S. S. Moganty, J. L. Schaefer, L. A. Archer, *Journal of Materials Chemistry* 2012, 22, 4066.
- [8] Y. Lu, S. K. Das, S. S. Moganty, L. A. Archer, *Advanced Materials* 2012, 24, 4430.
- [9] M. S. Whittingham, *Science* 1976, 192, 1126.
- [10] M. S. Whittingham, *United States Patent* 1977, 4009052.
- [11] M. Armand, J.-M. Tarascon, *Nature* 2008, 451, 652.
- [12] P. G. Bruce, L. J. Hardwick, K. M. Abraham, *MRS Bulletin* 2011, 36, 506.
- [13] D. Bresser, S. Passerini, B. Scrosati, *Chemical Communications* 2013, 49, 10545.
- [14] Xu, J. Wang, F. Ding, X. Chen, E. Nasybulin, Y. Zhang, J.-G. Zhang, *Energy & Environmental Science* 2013.
- [15] D. Aurbach, Y. Talyosef, B. Markovsky, E. Markevich, E. Zinigrad, L. Asraf, J. S. Gnanaraj, H.-J. Kim, *Electrochimica Acta* 2004, 50, 247.
- [16] R. Bouchet, S. Maria, R. Meziane, A. Aboulaich, L. Lienafa, J.-P. Bonnet, T. N. T. Phan, D. Bertin, D. Gigmes, D. Devaux, R. Denoyel, M. Armand, *Nature Materials* 2013, 12, 452.

- [17] J. Yamaki, S. Tobishima, K. Hayashi, K. Saito, Y. Nemoto, M. Arakawa, Journal of Power Sources 1998, 74, 219.
- [18] T. Tatsuma, M. Taguchi, M. Iwaku, T. Sotomura, N. Oyama, Journal of Electroanalytical Chemistry 1999, 472, 142.
- [19] M. Dolle, L. Sannier, B. Beaudoin, M. Trentin, J.-M. Tarascon, Electrochemical and Solid-State Letters 2002, 5, A286.
- [20] P. C. Howlett, D. R. MacFarlane, A. F. Hollenkamp, Journal of Power Sources 2003, 114, 277.
- [21] I. W. Seong, C. H. Hong, B. K. Kim, W. Y. Yoon, Journal of Power Sources 2008, 178, 760.
- [22] L. Gireaud, S. Gruegeon, S. Laruelle, B. Yrieix, J.-M. Tarascon, Electrochemistry Communications 2006, 1639.
- [23] J.-N. Chazalviel, Physical Review A 1990, 42, 7355.
- [24] C. Brissot, M. Rosso, J.-N. Chazalviel, S. Lascaud, Journal of Power Sources 1999, 81-82, 925.
- [25] M. Rosso, T. Gobron, C. Brissot, J.-N. Chazalviel, S. Lascaud, Journal of Power Sources 2001, 97-98, 804.
- [26] C. Brissot, M. Rosso, J.-N. Chazalviel, S. Lascaud, Journal of The Electrochemical Society 1999, 146, 4393.
- [27] S. Liu, N. Imanishi, T. Zhang, A. Hirano, Y. Takeda, O. Yamamoto, J. Yang, Journal of Power Sources 2010, 195, 6847.
- [28] S. Liu, N. Imanishi, T. Zhang, A. Hirano, Y. Takeda, O. Yamamoto, J. Yang, Journal of The Electrochemical Society 2010, 157, A1092.

- [29] S. Liu, H. Wang, N. Imanishi, T. Zhang, A. Hirano, Y. Takeda, O. Yamamoto, J. Yang, Journal of Power Sources 2011, 196, 7681.
- [30] C. Monroe, J. Newman, Journal of The Electrochemical Society 2005, 152, A396.
- [31] G. M. Stone, S. A. Mullin, A. A. Teran, D. T. H. Jr., A. M. Minor, A. Hexemer, N. P. Balsara, Journal of The Electrochemical Society 2012, 159, A222.

## CHAPTER 2.

### ELECTROLYTES FOR HIGH-ENERGY LITHIUM BATTERIES

Reproduced with Permission from Applied Nanoscience, 2012, by Jennifer L. Schaefer, Yingying Lu, Surya S. Moganty, Praveen Agarwal, N. Jayaprakash, and Lynden A. Archer.

**Abstract:** From aqueous liquid electrolytes for lithium-air cells to ionic liquid electrolytes that permit continuous, high-rate cycling of secondary batteries comprised of metallic lithium anodes, we show that many of the key impediments to progress in developing next-generation batteries with high specific energies can be overcome with clever designs of the electrolyte. When these designs are coupled with as cleverly engineered electrode configurations that control chemical interactions between the electrolyte and electrode or by simple additives-based schemes for manipulating physical contact between the electrolyte and electrode, we further show that rechargeable battery configurations can be facilely designed to achieve desirable safety, energy density, and cycling performance.

#### 1. Introduction

Most commercial secondary/rechargeable lithium batteries are based on the lithium ion cell depicted in Figure 1. A carbonaceous material such as graphite serves as the anode and hosts lithium as  $\text{LiC}_6$  in the charged state. A lithiated metal oxide ( $\text{LiMO}$ , e.g.  $\text{LiCoO}_2$ ) cathode hosts

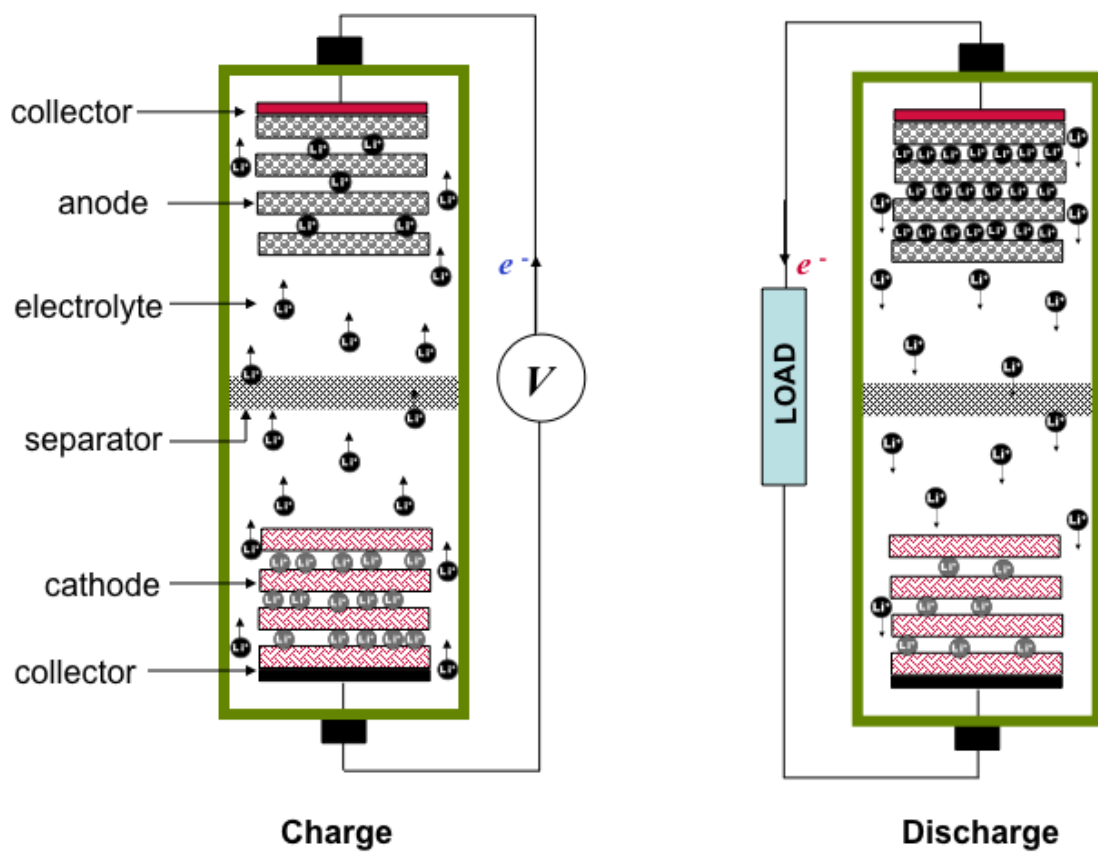


**Figure 1.1.** Schematic of a lithium ion battery during charge (left) and discharge (right)

the lithium in the discharged state. The anode and cathode are coupled internally by a lithium-ion conducting, aprotic organic ester or ether doped with a lithium salt (e.g. lithium hexafluorophosphate ( $\text{LiPF}_6$ )). Shuttling of lithium ions between the anode and cathode produces an electric current in an external circuit that drives a desired load. To prevent electrode/electrode contact and short circuits, a porous polyolefin film (separator) is typically inserted between the electrodes. Since the early 1990s, lithium ion batteries based on this design have been subjects of intense scientific and commercial interest for portable electronics applications. In recent years, the demand for secondary batteries with higher operating voltages, improved cycling stability, higher power densities, enhanced safety, and lower initial and life cycle costs has increased to meet new needs for smaller, lighter, more powerful electronic devices, as well as to accommodate growing interest in hybrid electric vehicles (HEV) and plug-in hybrid electric vehicles (PHEVs).

As illustrated in Figure 2, the  $\text{LiC}_6/\text{LiCoO}_2$  cell delivers one of the lowest specific energies of possible secondary battery configurations. Yet it remains attractive because this cell configuration offers superior energy densities, attractive operating voltages, lower self-discharge rates and a performance/cost structure that is competitive with the nickel metal hydride (NiMH) and other rechargeable battery configurations already in commercial use for HEVs. Additionally, even after taking into account the substantially lower practical specific energies of the  $\text{LiC}_6/\text{LiCoO}_2$  ion battery (typically only about 1/3 of the maximum energy density is available in a fully packaged battery), this LIB configuration delivers a specific energy that exceeds the medium-term and comes close to the long-term goals set out by the US Advanced Battery Consortium<sup>1</sup>. Finally, all of the alternative cell configurations depicted in the figure, particularly those that offer exceptional specific energies, suffer from one or more debilitating limitations,

most involving the electrolyte, which prevent their widespread use. This review focuses on the modern search for electrolytes suitable for large-scale deployment in secondary lithium-based battery technologies that offer significantly improved performance and safety relative to the LiC<sub>6</sub>/LiCoO<sub>2</sub>-based platform.

A successful electrolyte is required to play multiple, critical roles in an electrochemical cell. First, it should isolate the electron and ion transport pathways in the cell. Second, it should promote ion pair dissociation and selectively facilitate transport of the active ionic species (e.g. Li<sup>+</sup> ions in a lithium battery). Third, it must penetrate and wet the porous, chemically heterogeneous hybrid materials that constitute the electrodes and separator. Fourth, it should not leak, combust, or vaporize during cell storage or operation. Fifth, it should be chemically robust in the presence of the electrodes and their redox products. Finally, it must itself be stable in the normal operating voltage range for the electrochemical cell. Significantly, these features must be maintained over thousands, even tens of thousands of charge-discharge cycles spanning many years of cell operation. Because it is rare for all six requirements to be met in a single material, the search for a successful electrolyte typically requires years of trial-and-error experimentation, including independent searches for suitable additives that might correct one or more shortcomings of an attractive material.

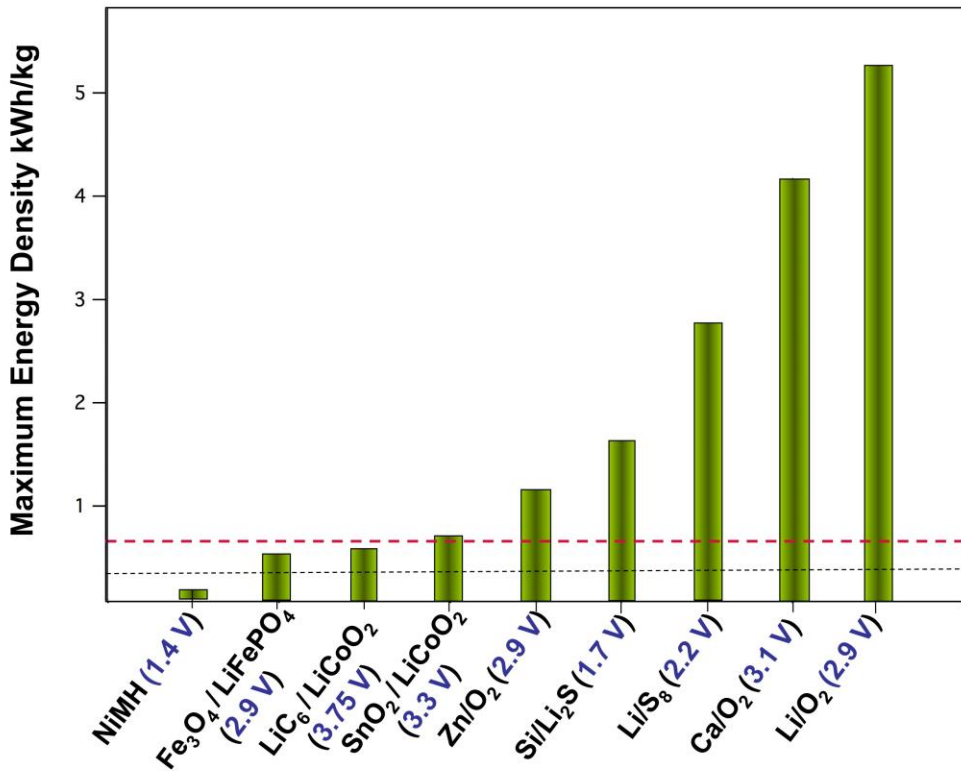


Figure 2. Theoretical specific energy and open circuit potentials for various high-energy density secondary battery configurations. The specific energies for all of the metal/air battery configurations include the weight of oxygen. The horizontal lines are the USABC medium-(black) and long-term (red) targets escalated by a factor of 3 to account for the typical factor of three reduction in energy density that occurs when inert cell components (packaging, electrolyte, conductivity aid, and current collectors) are included.

Organic esters and ethers, which have polar groups are attractive as LIB electrolytes because they possess good affinity for lithium ions, moderate dielectric constants, and moderate to low viscosities at room temperature (Table 1). Small Bjerrum lengths,

$$l_B = \frac{e^2}{4\pi\epsilon kT},$$

and attractive Stokes ion mobilities,

$$u_i \approx \frac{z_i e}{6\pi a_i \eta}$$

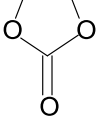
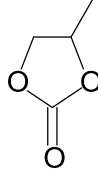
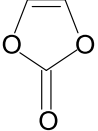
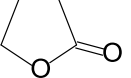
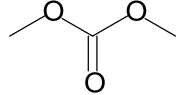
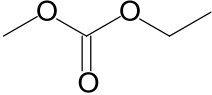
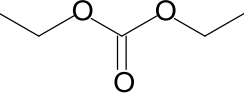
are also typical of these electrolytes under normal LIB operation conditions. Here,  $e$  is the elementary charge;  $\epsilon$  is the dielectric constant of the medium;  $k$  is Boltzmann's constant;  $T$  the absolute temperature;  $z_i$  and  $a_i$  are, respectively the valency and radius of ionic species " $i$ "; and  $\eta$  is the viscosity of the medium. Thus, even a moderately large counterion (radius:  $a_- > l_B$ ), is sufficient to produce high levels of ion-pair dissociation from the compact lithium ions (radius:  $a_+ = 0.076\text{nm}$ ). The most common choices, ethylene carbonate (EC) coupled with a linear carbonate co-solvent – dimethyl carbonate (DMC), diethyl carbonate (DEC), ethylmethyl carbonate (EMC) - and doped with LiPF<sub>6</sub>, also offer superior ionic conductivities to all alternatives: ionic-liquids, polymers, and ceramics. However, these electrolytes are volatile, flammable, leak, display poor thermal stability, possess high reduction potentials (Table 1), narrow electrochemical stability windows, and poor mechanical stability, which present obvious challenges for their large-scale deployment in batteries. Additionally, electrolytes based on organic ethers dissolve lithium polysulfides LiS<sub>x</sub>, which erodes the cathode in high-energy lithium/sulfur and silicon/Li<sub>2</sub>S secondary batteries, and do not dissolve Li<sub>2</sub>O<sub>2</sub>, clogging the

porous cathode in ultra-high energy density lithium-air batteries (Fig. 2); making them incompatible with the most energy dense lithium battery platforms.

Efforts to manage and/or ameliorate the most serious problems with aprotic organic electrolytes are extensive and nicely documented in several excellent reviews<sup>1-6</sup>. It is now understood, for example, that because the potential at either LIB electrode decays over a distance of order the Debye length,

$$l_D = \left( \frac{\epsilon_0 \epsilon_r kT}{(n_+^2 + n_-^2 z_-^2) e^2} \right)^{1/2},$$

the high relative electrolyte permittivity,  $\epsilon_r$ , and salt concentrations ( $n = n_+ + n_-$ : QM) typically employed to ensure high ionic conductivities also means that the electrolyte in the vicinity of the electrode is subjected to large potential gradients. Where  $\epsilon_0$  is the permittivity of vacuum and  $n_i$  is the molar concentration of unassociated ionic species  $i$  in solution. Thus, even under moderate cell potentials where the pure electrolyte may be nominally stable, it will degrade continuously when in contact with either electrode. Several studies have shown that the degradation product is an electrically insulating but ionically conducting polymer, and that its thickness and porosity can be controlled (by introducing additives to the electrolyte and/or by initially cycling the cell at a low rate) to create a passivating coating that slows/stops subsequent electrolyte degradation.<sup>5-7</sup> This benefit is perhaps intuitive since an electronically insulating polymer coating of any thickness reduces the magnitude of the potential gradients at the solid electrolyte interface (SEI). Numerous approaches for controlling the SEI in aprotic

			
RP = 1.36 V	1.00-1.60 V	1.40 V	1.25 V
OP = 6.2 V	4.0-6.6 V		
FP = 160°C	132°C	73°C	97°C
$\epsilon$ = 89.78	64.92	VC	39
$\eta$ = 1.90 cP (40°C)	2.53 cP		1.73 cP
EC	PC		GBL
			
1.32 V	6.7 V	1.32 V	
5.0-6.7 V	27°C	6.7 V	
18°C	2.958	31°C	
3.107	0.65 cP	2.805	
0.59 cP (20°C)	EMC	0.75 cP	
DMC		DEC	

**Table 1.** Chemical structures of common liquid electrolyte components and their properties: RP = reduction potentials (as reported by Yoshio, et al. [6]), OP = oxidation potentials (as summarized from Xu3), FP = flash point,  $\epsilon$  = dielectric constant at 25°C,  $\eta$  = viscosity at 25°C unless otherwise noted

organic electrolytes have been reported, we will review the most recent methods at the end of Section 2 of the review.

The review is organized as follows. In Section 2 we report on progress in development and characterization of novel liquid electrolyte systems for high energy density lithium batteries. In Section 3 we review progress on solid-state electrolytes based on ceramics and polymers, and in Section 4 discuss mixed phase solid-liquid electrolytes.

## **2.0 Liquid Electrolytes for High Energy Batteries**

### **2.1 Aqueous Electrolytes for Lithium Batteries**

Aqueous electrolytes preserve many of the advantages of aprotic liquid electrolytes but provide an environmentally friendly, non-flammable, low cost solution for some of their shortcomings.

Until recently, the narrow electrochemical stability window of liquid water (1.23 V) and its reactivity with metallic electrodes prevented successful implementation in lithium batteries. Lou et al. recently reported results from a detailed study of the reactivity of various electrode materials in aqueous electrolytes.<sup>8</sup> These authors showed that by manipulating the pH of the electrolyte it is possible to shift the electrochemical stability window. Further, they demonstrated that if dissolved oxygen is eliminated and carbon-coated electrodes employed, aqueous lithium-ion batteries based on materials such as  $\text{LiTi}_2(\text{PO}_4)_3/\text{LiFePO}_4$  can be cycled at a rate of 1 C to yield a specific energy of  $50 \text{ W h kg}^{-1}$  based on the total weight of the electrode materials. This energy density is competitive with lead-acid and Ni-Cd batteries. However, the aqueous lithium-ion battery offers a much higher power density, retaining 80% of the reversible capacity when

the rate is increased to 10 C. Furthermore, the battery manifested over 90% capacity retention over 1000 charge/discharge cycles.

The benefits of aqueous electrolytes for lithium batteries are even more markedly evident for Li-air batteries.<sup>9,10</sup> As illustrated in Figure 2, the theoretical specific energy of the lithium/air battery (including the oxygen cathode) is 5.2 kWh/kg. Most designs utilize a porous/open carbon cathode configuration designed to facilitate continuous re-supply of oxygen from the surroundings and therefore potentially offer substantially higher specific energies, 11 kWh/kg. These values are comparable to typical energy densities for coal, 6.7 kW·h/kg, and are only marginally lower than the specific energy of commercial-grade gasoline, 12 kW·h/kg. Works on Li-air batteries employing aqueous electrolytes rely upon the high solubility of  $\text{Li}_2\text{O}_2$  in water to avert problems with premature fouling of the porous cathode, but achieve this effect by employing decidedly different approaches for protecting the metallic lithium anode from water. The all-aqueous Li-air battery utilizes an inert ceramic solid-state electrolyte coating on the anode which protects it from water, but is sufficiently conductive for  $\text{Li}^+$  ions to facilitate the shuttling reaction. In the mixed electrolyte Li-air battery configuration proposed by Zhou and co-workers,<sup>9</sup> the anode and porous cathode are separated by a water impermeable, lithium ion conductive membrane (e.g. LISICON). The cathode is in contact with the aqueous electrolyte and the metallic lithium anode is in contact with an aprotic liquid electrolyte. The primary advantage of these designs is that the cathode is submerged in water, the discharge reaction product is soluble in water and so this eliminates problems of cathode clogging, expansion, and electrical conductivity that result with the use of an aprotic electrolyte. Wang, et. al.<sup>11</sup> reported cathode capacities of 50,000 mAh/g (based on the total mass of porous catalytic electrode) when the Li-air cells were cycled at a low rate (100 mAh/g).

## 2.2 Electrolytes for Secondary Lithium-Sulfur Batteries

As illustrated in Figure 2, the Li-S and Si-Li<sub>2</sub>S secondary batteries provide among the highest specific energies of lithium-based cells. Sulfur, the active material used in both cathode configurations, is inexpensive, abundant, and non-toxic. Early reports showed Li/S cells with organic liquid electrolytes display poor cycle life and low Columbic efficiencies. Cycling of a sulfur cathode results in the formation of various lithium polysulfides such as Li<sub>2</sub>S, Li<sub>2</sub>S<sub>2</sub>, Li<sub>2</sub>S<sub>3</sub>, and Li<sub>2</sub>S<sub>4</sub>.<sup>12-14</sup> These polysulfides are soluble in the typical aprotic carbonate liquid electrolytes, resulting in dissolution/erosion of the cathode by the electrolyte upon cycling. The resultant fall-off/fading of the cathode capacity presents a significant barrier for successful implementation of sulfur cathodes.

Many investigations have focused on combinations of liquid electrolytes, as well as of electrolytes and additives, which display various levels of success in reducing polysulfide dissolution, while still demonstrating sufficient ionic conductivity, safety, and electrochemical stability. For example, tetrahydrofuran (THF),<sup>15</sup> 1,3-dioxolane (DOXL),<sup>13,16,17</sup> dimethoxy ethane (DME), carbonates,<sup>18,19</sup> and polyethylene glycol dimethyl ethers (PEGDME)<sup>12,16,19-23</sup> have been investigated. Among these electrolytes, tetra(ethylene glycol)dimethyl ether (TEGDME), a dimethyl terminated polyethylene oxide oligomer, has been found to be particularly attractive. Without any efforts to modify the cathode, Li/S cells employing TEGDME-based electrolytes have been shown to provide specific capacities over 1200 mAh g<sup>-1</sup> during the first charge at room temperature.<sup>13,15,23,24</sup> Choi, Kim, and their co-workers<sup>20,25</sup> reported the performance of TEGDME / 1M LiCF<sub>3</sub>SO<sub>3</sub> electrolyte solution and compared its performance with a variety of

other electrolyte formulations. Significantly, a cell employing a solution of 5 vol.% toluene in TEGDME was reported to maintain a discharge capacity of 533 mAh g<sup>-1</sup> following 50 cycles at a low rate (1/16 C) and exhibited near stable impedance spectra upon cycling.

Mikhaylik et al.<sup>26</sup> and Ryu et al.<sup>23</sup> both show that performance of TEGDME electrolytes in Li/S cells is markedly worse at low-temperature. By adding 1,3-dioxolane (DOXL) and methylacetate (MA) to the TEGDME electrolyte in the ratio of MA–DOXL–TEGDME (5:47.5:47.5, v/v), Ryu et. al. observed that the first discharge capacity can be significantly improved to 994 mAh g<sup>-1</sup> at -10°C from 357 mAh g<sup>-1</sup>. Shin and Cairns showed that Li/S cells could be successfully cycled with an electrolyte mixture of PEGDME M<sub>n</sub> = 250 and 1-butyl-1-methylpyrrolidinium bis(trifluoromethanesulphonyl)imide (C4mpyr TFSI) ionic liquid.<sup>27</sup> The addition of PEGDME to the ionic liquid was found to reduce its viscosity and enhance ionic conductivity to 4.2 x 10<sup>-3</sup> S/cm at 29°C. When cycled at room temperature and at low rates, the Li/S cell with C4mpyr TFSI-0.5 M LiTFSI-2 PEGDME electrolyte maintained a discharge capacity of 269 mAh g<sup>-1</sup> after 100 cycles; the cells exhibited poor performance at lower temperatures, however. Cells containing pure C4mpyr-LiTFSI electrolyte, without PEGDME, exhibited poor cycling performance at all temperatures due to polysulfide dissolution.

Recently, several studies have reported that encapsulation of the sulfur into a porous carbon framework wetted by the electrolyte can significantly improve performance of Li/S batteries. Nazar and co-workers<sup>28</sup> for example showed that Li/S cells based on a nanocomposite cathode, created by wicking molten sulfur into a conductive, mesoporous carbon framework, and an

electrolyte comprised of 1.2 M LiPF<sub>6</sub> solution in ethyl methyl sulphone can be cycled at moderate rates (~0.2 C) to yield specific capacities exceeding 800 mAh g<sup>-1</sup>, with some capacity fade after 20 cycles. When a layer of polyethylene glycol was appended to the particles, the authors reported that the Li/S cell capacity improved noticeably, to above 1100 mAh g<sup>-1</sup>, and that the cells show no evidence of capacity fade after 20 charge/discharge cycles. Figure 3 reports results from a more recent study by Jayaprakash et al.,<sup>29</sup> which employed a high-pressure method to infuse sulfur sublimate in the vapor phase into mesoporous, hollow carbon particles (Fig. 3(a)) synthesized by high-temperature calcination of petroleum pitch. Cyclic voltammetry measurements (Fig. 3b) of Li/S cells employing these S@C composite materials and an electrolyte comprised of 1 M lithium bis (trifluoromethane sulfone) imide (LiTFSI) in TEGDME indicate stable electrochemical performance after 50 cycles. Figure 3(c) shows the first-cycle voltage profile of the material during galvanostatic cycling at low (0.1C) as well as high (3C) charge rates, Figure 3(d) reports the discharge capacity based on the active sulfur, which comprises 70 w% of the S@C composite, measured at a rate of 0.5 C. Although small levels of capacity fading is evident in Fig 3(d), these results attest to the electrochemical stability of the composite sulfur-carbon cathode material in the TEGDME-based electrolyte.

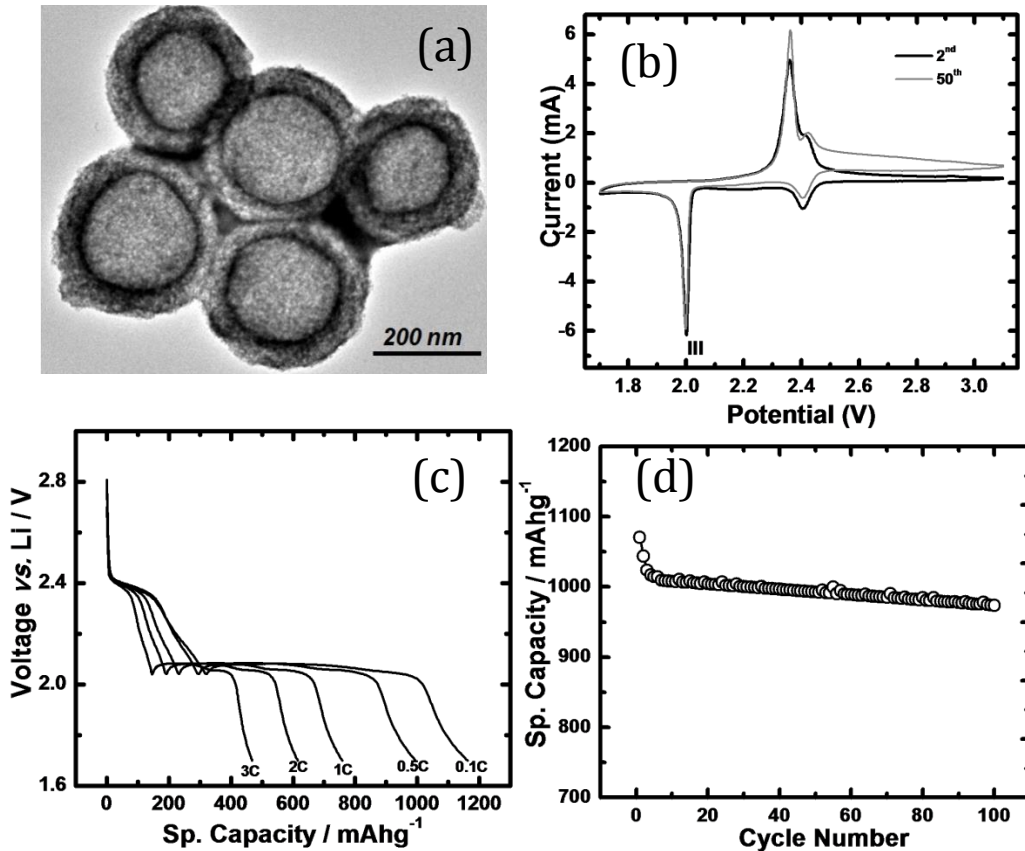


**Figure 3.** Li/S secondary battery based on S@C composite and PEGME/LiTFSI electrolyte. (a) Transmission Electron micrograph of sulfur infused mesoporous, hollow carbon particles; (b) Cyclic voltammetry data for S@C at a scan rate of 0.2 mV/s. Results are for the 2nd and 50th cycle; (c) First discharge voltage profiles for Li/S at various discharge rates; (d) Specific discharge capacity versus cycle number for Li/S cell at a fixed discharge rate of 0.5C.

### **2.3 Electrolytes based on Ionic Liquids**

One of the most straightforward changes that can be made within the current LIB framework ( $\text{LiMO}/\text{LiC}_6$ ) to increase specific energies is to increase the Li-ion insertion potential at the cathode. Cathodes based on  $\text{LiM}_{0.5}\text{Mn}_{1.5}\text{O}_4$  or  $\text{LiMMnO}_4$  spinels, where M is a divalent or trivalent metal (e.g. copper, nickel, iron, cobalt, chromium), can form the basis of LIBs with open circuit potentials close to, or even exceeding, 5V.<sup>30</sup> Unfortunately, none of the currently used aprotic liquid electrolytes can be safely used at such high cell potentials. High temperature molten salts (liquid oxides, silicates, etc.) have been studied for a long time<sup>31</sup> and have been speculated for some time as potential LIB electrolytes for high-voltage cells. Typical cation and anion structures that are suitable for creating ILs are depicted in Figure 4. Unlike molten salts, room temperature ionic liquids (ILs) are organic salts having melting points below 100 °C.<sup>32</sup> The earliest IL, ethyl-ammonium nitrate, was synthesized in 1914 with a melting point of 12 °C.<sup>33</sup> A few ionic liquids were later developed for electroplating,<sup>34</sup> catalysis,<sup>35</sup> and organic synthesis. In 1992, Wilkes and Zaworotko<sup>36</sup> developed air and water stable low melting point tetrafluoroborate ionic liquids.

ILs exhibit many interesting properties, including ultra-low vapor pressure, good thermal stability, wide range of solubility of organic and inorganic compounds, high polarity and non-coordinating nature, hydrophilic and lipophilic nature, high ionic conductivity, wide electrochemical stability windows, and tunability, which make them attractive as battery electrolytes.<sup>37-39</sup> Among the large number of possible IL configurations, imidazolium and pyrrolidinium based ILs are most widely studied for their potential as next generation Li-ion

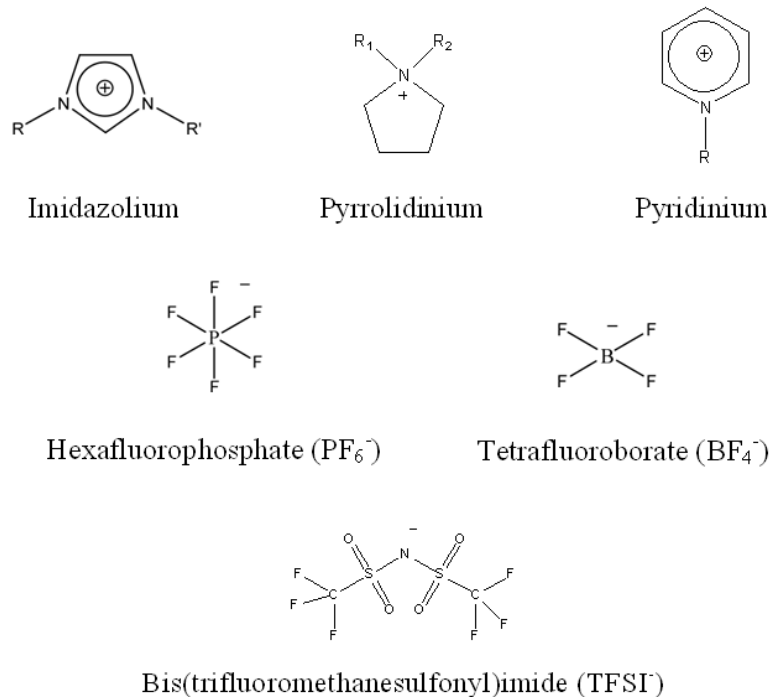


**Figure 4.** Chemical stuctures of representative cations and ions used for ionic liquid electrolytes.

battery electrolytes. The inherent robustness of the cation and anion of IL plays a vital role in dictating the overall redox stability of the IL.<sup>40</sup> Imidazolium based ILs exhibits stability window of about 4V and other cyclic amine based ILs, pyrrolidinium and piperdinium cations, show stability limits of about 6V (Figure 5).<sup>41-43</sup> Imidazolium based cations suffer from cathodic instabilities. Improvements in this area was demonstrated by Seki et al.,<sup>44</sup> whereas a ring substitution allowed for improved cycling efficiency against lithium metal. High stability windows have been reported for ILs containing TFSI anion.<sup>45</sup>

High lithium ion conductivity is a desirable characteristic for Li ion battery electrolytes. Total ionic conductivities of ILs range from  $10^{-4}$  to  $10^{-2}$  S/cm at room temperature<sup>46</sup> Imidazolium based ILs shows comparatively higher values of conductivities than pyrrolidinium based ILs. Irrespective of the type of cation and anion, addition of Li salt to the IL decreases the overall ionic conductivity due to an increase in viscosity and the formation of ionic clusters with  $\text{Li}^+$ . The effect of Li salt concentration on 1-2-Dimethyl-3-propyl imidazolium bis(trifluoromethyl sulfonyl)imide IL electrochemical properties, such as ionic conductivity, viscosity, and interfacial resistances at the  $\text{LiCoO}_2$  and Li metal interfaces, was studied by Seki et al.; they found that an optimum Li salt concentration exists for high rate performance batteries.<sup>47</sup> Appetecchi et al found that increase alkyl chain length resulted in decrease in ionic conductivity of N-alkyl-N-methylpyrrolidinium bis(trifluoromethylsulfonyl)imide ILs.<sup>48</sup> Watanabe and coworkers<sup>49</sup> investigated the effect of anion on the physicochemical properties of 1-butyl-3-methylimidazolium cation based ILs. They concluded that the molar conductivity ratio has the

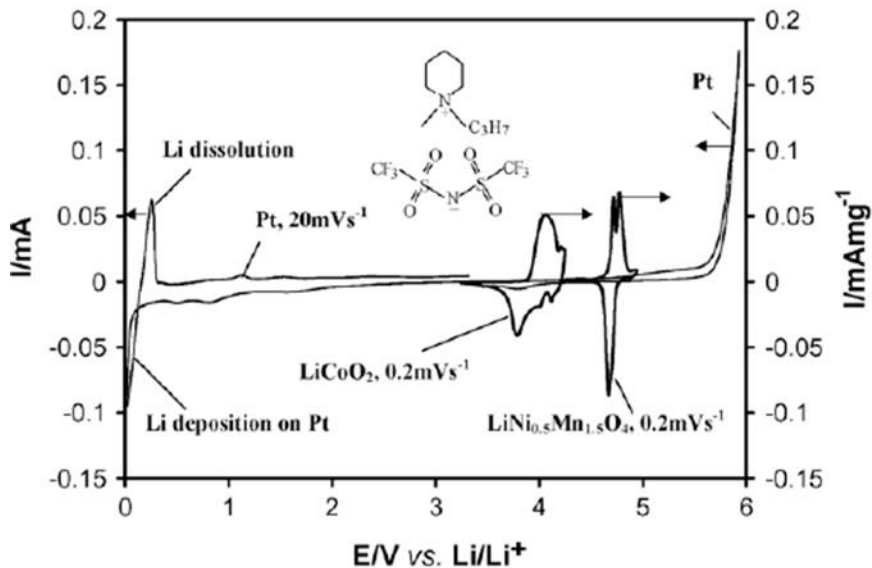


**Figure 5.** The electrochemical stability window of 0.5M LiTFSI in a N-methyl-N-propylpiperdinium bis(trifluoromethanesulfonyl)imide electrolyte solution measured on a Pt electrode and cyclic voltammograms of LiCoO<sub>2</sub> and LiNi<sub>0.5</sub>Mn<sub>1.5</sub>O<sub>4</sub> spinel electrodes, as indicated. Reprinted from J. Power Sources, 189, S.K. Martha, E. Markevich, V. Burgel, G. Salitra, E. Zinigrad, B. Markovsky, H. Sclar, Z. Pramovich, O. Heik, D. Aurbach, I. Exnar, H. Buqa, T. Drezen, G. Semrau, M. Schmidt, D. Kovacheva, N. Saliyski, A short review on surface chemical aspects of Li batteries: A key for a good performance, 288-296, (2009), with permission from Elsevier.

following order in the IL anions studied: hexafluorophosphate (PF<sub>6</sub>) > tetrafluoroborate (BF<sub>4</sub>) > bis (pentafluoroethylsulfonyl) imide (BETI) > bis(trifluoromethylsulfonyl)imide (TFSI) >

trifluoromethanesulfonate (TfO) > trifluoroacetate(TFA). The observed trend is related to the anionic characteristics such as charge delocalization and fluorine content, where a higher molar conductivity ratio is found for ILs that dissociate more readily. And while ionic liquids display high total ionic conductivities, they exhibit low lithium transference numbers and thus lower lithium ion conductivity when compared to other liquid electrolytes. Addition of neutral molecules such as vinylene carbonate, tetrahydrofuran, ethylene carbonate, and toluene have been reported by MacFarlane and coworkers to significantly change transport properties of N-ethyl-N-propylpyrrolidinium bis(trifluoromethane sulfonyl)imide.<sup>50</sup> The chemical identity and donor ability of diluents play a major role in enhancing the Li-ion transport properties of LiTFSI solutions of IL.

Lee et al. reported synthesis and electrochemical characterization of a series of ILs with methyl acetate moiety.<sup>51</sup> These ILs exhibited large redox stabilities and high ionic conductivities, with an increase in conductivity with the presence of Li salt due to the interaction between Li<sup>+</sup> and the ester group on the cation of the ILs. Similarly, Egashira showed the improved properties of the quaternary ammonium based ILs containing cyano functional groups.<sup>52</sup> Most recently, Hussey and coworkers designed and synthesized a series of piperdinium cation based ILs with a propylene carbonate (PC) moiety that showed favorable electrochemical characteristics for Li metal batteries.<sup>53</sup>

Some ionic liquids, such as 1-butyl-1-methylpyrrolidinium bis (trifluoro methanesulphonyl) imide (C4mpyr TFSI),<sup>54-58</sup> have been shown to enhance uniform deposition on the lithium metal anode thus reducing dendrite formation without additional additives. This opens up the way for the highest energy density lithium batteries of all: those doped with LiTFSI is thought to occur due to formation of crystalline-like liquid layers at the interface with the

crystalline electrode.<sup>59</sup> This phenomenon is not understood, and varying effects are seen experimentally with chemical changes to the plating substrate or electrolyte.

The tunability of ILs evidently offers a spectrum of opportunities to modify the properties required for successful preparation of next generation Li battery electrolytes that are non-volatile, non-flammable, and thermally stable at high temperatures. Significant challenges exist in developing ionic liquids with sufficiently high lithium ion conductivity that also function well with high-energy-storage capacity electrodes such as sulfur and lithium metal. However, the recent upsurge of broad-based interest in ILs leads us to the perhaps hopeful conclusion that in a matter of years IL electrolyte configurations suitable for the most energy dense batteries of all (metal-air cells) will be found.

## 2.5 Additives for Aprotic Liquid Electrolytes

Easily polymerizable electrolyte additives, such vinylene carbonate (VC) and catechole carbonate, have been shown to be particularly effective in producing stable SEI coatings on LiC<sub>6</sub> and LiCoO<sub>2</sub>.<sup>54,55</sup> Their use results in very small irreversible capacity loss upon SEI creation without sacrifices in the stability of electrodes or ionic conductivity, thus extending the life cycle of lithium-ion cells. The discharge capacity and cycling performance of PC-based electrolytes containing butyl sultone (BS) have been studied by Xu et al.<sup>56</sup> These authors show that BS rapidly formed a protective film on the graphite electrode and improved room temperature battery performance. Other sulfones, including 1, 3-propane sulfone (PS),<sup>57</sup> have been used as additives in LIBs employing mixed carbonate electrolytes EC/DEC/DMC-1 M PF<sub>6</sub> electrolyte. Significantly, when paired with another SEI additive, succinic anhydride (SA), Lee et al. showed

that PS additives are suitable for stabilizing a mixed 1:2 EC/EMC-1M LiPF<sub>6</sub> electrolyte in a LiNi<sub>0.5</sub>Mn<sub>1.5</sub>O<sub>4</sub>/graphite 5V cells.<sup>58</sup> Butylene sulfite has recently been shown to be a good SEI additive for PC-based electrolytes employed in both high-voltage, LiMn<sub>1.99</sub>Ce<sub>0.01</sub>O<sub>4</sub>/graphite, and high-power, LiFePO<sub>4</sub>/graphite electrodes.<sup>59</sup>

Another approach proposed by Menkin, Golodnitsky and their co-workers<sup>60</sup> is to employ a pre-formed, artificial, SEI to stabilize the interface. These authors used electropainting and vacuum-insertion techniques to deposit a polymer based on poly(ethylene-co-acrylic acid) and carboxymethylcellulose on graphite as well as Sn–Cu composite anode. They showed that the artificial SEI produced close to a five-fold improvement in the cycling performance of the battery. Likewise, Song<sup>61</sup> employed Fourier transform infrared spectroscopy to show that trimethoxy methyl silane spontaneously polymerizes on a metallic Si anode in an EC/DC (1:1) electrolyte. These authors reported capacities of 2400 mAh/g for over 200 charge/discharge cycles. An even more dramatic illustration of this concept comes from work by Lee et al.<sup>62</sup>, which investigated the effect of triacetoxymethylsilane (VS) on the surface morphology of a metallic lithium electrode cycled at 1.25 mA cm<sup>-2</sup> (C/2) in 1:1 EC/DMC-1 M PF<sub>6</sub> with varying VS content. Remarkably, these authors showed that an electrolyte containing 2 wt.% VS minimized the formation of lithium dendrites and maintained 80% of the initial capacity after 200 cycles in the LiCoO<sub>2</sub>/Li cell.

The flammability of aprotic liquid electrolytes represents another significant threat to their large-scale deployment, particularly in large secondary batteries.<sup>63</sup> Flame retardant (FR) additives aim

to reduce this threat while maintaining good ionic conductivity and cycling characteristics. Most FRs act by chemical radical scavenging, which terminates the radical chain combustion reaction.<sup>64</sup> Ideally, the amount of the FR should be kept below 20 vol.%, to minimize deleterious effects on battery performance;<sup>65</sup> however, ignition under high pressure of oxygen or other kinds of abuse conditions is still possible with the highly flammable linear carbonate solvents in this range. Organic phosphates (alkyl phosphates and aryl phosphates),<sup>66</sup> halogens, biphenyls, their combination or derivatives,<sup>67</sup> and nitrogen-containing compounds are by far the most common FRs. Hyung and co-workers<sup>68</sup> investigated a group of organic phosphate compounds, triphenylphosphate (TPP) and tributylphosphate (TBP) and found that they markedly improved the thermal stability of lithium-based cells. Shigematsu et al.<sup>69</sup> found that in a C/VEC-VC-LiPF<sub>6</sub>/Li<sub>x</sub>CoO<sub>2</sub> cell, trimethyl phosphate (TMP) promotes thermal stability of both electrodes. Morita et al.<sup>70</sup> showed that TMP perhaps achieves this benefit by preventing thermal decomposition of LiPF<sub>6</sub>. Cresyl diphenyl phosphate (CDP) FRs have been studied by Shim et al.<sup>71</sup>, as well as by Zhou et al.<sup>72</sup> Both groups showed the thermal stability and non-flammability of aprotic liquid electrolytes can be markedly improved by adding only 5wt% CDP. Zhang et al.<sup>73</sup> reported a new flame-retardant called vinyl-tris-(methoxydiethoxy)silane (VTMS). Their combustion tests revealed that the addition of VTMS at 5–15 vol % could dramatically reduce the flammability of a 1 M LiPF<sub>6</sub>-EC/EMC/DMC (1:1:1, v/v/v) electrolyte. Recently, Fei and Allcoc<sup>74</sup> reported that a PC electrolyte containing methoxyethoxyethoxy phosphazene oligomers and the corresponding high molecular weight polymer simultaneously exhibits attractive flame retardance and good ionic conductivity.

### **3.0 Solid State Electrolytes: Ceramics, Polymers, Composites, and Hybrids**

All-solid-state batteries have some inherent advantages over liquid electrolytes, namely no chance of electrolyte leakage and reduced flammability. They also allow for the implementation of advanced battery architectures and the possibility of safe implementation of rechargeable, high energy density batteries employing lithium metal anodes by mechanical inhibition of lithium dendrite formation that can cause cell short-circuiting. However, the ionic conductivity of dry cells is often less, especially at room temperature, than that of liquid cells. Current work in the solid-state electrolyte field aims to mitigate losses in ionic conductivity, and therefore cell rate capability, while still improving safety and efficient cycling behavior.

#### **3.1 Ceramic electrolytes**

Ceramic electrolytes are non-flammable and thermally stable to high temperatures. They are also mechanically strong- nanoindentation measurements of lithium phosphonate oxide (LiPON) demonstrate elastic modulus of 77 GPa,<sup>81</sup> this is well beyond the minimum value of 3.4 GPa predicted by Newman<sup>82</sup> that is required of an electrolyte to suppress metallic lithium dendrite formation. And despite their mechanical strength, many ceramic electrolytes demonstrate excellent room temperature ionic conductivity ( $> 10^{-3}$  S/cm) with lithium transference  $\sim 1$ . Fergus<sup>83</sup> recently published a comprehensive review of ionic conductivity data for ceramic and polymer electrolytes, which provides an excellent comparison of the ionic conductivity of the three main classes of ceramic electrolytes- sulfides, oxides, and phosphates. Another review by Patil, et al.<sup>84</sup> provides a comprehensive history of thin film battery development, including ceramic electrolytes, through 2008. It is important to note that while many ceramics exhibit

ionic conductivity on the order of  $10^{-3}$  S/cm at room temperature, it is LiPON with an ionic conductivity of only  $2 \times 10^{-6}$  S/cm that has had gained widespread use, suggesting that other properties play an important role in the success of the electrolyte. Vacuum-sputtered LiPON is an amorphous ceramic with a wide electrochemical stability window (5.5 V vs. Li), interfacial stability in contact with metallic lithium, thermal stability up to 300°C, and an ionic conductivity which is acceptable for use in a thin film battery with micron-scale (or thinner) electrolyte thickness.<sup>85</sup>

Solid-state batteries utilizing ceramic electrolytes can exhibit high interfacial impedances, as some ceramics, including many sulfides, react with common anode and cathode chemistries such as LiCoO<sub>2</sub>. Since reactivity of a pair of electrolyte-electrode materials is not always obvious, interfacial impedance characterization must be performed. For example, one report showed a stable SEI formed between an alloy Li-Al anode and thio-LISICON type electrolytes with compositions Li<sub>3.4</sub>Si<sub>0.4</sub>P<sub>0.6</sub>S<sub>4</sub> and Li<sub>3.25</sub>Ge<sub>0.25</sub>P<sub>0.75</sub>S<sub>4</sub>, with activation energies at the interface smaller or comparable to those reported for a lithium metal/composite polymer electrolyte interface.<sup>86</sup> However, Li<sub>3</sub>PO<sub>4</sub>-Li<sub>2</sub>S-SiS<sub>2</sub> and thio-LISICON Li<sub>3.325</sub>P<sub>0.935</sub>S<sub>4</sub> electrolytes reacted continuously with the Li-Al anode. Takahara has reported decomposition at the Li<sub>3</sub>PO<sub>4</sub>-Li<sub>2</sub>S-SiS<sub>2</sub> and Li metal interface.<sup>87</sup> Electronic conductivity of perovskite type lithium lanthanum titanate oxide (LLT) is enhanced significantly by contact with metallic lithium due to Ti<sup>4+</sup> reduction.<sup>88</sup> Oxide impurities form at interface of LLT and LiCoO<sub>2</sub> cathode with sintering, creating high interfacial resistance that dominates cell behavior, while LiMnO<sub>4</sub> was shown to form a low resistance interface with LLT. Similarly, the formation of inert oxide layer increases the LiNi<sub>0.5</sub>Mn<sub>0.5</sub>O<sub>2</sub>/LATSP interfacial resistance, blocking the Li-ion diffusion through the interface.<sup>89</sup> Li<sub>7</sub>La<sub>3</sub>Zr<sub>2</sub>O<sub>12</sub> (LLZ) was calcined to obtain a garnet-like structure pellet that in a

symmetric Li cell showed interfaced stability, reversible plating and de-plating with no reaction. However, Li/LLZ/LiCoO<sub>2</sub> cell that was successfully cycled showed irreversible behavior between LLZ and LiCoO<sub>2</sub>.<sup>90</sup>

In order to improve ceramic electrolyte-electrode compatibility and still maintain good overall cell capacity, nanoscale intermediary films have been used to prevent interfacial reactions. LiCoO<sub>2</sub> cathodes were spray coated with Li<sub>4</sub>Ti<sub>5</sub>O<sub>12</sub> to form a protective layer between the cathode and sulfide electrolyte thio-LiSICON which prevented formation of a highly resistive space-charge layer.<sup>91</sup> In more recent work, Li<sub>2</sub>O-SiO<sub>2</sub>, a coating without a transition metal oxide, was shown as effective in protecting LiCoO<sub>2</sub> with use with sulfide electrolyte Li<sub>2</sub>S-P<sub>2</sub>S<sub>5</sub>.<sup>92</sup>

Ceramic electrolytes as a whole also have drawbacks that limit their implementation. They are brittle and can require more expensive processing conditions such as high temperature sintering (> 1300°C) and deposition by sputtering.<sup>93</sup> The brittleness of the ceramic electrolyte can result in cracking, as the electrolyte is unable to accommodate volume changes in the electrodes due to lithium insertion/de-insertion. To mitigate this concern, recent work has investigated pairing the ceramic electrolyte against a polymer electrolyte that allows for volume expansion.<sup>94</sup> The brittleness of the ceramic electrolyte also limits the cell configurations it may be used in – traditionally, ceramic electrolytes were considered only for flat, thin film batteries. The growing field of micro electromechanical systems (MEMS) being developed requires a power source with maximum energy density and a minimized footprint; to meet this end, 3D battery configurations are being explored.

Ceramic electrolytes are ideal candidates for MEMS applications because not only are they immobile solids, they are thermally stable at the high temperatures present locally in microcircuits. Recently, conformal LiPON films were successfully deposited by magnetron sputtering in N<sub>2</sub> gas at 2.6 Pa on both off-axis planar substrates and 3D substrates with 10-100 micron features.<sup>95</sup> While the deposition rate decreases for off-axis areas and the film composition varies, the electrolyte still provides a nearly uniform Li<sup>+</sup> ionic conductivity of 2+-1 x 10<sup>-6</sup> S/cm throughout. In other work, 3D batteries were fabricated using a honeycomb, LLT electrolyte filled with oxide cathode particles and sol gel precursors.<sup>96</sup> Good electrolyte-electrode contact was formed via this method, and a battery utilizing a LiMnO<sub>4</sub> cathode displayed low interfacial impedance. The batteries were successfully cycled, but suffered from very poor discharge capacities, attributed to the large size of the electrolyte honeycomb pores (180 μm).

### 3.2 Polymer electrolytes

Polymers have long been recognized as promising electrolyte candidates. Unlike brittle ceramic electrolytes, polymer-based electrolytes have the advantage of being lightweight and flexible, allowing for coiled cell configurations. Polymer electrolytes, unlike some ceramics, are unreactive with common oxide electrodes; they also perform better than liquid electrolytes in conjunction with sulfur cathodes and display wide electrochemical stability windows. The main drawback of polymer electrolytes is their low ionic conductivity, especially at room temperature.

In 1973, polyethylene oxide (PEO) was found to be conductive when complexed with an alkali metal salt.<sup>97</sup> In 1979, the first battery using a solid polymer electrolyte (SPE), PEO complexed with a lithium salt, was produced.<sup>98</sup> Remarkably, the majority of work in this field is still dedicated to PEO due to its relatively high ionic conductivity when compared with other polymers. PEO-based electrolytes have traditionally been plagued with poor room temperature conductivity due to crystallization of the matrix, so efforts have been made to extend amorphicity into the room temperature range. Large organic salts such as LiTFSI aid in this regard, as the anions act as a plasticizer, allowing the polymer chains to move more freely.

While improvements in conductivity are desirable, studies have shown that among electrolytes with similar lithium ion conductivity, those with high total ionic conductivity and low lithium transference numbers exhibit poorer electrochemical properties.<sup>99</sup> In addition, theoretical predictions by Rosso et. al. suggest that the onset time for dendritic lithium growth, and subsequent short circuit time, has an inversely squared dependence on the anion transference number.<sup>100</sup> Thus it is desirable to make single ion polymer conductors, or ionomers - polymer backbones with tethered anions that associate with free Li<sup>+</sup>. Colby, et. al. have shown that ions in these environments tend to aggregate into pairs, trimers, quadrapoles, with few free lithium ions.<sup>101-104</sup> Therefore, conduction is governed by the trimer, which moves by segmental motion of the backbone, dissociating and reforming as it travels. This mechanism leads to impractically low conductivities in these systems, though lithium transference is unity. Recently, mixed polymer systems of PEO and poly(lithium acrylate) salts were shown to have improved conductivity ( $10^{-6}$  S/cm at room temperature and  $10^{-4}$  S/cm at elevated temperatures) in the presence of the additive BF<sub>3</sub>OEt<sub>2</sub>, which coordinates with the tethered carboxylate anion and

promotes ion-pair dissociation.<sup>105</sup> This work suggests that single ion-conducting conductors with high conductivity may be possible with improvements in anion coordinating additives.

Amorphous polymer electrolytes typically soften with improvements in ionic conductivity; this loss of mechanical integrity makes them less desirable for application in lithium-metal based batteries. Improvements in mechanical properties of solid-state polymer-based electrolytes have been demonstrated via crosslinked polymer, block co-polymer, and small molecule polymer crystalline electrolytes, as well as polymer-ceramic composite and polymer-ceramic hybrid electrolytes, discussed in later sections.

Crosslinked polymer electrolyte films have been synthesized by a number of methods, including chemical cross-linking,<sup>106-108</sup> photochemically cross-linking,<sup>109</sup> UV-cross-linking,<sup>110</sup> and electron-beam cross-linking.<sup>111</sup> Solid cross-linked electrolytes based on PEO, without added solvent, generally exhibit ionic conductivities around  $10^{-5}$  S/cm at room temperature as the cross-linking inhibits chain crystallization, though it slows chain mobility. Cross-linking also increases the tensile strength of the films to the MPa range.

The majority of work in the block copolymer electrolyte field has centered on materials with continuous, majority PEO blocks and minority blocks of a stiffer, typically non-conducting, polymer to enhance mechanical properties. We will highlight two recent works. Kofinas, et al.<sup>112,113</sup> have synthesized a PEO-b-(PMMA-ran-PMMALi) diblock copolymer with a minority random copolymer block of methyl methacrylate (MMA) and lithium salt of methacrylic acid (MMALi) to provide an additional lithium source. When doped with LiBC<sub>4</sub>O<sub>8</sub> (LiBOB), the copolymer electrolyte is a transparent, flexible film with an ionic conductivity of  $1 \times 10^{-5}$  S/cm, lithium transference of 0.9, and electrochemical stability above 5V at room temperature. Niitani,

et al.<sup>114</sup> reported a polystyrene (PS)-block- polyethylene glycol methyl ethyl methacrylate (PPEGMA)<sub>2</sub> star shaped copolymer with a PS core and PPEGMA arms. When doped with LiBETI, the star copolymer electrolyte is a flexible film with a total ionic conductivity on the order of  $10^{-4}$  S/cm at room temperature. The notable enhanced total ionic conductivity of this electrolyte may be attributed to the geometric configuration of the block copolymer, where many short ethylene oxide chains are employed instead of one long chain, which inhibits crystallization of the conducting phase.

Decoupling of mechanical and conduction properties in a block copolymer electrolyte has been demonstrated by Balsara, et al. using a material with a continuous non-conducting phase (Fig. 6).<sup>115,116</sup> The PS-block-PEO lamellar electrolytes, doped with LiTFSI, manifested ionic conductivities in the range  $10^{-4}$ - $10^{-5}$  S/cm from 90-120°C and dynamic storage moduli of  $10^7$ - $10^8$  Pa. The lamellar block copolymer electrolyte exhibited significant improvement in mechanical properties with little change in conductivity, thereby demonstrating that independent control of these properties is possible. Energy-filtered TEM showed that ions were accumulating, increasingly localized, in the center of the PEO lamellae as the chain molecular weight increased. Stress calculations indicate that local stress interferes with the ability of the PEO near to the phase boundaries to interact with the salt, thus decreasing ion concentration in wall regions that have lower mobility. Overall, the properties of the lamellar block copolymer electrolyte are quite attractive at elevated temperatures ( $\sim 100^\circ\text{C}$ ); improvement in conductivity at lower temperatures appears necessary for use of the system in a room-temperature secondary battery.

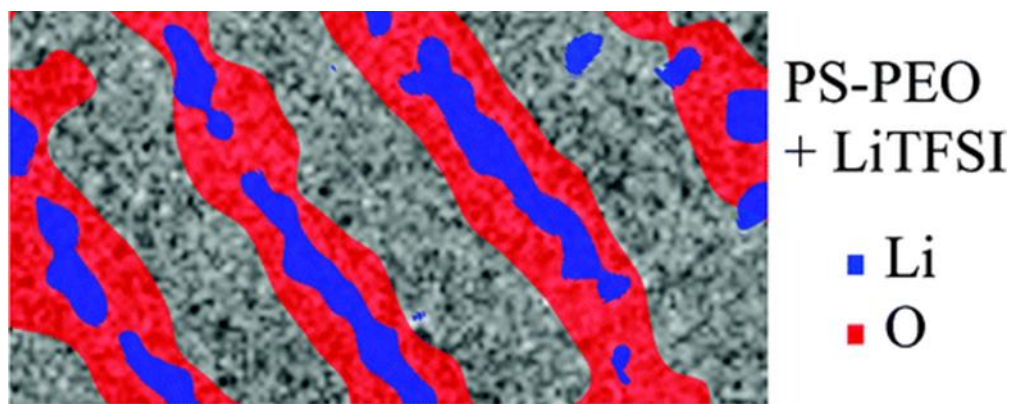


**Figure 6.** Distribution of lithium in a PS-PEO block copolymer electrolyte doped with LiTFSI as determined by energy-filtered transmission electron microscopy. Reprinted with permission from Nano Letters, 9(3), E. D. Gomez, A. Panday, E. H. Feng, V. Chen, G. M. Stone, A. Minor, C. Kisielowski, K. H. Downing, O. Borodin, G. D. Smith, N. P. Balsara, Effect of ion distribution on conductivity in block copolymer electrolytes, 1212-1216, (2009). Copyright (2009) American Chemical Society.

Decoupling of mechanical and conduction properties in polymers has also been demonstrated by a relatively new class of materials, crystalline polymer-salt complexes or small molecule electrolytes.<sup>117-120</sup> These complexes of short PEO chains (glymes) and lithium salt form crystals with varying structures depending on the EO/Li<sup>+</sup> ratio and glyme length. In most cases, the glyme chain forms a helix around the lithium ions and anions are free outside of the helix. The lithium ions are then able to conduct through the helix tunnel and along the glyme backbone. Increasing order, and therefore decreasing defects between tunnels, improves the ionic conductivity. Dopants of lithium salts with a different ion (i.e. addition of a small amount of LiTFSI to a LiAsF<sub>6</sub> doped electrolyte) have been shown to improve conductivity, as have an increasing the number of chain ends per crystallite and having chains with -OC<sub>2</sub>H<sub>5</sub> ends. The ionic conductivity of crystalline electrolytes is still low, 10<sup>-8</sup> to 10<sup>-6</sup> S/cm at room temperature, but this field is relatively new. And like all polymer electrolytes, they are easily processable – an advantage over their ceramic electrolyte counterparts.

### 3.3 Polymer-ceramic composite electrolytes

The addition of ceramic nanoparticles, such as TiO<sub>2</sub>,<sup>121,122</sup> SiO<sub>2</sub>,<sup>134,124</sup> Al<sub>2</sub>O<sub>3</sub>,<sup>125-127</sup> Fe<sub>3</sub>O<sub>4</sub>,<sup>128</sup> and S-ZrO<sub>2</sub>,<sup>129</sup> to polymer electrolytes has been shown to improve ionic conductivity, mechanical and electrochemical properties of the polymer electrolyte. The increase in ionic conductivity in composite electrolytes (CPEs) with inert fillers has been attributed to the nanoparticles acting as solid plasticizers, disturbing polymer crystallization. Comparative studies of nanofillers with varying chemistries and surface functionalized nanofillers reveal that the electrostatic environment near the particle surface can promote conduction of one species over another. It is

understood that Lewis acid-base surface groups interact with ions and PEO segments to create additional conduction pathways along the particle surfaces for lithium cations and/or interfere with anion transport.

Inadequate movement of polymer chains next to an electrode surface leads to a decline in salt transport and thus an increase in a salt concentration gradient.<sup>130</sup> The addition of ceramic additives increases polymer amorphicity and chain mobility. Ceramic fillers also can scavenge impurities from the electrolyte, which may have undesirable reactions with the electrode<sup>131</sup>. These combined effects reduce the interfacial resistance at the lithium electrode.<sup>125,128</sup> Reduction in the SEI improves the interface stability and reduces dendrite formation on lithium metal anodes. CPEs also have enhanced mechanical properties, with an increase in the Young's modulus and yield strength. Still, even with use of additives such as calix(6)pyrrole,<sup>129,131</sup> solid-state composite polymer systems based on high molecular weight PEO suffer from low ionic conductivity at room temperature and below which limits their practical application.

### **3.4 Polymer-ceramic hybrid electrolytes**

Polymer-ceramic hybrid electrolytes are studied for their potential to improve mechanical properties and prevent crystallization of polymer-based electrolytes. Miscibility between the organic and inorganic constituents of these materials is a concern that can be alleviated by appropriate chemistry. The majority of these hybrid materials have molecular scale inorganic regions crosslinked by an organic component. They are often synthesized by a sol-gel technique, polycondensation reactions of alkoxy silanes and end-functionalized homopolymers or copolymers.<sup>132-134</sup> Hybrids materials of similar form but varying chemistry were recently

demonstrated by reaction of polyethylene glycol with organometallic precursor methylalumoxane, an oxyaluminum cluster that contains up to twelve active reaction sites.<sup>135</sup> A deviation from this form was reported by Kao et al. who synthesized a mesoscopically ordered electrolyte with hexagonal arrays of inorganic cylinders by cocondensation of glydicyloxypropyl trimethoxysilane (GLYMO) and tetraethoxysilane (TEOS) and self-assembly of PEO-PPO-PEO triblock copolymer.<sup>136</sup> Ionic conductivities in the range of  $10^{-6}$  to  $10^{-4}$  S/cm at room temperature are typical of these hybrids; the framework is typically successful in preventing polymer crystallization above room temperature. Notably, all of these works fail to characterize the mechanical properties of the electrolyte and it is not clear how their strength compares to that of pure polymer and composite polymer electrolytes.

Recently, we reported on the synthesis of organic-inorganic hybrids created by dense functionalization of nanoscale ceramic particles with short polymer chains.<sup>137</sup> Physical properties of these materials are facilely tuned by changing the polymer chain (corona) length, grafting density, as well as the particle size, and inorganic content of the hybrids. The systems exist as jammed, self-suspended-suspensions of nanoparticles,<sup>137,138</sup> which manifest a yield-stress and, depending on the corona molecular weight, exhibit room-temperature ionic conductivities from  $10^{-3}$  to  $10^{-6}$  S/cm. Hybrids based on corona chains with terminal, reactive functional groups, allow the nanoparticle cores to be cross-linked to yield homogeneous organic-inorganic hybrid films with tensile moduli exceeding 0.1 GPa at room temperature.<sup>138</sup> Doping these films with a 1 M solution of LiTFSI in TEGDME produces a 10 fold reduction in the modulus to ~10 MPa (Figure 7), and room temperature ionic conductivities of  $2 \times 10^{-5}$  S/cm.

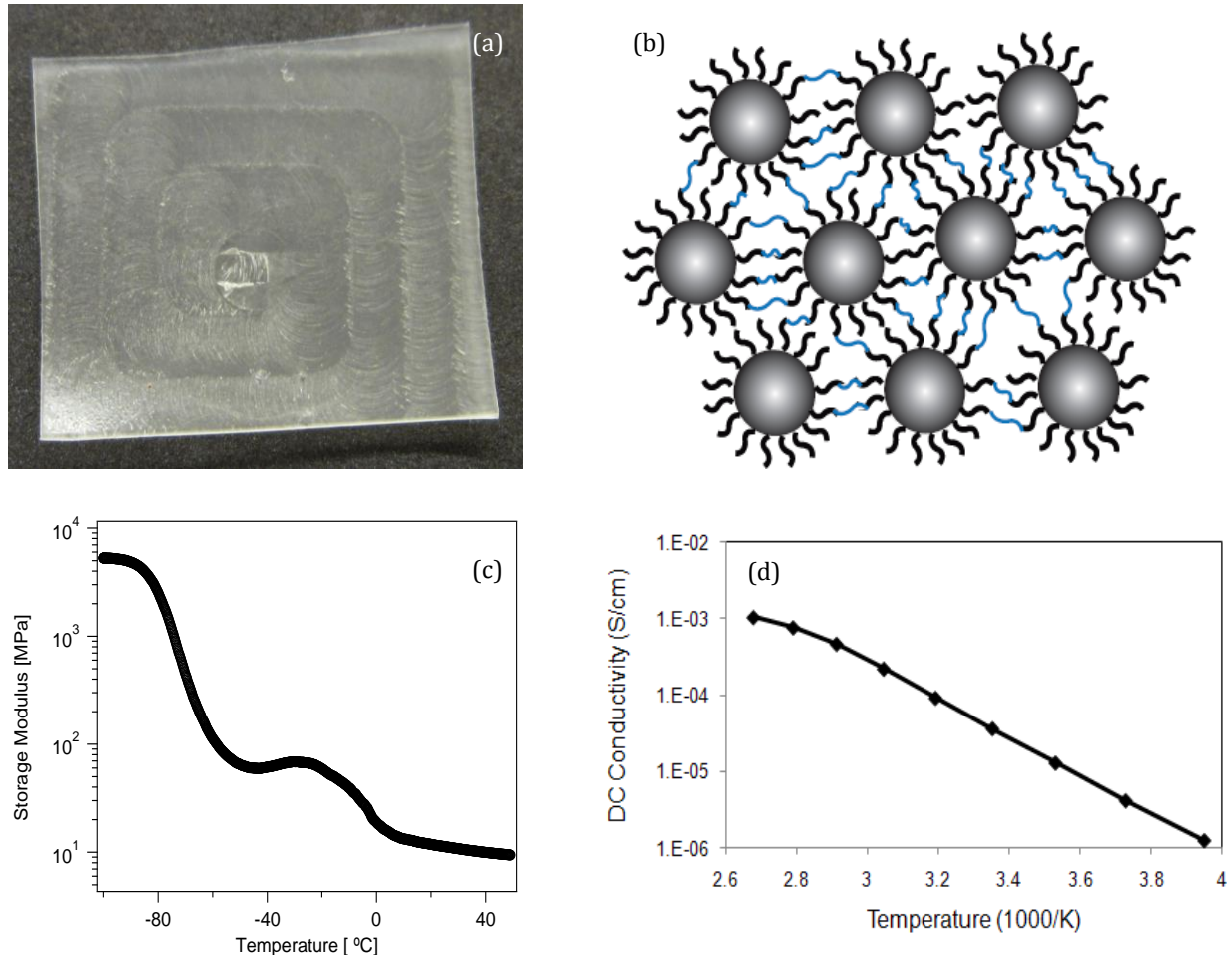


**Figure 7.** Cross-linked, nanoporous  $\text{SiO}_2$ -PEG film (a) photograph and (b) schematic of PEG hybrid's highlighting cross-linked chains; (c) Dynamic elastic modulus; and (d) Ionic conductivity of cross-linked hybrid film as a function of temperature, after swelling with 1 M LiTFSI in TEGDME.

## **4.0 Mixed Phase Electrolytes**

Mixed phase electrolytes, containing both solid and liquid components, offer a compromise in material properties whereas the liquid aids in conduction and the solid enhances mechanical properties. The majority of work in this field has previously been devoted to gel polymer electrolytes and soggy-sand electrolytes.

### **4.1 Polymer-liquid electrolytes**

Gel polymer electrolytes are comprised of a polymer matrix swollen with a liquid electrolyte, with or without a ceramic particle additive. The gel polymer is a free-standing film that eliminates the problem of leakage as with a traditional liquid electrolyte and thus the need for a separator, but still has nearly the same ionic conductivity and electrochemical properties of the imbibing fluid. The polymer matrix may be cross-linked or uncross-linked.

In the 1990s, Bellcore commercially produced the first plastic Li-ion battery. It utilized a poly(vinylidene fluoride)-hexafluoropropylene (PVdF-HFP) matrix with a EC-DMC-LiPF<sub>6</sub> liquid electrolyte and SiO<sub>2</sub> filler in a LiMn<sub>2</sub>O<sub>4</sub>/C cell.<sup>139</sup> PVdF-HFP is a copolymer with good mechanical integrity, chemical stability, and miscibility with carbonate-based electrolytes, unlike PEO. Still, the Bellcore electrolyte suffers from the other problems associated with aprotic liquid electrolytes: low thermal stability, low cathodic stability, volatility, flammability, and insufficient moduli to prevent dendritic lithium growth. Ionic liquid based gel polymer electrolytes are now widely studied as a possible solution to some of these issues,<sup>109,140-143</sup> PEO-based gel polymer electrolytes have also been explored, by swelling a high molecular weight PEO matrix with PEG oligomers.<sup>106</sup>

## 4.2 Ceramic-liquid electrolytes

“Soggy sand” electrolytes are created by doping a liquid electrolyte with ceramic nanoparticles.<sup>144-147</sup> At a given particle volume fraction  $\phi_{\text{onset}} << 0.01$ , a percolating particle network forms in the system (Fig. 8) and the physical nature of the bulk material may become gel-like. This gel state, similar to that achieved in polymer-liquid gel electrolytes, may render the separator in Li-ion cells unnecessary. The onset percolation threshold  $\phi_{\text{onset}}$  is a function of the chemical moieties on the particle surface for a given particle size, and the network is formed by hydrogen bonding and/or Van der Waal’s interactions between surface groups.

Certain dopants, such as unmodified aerosol silica,<sup>144</sup> methyl-capped aerosol silica,<sup>144</sup> or Li-exchanged hectorite nanoclay,<sup>146</sup> may increase ionic conductivity of the electrolyte up to half an order of magnitude at low  $\phi > \phi_{\text{onset}}$  by attracting the anion, thus breaking up an ion pair and freeing  $\text{Li}^+$  for conduction. Beyond a threshold volume fraction  $\phi_{\text{max}}$ , the ionic conductivity then declines due to blocking of the ionic conduction pathways. A soggy sand electrolyte of lithium perchlorate-ethylene glycol solution doped with unmodified aerosol silica at  $\phi = 0.07$  has a storage modulus  $G' = 5 \times 10^4$  Pa and ionic conductivity of  $7 \times 10^{-4}$  S/cm at room temperature, a 30% increase in conductivity compared with the pure electrolyte solution.<sup>144</sup> However, a change in the liquid to lithium perchlorate-methoxy polyethylene glycol solution resulted in a gel with  $G' = 1 \times 10^{-6}$  Pa and ionic conductivity of  $1 \times 10^{-4}$  S/cm, no improvement in conductivity over the undoped solution.<sup>145</sup> The effect of bonding structure and surface chemistry on conductivity in soggy sand electrolytes is still under investigation.

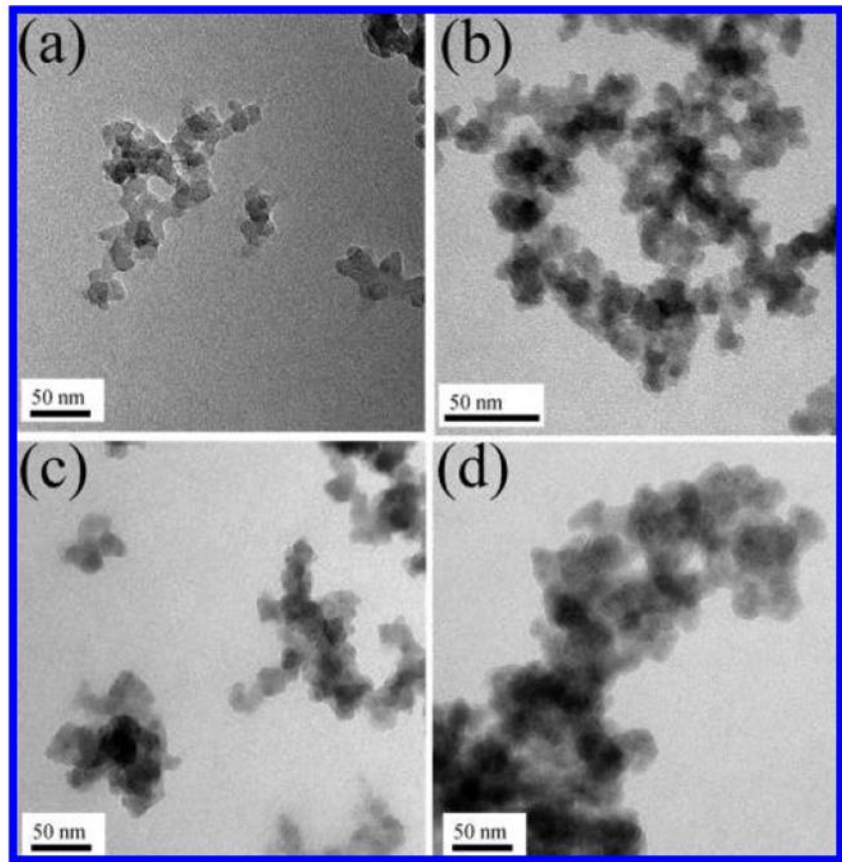


**Figure 8.** Transmission electron micrographs showing the intrinsic morphology of nonfunctionalized and functionalized aerosil silica particles used in the preparation of soggy sand electrolytes: (a) as-received; (b) methyl-capped; (c) amine-capped; and (d) octyl-capped.

Reprinted with permission from The Journal of Physical Chemistry C, 113(16), S. Das, A.

Bhattacharyya, 6699-6705, (2009). Copyright (2009) American Chemical Society

Ceramic-IL nanocomposites ILs have been investigated as electrolytes for dye sensitized solar cells. Graztel et al.<sup>146</sup> and Watanabe and et al.<sup>147</sup> have both noted improved properties by doping an IL electrolyte with silica.

Recently, Syzdek, et al. reported on a liquid-in-ceramic composite, where the ceramic provides a continuous supporting phase and is soaked with a liquid electrolyte.<sup>148</sup> The porous ceramic matrix was formed by a tape casting method, uni-axial pressing and grain sintering of a slurry of  $\square\text{-Al}_2\text{O}_3$  particles. Electrolytes were prepared by soaking the ceramic matrix in various PEGDME/LiClO<sub>4</sub> liquids. The electrochemical properties of the resulting electrolyte were found to depend on the liquid component and porosity of the support matrix.

### 4.3 Nanoporous hybrid electrolytes

Recently, we reported on a new class of mixed phase electrolytes, nanoporous hybrid electrolytes, of zirconia-imidazolium based ionic liquid hybrid (ZrO<sub>2</sub>-IL) doped with LiTFSI (Fig. 9)<sup>149</sup> and silica-polyethylene glycol (SiO<sub>2</sub>-PEG) hybrids suspended in PEGDME/LiTFSI (Fig. 10).<sup>150</sup> Like the solvent-free, cross-linked electrolytes introduced in section 3.4 of the review, both of these systems have uniformly dispersed, non-agglomerated ceramic nanocores surrounded by a percolating, organic ionic conduction pathway. This percolating conduction pathway allows for good ionic conductivities even at high particle loadings. A SiO<sub>2</sub>-PEG suspension electrolyte with  $\phi = 0.38$  displays a storage modulus close to 1 MPa and an ionic conductivity of  $3.5 \times 10^{-4}$  S/cm at 35°C, and even a practical conductivity of  $1.0 \times 10^{-4}$  S/cm at 10°C. In comparison, the ZrO<sub>2</sub>-IL electrolyte displayed an ionic conductivity of  $7 \times 10^{-4}$  S/cm at 100°C and  $2 \times 10^{-5}$  S/cm at 25°C with a storage modulus of 5 MPa at 150°C.

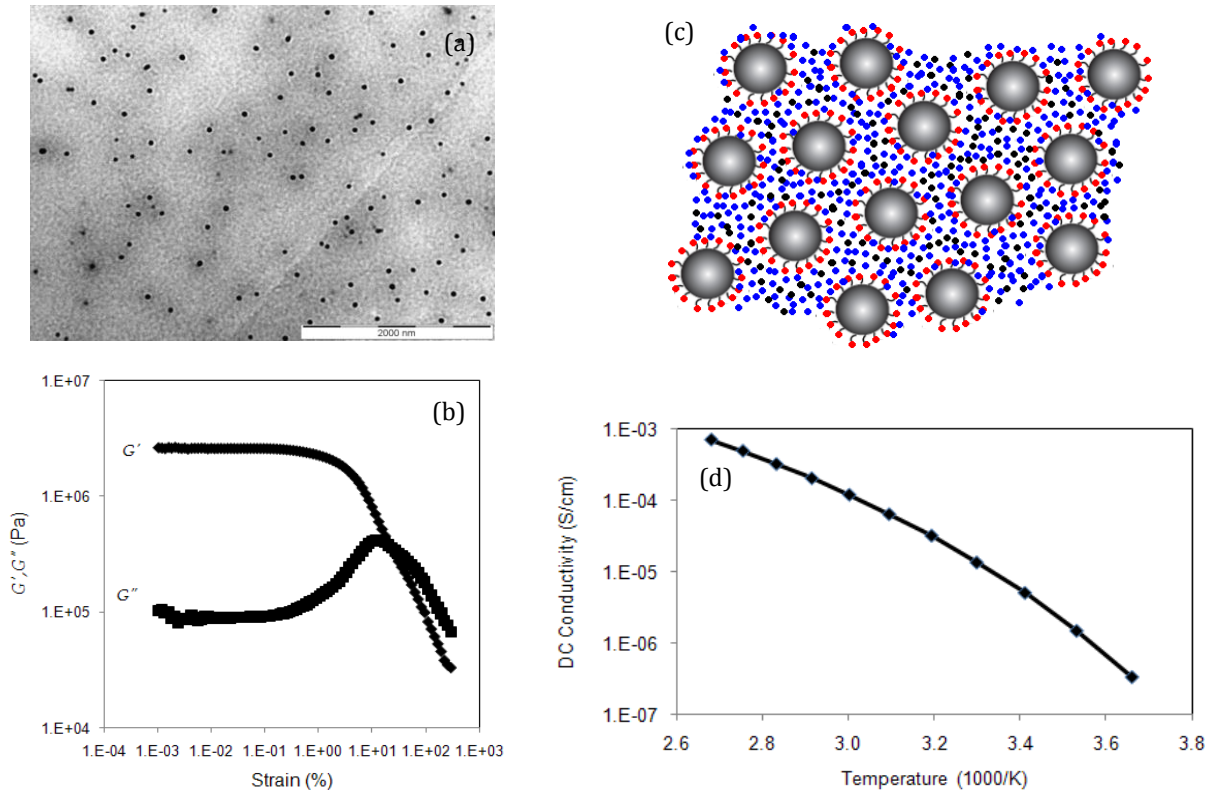


**Figure 9.**  $\text{ZrO}_2$ -IL hybrid electrolyte with a tethered imidazolium-based cation and free TFSI anion, doped with 1 M LiTFSI: (a) Transmission electron micrograph of  $\text{ZrO}_2$ -IL particles; (b) Dynamic shear moduli as a function of shear strain at 50°C; (c) Schematic, where red = imidazolium cation, black =  $\text{Li}^+$ , and blue =  $\text{TFSI}^-$ ; (d) Ionic conductivity.

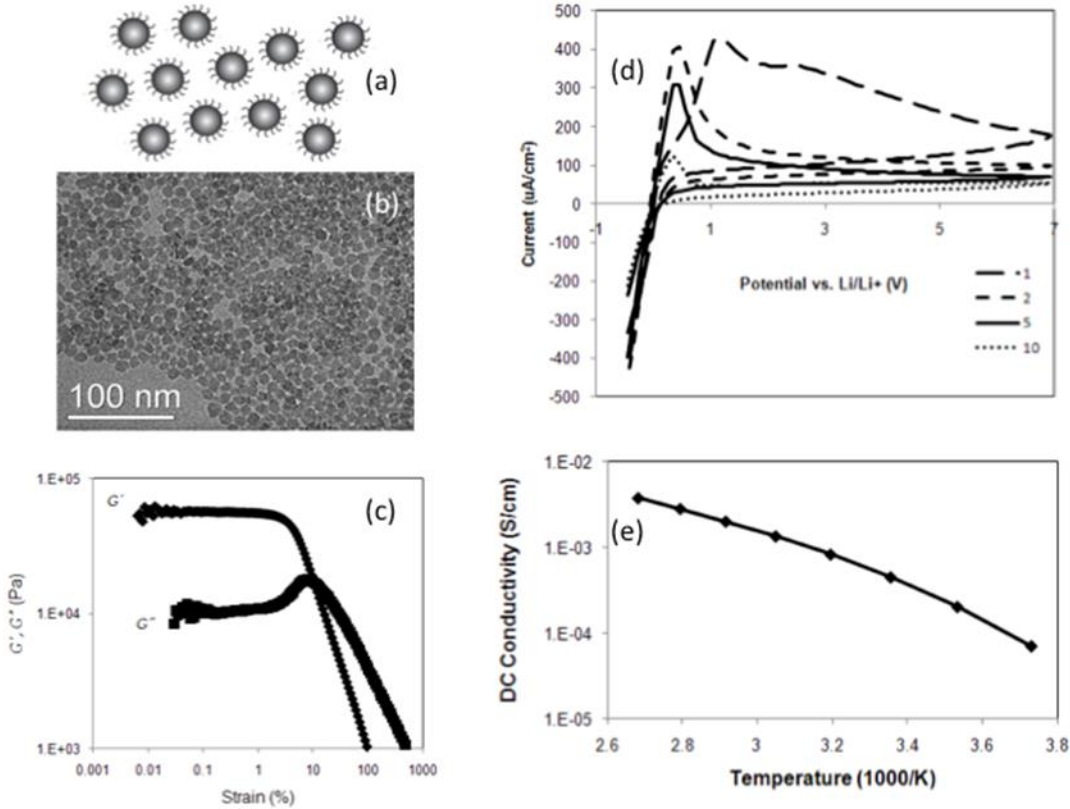


**Figure 10.** SiO<sub>2</sub>-PEG hybrid suspended in PEGDME and doped to 1 M LiTFSI in the organic phase,  $\phi = 0.3$ : (a) Schematic of hybrid suspensions; (b) Transmission electron micrograph of SiO<sub>2</sub>-PEG/PEGDME; (c) Dynamic shear moduli as a function of strain at 35°C; (d) cyclic voltammetry of a Li/electrolyte/Li cell at a scan rate of 1 mV/s for 10 cycles from -0.5 to 7.0 V vs. Li/Li<sup>+</sup>; (e) Ionic conductivity of SiO<sub>2</sub>-PEG/PEGDME suspension with  $\phi = 0.3$ .

Significantly, the ZrO<sub>2</sub>-IL electrolyte has a lithium transference number  $T_{Li^+} = 0.35 \pm 0.04$ , seven times larger than the value for the pure IL electrolytes (0.05).<sup>151</sup> This improvement in lithium

transference is attributed to the tethering of the IL imidazolium cation, leaving Li<sup>+</sup> as the only mobile cation in the system. Both of these systems display wide electrochemical stability windows and stable interfacial impedances against lithium metal.

Unlike previously studied electrolytes, these nanoporous hybrids behave mechanically as soft glasses when  $\phi > \phi^*$ , the threshold value for particle jamming. At ceramic fractions above  $\phi^*$  and at rest or under low strain ( $\gamma$ ), the electrolyte is jammed and behaves as a solid. When the applied strain exceeds the yield strain  $\gamma_y$ , the electrolyte flows as a liquid; this property is significant because it means that the electrolyte behaves as a solid in static conditions, such as inside a battery, yet can be facilely processed during normal cell assembly.

## 5.0 Conclusions

From aqueous liquid electrolytes for lithium-air cells to ionic liquid electrolytes that permit continuous, high-rate cycling of secondary batteries comprised of metallic lithium anodes we show that many of the key impediments to progress in developing next-generation batteries with high specific energies can be overcome with clever designs of the electrolyte. When these designs are coupled with cleverly engineered electrode configurations that control chemical interactions between the electrolyte and electrode (e.g. in Li/sulfur cells that employ encapsulation/ physisorption strategies for limiting dissolution of redox products in the electrolyte) or by simple additives-based schemes for manipulating physical contact between the electrolyte and electrode (e.g. through sacrificial additives that spontaneously form a stabilizing SEI layer), we further show that rechargeable battery configurations can be facilely designed to maximize performance and cycling stability. Judging from the large number of degrees of

freedom inherent in synthesizing organic-inorganic hybrid materials systems with explicit, desired properties, and the recent upsurge in interest in synthesizing ionic liquids with tunable solvation and ion transport properties, while preserving their desirable thermal and electrochemical stability, we are optimistic that in a matter of years commercially viable electrolytes will begin to appear that are suitable for safe deployment in the most energy-dense battery configurations of all, those based on the metal-air cell.

**Acknowledgements:** Work on synthesis, mechanical, and electrochemical characterization of nanoscale organic hybrid materials (NOHMs) was supported in part by Award No. KUS-C1-018-02, made by King Abdullah University of Science and Technology (KAUST), and by the National Science Foundation, Award No. DMR-1006323. Work on C@S hybrid lithium battery cathodes and the search for electrolytes for these systems was supported as part of the Energy Materials Center at Cornell, an Energy Frontier Research Center funded by the U.S. Department of Energy, Office of Basic Energy Sciences under Award Number DE-SC0001086. JLS also gratefully acknowledges support from the Materials for a Sustainable Future IGERT program, NSF grant # DGE-0903653.

## References

1. Miller TJ (2009) Electrical Energy Storage for Vehicles: Targets and Metrics, Ford Motor Company
2. Zhang SS (2006) A review on electrolyte additive for lithium-ion batteries. *J Power Sources* 162(2):1379-1394
3. Xu K (2004) Nonaqueous liquid electrolytes for lithium-based rechargeable batteries. *Chem Rev* 104(10):4303-4417.
4. Verma P, Maire P, Novak P (2010) A review of the features and analyses of the solid electrolyte interphase in Li-ion batteries. *Electrochim. Acta* 55(22):6332-6341
5. Aurbach D, Markovsky B, Salitra G, Markevich E, Talyossef Y, Koltypin M, Nazar L, Ellis B, Kovacheva D (2007) Review on electrode-electrolyte solution interactions, related to cathode materials for Li-ion batteries. *J. Power Sources* 165(2):491-499
6. M. Yoshio, R.J. Brodd, A. Kozawa (Eds) (2009), Lithium-Ion Batteries: Science & Technologies, Springer.
7. Scrosati B, Garche J (2010) Lithium batteries: Status, prospects and future. *J. Power Sources* 195(9):2419-2430
8. Luo J-Y, Cui W-J, He P, Xia Y-Y (2010) Raising the cycling stability of aqueous lithium-ion batteries by eliminating oxygen in the electrolyte. *Nature Chem* 2(9):760-765
9. Zhou H, Wang Y, Li H, He P (2010) The development of a new type of rechargeable batteries based on hybrid electrolytes. *Chem Sus Chem*. 3(9):1009-1019

10. Girishkumar G, McCloskey B, Luntz AC, Swanson S, Wicke W (2010) Lithium-air battery: promise and challenges. *J Phys Chem Lett* 1(14):2193-2203
11. Wang Y, Zhou H (2010) A lithium-air battery with a potential to continuously reduce O(2) from air for delivering energy. *J Power Sources* 195(1):358-361
12. Ryu HS, Ahn HJ, Kim KW, Ahn JH, Lee JY, Cairns EJ (2005) Self-discharge of lithium-sulfur cells using stainless-steel current-collectors. *J Power Sources* 140(2):365-369
13. Chang DR, Lee SH, Kim SW, Kim HT (2002) Binary electrolyte based on tetra(ethylene glycol) dimethyl ether and 1,3-dioxolane for lithium-sulfur battery. *J Power Sources* 112(2):452-460
14. Yamin H, Gorenstein A, Penciner J, Sternberg Y, Peled E (1988) Lithium sulfur battery – oxidation reduction mechanisms of polysulfides in THF solutions. *J Electrochem Soc* 135(5):1045-1048
15. Hamlen R, Au G, Brundage M, Hendrickson M, Plichta E, Slane S, Barbarell J (2001) US Army portable power programs. *J Power Sources* 97-8(SI):22-24
16. Wang WK, Wang Y, Huang YQ, Huang CJ, Yu ZB, Zhang H, Wang AB, Yuan KG (2010) The electrochemical performance of lithium-sulfur batteries with LiClO<sub>4</sub> DOL/DME electrolyte. *J Appl Electrochem* 40(2):321-325
17. Jin B, Kim J-U, Gu H-B (2003) Electrochemical properties of lithium-sulfur batteries. *J Power Sources* 117(1-2):148-152

18. Wang J, Wang Y, He X, Ren J, Jiang C, Wan C (2004) Electrochemical characteristics of sulfur composite cathode materials in rechargeable lithium batteries. *J Power Sources* 138(1-2):271-273
19. Wang J, Liu L, Ling Z, Yang J, Wan C, Jiang C (2003) Polymer lithium cells with sulfur composites as cathode materials. *Electrochim Acta* 48(13):1861-1867
20. Choi J-W, Cheruvally G, Kim D-S, Ahn J-H, Kim K-W, Ahn H-J (2008) Rechargeable lithium/sulfur battery with liquid electrolytes containing toluene as additive. *J Power Sources* 183(1):441-445
21. Cheon SE, Ko KS, Cho JH, Kim SW, Chin EY, Kim HT (2003) Rechargeable lithium sulfur battery – I. Structural change of sulfur cathode during discharge and charge. *J Electrochem Soc* 150(6):A796-A799
22. Cheon SE, Ko KS, Cho JH, Kim SW, Chin EY, Kim HT (2003) Rechargeable lithium sulfur battery – II. Rate capability and cycle characteristics. *J Electrochem Soc* 150(6):A800-A805
23. Ryu HS, Ahn HJ, Kim KW, Ahn JH, Cho KK, Nam TH, Kim JU, Cho GB (2006) Discharge behavior of lithium/sulfur cell with TEGDME based electrolyte at low temperature. *J Power Sources* 163(1):201-206.
24. Ryu HS, Ahn HJ, Kim KW, Ahn JH, Lee JY (2006) Discharge process of Li/PVdF/S cells at room temperature. *J Power Sources* 153(2):360-364
25. Choi J-W, Kim J-K, Cheruvally G, Ahn J-H, Ahn H-J, Kim K-W (2007) Rechargeable lithium/sulfur battery with suitable mixed liquid electrolytes. *Electrochim Acta* 52(5):2075-2082

26. Mikhaylik YV, Akridge JR (2003) Low temperature performance of Li/S batteries. *J Electrochem. Soc* 150(3):A306-A311
27. Shin JH, Cairns EJ (2008) N-methyl-(n-butyl)pyrrolidinium bis(trifluoromethanesulfonyl)imide-LiTFSI-poly(ethylene glycol) dimethyl ether mixture as a Li/S cell electrolyte. *J Power Sources* 177(2):537-545
28. Ji X, Lee KT, Nazar LF (2009) A highly ordered nanostructured carbon-sulphur cathode for lithium-sulfur batteries. *Nature Mater* 8(6):500-506
29. Jayaprakash N, Shen J, Moganty SS, Corona A, Archer LA (2011) Porous hollow carbon@sulfur composites for high-power lithium-sulfur batteries. *Angew Chem Int Ed* 50(26):5904-5908
30. Todorov YR, Hideshima Y, Noguchi H, Yoshio M (1999) Determination of theoretical capacity of metal-ion doped LiMn<sub>2</sub>O<sub>4</sub> as the positive electrode in Li-ion batteries. *J Power Sources* 77(2):198-201
31. Terada Y, Yasaka K, Nishikawa F, Konishi T, Yoshio M, Nakai I (2001) In situ XAFS analysis of Li(Mn,M)(2)O-4 (M = Cr, Co, Ni) 5 V cathode materials for lithium-ion secondary batteries. *J Solid State Chem* 156(2): 286-291
32. Bennemann H, Brouers F, Quitmann D (1982) Ionic liquids, molten salts and polyelectrolytes. Proc. of international conference on molten salts, Springer-Verlag, NY.
33. Hussey CL (1983) Ionic Liquids. Advances in Molten Salt Chemistry, Vol 5 p.185; Walden P (1914) Bull Acad Imper Sci (St. Petersburg) 1800

34. Zhao Y, Van der Noot T (1997) Electrodeposition of aluminum from nonaqueous organic electrolytes systems and room temperature molten salts. *Electrochim Acta*. 42(1):3-13.
35. Welton T (1999) Room-temperature ionic liquids. Solvents for synthesis and catalysis. *Chem Rev* 99(8):2071-2083
36. Wilkes JS, Zaworotko MJ (1992) Air and water stable 1-ethyl-3-methylimidazolium based ionic liquids. *J Chem Soc- Chem Comm* 13:965-967
37. Wasserschied P., Welton T. (2003). Ionic liquids in synthesis, Wiley-VCH, Weinheim.
38. Davis JH (2004) Task-specific ionic liquids. *Chem Lett* 33(9):1072-1077
39. Ohno H (2005) Electrochemical Aspects of Ionic Liquids. John Wiley & Sons, Inc., New Jersey.
40. Moganty SS, Baltus RE, Roy D (2009) Electrochemical windows and impedance characteristics of [Bmim(+)][BF<sub>4</sub>(-)] and [Bdmim(+)][BF<sub>4</sub>(-)] ionic liquids at the surfaces of Au, Pt, Ta and glassy carbon electrodes. *Chemical Physics Lett* 483(1-3):90
41. Martha SK, Markevich E, Burgel V, Salitra G, Zinigrad E, Markovsky B, Sclar H, Pramovich Z, Heik O, Aurbach D, Exnar I, Buqa H, Drezen T, Semrau G, Schmidt M, Kovacheva D, Salyski N (2009) A short review on surface chemical aspects of Li batteries: A key for good performance. *J Power Sources* 189(1):288-296
42. Lewandowski A, Swiderska-Mocek A (2009) Ionic liquids as electrolytes for Li-ion batteries- An overview of electrochemical studies. *J Power. Sources* 194(2):601-609

43. Lewandowski A, Swiderska-Mocek A (2010) Lithium-metal potential in Li(+) containing ionic liquids. *J Appl Electrochem* 40(3):515-524
44. Seki S, Kobayashi Y, Miyashiro H, Ohno Y, Usami A, Mita Y, Kihira N, Watanabe M, Terada N (2006) Lithium secondary batteries using modified-imidazolium room-temperature ionic liquid. *J Phys Chem B* 110(21):10228-10230
45. Borgel V, Markevicha E, Aurbach D, Semrau G, Schmidt M (2009) On the application of ionic liquids for rechargeable Li batteries: High voltage systems. *J Power. Sources* 189(1):331-336
46. Goodenough JB, Kim J (2010) Challenges for rechargeable Li batteries. *Chem Mater* 22(3):587-603
47. Seki S, Mita Y, Tokuda H, Ohno Y, Kobayashi Y, Usami A, Watanabe M, Terada N, Miyashiro N (2007) Effects of alkyl chain in imidazolium-type room-temperature ionic liquids as lithium secondary battery electrolytes. *Electrochim Solid. State. Lett* 10(10):A237-A240
48. Appetecchi GB, Montanino M, Zane D, Carewska M, Alessandrini F, Passerini S (2009) Effect of the alkyl group on the synthesis and the electrochemical properties of N-alkyl-N-methyl-pyrrolidinium bis(trifluoromethanesulfonyl)imide ionic liquids. *Electrochim Acta* 54(4):1325-1332
49. Tokuda H, Hayamizu K, Ishii K, Abu Bin Hasan Susan M, Watanabe M (2004) Physiochemical properties and structures of room temperature ionic liquids. 1. Variation of anionic species. *J Phys Chem B* 108(42):16593-16600

50. Bayley PM, Lane GH, Rocher NM, Clare BR, Best AS, MacFarlane DF, Forsyth M (2009) Transport properties of ionic liquid electrolytes with organic diluents. *Phys. Chem. Chem. Phys.* 11(33):7202-7208
51. Lee JS, Quan ND, Hwang JM, Bae JY, Kim H, Cho BW, Kim HS, Lee H (2006) Ionic liquids containing an ester group as potential electrolytes. *Electrochim Comm* 8(3):460-464
52. Egashira M, Okada S, Yamaki J, Dri DA, Bonadies F, Scrosati B (2004) The preparation of quaternary ammonium-based ionic liquid containing a cyano group and its properties in a lithium battery electrolyte. *J Power Sources* 138 (1-2):240-244
53. Tsuda T, Kondo K, Tomioka T, Takahashi Y, Matsumoto H, Kuwabata S, Hussey CL (2011) *Angew Chem Int Ed* 50(6):1310-1313
54. Howlett PC, MacFarlane DR, Hollenkamp AF (2004) High lithium metal cycling efficiency in a room-temperature ionic liquid. *Electrochim Solid-State Lett* 7(5)A97-A101
55. Howlett PC, Brack N, Hollenkamp AF, Forsyth M, MacFarlane DR (2006) Characterization of the lithium surface in N-methyl-N-alkylpyrrolidinium bis(trifluoromethanesulfonyl)amide room-temperature ionic liquids electrolytes. *J Electrochim Soc* 153(3)A595-A606
56. Liu H, Liu Y, Li J (2010) Ionics liquids in surface electrochemistry. *Phys Chem Chem Phys* 12(8): 1685-1697
57. Bhatt AI, Best AS, Huang J, Hollenkamp AF (2010) Application of the N-propyl-N-methyl-pyrrolodinium bis(fluorosulfonyl)imide RTIL containing lithium bis(fluorosulfonyl)imide in ionic liquid based lithium batteries. *J Electrochim Soc* 157(1):A66-A74

58. Lane GH, Best AS, MacFarlane DR, Hollenkamp AF, Forsyth M, (2010) An azo-spiro mixed ionic liquid electrolyte for lithium metal-LiFePO<sub>4</sub> batteries. *J Electrochem Soc* 157(7):A876-A884
59. Valencia H, Kohyama M, Tanaka S, Matsumoto H (2002) Ab initio study of EMIM-BF<sub>4</sub> crystal interaction with a Li (100) surface as a model for ionic liquid/Li interfaces in Li-ion batteries. *J Chem Phys* 131(24):244705
60. El Ouatani L, Dedryvère R, Siret C, Biensan P, Reynaud S, Iratçabal P, Gonbeau D (2009) The effect of vinylene carbonate additive on surface film formation on both electrodes in Li-ion batteries. *J Electrochem Soc* 156 (2):A103-A113
61. Oesten R, Heider U, Schmidt M (2002) Advanced electrolytes. *Solid State Ionics* 148(3-4):391-397
62. Xu MQ, Li WS, Zuo XX, Liu JS, Xu X (2007) Performance improvement of lithium ion battery using PC as a solvent component and BS as an SEI forming additive. *J Power Sources* 174(2):705-710
63. Park G, Nakamura H, Lee Y, Yoshio M (2009) The important role of additives for improved lithium ion battery safety. *J Power Sources* 189(1):602-606
64. Chen R, Wu F, Li L, Guan Y, Qiu X, Chen S, Li Y, Wu S (2007) Butylene sulfite as a film-forming additive to propylene carbonate-based electrolytes for lithium ion batteries. *J Power Sources* 172(1):395-403

65. Yao W, Zhang Z, Gao J, Li J, Xu J, Wang Z, Yang Y (2009) Vinyl ethylene sulfite as a new additive in propylene carbonate-based electrolyte for lithium ion batteries. *Energy and Env Sci* 2(10):1102-1108
66. Menkin S, Golodnitsky D, Peled E (2009) Artificial solid-electrolyte interphase (SEI) for improved cycleability and safety of lithium-ion cells for EV applications. *Electrochem Comm* 11(9):1789-1791
67. Song S-W, Baek S-W (2009) Silane-derived SEI stabilization on thin-film electrodes of nanocrystalline Si for lithium batteries. *Electrochim Solid-State Lett* 12(2):A23-A27
68. Lee YM, Seo JE, Lee YG, Lee SH, Cho KY, Parka J-K (2007) Effects of triacetoxymethylsilane as SEI layer additive on electrochemical performance of lithium metal secondary battery. *Electrochim Solid-State Lett* 10(9):A216-A219
69. Balakrishnan PG, Ramesh R, Kumar TP (2006) Safety mechanisms in lithium-ion batteries. *J Power Sources* 155(2):401-414
70. Wang X, Yasukawa E, Kasuya S (2001) Nonflammable trimethyl phosphate solvent-containing electrolytes for lithium-ion batteries – I. Fundamental properties. *J Electrochem Soc* 148(10):A1058-A1065
71. Arai J (2003) Nonflammable methyl nonafluorobutyl ether for electrolyte used in lithium secondary batteries. *J Electrochim Soc* 150(2):A219-A228
72. Mandal BK, Padhi AK, Shi Z, Chakraborty S, Filler R (2006) Thermal runaway inhibitors for lithium battery electrolytes. *J Power Sources* 161(2):1341-1345

73. Jow TR, Xu K, Zhang SS, Ding MS (2005) Nonflammable non-aqueous electrolyte and non-aqueous electrolyte cells comprising the same. U. S. Patent 6,924,061
74. Hyung YE, Vissers DR, Amine K (2003) Flame-retardant additives for lithium-ion batteries. *J Power Sources* 119(SI):383-387
75. Shigematsu Y, Ue M, Yamaki J-i (2009) Thermal behavior of charged graphite and Li(x)CoO(2) in electrolytes containing alkyl phosphate for lithium-ion cells. *J Electrochem Soc* 156(3):A176-A180
76. Morita M, Niida Y, Yoshimoto N, Adachi K (2005) Polymeric gel electrolyte containing alkyl phosphate for lithium-ion batteries. *J Power Sources* 146(1-2):427-430
77. Shim EG, Nam TH, Kim JG, Kim HS, Moon SI (2009) Effects of trioctyl phosphate and cresyl diphenyl phosphate as flame-retarding additives for Li-ion battery electrolytes. *Met Mater Int* 15(4):615-621
78. Zhou DY, Li WS, Tan CL, Zuo XX, Huang HJ (2008) Cresyl diphenyl phosphate as flame retardant additive for lithium-ion batteries. *J Power Sources* 184(2):589-592
79. Zhang HP, Xia Q, Wang B, Yang LC, Wu YP, Sun DL, Gan CL, Luo HJ, Bebeda AW, van Ree T (2009) Vinyl-tris-(methoxydiethoxy)silane as an effecctive and ecofriendly flame retardant for electrolytes in lithium ion batteries. *Electrochem Comm* 11(3):526-529
80. Fei S-T, Allcock HR (2010) Methoxyethoxyethoxyphosphazenes as ionic conductive fire retardant additives for lithium battery systems. *J Power Sources* 195(7):2082-2088
81. Herbert EG, Tenhaeff WE, Dudney NJ, Pharr GM (2011) Mechanical characterization of LiPON films using nanoindentation. *Thin Solid Films* 520(1):413-418

82. Monroe C, Newman J (2005) The impact of elastic deformation on deposition kinetics at lithium/polymer interfaces. *J Electrochem Soc* 152(2):A396-A404
83. Fergus JW (2010) Ceramic and polymeric solid electrolytes for lithium-ion batteries. *J Power Sources* 195(15):4554-4569
84. Patil A, Patil V, Shin DW, Choi J-W, Paik D-S, Yoon S-J (2008) Issues and challenges facing rechargeable thin film lithium batteries. *Mater Res Bull* 43(8-9):1913-1942
85. Yu X, Bates JB, Jellison Jr GE, Hart FX (1997) A stable thin-film lithium electrolyte: lithium phosphorus oxynitride. *J Electrochem Soc* 144(2):524-532
86. Kobayashi T, Yamada A, Kanno R (2008) Interfacial reactions at electrode/electrolyte boundary in all solid-state lithium battery using inorganic solid electrolyte, thio-LISICON. *Electrochim Acta* 53(15):5045-5050
87. Takahara H, Tabuchi M, Takeuchi T, Kageyama H, Ide J, Handa K, Kobayashi Y, Kurisu Y, Kondo S, Kanno R (2004) Application of lithium metal electrolytes to all-solid-state lithium secondary batteries using Li<sub>3</sub>PO<sub>4</sub>-Li<sub>2</sub>S-SiS<sub>2</sub> glass. *J Electrochem Soc* 151(9):A1309-A1313
88. Kotobuki M, Suzuki Y, Munakata H, Kanamura K, Sato Y, Yamamoto K, Yoshida T (2010) Compatibility of LiCoO<sub>2</sub> and LiMn<sub>2</sub>O<sub>4</sub> cathode materials for Li<sub>(0.55)</sub>La<sub>(0.35)</sub>TiO<sub>3</sub> electrolyte to fabricate all-solid-state lithium battery. *J Power Sources* 195(17):5784-5788
89. Xie J, Imanishi N, Zhang T, Hirano A, Takeda Y, Yamamoto O, Zhao XB, Cao GS (2010) Electrochemical performance of all-solid-state Li batteries based LiMn<sub>(0.5)</sub>Ni<sub>(0.5)</sub>O<sub>2</sub> bathode and NASICON-type electrolyte. *J Power Sources* 195(24):8341-8346

90. Kotobuki M, Munakata H, Kanamura K, Sato Y, Yoshida T (2010) Compatibility of Li(7)La(3)Zr(2)O(12) solid electrolyte to all-solid-state battery using Li metal anode. *J Electrochem Soc* 157(10):A1076-A1079
91. Ohta N, Takada K, Zhang L, Ma R, Osada M, Sasaki T (2006) Enhancement of the high-rate capability of solid-state lithium batteries by nanoscale interfacial modification. *Adv Mater* 18(17):2226
92. Sakuda A, Kitaura H, Hayashi A, Tadanaga K, Tatsumisago M (2008) Improvement of high-rate performance of all-solid-state lithium secondary batteries using Li-CoO(2) coated with Li(2))-SiO(2) glasses. *Electrochim Solid-State Lett* 11(1): A1-A3
93. Mei A, Jiang Q-H, Lin Y-H, Nan C-W (2009) Lithium lanthanum titanium oxide solid-state electrolyte by spark plasma sintering. *J Alloys and Compounds* 486(1-2):871-875
94. Tenhaeff W, Yu X, Hong K, Perry KA, Dudney NJ (2011) Ionic transport across interfaces of solid glass and polymer electrolytes for lithium ion batteries. *J Electrochem Soc* 158(10):A1143-A1149
95. Xu F, Dudney NJ, Veith GM, Kim Y (2010) Properties of lithium phosphorus oxynitride (Lipon) for 3D solid-state lithium batteries. *J Mater Res* 25(8):1507-1515
96. Kotobuki M, Suzuki Y, Munakata H, Kanamura K, Sato Y, Yamamoto K, Yoshida T (2010) Fabrication of three-dimensional battery using ceramic electrolyte with honeycomb structure by sol-gel process. *J Electrochem Soc* 157(4):A493-A498
97. Fenton DE, Parker JM, Wright PV (1973) Complexes of alkali-metal ions with poly(ethylene oxide). *Polymer*,14(11):589-589

98. Armand MB, Chabagno JM, Duclot MJ (1979) Fast Ion Transport in Solids. Vashista P, Mundy JN, Shenoy GK, Eds. North-Holland, New York, pp. 131
99. Doyle M, Fuller TF, Newman J (1994) The importance of the lithium ion transference number in lithium polymer cells. *Electrochim Acta*, 39(13):2073-2081
100. Rosso M, Gobron T, Brissot C, Chazalviel J-N, Lascaud S (2001) Onset of dendritic growth in lithium/polymer cells. *J Power Sources* 97-98(SI):804-806
101. Klein RJ, Zhang S, Dou S, Jones BH, Colby RH, Runt J (2006) Modeling electrode polarization in dielectric spectroscopy: ionic mobility and mobile ion concentration of single-ion polymer electrolytes. *J Chem Phys* 124(14):144903.
102. Fragiadakis D, Dou S, Colby RH, Runt J (2008) Molecular mobility, ion mobility, and mobile ion concentration in poly(ethylene oxide)-based polyurethane ionomers. *Macromolecules* 41(15):5723-5728
103. Fragiadakis D, Dou S, Colby RH, Runt J (2009) Molecular mobility and Li(+) conduction in polyester copolymer ionomers based on poly(ethylene oxide). *J Chem Phys* 130(6): 064907
104. Wang W, Liu W, Tudry GJ, Colby RH, Winey KI (2010) Multi-length scale morphology of poly(ethylene oxide)-based sulfonate ionomers with alkali cations at room temperature. *Macromolecules* 43(9):4223-4229
105. Itoh T, Yoshikawa M, Uno T, Kubo M (2009) Solid polymer electrolytes based on poly(lithium carboxylate) salts. *Ionics* 15(1):27-33
106. Borghini MC, Mastragostino M, Zanelli A (1996) Reliability of lithium batteries with crosslinked polymer electrolytes. *Electrochim Acta* 41(15):2369-2373

107. Matoba Y, Y. Ikeda, Kohjiya S (2002) Ionic conductivity and mechanical properties of polymer networks prepared from high molecular weight branched poly(oxyethylene)s. Solid State Ionics 147(3-4): 403-409
108. Fogeling J, Kunze M, Schonhoff M, Stolwijk NA (2010) Foreign-ion and self-ion diffusion in a crosslinked salt-in-polyether electrolyte. Phys Chem Chem Phys 12(26):7148-7161
109. Rupp B, Schmuck M, Balducci A, Winter M, Kern W (2008) Polymer electrolyte for lithium batteries based on photochemically crosslinked poly(ethylene oxide) and ionic liquid. European Polymer Journal 44(9):2986-2990
110. Choi N-S, Park J-K (2009) A comparative study of coordination between host polymer and Li(+) ions in UV-cured gel polymer electrolytes. Solid State Ionics 180(20-22):1204-1208
111. Uchiyama R, Kusagawa K, Hanai K, Imanishi N, Hirano A, Takeda Y (2009) Development of dry polymer electrolytes based on polyethylene oxide with co-bridging agent crosslinked by electron beam. Solid State Ionics 180(2-3):205-211
112. Ghosh A, Wang C, Kofinas P (2010) Block copolymer solid battery electrolyte with high Li-ion transference number. J Electrochem Soc 157(7):A846-A849
113. Ghosh A, Kofinas P (2008) Nanostructured block copolymer dry electrolyte. J Electrochem Soc 155(6):A428-A431
114. Niitani T, Amaike M, Nakano H, Dokko K, Kanamura K (2009) Star-shaped polymer electrolyte with microphase separation structure for all-solid-state lithium batteries. J Electrochem Soc 156(7):A577-A583

115. Singh M, Odusanya O, Wilmes GM, Eitouni HB, Gomez ED, Patel AJ, Chen VL, Park MJ, Fragouli P, Iatrou H, Hadjichristidis N, Cookson D, Balsara NP (2007) Effect of molecular weight on the mechanical and electrical properties of block copolymer electrolytes. *Macromolecules* 40(13): 4578-4585
116. Gomez ED, Panday A, Feng EH, Chen V, Stone GM, Minor A, Kisielowski C, Downing KH, Borodin O, Smith GD, Balsara NP (2009) Effect of ion distribution on conductivity of block copolymer electrolytes. *Nano Lett* 9(3):1212-1216
117. Gadjourova Z, Andreev YG, Tunstall DP, Bruce PG (2001) Ionic conductivity in crystalline polymer electrolytes. *Nature* 412(6846):520-523
118. Christie AM, Lilley SJ, Staunton E, Andreev YJ, Bruce PG (2005) Increasing the conductivity of crystalline polymer electrolytes. *Nature* 433(7021):50-53
119. Bruce PG (2008) Energy storage beyond the horizon: rechargeable lithium batteries. *Solid State Ionics* 179(21-26):752-760
120. Bruce PG, Scrosati B, Tarascon J-M (2008) Nanomaterials for rechargeable lithium batteries. *Angew Chem Inter Ed* 47(16):2930-2946
121. Croce F, Appetecchi GB, Persi L, Scrosati B (1998) Nanocomposite polymer electrolytes for lithium batteries. *Nature* 394(6692):456-458; Croce F, Curini R, Martinelli A, Persi L, Ronci F, Scrosati B, Caminiti R (1999) Physical and chemical properties of nanocomposite polymer electrolytes. *J Phys Chem B* 103(48):10632-10638

122. Jeon J-D, Kim M-J, Kwak S-Y (2006) Effects of addition of TiO<sub>2</sub> nanoparticles on mechanical properties and ionic conductivity of solvent-free polymer electrolytes based on porous P(VdF-HFP)/P(EO-EC) membranes. *J Power Sources* 162(2):1304-1311
123. Raghaven P, Choi JW, Ahn JH, Cheruvally G, Chauhan GS, Ahn HJ, Nah C (2008) Novel electrospun poly(vinylidene fluoride-co-hexafluoropropylene)-in situ SiO<sub>2</sub> composite membrane-based polymer electrolyte for lithium batteries. *J Power Sources* 184(2):437-443
124. Capiglia C, Mustarelli P, Quartarone E, Tomasi C, Magistris A (1999) Effects of nanoscale SiO<sub>2</sub> on the thermal and transport properties of solvent-free, poly(ethylene oxide) (PEO)-based polymer electrolytes. *Solid State Ionics* 118(1-2):73-79
125. Krawiec W, Scanlon LG, Fellner JP, Vaia RA, Vasudevan S, Giannelis EP (1995) Polymer nanocomposites – a new strategy for synthesizing solid electrolytes for rechargeable lithium batteries. *J Power Sources* 54(2):310-315
126. Jayathilaka PARD, Dissanayake MAKL, Albinsson I, Mellander B-E (2002) Effect of nano-porous Al<sub>2</sub>O<sub>3</sub> on thermal, dielectric and transport properties of the (PEO)(9) LiTFSI polymer electrolyte system. *Electrochim Acta* 47 (20):3257-3268
127. Reddy MJ, Chu PP, Kumar JS, Rao UVS (2006) Inhibited crystallization and its effect on conductivity in a nano-sized Fe oxide composite PEO solid electrolyte. *J Power Sources* 161(1):535-540
128. Croce F, Sacchetti S, Scrosati B (2006) Advanced, high-performance composite polymer electrolytes for lithium batteries. *J Power Sources* 161(1):560-564

129. Panero S, Scrosati B, Sumathipala HH, Wieczorek W (2007) Dual-composite polymer electrolytes with enhanced transport properties. *J Power Sources* 167(2):510-514
130. Kerr JB, Han YB, Liu G, Reeder C, Xie J, Sun X (2004) Interfacial behavior of polymer electrolytes. *Electrochim Acta*, 50(2-3):235-242
131. Mazor H, Golodnitsky D, Peled E, Wieczorek W, Scrosati B (2008) Search for a single-ion-conducting polymer electrolyte: combined effect of anion trap and inorganic filler. *J Power Sources* 178(2):736-743
132. Popall M, Andrei M, Kappel J, Kron J, Olma K, Olsowski B (1998) ORMOCERS as inorganic-organic electrolytes for new solid state lithium batteries and supercapacitors. *Electrochim Acta* 43(10-11):1155-1161
133. Kao H-M, Chao S-W, Chang P-C (2006) Multinuclear solid-state NMR, self-dissusion coefficients, differential scanning Calorimetry, and ionic conductivity of solid organic-inorganic hybrid electrolytes based on PPG-PEG-PPG diamine, siloxane, and lithium perchlorate. *Macromolecules* 39(3):1029-1040
134. Jeyapandian M, Lavina S, Thayumanasundaram S, Ohno H, Negro E, Noto VD (2010) New hybrid inorganic-organic polymer electrolytes based on Zr(O(CH(2))(3)CH(3))(4), glycerol and EMIm-TFSI ionic liquid. *J Power Sources* 195(1):341-353
135. Piszcza M, Marzantowicz M, Plewa-Marczewska A, Zukowska GZ, Zalewska A, Pietrzykowski A, Siekierski M (2010) Hybrid polymeric electrolyte based on methylalumoxane. *J Power Sources* 195(22):7495-7505

136. Kao H-M, Chen C-L (2004) An organic-inorganic hybrid electrolyte derived from self-assembly of a poly(ethylene oxide)-poly(propylene oxide)-poly(ethylene oxide) triblock copolymer. *Angew Chem Int Ed* 43(8):980-984
137. Nugent JL, Moganty SS, Archer LA (2010) Nanoscale organic hybrid electrolytes. *Adv Mater* 22(33):3677
138. Agarwal P, Qi H, Archer LA (2010) The ages in a self-suspended nanoparticle liquid. *Nano Lett* 10(1):111-115; Agarwal P, Chopra M, Archer LA (2011) Nanoparticle netpoints for shape-memory polymers. *Angew Chem Int Ed* 50(37):8670-8673
139. Tarascon J-M, Gozdz AS, Schmutz C, Shokoohi F, Warren PC (1996) Performance of Bellcore's plastic rechargeable Li-ion batteries. *Solid State Ionics* 86(8):49-54
140. Fuller J, Breda AC, Carlin RT (1998) Ionic liquid-polymer gel electrolytes from hydrophilic and hydrophobic ionic liquids. *J Electroanal Chem* 459 (1):29-34
141. Nakagawa H, Izuchi S, Kuwana K, Nukuda T, Aihara Y (2003) Liquid and polymer gel electrolytes for lithium batteries composed of room-temperature molten salt doped by lithium salt. *J Electrochem Soc* 150(6):A695-A700
142. Cheng H, Zhu C, Huang B, Lu M, Yang Y (2007) Synthesis and electrochemical characterization of PEO-based polymer electrolytes with room temperature ionic liquids. *Electrochim Acta* 52 (19):5789-5794
143. Liao K-S, Sutto TE, Andreoli E, Ajayan P, McGrady KA, Curran SA (2010) Nano-sponge ionic liquid-polymer composite electrolytes for solid-state lithium power sources. *J Power Sources* 195(3):867-871

144. Bhattacharyya A, Dolle M, Maier J (2004) Improved battery electrolytes by heterogeneous doping of nonaqueous Li-salt solutions. *Electrochim Solid State Lett* 7(11):A432-A434
145. Das S, Bhattacharyya A (2009) Oxide particle surface chemistry and ion transport in “soggy sand” electrolytes. *J Phys Chem C* 113(16):6699-6705
146. Das S, Bhattacharyya A (2010) Influence of oxide particle network morphology on ion solvation and transport in “soggy sand” electrolytes. *J Phys Chem B* 114(20):6830-6835
147. Walls HJ, Riley MW, Singhal RR, Spontak RJ, Fedkiw PS, Khan SA (2003) Nanocomposite electrolyte with fumed silica and hectorite clay networks: passive versus active fillers. *Adv Funct Mater* 13(9):710-717
148. Wang P, Zakeeruddin SM, Comte P, Exnar I, Gratzel M (2004) Ionic liquid-based electrolytes with silica nanoparticles for quasi-solid-state dye-sensitized solar cells. *J Am Chem Soc* 125(5):1166-1167
149. Katakabe T, Kawano R, Watanabe M (2007) Acceleration of redox diffusion and charge-transfer rates in an ionic liquid with nanoparticle addition. *Electrochim Solid- State Lett* 10(6):F23-F25
150. Syzdek J, Armand M, Gizowska M, Marcinek M, Sasim E, Szafran M, Wieczorek W (2009) Ceramic-in-polymer versus polymer-in-ceramic polymeric electrolytes – A novel approach. *J Power Sources* 194(1):66-72
151. Moganty SS, Jayaprakash N, Nugent JL, Shen J, Archer LA (2010) Ionic-liquid-tethered nanoparticles: hybrid electrolytes. *Angew Chem Int Ed* 49(48):9158-9161

152. Schaefer JL, Moganty SS, Yanga DA, Archer LA (2011) Nanoporous hybrid electrolytes. J Mat Chem 21(27):10094-10101

153. Hayamizu K, Aihara Y, Nakagawa H, Nukuda T, Price WS (2004) Ionic conduction and ion diffusion in binary room-temperature ionic liquids composed of [emim][BF<sub>4</sub>] and LiBF<sub>4</sub>. J Phys Chem B 108(50):19527-19532

## CHAPTER 3.

### APPLICATIONS OF NANOCOMPOSITES IN LITHIUM BATTERY ELECTROLYTES

Reproduced with Permission from Advanced Materials, DOI: 10.1002/adma.201303070, by Samanvaya Srivastava, Jennifer L. Schaefer, Zichao Yang, Zhengyuan Tu, and Lynden A. Archer.

Weston and Steele in 1982 reported a significant improvement in the mechanical stability of a polymer electrolyte upon the addition of an inert filler, with negligible reductions in ionic conductivity at low loadings.<sup>[1]</sup> Numerous works have appeared in the literature on polymer nanocomposite electrolytes since then, and the beneficial influence of inorganic nanoparticles on ion transport within the electrolyte is a subject of ongoing active study by research groups worldwide. In this section, we consider ion transport mechanisms in electrolytes containing nanoparticles with the goal of elucidating opportunities for designing novel types of electrolytes with tunable mechanical and ion-transport properties, and which offer improvements in lithium battery safety.

#### Charge transport mechanisms in nanocomposites

Once solvated, ionic species in an electrolyte will move in response to an applied electric field. It has been experimentally observed that in common liquid electrolytes, such as alkyl carbonate mixtures used in lithium-ion batteries, Li<sup>+</sup> ions coordinate and diffuse in concert with the solvent molecules owing to its strong electropositive nature and small size. The bulky counter-anion diffuse alone, and as a result, the anion typically has smaller hydrodynamic radius and greater

mobility than that of  $\text{Li}^+$ . In a dry polymer electrolyte,  $\text{Li}^+$  typically coordinates with hydrophilic regions of the polymer backbone and  $\text{Li}^+$  conduction is primarily achieved by ion-hopping between coordination sites, resulting in an activated, temperature-dependent ionic conductivity of the following form:

$$\sigma = A_{Arr} \exp \frac{-E_a}{T}$$

where  $A_{Arr}$  is the Arrhenius pre-exponential factor,  $E_a$  is the activation energy in thermal units, and  $T$  is the absolute temperature. Segmental motion of polymer chains also aids  $\text{Li}^+$  ion hopping between coordination sites when the temperature is above the melting temperature,  $T_m$ , and the polymer is amorphous. This contribution leads to a Vogel–Fulcher–Thamman (VFT) temperature dependent ionic conductivity:

$$\sigma = A_{VFT} \exp \frac{-B}{T - T_0}$$

where  $A_{VFT}$  is the VFT pre-exponential factor,  $B$  is a pseudo activation energy and  $T_0$  is the reference temperature, related to the glass transition temperature,  $T_g$ , of the material. If the polymer matrix is swollen with a liquid electrolyte, the polymer backbone and liquid are each able to interact with the ionic species and both participate in ion transport.

There are two other modes of ion transport in polymers where mobility is decoupled from segmental relaxation. Oligomeric PEO molecules have been reported to arrange in ordered helices at specific PEO/salt ratios; cation conduction occurs through the helix tunnel of these “small molecule crystalline polymer electrolytes”.<sup>[2,3]</sup> It is expected that with complete ordering of the helices to form direct conduction pathways, significantly higher lithium ion conductivities may be achievable than in typical crystalline electrolytes where the crystalline domains are

randomly oriented. More recently, reports have suggested that in rigid polymers, such as polyethylene oxide-styrene copolymers, ionic conductivity is a much weaker function of temperature than expected from the segmental dynamics of the solvating polymer.<sup>[4,5]</sup> It has been proposed that ions diffuse through the polymer matrix even with slow or negligible segmental motion due to the loose packing structure of the polymer chains.

The most extensively studied Li-ion conducting polymer is PEO; each  $\text{Li}^+$  typically coordinates on average with 4 EO sites. The  $T_m$  of pristine high-molecular weight PEO is about 65°C. Ionic conductivities considered acceptable for practical applications (minimum of  $10^{-4}$  S/cm, ideally greater than  $10^{-3}$  S/cm), have been achieved only at temperatures above  $T_m$  for salt-in-polymer electrolytes.

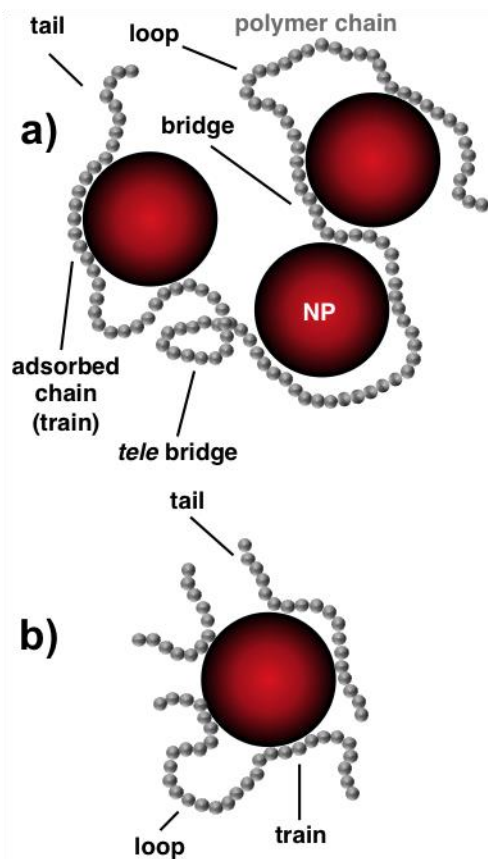
For a typical lithium salt doped, polymer or liquid electrolyte, the measured conductivity is the sum of contributions from  $\text{Li}^+$  and the counter-anion; for systems containing a supporting electrolyte such as an ionic liquid, other ions contribute to the measured conductivity as well. As only the  $\text{Li}^+$  transport actively contributes to the charge/discharge of a lithium battery, it is desirable to have an electrolyte with high conductivities as well as a high ratio of  $\text{Li}^+$  mobility relative to that of all mobile ions, which is characterized by the lithium transference number  $T_{\text{Li}^+}$ . Electrolytes with high  $T_{\text{Li}^+}$  are also desirable because they can sustain higher charging rates, even with lower total measured ionic conductivities, due to a reduction in deleterious ion concentration gradients and anion build-up at the electrode interface.<sup>[6,7]</sup> High  $T_{\text{Li}^+}$  electrolytes also allow for the use of thicker lithium-ion electrodes, thus increasing overall cell energy density by reducing non-active material weight and volume. Salt-doped polymer electrolyte

typically exhibit moderate  $T_{\text{Li}^+}$ , in the range of 0.15–0.3, in comparison to those for liquid electrolytes (0.2–0.4).<sup>[8,9]</sup> Close to unity  $T_{\text{Li}^+}$  have been reported for some ionomers, which may serve as single-ion conducting electrolytes (the other notable single ion conductors are solid-state ceramics). The ionomers achieve high  $T_{\text{Li}^+}$  because the anion is typically incorporated into a polymer backbone. Unfortunately, these materials suffer from unacceptably low ionic conductivities (often  $< 10^{-5}$  S/cm for dry ionomeric electrolytes at room temperature), due to poor ion pair dissociation and thus low mobile ion concentrations.<sup>[10,11]</sup>

Incorporation of nanoparticles in polymer electrolytes may affect ion transport in two main ways - as passive and, at times, active fillers. Nanoparticle fillers may also affect transport at the electrode–electrolyte interface, and may facilitate uniform electrodeposition of metals such as lithium prone to form non-uniform electrodeposits and dendrites.

### **Passive nanoparticle-based composite electrolytes**

Nanoparticle fillers can influence the ion transport mechanisms in polymers in a variety of indirect ways. Small nanoparticles are, for example, known to inhibit polymer crystallization. Analogous to molecular plasticizers, they may also add free volume and speed up segmental dynamics. The former leads to amorphicity at lower temperatures than the host polymer  $T_m$  and/or  $T_g$ , and thus enhances conductivities with increasing filler content up to 10–15 wt%.<sup>[1,12,13,14,15]</sup> Annealing of the composite at a temperature greater than  $T_m$  is sometimes required for “freezing amorphicity” in the lower temperature range and leads to increased conductivities.<sup>[12,16]</sup> Larger or poorly dispersed nanoparticles can have the opposite effect on ion conduction by serving as bridging/cross-linking sites between the polymer chains (Figure 3.1), thus reducing their mobility and reducing conductivities.<sup>[17,18]</sup> Above the optimum loading the



Schematic by S. Srivastava

**Figure 3.1** a, b. Typical polymer chain conformations around nanoparticles in a polymer nanocomposite.

ionic conductivity of the electrolyte decreases due to the decreasing volume fraction of the polymer matrix available for conduction and disruption of ion transport pathways.

The optimum nanoparticle loading in a polymer electrolyte is a sensitive function of the dispersion state of the particles in the host. Polymer-tethered particles provide a well-researched strategy for avoiding agglomeration and thus decreasing the effective particle size.<sup>[19,20,21]</sup> These effects have been shown to lead to improvement in ionic conductivities of nanocomposites containing as much as 40 wt% particles.<sup>[22]</sup> An often-overlooked benefit is that because the grafted molecules prevent particle-particle contacts, the composite electrolytes will be stable over time. Nanoparticles densely grafted with ion-conducting polymers of intermediate chain lengths are unable to aggregate and as such are expected to form stable, ion-conducting dispersions at all particle loadings. The self-suspended SiO<sub>2</sub>-PEG materials introduced in Chapter 4 provide an extreme example of this stability; they have been reported to function as effective Li<sup>+</sup> conductors when doped with lithium salt - without the need for a high molecular weight polymer host or liquid plasticizer (Figure 3.2).<sup>[23]</sup> In particular, the tethering of oligomeric PEG ligands to SiO<sub>2</sub> nanoparticle cores inhibits crystallization of the polymer, leading to enhanced conductivities at room temperature. An optimum tethered PEG ligand length exists, where crystallization is mitigated but segmental dynamics are not significantly depressed. In the case where short PEG ligands are utilized,<sup>[24]</sup> addition of a liquid plasticizer such as oligomeric PEG leads to enhanced conductivity, without compromising colloidal or thermal stability. Significantly, these hybrid particle-oligomeric PEG electrolytes become mechanically jammed at a particle volume fraction around 30% at which their mechanical properties increase by as many as six orders of magnitude while the room-temperature ionic conductivities change by a

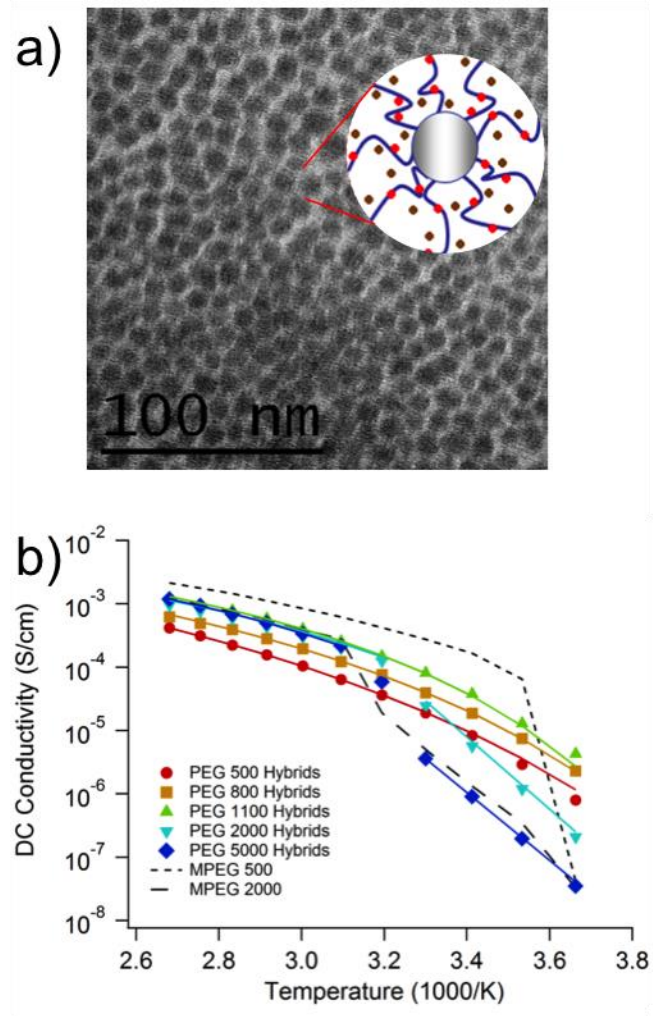


**Figure 3.2** a) Transmission electron micrograph and schematic of an all-solid-state  $\text{SiO}_2$ -PEG hybrid electrolyte and b) DC ionic conductivity of the hybrid electrolytes doped with 1 M LiTFSI in the organic phase as a function of the tethered PEG chain length. The ionic conductivity of free MPEGs + 1 M LiTFSI is displayed for comparative purposes. Adapted from [23].

factor of at most three. These hybrid particle-polymer materials may possess a high yield stress in the static state, but can be deformed by application of force making them amenable for processing. Similar decoupling of mechanical properties and ionic conductivity have been reported in organic-inorganic hybrids of varying structures—inorganic particles,<sup>[25-28]</sup> channels,<sup>[29]</sup> or networks<sup>[30]</sup> with tethered or cross-linked organic ligands. In all cases, presence of the inorganic solid not only improves mechanical properties, but also promotes amorphicity of tethered polymeric ligands. The inherent ability afforded by such hybrid electrolytes to independently manipulate ionic conductivity and mechanical properties has obvious and potentially far-reaching implications for battery designs in complex form factors.

### Active nanoparticle-based composite electrolytes

Nanocomposite electrolytes containing active particles have attracted considerable recent interest. In these nanocomposites, the particles directly participate in ion transport by providing either for enhanced free Li<sup>+</sup> concentrations, Li<sup>+</sup> surface conduction, anion attraction, or as a Li<sup>+</sup> source. Initial insight into the active role of the nanoparticle in ion transport was provided by transference measurements in polymer nanocomposite electrolytes containing bare nanoparticles as so-called *fillers*. While the majority of the conductivity enhancement was in early works attributed to increased amorphicity and segmental motion of the polymer matrix, some nanocomposite electrolytes were found to exhibit markedly higher  $T_{\text{Li}^+}$  values, as high as 0.6 for some TiO<sub>2</sub>-containing materials while the total ionic conductivity of the matrix simultaneously increased, as shown in Figure 3.3, adapted from seminal work by Croce, et. al. in 1998 and 1999.<sup>[12,16]</sup> The following mechanisms have since been proposed in which the particles are thought to decidedly deviate from their early, incorrect designation as mere fillers (see Figure

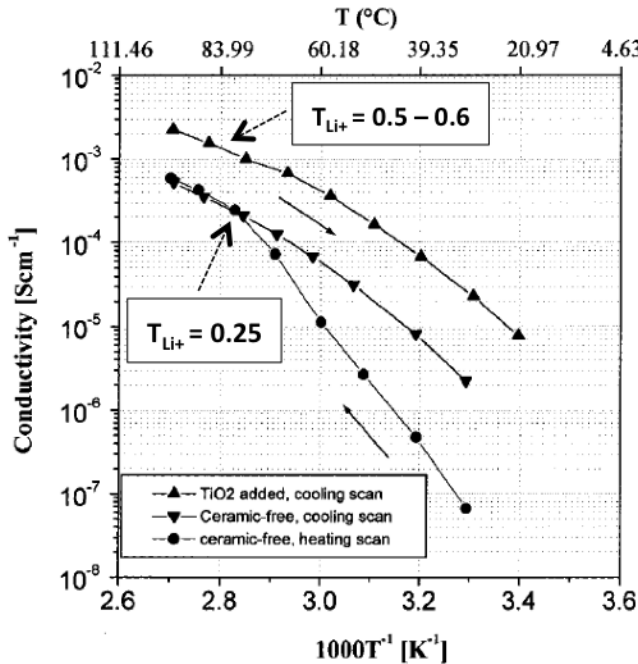
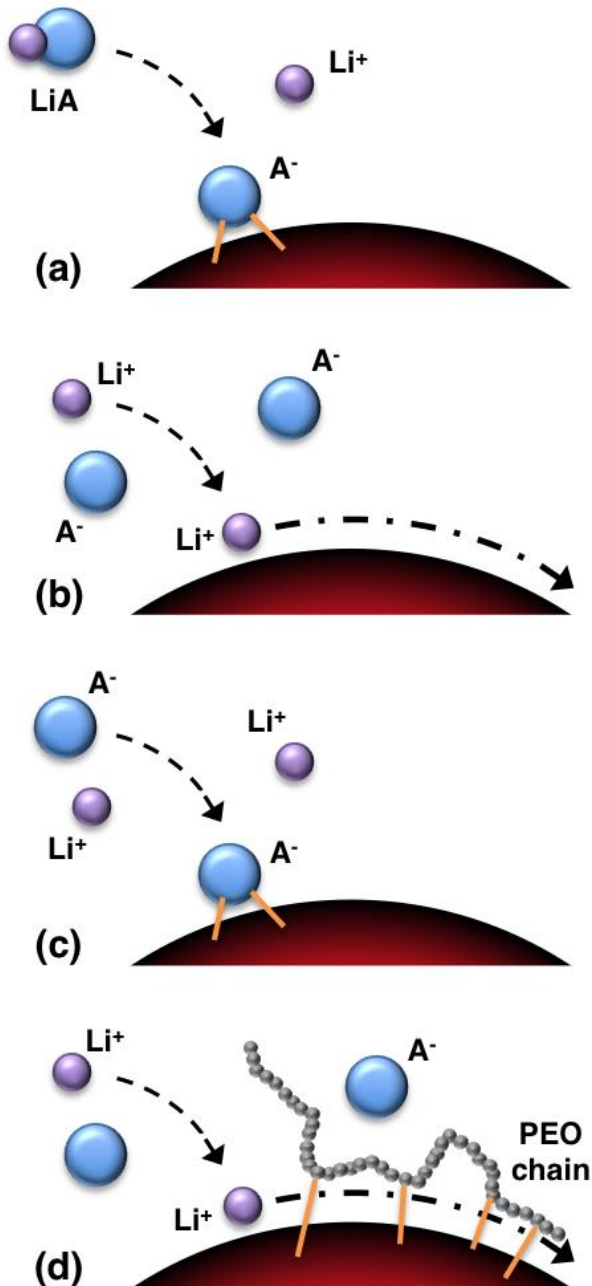


**Figure 3.3** Conductivity of a pristine  $\text{PEO}_8\text{-LiClO}_4$  electrolyte and a nanocomposite  $\text{PEO}_8\text{-LiClO}_4$  electrolyte containing 10wt%  $\text{TiO}_2$ . Lithium transference numbers,  $T_{\text{Li}^+}$ , were obtained at 91°C. Conductivity of the ceramic-free electrolyte at low temperatures decreases from that obtained during the cooling scan with time; the conductivity of the  $\text{TiO}_2$  added electrolyte is maintained during the investigated 2 week period. Adapted from <sup>[16]</sup>

3.4): i) By actively interacting with the ion pair, nanoparticles with specific surface chemistries promote ion-pair dissociation and increase the number of ions able to participate in conduction. Acidic surface sites are in particular thought to attract anions, while basic surfaces attract cations. In either case, the counter-ion is then a charge, mobile species (Fig. 3.4a).<sup>[14,31]</sup> ii) The surface of the nanoparticle in the composite electrolyte then provides an additional site for anion and/or cation migration, due to Lewis acid–base interactions between the salt and the particle surface (Fig. 3.4b).<sup>[14,32]</sup> iii) The particle surface attracts either the anion or cation, leading to a reduction in its mobility (Fig. 3.4c).<sup>[33]</sup> iv) Nanoparticles behave as crosslinking sites for EO–segments and anions, changing the polymer chain structure at the interface and creating pathways for Li<sup>+</sup> transport independent of segmental motion (Fig. 3.4d).<sup>[14,31,34]</sup>

Zhou and Fedkiw<sup>[14]</sup> have provided a comprehensive summary of work on nanocomposite electrolytes until 2004. Most notably, the authors concluded that no clear trend exists between particle surface chemistry and conductivity of the composite electrolyte, and thus type of polymer and salt used also must play a role. In addition, a single surface chemistry may have multiple competing effects within a system. For example, acidic fillers may attract anions, thereby freeing additional cations for conduction (mechanism i). These same fillers may also crosslink surrounding PEO chains, reducing their segmental dynamics (mechanism iv). Differences in preparation methods have also been shown to create differences in measured properties of composites comprising of similar constituents. For example, calcining the silica filler at 900°C versus 100°C showed a greater improvement in ionic conductivity enhancement.<sup>[35]</sup> Water can negatively affect ion transport along the grain boundary (particle surface), and therefore presence of residual water may have skewed the outcomes of early



Schematic by S. Srivastava and J. L. Schaefer

**Figure 3.4** Schematic of the active ion transport mechanisms in polymer nanocomposites. **a.** Ion pair dissociation, **b.** Surface transport, **c.** Anion attraction, and **d.** PEO chain promoted surface transport.

studies. Also, in nearly all reported studies, the composite structure is not characterized. The extent of particle agglomeration or percolation, effective active filler surface area, and phase separation can all be affected by the synthesis scheme and can lead to variations in the composite electrolyte structure<sup>[36]</sup> which result in differences in measured properties.

More recent reports demonstrate the utility and specific role of nanoparticle additives in electrolytes. A 2012 study by Fullerton-Shirey, et al. using high aspect ratio particles has, for example, convincingly demonstrated the role played by surface conduction,<sup>[13]</sup> where percolation allows optimal ionic conductivities to be achieved at very low particle loadings (0.5–1 wt%), as compared to 10 wt% loading for spherical particles, as shown in Figure 3.5. These results imply that the particle surface provides an additional ion transport pathway within the electrolyte, though without characterization of mobile ion concentrations, activation energies, transference numbers, or ion mobilities, it is unknown if the active transport mechanism in this system is mechanism (ii) as described above, or the combined result of both mechanisms (i) and (ii). Scrosati, et. al. demonstrated the concept of an anion withdrawing nanoparticle surface (mechanism (iii)) with super-acidic modified zirconia in PEO,<sup>[32,37,38]</sup> which, remarkably, provides  $T_{\text{Li}^+} = 0.81 \pm 0.05$ . Most recently in 2013, boron containing silica nanoparticles were also shown to be an effective anion withdrawer in a polymeric matrix by Mathews, et. al.;  $T_{\text{Li}^+}$  values of  $0.89 \pm 0.05$  are achieved with simultaneous increases in total ionic conductivity at a 10 wt% loading.<sup>[39]</sup> These results are impressive, but again, without further characterization of mobile ion concentrations or ion mobilities is it unknown if the active transport mechanism is only through mechanism (iii), or a combination of mechanisms (i), (ii), and/or (iii). Importantly,

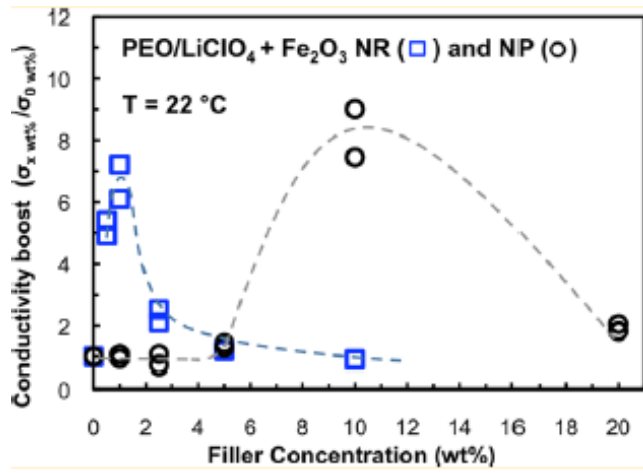


**Figure 3.5** Conductivity enhancement for polymer nanocomposite electrolytes containing nanorods (NR) and nanoparticles (NP). Adapted from [13]

no polymer nanocomposite has yet been produced with sufficiently high ionic conductivity and  $T_{\text{Li}^+}$  values suitable for room temperature use.

Bhattacharyya and Maier in 2004 showed that active  $\text{Li}^+$  surface conduction also occurs in liquid-based nanocomposite suspension electrolytes, or “soggy–sands”,<sup>[40]</sup> which comprise of inert inorganic particles added to a molecular liquid or low molecular weight oligomeric matrix. The liquid matrix allows for percolation of spherical particles at a lower loading, as in the absence of an adsorbed polymer layer the particles readily aggregate to form strings and networks of complex fractal dimensionalities. Because of the low particle loading (<1–3wt%), soggy sand electrolytes with significant  $\text{Li}^+$  surface transport display ionic conductivity above that of the pure salt-doped liquid.<sup>[41]</sup>

The mechanism for ion transport in soggy sands (Figure 3.6) has analogous aspects to that observed in some polymer nanocomposite systems.<sup>[41]</sup> When oxide particles are added to a liquid electrolyte, attraction of the ion pair at the surface facilitates dissociation. The counter-ion will then exist in the space-charge region at the particle–liquid interface. At a given particle loading,  $\varphi_{\text{onset}}$ , a sudden increase in ionic conductivity is observed as percolation allows for long-range transport of the free ions in the space charge layer. The conductivity will continue to increase with increasing particle content until  $\varphi_{\text{max}}$ . Beyond this volume fraction, conductivity decreases due to blocking of the percolative pathways and volume depletion effects. Ultimately, beyond  $\varphi > \varphi_{\text{offset}}$ , the conductivity of the composite decreases below that of the pure liquid itself. Also, it should be noted that in some particle–liquid combinations a network is formed, but no enhancement in conductivity observed.<sup>[41]</sup>

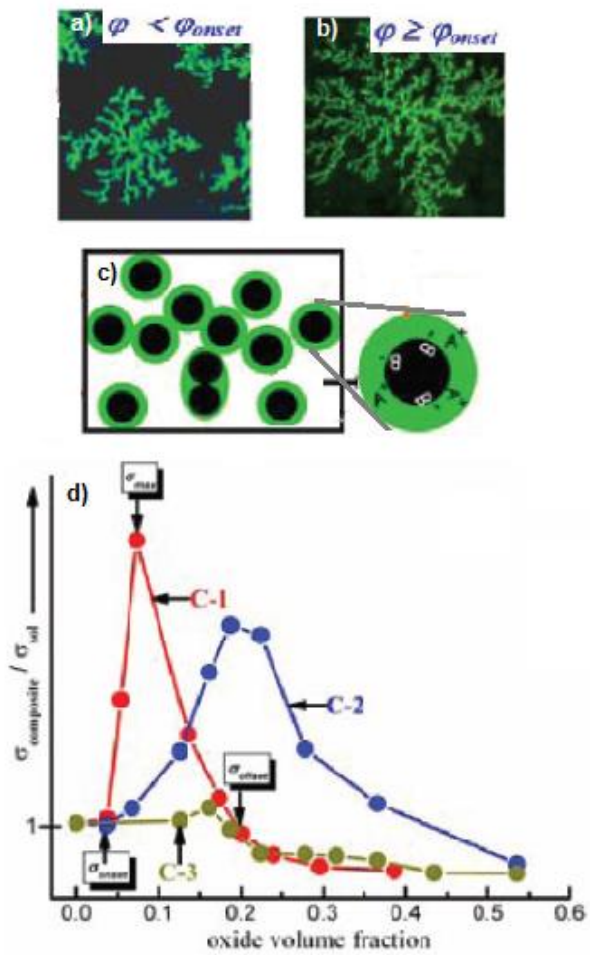


**Figure 3.6** Transport mechanism in soggy sands. **a.** Non-percolating and **b.** percolating oxide particle networks that lead to dissociation of ion pairs, where **c.** trapping of ionic species (B-) leads to a rich concentration of (A+) at the space charge region at the particle-liquid interface. **d.** Representative conductance enhancement for three different particle-liquid electrolytes. Adapted from [41]

Recent work has focused on the understanding of the effect of nanoparticle chemistry and liquid medium chemistry on particle network formation and  $\text{Li}^+$  transport in the space charge layer that exists at the particle–liquid interface.<sup>[41]</sup> The propensity to form networks depends significantly on the form of inter–particle interactions; particles with moderately acidic or basic surface chemistries are found to form gels with a fractal particle network when mixed with solvents such as ethylene glycol or polyethylene glycol while particles with strongly hydrophilic surfaces are found to be well dispersed in the solvent, likely due to short–range repulsive forces between the particles. High dielectric constant,  $\varepsilon$ , of the liquid solvent is expected to allow retention of free  $\text{Li}^+$  as well as screen interparticle forces, allowing for the formation of a percolating space charge layer with a considerable concentration of  $\text{Li}^+$  that may participate in conduction. Predicted ionic conductivity values that account for the number of percolating pathways, ion adsorption concentration at the particle surface, and assume single-ion  $\text{Li}^+$  transport in the space charge layer agree with experimentally measured values.<sup>[42]</sup>

Low molecular weight polyethylene glycols,  $\varepsilon \approx 10$ , are of course the same chemistry as PEO and therefore have received much interest as the liquid component of the soggy sand electrolyte. Multiple reports have detailed studies on  $\text{SiO}_2$ –PEG composites.<sup>[14,43–46]</sup> The size, chemistry, and density of the surface moiety are known to play a significant role in the network formation and ion transport. Enhancements in ionic conductivity of 3–4 times that of the liquid have been observed by doping to  $\varphi = 0.005 – 0.05$  with silica with native hydroxyl surface termination;  $T_{\text{Li}^+}$  as high as 0.8 was measured, in comparison with 0.33 for the liquid. Importantly, PEG– $\text{SiO}_2$  systems with  $\varphi < 0.05$  are found to only partially coarsen over the period of a day, seemingly reaching steady–state ionic conductivities.

Current challenges in these systems stem from a lack of fundamental understanding of how surface chemistry of the particles influences both aging and surface transport, and conductivity of a soggy sand electrolyte may change drastically with a function of time.<sup>[41]</sup> Typically, conductivity has a stepwise improvement with time while the percolating particle networks forms and continues to increase until an optimum network is formed. Beyond this point, further coarsening, and potentially phase separation, with time often leads to depressed conductivities below that of the pure liquid. This is in striking contrast to polymer nanocomposite electrolytes, where the morphology and properties of the composite is typically assumed to be time invariant after annealing. Undoubtedly these effects are caused by time-dependent particle aggregation, which leads to loss of access to surface sites in soggy sands. The inherently high conductivities (derived from the liquid electrolyte) of such systems demands more systematic studies aimed at stabilizing the particles against aggregation, without significantly reducing electrolyte contact with the particle surfaces. We expect that particles sparsely grafted with polymer chains or with mixtures of polymers and molecular species as recently reported will play an important role in advancing this field.<sup>[47-50]</sup>

### **Ionically-functionalized nanoparticle-based electrolytes**

A third category of nanocomposites is created by incorporation of salt or ionic-liquid functionalized particles in polymeric or liquid hosts. With potentially many hundreds of active surface sites that can be decorated with a salt, nanoparticles in the former category can directly function as sources of Li<sup>+</sup> ions in the electrolyte, for example by the use of lithiated tethered anions<sup>[47,48,51-54]</sup> or polyanions<sup>[49,50]</sup> onto the particle surface or by Li<sup>+</sup> exchange of the native

hydroxyl termination.<sup>[46,55]</sup> This concept has been demonstrated by several groups, for the purposes of creating a single-ion conducting electrolyte<sup>[48,46,51-54]</sup> or performance enhancement of the traditional salt-doped<sup>[49,50,56]</sup> or ionic liquid<sup>[52,53]</sup> electrolyte. Immobilization of the anion onto a particle surface provides an alternative to ionomers, and because of the large number of active sites available on the particles, potentially provides flexibility with regards to exposing the anion to a solvating medium and enhancing Li<sup>+</sup> dissociation.

Table 1 summarizes the room temperature ionic conductivity and T<sub>Li<sup>+</sup></sub> values of reported electrolytes containing lithiated nanoparticles. The choice of the solvating matrix has a significant impact on ionic conductivity, as evident by Table 1 and Figure 3.7, however it should be noted that many liquid solvent chemistries are not chemically compatible with lithium-ion electrode materials and/or lithium metal, or may be volatile and/or flammable.<sup>[57]</sup> Further improvements in conductivity may be achieved by optimization of the chemistry of the anion, specifically by delocalizing the negative charge.

Recent work has applied lithiated nanoparticle electrolytes to coin cell studies. Reports by Kim and coworkers<sup>[49,50]</sup> showed that doping a traditional, carbonate-based gel electrolyte with lithiated nanoparticles improved the discharge capacity of lithium-ion cells operating at all rates, but more so as the discharge rate increased up to 5 C. The best enhancement in performance was noted for electrolytes containing nanoparticles with the highest degree of lithiation, for which the greatest improvement in T<sub>Li<sup>+</sup></sub> was measured. A 2013 study by Schaefer et. al.<sup>[47]</sup> on a high T<sub>Li<sup>+</sup></sub> electrolyte created with lithiated nanoparticles in a tetraethylene glycol dimethyl ether host

Host Matrix	Filler Chemistry	Filler Loading	Filler Size (nm)	$\sigma$ (S/cm) at 25°C	T <sub>Li+</sub>	Ref.
<b>PEG200</b>	MMT-Li	10 wt.%	---	$2 \times 10^{-6}$	---	[55]
<b>PEG600</b>	SiO <sub>2</sub> -GLYMO-PO <sub>2</sub> CH <sub>3</sub> Na	1:12.8, Na:EO	15	$9.1 \times 10^{-5}$	0.9	[58]
<b>PEGdm250</b>	SiO <sub>2</sub> -poly(2-acrylamido-2-methyl-1-propane-SO <sub>3</sub> Li)	1:100, Li:EO	12	$4.5 \times 10^{-6}$	0.78	[56]
<b>PEGdm250</b>	SiO <sub>2</sub> -poly(2-acrylamido-2-methyl-1-propane-SO <sub>3</sub> Li)	7.5wt%	^	$1.1 \times 10^{-6}$	---	[59]
<b>PEGdm250</b>	SiO <sub>2</sub> -PEG-SO <sub>3</sub> Li	30 wt.%	7	$2 \times 10^{-6}$	---	
<b>PEO/PEGdm250</b>	SiO <sub>2</sub> -PEG-SO <sub>3</sub> NSO <sub>3</sub> CF <sub>3</sub> Na	1:20, Na:EO	7	$3 \times 10^{-5}$	→ 1	[48]
<b>PEO/PEGdm250</b>	SiO <sub>2</sub> -SO <sub>3</sub> NSO <sub>3</sub> CF <sub>3</sub> Na	1:10, Na:EO	7	$3 \times 10^{-5}$	→ 1	[48]
<b>PEO</b>	POSS-benzyl <sub>7</sub> (BF <sub>3</sub> Li) <sub>3</sub>	1:14, Li:EO	1.5	$4 \times 10^{-4}$	0.6	[60]
<b>TEGdm</b>	SiO <sub>2</sub> -PEG-SO <sub>3</sub> Li	30 wt.%	7	$3 \times 10^{-6}$	---	[47]
<b>TEGdm</b>	SiO <sub>2</sub> -PEG-SO <sub>3</sub> BF <sub>3</sub> Li	30 wt.%	7	$1 \times 10^{-4}$	0.96	[47]
<b>POSS-PEG8</b>	POSS-benzyl <sub>7</sub> (BF <sub>3</sub> Li) <sub>3</sub>	1:16, Li:EO	1.5	$2.4 \times 10^{-4}$ <sup>‡</sup>	0.50	[61]
<b>POSS-PEG8</b>	POSS-benzyl <sub>7</sub> (Li) <sub>3</sub>	1:16, Li:EO	1.5	$3 \times 10^{-6}$ <sup>‡</sup>	---	[61]
<b>EC</b>	SiO <sub>2</sub> -PEG-SO <sub>3</sub> Li	30 wt.%	7	$4 \times 10^{-6}$	---	
<b>EC/DMC</b>	SiO <sub>2</sub> -PEG-SO <sub>3</sub> Li	30 wt.%	7	$3 \times 10^{-5}$	---	
<b>EC/PEGdm250</b>	Hectorite-Li	30 wt.%	250*	$2.5 \times 10^{-4}$	---	[46]
<b>EC/DMA</b>	SiO <sub>2</sub> -SO <sub>3</sub> Li	10 wt.%	12 [150-180]	$2.2 \times 10^{-3}$	---	[53]
<b>PVdF-HFP + EC/DEC + 1.15M LiPF<sub>6</sub></b>	SiO <sub>2</sub> -poly(styrene-SO <sub>3</sub> Li)	20 wt.%	200 + 320nm polymer shell	$1.7 \times 10^{-3}$ ( $4 \times 10^{-4}$ )	0.53 (0.35)	[49] [50]
<b>PC</b>	SiO <sub>2</sub> -poly(2-acrylamido-2-methyl-1-propane-SO <sub>3</sub> Li)	7.5 wt%	^	$3 \times 10^{-6}$		[59]
<b>PC</b>	SiO <sub>2</sub> -PEG-SO <sub>3</sub> Li	30 wt%	7	$2 \times 10^{-5}$	---	
<b>DMSO/PC</b>	SiO <sub>2</sub> -SO <sub>3</sub> Li	10 wt.%	11	$4.3 \times 10^{-4}$	0.95	[52]
<b>DMSO</b>	MMT-Li	10 wt.%	---	$2.5 \times 10^{-4}$	---	[55]
<b>DMSO</b>	SiO <sub>2</sub> -SO <sub>3</sub> Li	10 wt.%	12 [150-180]	$1.3 \times 10^{-3}$	---	[53]
<b>DMSO</b>	SiO <sub>2</sub> -PEG-SO <sub>3</sub> Li	30 wt.%	7	$5 \times 10^{-4}$	---	
<b>DMA</b>	SiO <sub>2</sub> -PEG-SO <sub>3</sub> Li	30 wt.%	7	$5 \times 10^{-4}$	---	
<b>Sulfolane</b>	SiO <sub>2</sub> -PEG-SO <sub>3</sub> Li	30 wt.%	7	$1 \times 10^{-5}$	---	

**Table 1.** Ionic conductivity ( $\sigma$ ) and T<sub>Li+</sub> for electrolytes containing functionalized nanoparticle fillers.

\*platelet, <sup>‡</sup> at 30°C, ^no size noted- surface area = 20 m<sup>2</sup>/g

( ) denotes value of property of base electrolyte without the nanoparticle additive

[ ] denotes size of filler aggregate

DMA – dimethyl acetamide, DMC – dimethyl carbonate, DMSO – dimethyl sulfoxide, EC – ethylene carbonate, MMT – montmorillonite, PC – propylene carbonate, PEGdm – polyethylene glycol dimethyl ether, POSS – polyoctahedral silsesquioxane

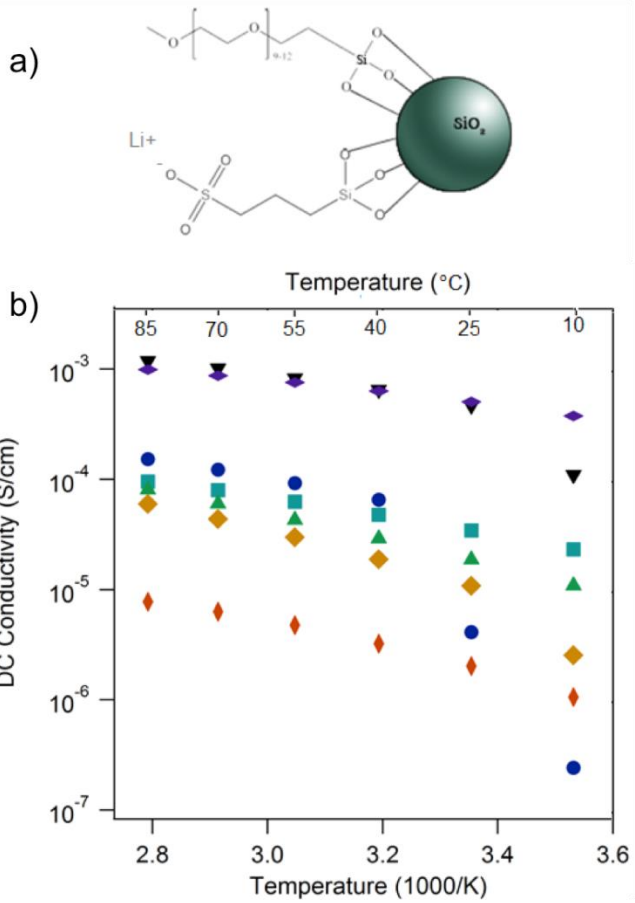


**Fig. 3.7** a) Schematic of a nanoscale lithium salt produced by the cofunctionalization of silica by silane-PEG and silane- $\text{SO}_3\text{Na}$  and subsequent Li exchange and b) DC ionic conductivity of electrolytes containing about 30wt% of the nanoscale lithium salt as a function of the suspending fluid:  $\blacktriangledown$ DMSO,  $\blacklozenge$  DMA,  $\bullet$  EC,  $\blacksquare$  EC/DMC,  $\blacktriangle$  PC,  $\blacklozenge$  sulfolane,  $\blacklozenge$  PEGdm250.

showed that when used in lithium metal batteries undergoing galvanostatic polarization, cell lifetimes were proportional to the inverse square of the applied current density as previously predicted theoretically.<sup>[62]</sup> This same theory predicts that lithium metal cell lifetimes may be increased considerably in electrolytes where  $T_{\text{Li}^+}$  approaches unity, and the increase might happen at lower  $T_{\text{Li}^+}$  for essentially single-ion conducting electrolytes with higher ionic conductivities and mobile ion concentrations. Thus, creation of high  $T_{\text{Li}^+}$  electrolytes with improved ionic conductivities is very desirable. Recent theoretical work suggests that immobilization of only a fraction of the anion in the electrolyte can have a dramatic effect on cell lifetimes in lithium batteries.<sup>[63]</sup> Composite electrolytes created by dispersing ionic–liquid functionalized nanoparticles in a polymer or fluid electrolyte host can serve this purpose by partially immobilized supporting electrolyte in conjunction with a free lithium salt containing matrix, or simply lithium salt alone.<sup>[64-67]</sup> In either case, use of ionically functionalized particles leads to reduced ion concentration gradients across the inter-electrode space and have been shown very recently to increase the time-to-failure of lithium batteries as much as ten-fold.

### **3.5 Interfacial Effects of Nanoparticles**

A consequence of incorporating nanoparticles into polymer and liquid electrolytes is that the particles migrate to the electrode-electrolyte interface and thereby potentially provide new strategies for stabilizing the interface. Several groups have noted decreased interfacial resistance and improved stability of the solid–electrolyte–interface (SEI) at the lithium metal anode by use of a ceramic particles in dry polymeric,<sup>[68-72]</sup> gel,<sup>[73]</sup> and liquid hosts,<sup>[74]</sup> or liquid-soaked separators.<sup>[75]</sup> The nanoparticles are thought to achieve these functions through a variety of mechanisms, including acting as sponges/scavengers for impurities in the bulk electrolyte,

mitigating their reaction with the electrode. In a dry polymer cell, the presence of the electrode slows the dynamics of chains close to the interface. Use of a nanoparticle additive is believed to increase these segmental dynamics, thus facilitating Li<sup>+</sup> transport at the interface. Furthermore, nanoparticle migration to interfaces is a well-studied effect and is anticipated to also be important in understanding interfacial effects of nanoparticles in lithium batteries. It is proposed that in a nanocomposite, the particles form a thin layer at the electrode–electrolyte interface.

Functionalization of the particles could aid in the development and structure of this solid-electrolyte interface (SEI) layer. An extreme example of the benefits one might derive from particles in the SEI is the capacity to localize functional groups at the interface that appear to facilitate even lithium metal deposition.<sup>[76]</sup> It has been suggested that electrolyte mechanics,<sup>[77-80]</sup> interfacial resistance,<sup>[72,79-83]</sup> supporting electrolyte content,<sup>[62,66]</sup> and bulk transport properties<sup>[62,80,82,84,85]</sup> such as ionic conductivity, T<sub>Li+</sub>, and mobile ion concentrations, all play a role in lithium dendrite onset and propagation in the lithium metal battery. Nanoparticle additives can affect all of the aforementioned properties, as demonstrated by several groups.<sup>[47,48,79-82,86]</sup> Despite the large amount of activity in this area, the literature is unsatisfying at present because most reports identify one or more arbitrarily selected parameters as the driving force for the improved performance upon nanoparticle addition and focus their investigations on these parameters, while changes in other parameters are ignored. We are hopeful that with the more recent focus on theoretical and fundamentally based approaches, progress in understanding in this area will be swift.

## **Conclusions and outlook**

Determining why dispersed nanoparticles increase ionic conductivity and lower the viscosity of polymer hosts is another area of tremendous opportunity. For example, while it is now well established from numerous studies that nanoparticles can enhance ion transport in polymers by a variety of mechanisms, it is quite unfortunate that in most cases the morphology of these polymer nanocomposite electrolytes are never characterized. It is also unfortunate that important parameters, such as mobile ion concentrations and ion mobilities, known to be important in ion conduction are rarely characterized. Review of the known ion conduction mechanisms for composites leads to the following conclusions: 1) In cases where  $\text{Li}^+$  conduction occurs along the particle surface, optimum  $\text{Li}^+$  conductivity should be achieved by maximization of accessible percolation pathways. 2) In cases where the particle restricts anion mobility alone, without contributing to  $\text{Li}^+$  transport, or promotes ion pair dissociation to increase  $\text{Li}^+$  concentration in the bulk, optimal construction maximizes available particle surface area. Particle coarsening into clumps decreases filler effectiveness by increasing the filler mass/volume relative to the effective surface area in both instances. However, in case 1 formation of strings or networks is preferred, while by case 2 homogeneous dispersion is optimal. Significant insights into these mechanisms would be gained by detailed morphological studies as well as from careful studies of electrolyte viscoelastic and rheological properties. Additionally, understanding why small particles migrate to electrode/electrolyte interfaces in batteries and how they stabilize these interfaces in lithium ion cells provides an important path towards leveraging favorable properties of well-established liquid electrolytes for applications with high voltage NMC-type electrodes.

As exciting is the possibility of taking advantage of nanoparticle-ion interactions to create polymer electrolytes with high Li<sup>+</sup> conductivities. As evidenced by work on soggy-sand electrolytes, long-range network formation with spherical inclusions may be facilely achieved in liquids at very low particle loadings, which facilitates Li<sup>+</sup> transport across the inter-electrode space by way of the particle surface rather than the host matrix and results in conductivity enhancement of 3–5 times relative to the pristine electrolytes. This magnitude of conductivity enhancement is not sufficient for advancement of room temperature polymer electrolytes as viable alternatives to currently used liquid electrolytes. Simultaneously mitigation of chain crystallization to extend VTF-temperature dependent conductivity and a step-wise enhancement of upwards of 2 orders of magnitude is necessary. Such a room temperature conductivity enhancement coupled with high T<sub>Li<sup>+</sup></sub> values could provide for a polymer-based electrolyte with transport properties that make it competitive with conventional liquid electrolytes while offering improved safety. Recent efforts aimed at creating particle-based salts in which an anion is covalently grafted to nanoparticles provides a promising direction for future studies. In addition to guaranteeing T<sub>Li<sup>+</sup></sub> ≈ 1, the large number of functional groups on the surface of nanoparticles provide opportunities for tethering molecules with more than one chemistry or molecular weight that provide good dispersion of the particles salts in polymers and at the same time increase free-volume of their polymer host to maximize conductivity. There is both existing<sup>[62,84,85]</sup> and emerging<sup>[63]</sup> theoretical support for the benefits of such electrolytes in delaying/eliminating failure of secondary batteries based on metals (e.g. Li, Na, Al) prone to failure by dendrite formation and short circuits is strong. We anticipate that this will lead to important opportunities for further work.

## References

- [1] J. E. Weston, B. C. H. Steele, Solid State Ionics 1982, 7, 75.
- [2] Z. Gadjourova, Y. G. Andreev, D. P. Tunstall, P. G. Bruce, Nature 2001, 412.
- [3] A. M. Christie, S. J. Lilley, E. Staunton, Y. G. Andreev, P. G. Bruce, Nature 2005, 433, 50.
- [4] Y. Wang, A. L. Agapov, F. Fan, K. Hong, X. Yu, J. Mays, A. P. Sokolov, Physical Review Letters 2012, 108, 088303.
- [5] R. Kumar, M. Goswami, B. G. Sumpter, V. N. Novikov, A. P. Sokolov, Phys. Chem. Chem. Phys. 2013, 15, 4604.
- [6] M. Dolle, T. F. Fuller, J. Newman, Electrochimica Acta 1994, 39, 2073.
- [7] J. Maier, Advanced Functional Materials 2011, 21, 1448.
- [8] K. Xu, Chemical Reviews 2004, 104, 4303.
- [9] M. Klett, M. Giesecke, A. Nyman, F. Hallberg, R. W. Lindstrom, G. Lindbergh, I. Furo, Journal of the American Chemical Society 2013, 134, 14654.
- [10] R. Meziane, J.-P. Bonnet, M. Courty, K. Djellab, M. Armand, Electrochimica Acta 2011, 57, 14.
- [11] S. Liang, U. H. Choi, W. Liu, J. Runt, R. H. Colby, Chemistry of Materials 2012, 24, 2316.
- [12] F. Croce, G. B. Appetecchi, L. Persi, B. Scrosati, Nature 1998, 394, 456.
- [13] N. S. T. Do, D. M. Schaetzl, B. Dey, A. C. Seabaugh, S. K. Fullerton-Shirey, The Journal of Physical Chemistry C 2012, 116, 21216.
- [14] J. Zhou, P. S. Fedkiw, Solid State Ionics 2004, 166, 275.
- [15] F. Capuano, F. Croce, B. Scrosati, Journal of The Electrochemical Society 1991, 138, 1918.

- [16] F. Croce, R. Curini, A. Martinelli, L. Persi, F. Ronci, B. Scrosati, R. Caminiti, The Journal of Physical Chemistry B 1999, 103, 10632.
- [17] M. Marcinek, A. Bac, P. Lipka, A. Zalewska, G. Zukowska, R. Borowska, W. Wieczorek, Journal of Physical Chemistry B 2000, 104, 11088.
- [18] W. Wieczorek, A. Zalewska, D. Raducha, Z. Florjanczyk, J. R. Stevens, Journal of Physical Chemistry B 1998, 102, 352.
- [19] P. F. Green, Soft Matter 2011, 7, 7914.
- [20] S. K. Kumar, N. Jouault, B. Benicewicz, T. Neely, Macromolecules 2013, 46, 3199.
- [21] N. J. Fernandes, H. Koerner, E. P. Giannelis, R. A. Vaia, MRS Communications 2013, 3, 13.
- [22] H.-M. Xiong, D.-P. Liu, H. Zhang, J.-S. Chen, Journal of Materials Chemistry 2004, 14, 2775.
- [23] J. L. Nugent, S. S. Moganty, L. A. Archer, Adv Mater 2010, 22, 3677.
- [24] J. L. Schaefer, S. S. Moganty, D. A. Yanga, L. A. Archer, Journal of Materials Chemistry 2011, 21, 10094.
- [25] M. Popall, M. Andrei, J. Kappel, J. Kron, K. Olma, B. Olsowski, Electrochimica Acta 1996, 43, 1155.
- [26] H.-M. Kao, S.-W. Chao, P.-C. Chang, Macromolecules 2006, 39, 1029.
- [27] M. Jeyapandian, S. Lavina, S. Thayumanasundararam, H. Ohno, E. Negro, V. D. Noto, Journal of Power Sources 2010, 195, 341.
- [28] M. Piszcza, M. Marzantowicz, A. Plewa-Marczewska, G. Z. Zukowska, A. Zalewska, A. Pietrzykowski, M. Siekierski, Journal of Power Sources 2010, 195, 7495.
- [29] H.-M. Kao, C.-L. Chen, Angewandte Chemie International Edition 2004, 43, 980.

- [30] D. Saikia, H.-Y. Wu, C.-P. Lin, Y.-C. Pan, J. Fang, L.-D. Tsai, G. T. K. Fey, H.-M. Kao, Polymer 2012, 53, 6008.
- [31] F. Croce, L. Persi, B. Scrosati, F. Serraino-Fiory, E. Plichta, M. A. Hendrickson, 2001.
- [32] P. A. R. D. Jayathilaka, M. A. K. L. Dissanayake, I. Albinsson, B.-E. Mellander, Electrochimica Acta 2002, 47, 3257.
- [33] F. Croce, L. Settimi, B. Scrosati, Electrochemistry Communications 2006, 8, 364.
- [34] Y. Dai, Y. Wang, S. G. Greenbaum, S. A. Bajue, D. Golodnitsky, G. Ardel, E. Strauss, E. Peled, Electrochimica Acta 1998, 43, 1557.
- [35] C. Capiglia, P. Mustarelli, E. Quartarone, C. Tomasi, A. Magistris, Solid State Ionics 1999, 118, 73.
- [36] J. Syzdek, M. Armand, M. Marcinek, A. Zalewska, G. Zukowska, W. Wieczorek, Electrochimica Acta 2010, 55, 1314.
- [37] S. Panero, B. Scrosati, H. H. Sumathipala, W. Wieczorek, Journal of Power Sources 2007, 167, 510.
- [38] G. Derrien, J. Hassoun, S. Sacchetti, S. Panero, Solid State Ionics 2009, 180, 1267.
- [39] K. L. Mathews, A. M. Budgin, S. Beeram, A. T. Joenathan, B. D. Stein, U. Werner-Zwansiger, M. Pink, L. A. Baker, W. E. Mahmoud, J. P. Carini, L. M. Bronstein, Journal of Materials Chemistry A 2013, 1, 1108.
- [40] A. J. Bhattacharyya, M. Dolle, J. Maier, Electrochemical and Solid-State Letters 2004, 7, A432.
- [41] A. J. Bhattacharyya, The Journal of Physical Chemistry Letters 2012, 3, 744.
- [42] C. Pfaffenhuber, J. Maier, Phys. Chem. Chem. Phys. 2013, 15, 2050.
- [43] S. K. Das, A. J. Bhattacharyya, Journal of Physical Chemistry B 2010, 114, 6830.

- [44] A. Jarosik, C. Pfaffenhuber, A. Bunde, J. Maier, Advanced Functional Materials 2011, 21, 3961.
- [45] A. Jarosik, S. Hore, N. Kaskhedikar, C. Pfaffenhuber, J. Maier, Electrochimica Acta 2011, 56, 8115.
- [46] H. J. Walls, M. W. Riley, R. R. Singhal, R. J. Spontak, P. S. Fedkiw, S. A. Khan, Advanced Functional Materials 2003, 13, 710.
- [47] J. L. Schaefer, D. A. Yanga, L. A. Archer, Chemistry of Materials 2013, 25, 854.
- [48] I. Villaluenga, X. Bogle, S. Greenbaum, I. Gil de Muro, T. Rojo, M. Armand, Journal of Materials Chemistry A 2013.
- [49] Y.-S. Lee, S. H. Ju, J.-H. Kim, S. S. Hwang, J.-M. Choi, Y.-K. Sun, H. Kim, B. Scrosati, D.-W. Kim, Electrochemistry Communications 2012, 17, 18.
- [50] S. H. Jun, Y.-S. Lee, Y.-K. Sun, D.-W. Kim, Journal of Materials Chemistry A 2013, 1, 395.
- [51] X.-W. Zhang, P. S. Fedkiw, Journal of The Electrochemical Society 2005, 152, A2413.
- [52] N.-S. Choi, Y. M. Lee, B. H. Lee, J. A. Lee, J.-K. Park, Solid State Ionics 2004, 167, 293.
- [53] J. Sun, P. Bayley, D. R. MacFarlane, M. Forsyth, Electrochimica Acta 2007, 52, 7083.
- [54] Y. Shekibi, J. M. Pringle, J. Sun, S. J. Pas, N. M. Rocher, B. R. Clare, A. J. Hill, D. R. MacFarlane, M. Forsyth, Journal of Materials Chemistry 2010, 20, 338.
- [55] J. Sun, D. R. MacFarlane, M. Forsyth, Solid State Ionics 2007, 178, 785.
- [56] X. W. Zhang, P. S. Fedkiw, Journal of the Electrochemical Society 2005, 152, A2413.
- [57] K. Xu, Chem Rev 2004, 104, 4303.
- [58] L. M. Bronstein, R. L. Karlinsey, B. Stein, Z. Yi, J. Carini, J. W. Zwanziger, Chemistry of Materials 2008, 18, 708-715.

- [59] H. Zhang, X. Zhang, E. Shiue, P. S. Fedkiw, Journal of Power Sources 2008, 177, 561-565.
- [60] P. R. Chinnam, S. L. Wunder, Journal of Materials Chemistry A 2013, 1, 1731.
- [61] P. R. Chinnam, S. L. Wunder, Chemistry of Materials 2011, 23, 5111.
- [62] J. Chazalviel, Phys Rev A 1990, 42, 7355.
- [63] M. Tikekar, D. L. Koch, L. A. Archer, in preparation.
- [64] S. S. Moganty, N. Jayaprakash, J. L. Nugent, J. Shen, L. A. Archer, Angew Chem Int Ed Engl 2010, 49, 9158.
- [65] S. S. Moganty, S. Srivastava, Y. Lu, J. L. Schaefer, S. A. Rizvi, L. A. Archer, Chemistry of Materials 2012, 24, 1386.
- [66] Y. Y. Lu, S. K. Das, S. S. Moganty, L. A. Archer, Advanced Materials 2012, 24, 4430.
- [67] S. Ito, A. Unemoto, H. Ogawa, T. Tomai, I. Honma, Journal of Power Sources 2012, 208, 271.
- [68] F. C. G. B. Appetecchi, G. Dautzenberg, M. Mastragostino, F. Ronci, B. Scrosati, F. Soavi, A. Zanelli, F. Alessandrini, P. P. Prosini, Journal of The Electrochemical Society 1998, 145, 4126.
- [69] B. Scrosati, F. Croce, L. Persi, Journal of The Electrochemical Society 2000, 147, 1718.
- [70] B. Scrosati, F. Croce, S. Panero, Journal of Power Sources 2001, 100, 93.
- [71] J. Kumar, S. J. Rodrigues, B. Kumar, Journal of Power Sources 2010, 195, 327.
- [72] S. Liu, N. Imanishi, T. Zhang, A. Hirano, Y. Takeda, O. Yamamoto, J. Yang, Journal of Power Sources 2010, 195, 6847.
- [73] R. Prasanth, N. Shubha, H. H. Hng, M. Srinivasan, European Polymer Journal 2012, 48, 307.

- [74] J. Fan, P. S. Fedkiw, Journal of The Electrochemical Society 1997, 144, 399.
- [75] E.-S. Choi, S.-Y. Lee, Journal of Materials Chemistry 2011, 21, 14747.
- [76] Y. Lu, Y. Kambe, L. A. Archer, in preperation.
- [77] C. Monroe, J. Newman, Journal of the Electrochemical Society 2005, 152, A396.
- [78] G. M. Stone, S. A. Mullin, A. A. Teran, D. T. Hallinan, A. M. Minor, A. Hexemer, N. P. Balsara, Journal of the Electrochemical Society 2012, 159, A222.
- [79] X. W. Zhang, Y. X. Li, S. A. Khan, P. S. Fedkiw, Journal of the Electrochemical Society 2004, 151, A1257.
- [80] S. H. Kim, K. H. Choi, S. J. Cho, E. H. Kil, S. Y. Lee, Journal of Materials Chemistry A 2013, 1, 4949.
- [81] S. Liu, N. Imanishi, T. Zhang, A. Hirano, Y. Takeda, O. Yamamoto, J. Yang, Journal of The Electrochemical Society 2010, 157, A1092.
- [82] S. Liu, H. Wang, N. Imanishi, T. Zhang, A. Hirano, Y. Takeda, O. Yamamoto, J. Yang, Journal of Power Sources 2011, 196, 7681.
- [83] K. Nishikawa, T. Mori, T. Nishida, Y. Fukunaka, M. Rosso, Journal of Electroanalytical Chemistry 2011, 661, 84.
- [84] C. Brissot, M. Rosso, J. N. Chazalviel, S. Lascaud, Journal of Power Sources 1999, 81, 925.
- [85] M. Rosso, T. Gobron, C. Brissot, J. N. Chazalviel, S. Lascaud, Journal of Power Sources 2001, 97-8, 804.
- [86] S. Liu, N. Imanishi, T. Zhang, A. Hirano, Y. Takeda, O. Yamamoto, J. Yang, Journal of Power Sources 2010, 195, 6847.

## **CHAPTER 4.**

### **SOLVENT-FREE NANOSCALE ORGANIC HYBRID ELECTROLYTES**

Reproduced with Permission from Advanced Materials, 22(33), 3677-3680, 2010 by J. L. Schaefer, S. S. Moganty, and L. A. Archer.

#### **4.1 Introduction**

Significant effort has been devoted by research groups worldwide to the development of polymer and composite polymer electrolytes for use in lithium batteries.<sup>[1,2]</sup> The best known polymer ionic conductor, polyethylene oxide (PEO), is crystalline and has low conductivity at room temperature. While short chain polyethylene glycol (PEG) oligomers exhibit good ionic conductivity at room temperature as well as chemical and thermal stability, amorphous low molecular weight electrolytes lack mechanical strength. The addition of free inorganic particles<sup>[3–7]</sup> as well as inorganic networks<sup>[8]</sup> and inorganic–organic constituents<sup>[9–11]</sup> to polymer electrolytes has been shown to improve both mechanical properties and conductivity.

In this communication, we report on a new class of solvent-free, nanoscale organic hybrid materials (NOHMs), which simultaneously manifest superionic conductivities, large electrochemical stability windows ( – 0.5 V to > 5 V, vs. Li/Li+), typical lithium ion transference numbers ( ~ 0.1 – 0.25), no volatility and thermal stabilities up to 400°C, and which offer multiple handles through which near molecular control can be exerted on mechanical properties. All of these features provide unusual opportunities for engineering new families of high-

performance, nanoscale hybrid electrolytes for lithium batteries with markedly improved safety, enhanced tunability, and comparable electrochemical properties to currently used aprotic liquids. Created by densely grafting polyethylene glycol oligomers to the surface of inorganic nanostructures (Figure 4.1 (a)), these hybrids have recently been reported<sup>[12]</sup> to display liquid-like transport properties, including a well-defined Newtonian flow regime, in the absence of any suspending solvent. This last feature makes them the first example of a system of particles of any size that is able to reach equilibrium in the absence of a suspending solvent. It also means that the materials are best visualized as a collection of nanoscale building blocks, which are themselves organic/inorganic hybrids (Figure 4.1 (b)) – making them the first example of a hybrid material designed from the bottom-up, i.e. where each and every building block is a nano-sized organic/ inorganic hybrid.

## 4.2 Experimental Section

NOHMs were synthesized using two approaches: (i) sulfonic acid functionalization of the silica nanoparticle suspension followed by reaction with an amine terminated polyethylene glycol methyl ether (Figure 4.1 , pathways 1 and 2); and (ii) direct reaction of a trimethoxysilane functionalized polyethylene glycol methyl ether with nanoparticle suspensions of either silica or titania (Figure 4.1 , pathway 3). Unattached polymer resulting from the procedure in scheme (ii) is removed by repeated dialysis in chloroform.

*Synthesis of Hybrids by Silane Chemistry (S2, S8-S9):* An alkaline stabilized dispersion of silica nanoparticles, Ludox SM-30 (Aldrich, 8 nm diameter) or Ludox HS-40 (Aldrich, 18 nm diameter), was diluted to 4 wt% particle fraction by addition of aqueous potassium hydroxide

solution, pH ~ 10–11. [Methoxy(polyethyleneoxy)propyl] trimethoxysilane, 90% (Gelest) at a ratio of 1.5 g silane-PEG per 1.0 g silica was added dropwise, while stirring, in three aliquots each separated by heating at 100 °C in an oil bath for 1 hour followed by 10–15 minutes of sonication. Following the addition of the final aliquot of silane-PEG, the reaction solution was heated for 6 hours in an oil bath at 100 °C. The reaction solution was then poured into wide petri dishes and heated overnight in a convection oven at 70 °C to drive off remaining water and complete the silane reaction. The following day, the product was put into dialysis tubing and dialyzed for several days in chloroform to remove any remaining free silane-PEG. An acidic stabilized dispersion of titania nanoparticles (MKNano, 15 nm diameter) was diluted to 4 wt% particle fraction by addition of aqueous acetic acid solution, pH ~ 3. The rest of the reaction was followed identically to the above silica based procedure, though a ratio of 2.0 g silane-PEG per 1.0 g titania was employed.

*Synthesis of Hybrids by Acid-Base Chemistry (S1, S3-S7):* Hybrids were prepared via procedure similar to that published in [ 18 ] with the following exceptions: the silica dispersion used was Ludox SM-30 (Aldrich) and the reaction was carried out at pH ~ 2. Following titration, amine terminated polyethylene glycol methyl ethers of varying molecular weights (Polymer Source) or tertiary amine polyethylene glycol Ethomeen C-25 (Talas) were added stoichiometrically to the acid-functionalized silica solution and allowed to stir at room temperature for 2–3 days. The resulting NOHMs were dried in a laboratory convection oven and then under vacuum overnight prior to use.

*Preparation of Electrolytes:* A solution of lithium bis(trifluoromethane sulfone imide) (LiTFSI, Aldrich) was prepared in dry methanol (Aldrich) in the glove box before use. The lithium salt solution was added to the NOHMs at a concentration of 1 M in PEG for all samples. After

mixing, samples were dried in the convection oven at 50 ° C overnight and for at least 24 hours under vacuum.

*Instrumentation:* TEM images were taken at 120 kV with a FEI Tecnai T-12 TWIN TEM. Sample was dissolved in methanol, dropped onto a copper grid, and solvent was evaporated off prior to imaging. TGA measurements were obtained on a TA Instruments model Q5000 under N<sub>2</sub> flow. DSC measurements were obtained on a TA Instruments model Q2000. Dielectric measurements were taken with a Novacontrol model N40 dielectric broadband spectrometer. Rheology measurements were performed using a Rheometric Scientific Ares rheometer outfitted with 10 mm diameter, 1° cone-and-plate fixtures, and an Anton Paar Rheometer (MCR 501) outfitted with 25 mm diameter parallel plates.

### 4.3 Results and Discussion

By varying the nanoparticle (core) size and organic polymer (corona) molecular weight and grafting density, the volume fraction of the inorganic component can be systematically varied and mechanical properties manipulated over a broad range. Figure 4.2, for example, illustrates the effect of the volume fraction  $\phi$  of SiO<sub>2</sub> nanoparticle cores on the dynamic shear moduli. The figure compares these properties with their equivalents for the pure corona polymer ( $\phi = 0$ ). It

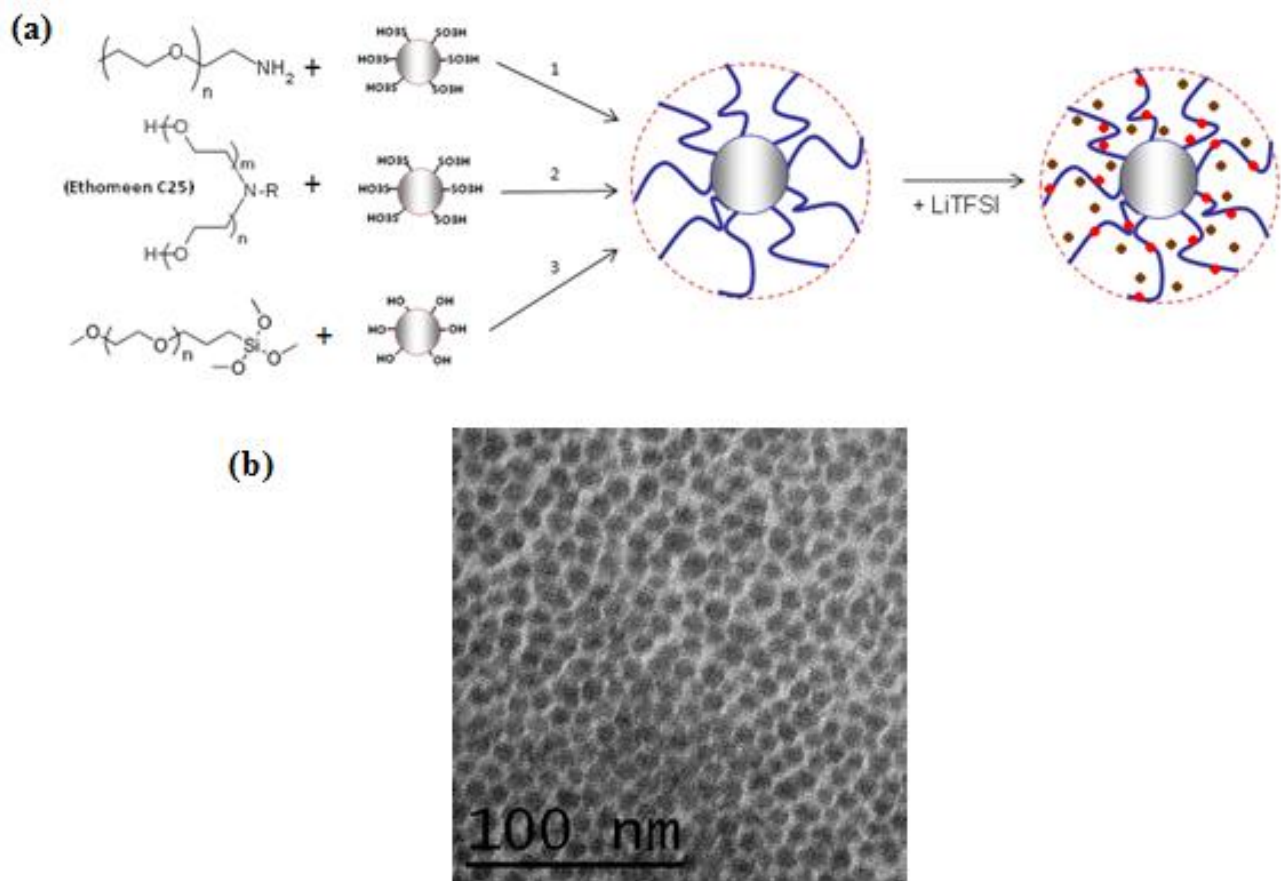


**Figure 4.1** (a) Schematic of NOHMs electrolyte synthesis. The red and brown dots represent  $\text{Li}^+$  and  $\text{TFSI}^-$  ions, respectively; (b) TEM of  $\text{SiO}_2$ -PEG NOHMs comprised of 8 nm  $\text{SiO}_2$  core and PEG corona, with  $M_n = 660 \text{ g mol}^{-1}$ , produced by pathway 3.

is immediately apparent that by tethering the PEG oligomers to nanoparticles, the mechanical modulus measured at any frequency is dramatically increased, relative to the untethered corona ( $\varphi = 0$ ). It is also evident that both the value of the mechanical moduli and the frequency dependence can be facilely altered by changing  $\varphi$ , in this case by varying the effective oligomer grafting density. At high core fractions, the real component (storage),  $G'$ , of the dynamic modulus dominates the imaginary component (loss),  $G''$ , and exhibits little if any variations with shear frequency; features normally associated with ideal elastic solids. On the other hand, at low  $\varphi$  both moduli are of comparable magnitude and a transition from solid-like ( $G' > G''$ ) to liquid-like ( $G'' > G'$ ) behaviors is observed in the NOHMs as the shear frequency is reduced. These behaviors should be contrasted with those of the untethered corona, which is liquid-like ( $G'' > G'$ ) and substantially softer than their NOHMs counterparts.

Figure 4.2 (b) shows that even at the highest core fractions, NOHMs are in reality not elastic solids, but are soft glasses. Specifically, the figure shows that with increasing shear strain  $\gamma$  the materials rapidly soften, and at a critical strain  $\gamma_y$  manifest a pronounced maximum in  $G''$ , after which they behave as simple fluids (i.e.  $G'' > G'$ ). The weak frequency dependence and pronounced loss maximum apparent at  $\gamma_y$  are characteristic of a class of yield-stress fluids termed soft-glasses.<sup>[13]</sup> In these fluids, individual elements are thought to be trapped in cages (see left cartoon, Figure 4.2 (b)) with barrier energies substantially higher than the thermal energy  $kT$ , produced by interactions with their neighbors. The maximum in  $G''$  coincides with a change in slope of the shear stress,  $\tau$ , versus strain (Figure 4.2 (a)) and reflects enhanced dissipation of mechanical energy produced when the cages break-apart (Figure 4.2 (b), right)

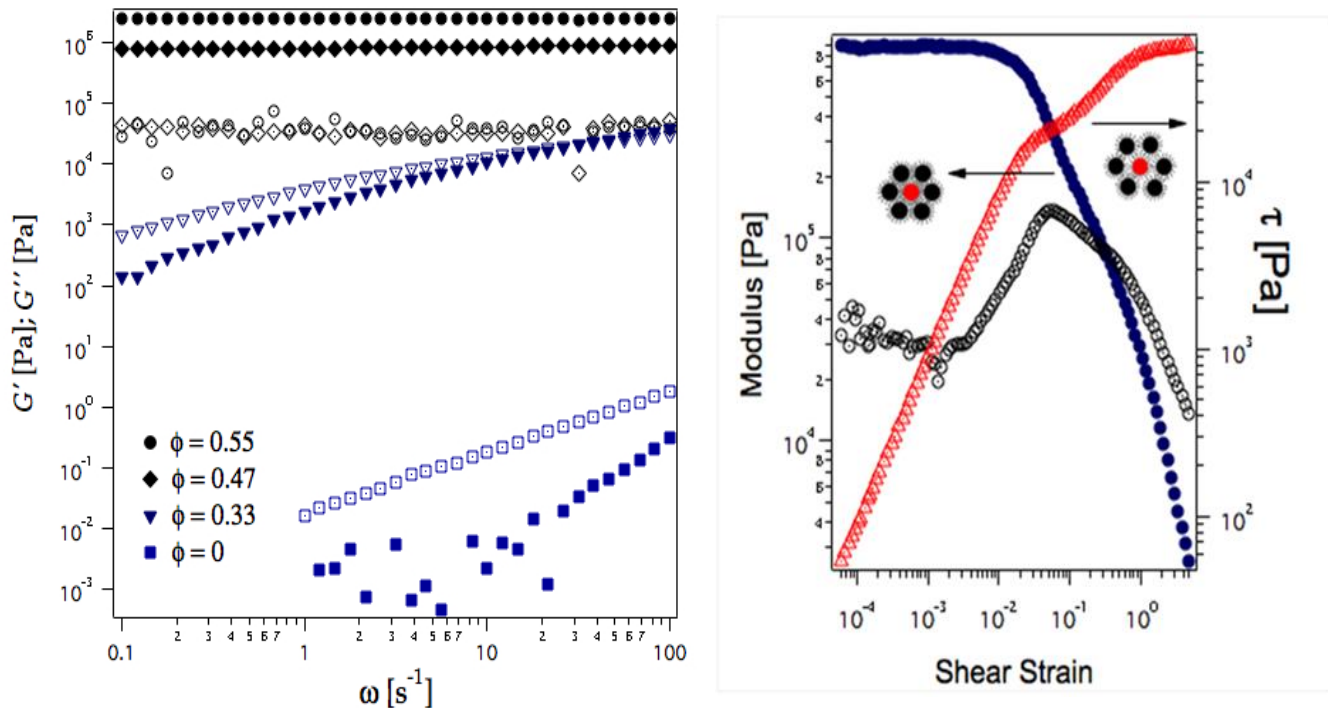


**Figure 4.2** (a) Dynamic shear moduli versus frequency for NOHMs comprised of 18 nm  $\text{SiO}_2$  core and PEG corona, with  $M_n = 660 \text{ g mol}^{-1}$  produced by pathway 3, as a function of core volume fraction  $\phi$ ; (b) Dynamic storage  $G'$  (filled circles), loss  $G''$  (open), and shear stress (triangles) versus strain for NOHMs in 4.2 (a) with  $\phi = 0.47$ .

cartoon) under the action of shear; the critical strain  $\gamma_y$  is the effective yield strain at the conditions of the measurement. These observations imply that NOHMs are solvent-free, homogeneous soft glasses that manifest tunable mechanical properties. To determine the effect of tethering on ionic conductivity of the oligomer corona, we synthesized a series of NOHMs doped with varying amounts of lithium bis(trifluoromethylsulfonyl)imide (LiTFSI) to form a 1M electrolyte in the organic phase. To investigate the effect of core particle size and chemistry and corona molecular weight, NOHMs with a range of physical characteristics (Table 1, Supporting Information) were synthesized. Electrochemical and thermal properties of the hybrid electrolytes and the inorganic fraction were characterized by a suite of experimental techniques, including linear scan voltammetry (LSV), differential scanning calorimetry (DSC) and thermal gravimetric analysis (TGA). The electrochemical stability window of hybrid electrolyte S2 in a symmetric lithium metal cell was determined to be approximately 6 V by LSV.

Broadband dielectric spectroscopy was used to quantify the ionic conductivities of the materials as a function of temperature. DC ionic conductivity values were extracted from this data using a standard procedure (see supporting information). Figure 4.3 (a) displays temperature dependent ionic conductivity data for NOHMs comprised of 8 nm silica cores and PEG corona with varying length, electrolytes S1-S7. Figure 4.3 (b) displays conductivity of hybrids with varying core sizes and chemistry, all with  $M_n = 660 \text{ g mol}^{-1}$  molecular weight PEG corona, electrolytes S2, S8-S9. Both figures include temperature-dependent conductivity data for free, MPEG oligomers with  $M_n = 500$  and  $2000$  also doped with 1 M LiTFSI, which allows the effect of tethering on conductivity to be evaluated. Lines in the figure are obtained by fitting the data to either of two theoretical forms: (i) Vogel- Fulcher-Tamman (VFT),  $\mu = A \exp(-B/(T - T_0))$ , where B is the effective activation energy barrier for coupled ion and local polymer segment motions/breathing,

in units of absolute temperature; T and  $T_0$  are the measurement and reference (typically the equilibrium glass transition) temperatures, respectively; and A is a pre-exponential factor equivalent to the ionic conductivity in the high-temperature limit; and (ii) Arrhenius,  $\mu = \Omega \exp(-E_a / T)$ , where  $E_a$  is the activation energy for ion hopping, again in units of temperature. Table 2 in the Supporting Information summarizes the parameters used for these fits. Transport properties displaying VFT temperature dependence are common in polymer systems in which local segmental motions and chain relaxations contribute significantly to the transport process. Arrhenius behavior is on the other hand typically found in systems where these motions do not play a significant role.

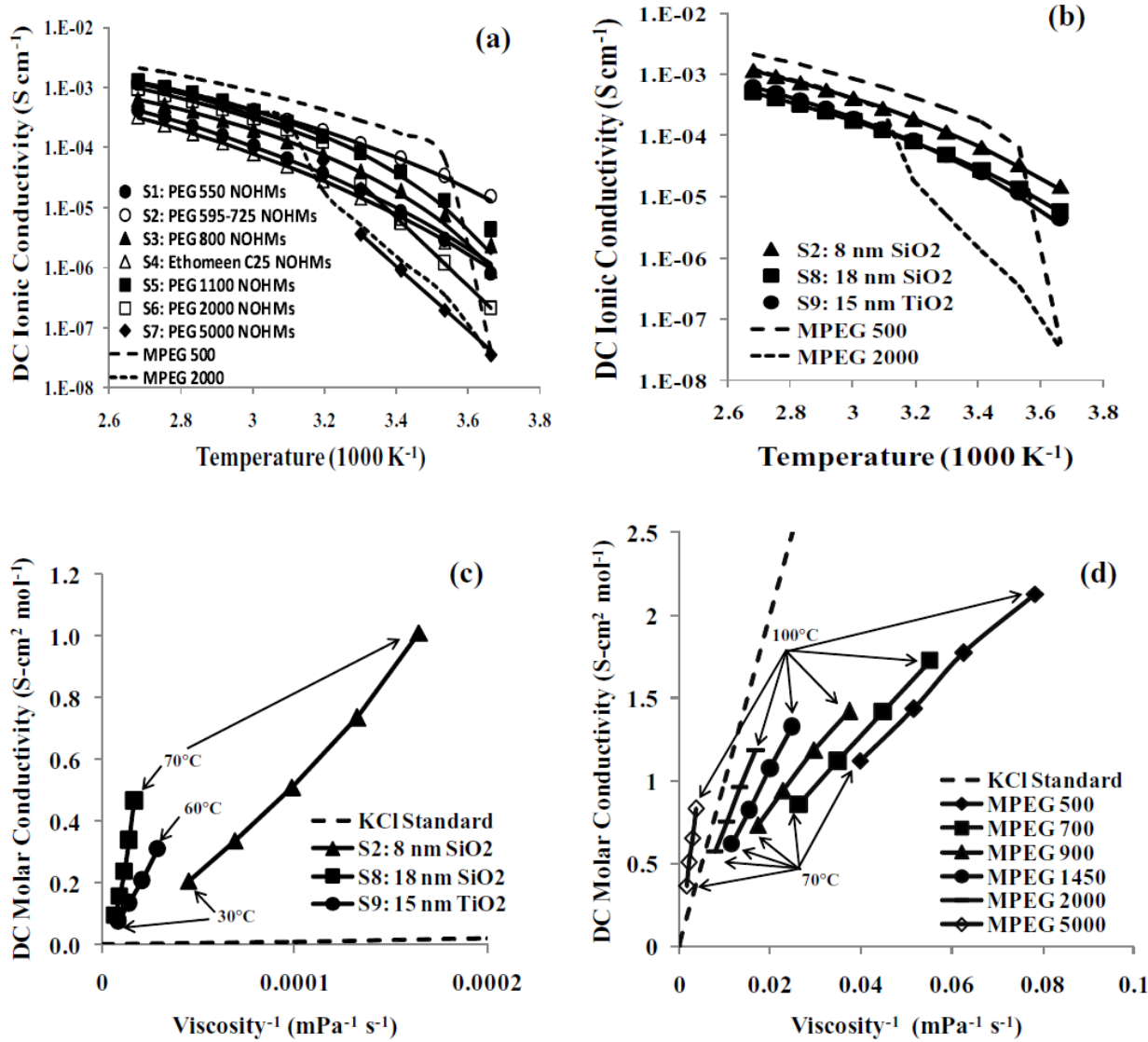


**Figure 4.3** a) DC ionic conductivity of un-tethered and particle-tethered PEG/hybrid electrolytes based on 8 nm SiO<sub>2</sub> cores and varying PEG corona molecular weights. The solid lines in the figure are fits to VFT or Arrhenius temperature dependence; (b) Conductivity of NOHMs electrolytes with varying core chemistry and size; (c) Walden plot of NOHMs electrolytes with varying cores and 660 PEG corona. The dashed line represents the standard result for dilute KCl in aqueous solution; (d) Walden plot of MPEG electrolytes.

It is immediately noticeable from Figure 4.3 (a) & (b) that tethering PEG chains to either  $\text{SiO}_2$  or  $\text{TiO}_2$  produces only a small decrease in ionic conductivity and no noticeable change in its temperature dependence above the crystallization transition, while extending VFT type conductivity into a lower temperature regime. As with the case for the pure MPEG electrolytes, however, materials S6 and S7, which exhibit both a crystalline and melting transition, manifest Arrhenius temperature-dependent ionic conductivity below the melt transition. All other samples exhibit VFT behavior throughout, implying that the ion conduction mechanism is dominated by segmental and chain motions of the tethered oligomers. Significantly, several of the hybrids are seen to attain the same conductivity, within error, at high temperatures; this conductivity value is close to that recorded for a pure high molecular weight PEO-LiTFSI system;<sup>[14]</sup> implying that polymer chains in the two systems have similar dynamics at the microscale.

It is also apparent from Figure 4.3 (b) that an increase in the hybrid core size, results in a fractional decrease in ionic conductivity. This finding is readily explained in terms of decreased segmental motion as a result of increased chain crowding and extension around the cores. Changing the NOHMs core chemistry from  $\text{SiO}_2$  to  $\text{TiO}_2$ , on the other hand, has a negligible effect on ionic conductivity; confirming that the mechanism of ion transport is through local motion of the PEG chains, and that the inorganic cores have little effect – a result different from reports by others<sup>[4,6]</sup> for composite electrolytes containing inorganic particles with surface functionality.

Figure 4.3 (c) displays the DC molar conductivity vs. the shear fluidity (inverse viscosity), the Walden plot, of the same electrolyte series (S2, S8, S9) with varying cores and PEG corona,  $M_n = 660$ . This approach for representing conductivity data has traditionally been used for understanding the microscopic motion of ions in molecular fluids; the standard KCl data used for

comparison is for a dilute, fully dissociated solution of ions of equal mobility.<sup>[15–16]</sup> While the conduction mechanism in polymer electrolytes is normally thought to be more closely associated with free volume than viscosity, the Walden plot provides a convenient mechanism for displaying two of the most important properties of electrolytes developed for use in lithium batteries: conductivity and viscosity. It is clearly evident from the figure that the NOHMs electrolytes, even those with the shortest PEG corona, are superionic, ie. manifest higher ionic conductivities than anticipated from their fluidity. In comparison, untethered MPEG electrolytes (Figure 3 (d)) only display superionic properties when the chain molecular weight exceeds the entanglement value,  $M_e \approx 3200$ .<sup>[17]</sup> Significantly, the superionic regime is accessible at room temperature.

#### 4.4 Conclusions

In summary, we report a new class of solvent-free nanoscale organic hybrid electrolytes composed of hard nanoparticles densely grafted with oligomers. These materials flow like soft glasses and, relative to the unattached oligomers, display more than a million-fold enhancement in mechanical modulus, but show negligible changes in ionic conductivity. Because properties of the materials can be facilely tuned, NOHMs provide a method for manipulating mechanical properties of an electrolyte, without compromising conductivity. Optimization of the NOHMs design is expected to lead to a novel family of yield-stress electrolytes in which the ion-conducting polymer phase exists as a tortuous interconnected network of corona-filled pores, constrained by an impenetrable array of inorganic core particles. By tuning the spacing and tortuosity of the conducting phase (e.g. by varying the core diameter and/or molecular weight of

the corona), these materials offer unique opportunities for retarding/suppressing dendrite growth in secondary lithium metal batteries.

#### 4.5 References

- [1] B. Scrosati , C. Vincent , Mater. Res. Bull. 2000 , 28 – 30 .
- [2] P. G. Bruce , B. Scrosati , J.-M. Tarascon , Angew. Chem., Int. Ed. 2008 , 47 , 2930 – 2946 .
- [3] W. Krawiec , L. Scanlon , J. Fellner , R. Vaia , S. Vasudevan , E. Giannelis , J. Power Sources , 1995 , 54 , 310 – 315 .
- [4] F. Croce , G. Appetecchi , L. Persi , B. Scrosati , Nature. 1998 , 394 , 456 ; F. Croce , R. Curini , A. Martinelli , L. Persi , F. Ronci , B. Scrosati , R. Caminiti , J. Phys. Chem. B , 1999 , 103 , 10632 – 10638 .
- [5] C. Capiglia , P. Mustarelli , E. Quartarone , C. Tomasi , A. Magistris , Solid State Ionics. 1999 , 118 , 73 – 79 .
- [6] F. Croce , S. Sacchetti , B. Scrotati , J. Power Sources. 2006 , 161 , 560 – 564 .
- [7] M. Reddy , P. Chu , J. Kumar , U. Rao , J. Power Sources. 2006 , 161 , 535 – 540 .
- [8] H.-M. Kao , C.-L. Chen , Angew. Chem., Int. Ed. 2004 , 43 , 980 – 984 .
- [9] H.-M. Kao , S.-W. Chao , P.-C. Chang , Macromolecules. 2006 , 39 , 1029 – 1040 .

- [10] H.-M. Xiong , D.-P. Liu , H. Zhang , J.-S. Chen , J. Mater. Chem. 2004 , 14 , 2775 – 2780 .
- [11] P. Maitra , S. Wunder , Chem. Mater. 2002 , 14 , 4494 – 4497 .
- [12] P. Agarwal , H. Qi , L. A. Archer , Nano Lett. 2010 , 10 , 111 – 115 ; L. A. Archer , L. L. Olenick , J. L. Nugent , A. Corona , Nanoscale Organic Hybrids, Invention Disclosure , ARCH-3001 ( 2009 )
- [13] P. Sollich , F. Lequeux , P. Hebraud , M. E. Cates , Phys. Rev. Lett. 1997 , 78 , 2020 – 2023
- [14] L. Edman , A. Ferry , M. Doeffer , J. Mater. Res. 2000 , 15 , 1950 – 1954 .
- [15] W. Xu , E. Cooper , C. Angell , J. Phys. Chem. B. 2003 , 107 , 6170 – 6178 .
- [16] M. Mendolia , F. C. Gregory Chem. Mater. 1993 , 5 , 174 – 181 .
- [17] J. D. Ferry , Viscoelastic Properties of Polymers , 3 rd Ed, Wiley , 1980 .
- [18] R. Rodriguez , R. Herrera , L. A. Archer , E. P. Giannelis , Adv. Mater. 2008 , 20 , 1 – 6 .

## 4.6 Appendix: Supporting Information

**Table 4.1. NOHMs Electrolyte – Sample specifications**

Sample	Synthesis Pathway # in Fig. 1	Core	Core Diameter (nm)	PEG Corona $M_n$ (g mol <sup>-1</sup> )	PEG PI	Core volume fraction, $\phi$	T <sub>c</sub> (°C)	T <sub>g</sub> (°C)
S1	1	SiO <sub>2</sub>	8	550	1.15	0.35	-36	10
S2	3	SiO <sub>2</sub>	8	660	- [ii]	0.33	-39	5
S3	1	SiO <sub>2</sub>	8	800	1.10	0.28	-35	10
S4	2	SiO <sub>2</sub>	8	865 [i]	- [iii]	0.31	-	-
S5	1	SiO <sub>2</sub>	8	1100	1.09	0.25	-	-
S6	1	SiO <sub>2</sub>	8	2000	1.05	0.16	-12	31
S7	1	SiO <sub>2</sub>	8	5000	1.06	0.07	23	44
S8	3	SiO <sub>2</sub>	18	660	- [ii]	0.35	-35	5
S9	3	TiO <sub>2</sub>	15	660	- [ii]	0.27	-30	9

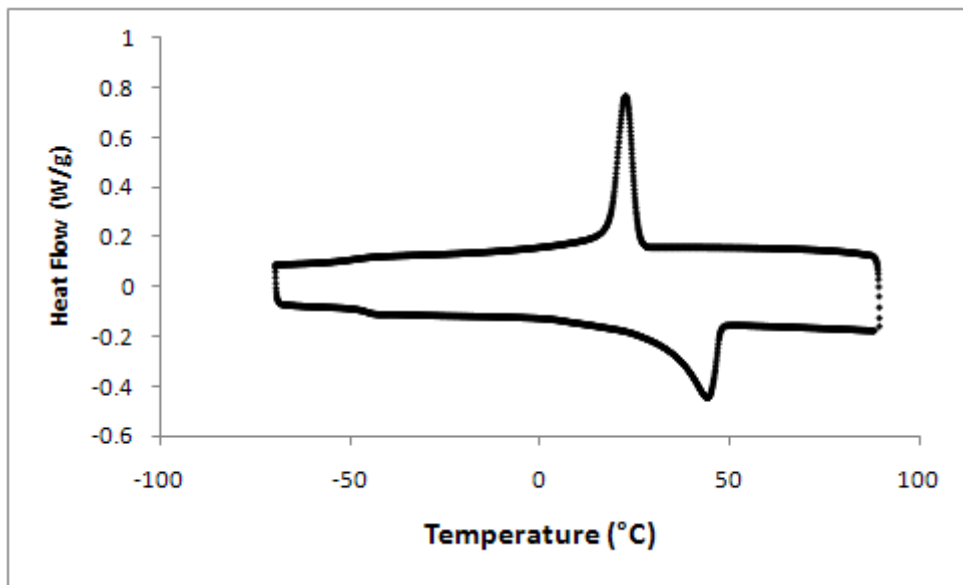
[i] Average total molecular weight of branched poly(ethylene glycol) functionalized amine (Ethomeen C25)

[ii] Commercial polymer (Gelest), molecular weight listed as 596-725

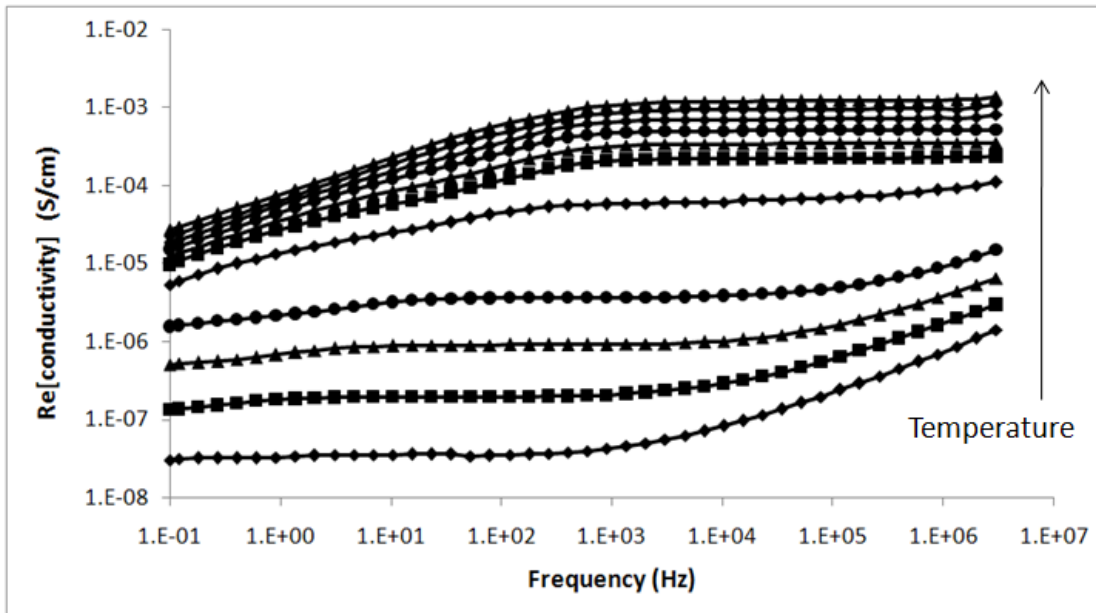
[iii] Commercial polymer (Talas), equivalent mass listed as 825-909

**Table 4.2. Parameters for VFT and Arrhenius fits as displayed in Fig. 3 (a) and Fig. 3 (b) at the 95% confidence interval**

Sample	VTF Fit Parameters			Arrhenius Fit Parameters	
	A (S cm <sup>-1</sup> )	B (K)	T <sub>0</sub> (K)	A (S cm <sup>-1</sup> )	Ea (K)
S1	0.07 ± 0.02	970 ± 80	185 ± 7	-	-
S2	0.047 ± 0.003	680 ± 20	190 ± 2	-	-
S3	0.014 ± 0.003	470 ± 60	224 ± 7	-	-
S4	0.07 ± 0.01	1050 ± 50	180 ± 4	-	-
S5	0.023 ± 0.005	420 ± 50	229 ± 6	-	-
S6	0.028 ± 0.003	540 ± 30	214 ± 4	2E12 ± 4E12	12360 ± 70
S7	0.06 ± 0.02	600 ± 100	210 ± 10	1.07E14 ± 5E12	13010 ± 20
S8	0.027 ± 0.001	760 ± 10	184 ± 1	-	-
S9	0.037 ± 0.008	720 ± 60	195 ± 7	-	-

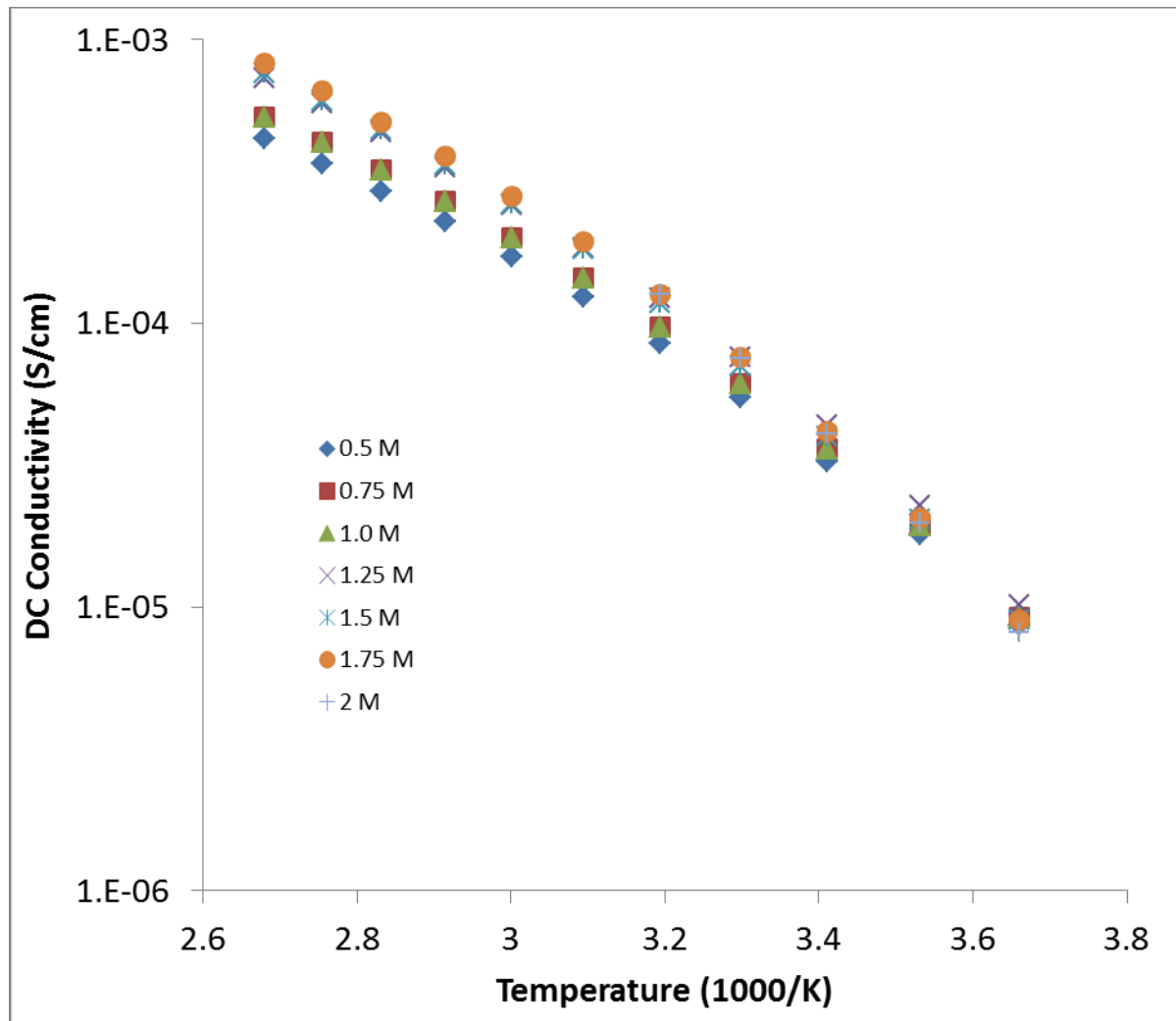


**Supplementary Figure 4.1** Differential Scanning Calorimetry, DSC, data as obtained for electrolyte S7 at a scan rate of 10°C/min. Displayed is the result for the cool – heat scans of a heat – cool – heat schedule. The melting transition temperature,  $T_m$ , and crystallization temperature,  $T_c$  are the temperatures at which the heat loss displays a local maximum and minimum, respectively.

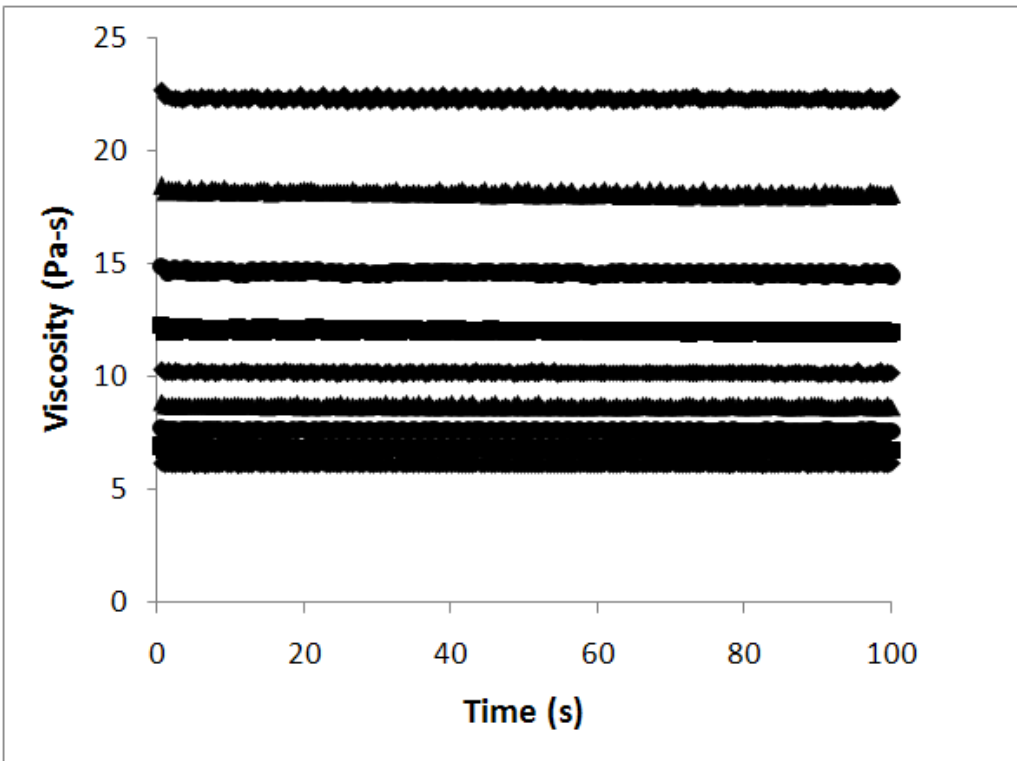


**Supplementary Figure 4.2** Data obtained via dielectric spectroscopy at temperatures of 0-100°C in increments of 10°C for the determination of the DC conductivity of sample S7.

The dielectric data for all studied electrolytes is consistent with a phenomena known as universal dynamic response (UDR), noted by Jonscher, whereas  $\sigma'(\omega) = \sigma_{DC} + A\omega^s$ . The DC conductivity may be estimated from the plateau value. Beyond a critical frequency above the plateau, a power law relationship between the real conductivity and frequency is displayed. Below the plateau, the decrease in conductivity with decreasing frequency is due to polarization of the cell.

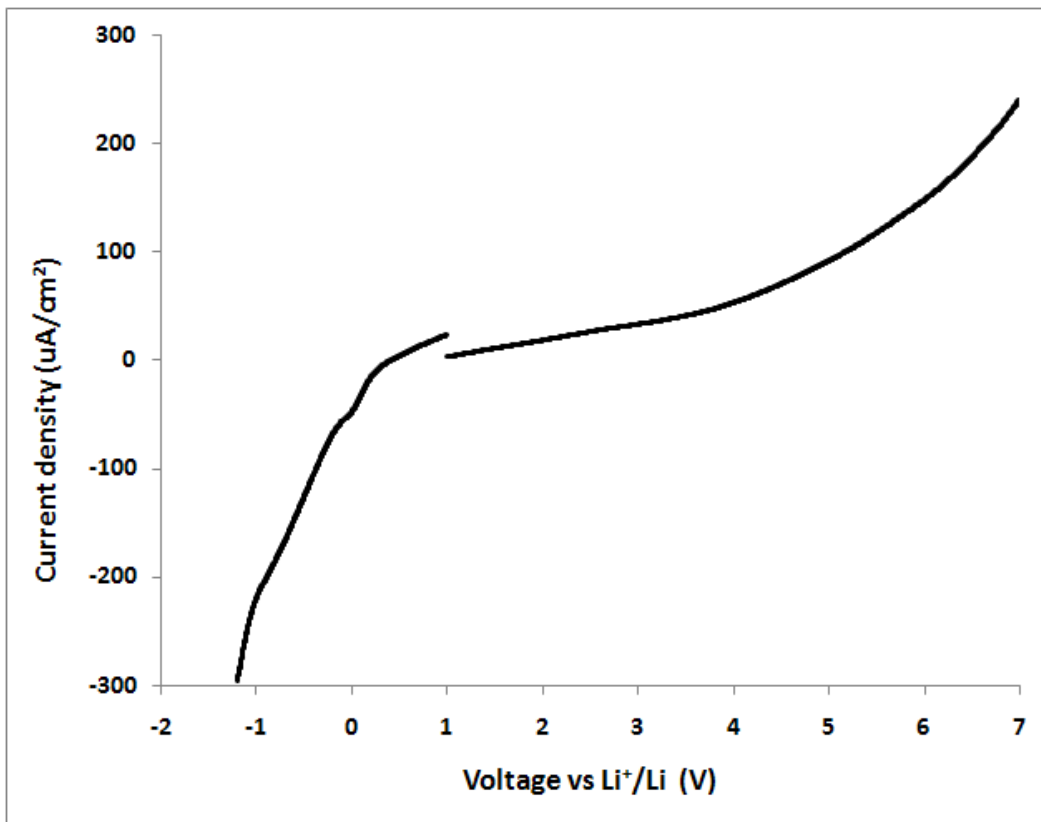


**Supplementary Figure 4.3** DC conductivity as a function of temperature of electrolyte variations of hybrid S2 containing differing amounts of LiTFSI in the organic phase. The electrolyte with 1.0 M LiTFSI is sample S2 as discussed in the main text.

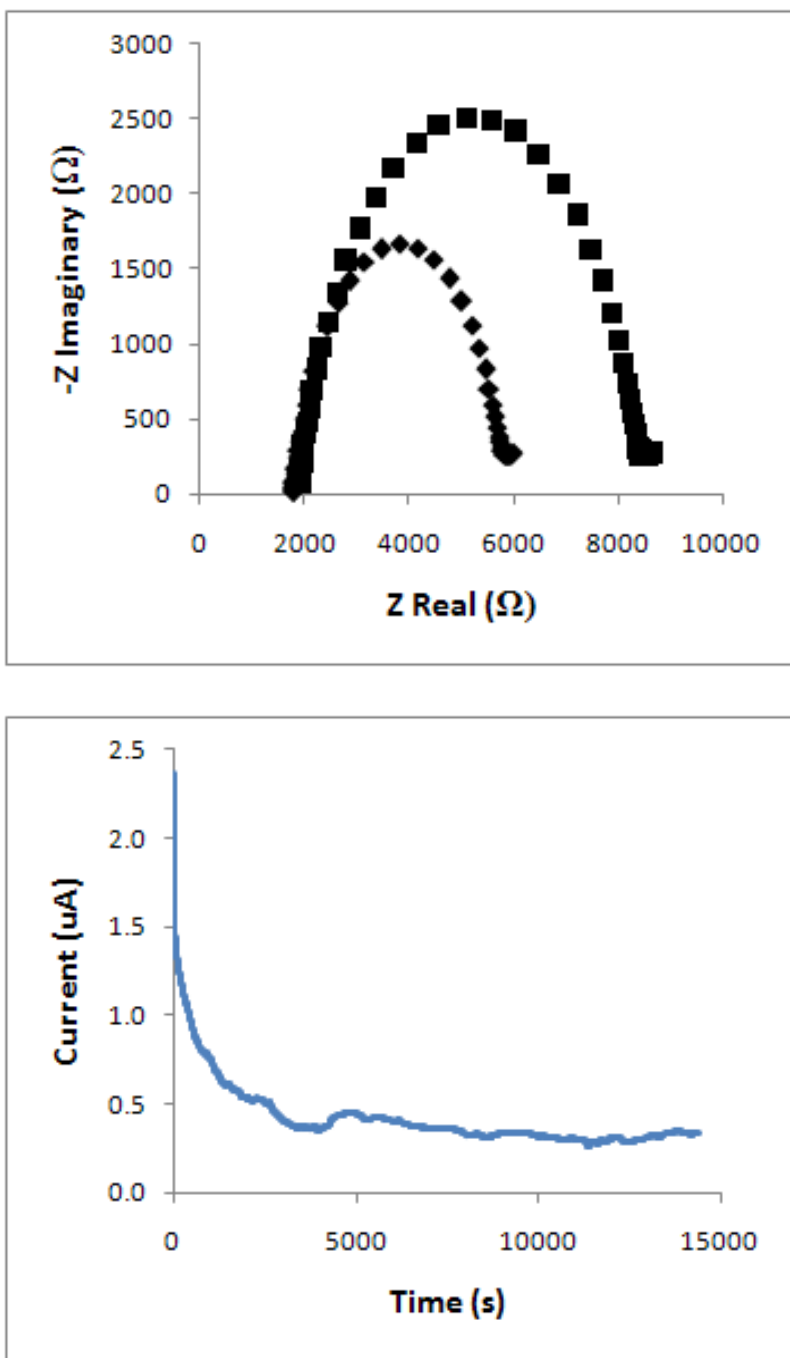


**Supplementary Figure 4.4** Shear rheology data for sample S2 at 10 Hz.

Viscosity measurements were taken on an Rheometrics Scientific, Ares rheometer and an Anton Paar Rheometer, MCR501. Temperature-dependent experiments were performed in increments of 5°C in the range 30-70°C for NOHMs electrolytes and in the range 70-100°C for MPEG electrolytes. Following temperature stabilization, NOHMs electrolyte samples were subjected to a shear rate of 10 Hz for 100 seconds; the data obtained for electrolyte S2 is displayed below. MPEG electrolytes were sheared at 100 Hz. The average steady state viscosity was taken to be the shear viscosity as displayed in the Walden plot.



**Supplementary Figure 4.6** Linear scan voltammetry of a symmetric lithium cell with hybrid polymer electrolyte S2: scan rate, 1 mV/s; temperature, 20°C; electrode area, 0.32 cm<sup>2</sup>. The discontinuity in the plot is due to the compilation of data from two scans, 1 to 7 V and 1 to -2 V.



**Supplementary Figure 4.7** The lithium transference number of S2 was measured at room temperature by the method developed by Bruce and by Scrosati. A) The impedance of the cell was measured before (squares) and after (diamonds) the imposition of a DC voltage pulse,  $\Delta V = 25\text{mV}$ . B) The current decay to steady state during the pulse was measured over time. The transference number was then calculated with the following equation:

$$T_{\text{Li}^+} = (I_{ss} * (\Delta V - R_0 I_0)) / (I_0 * (\Delta V - R_{ss} I_{ss}))$$

## CHAPTER 5:

### NANOPOROUS HYBRID ELECTROLYTES

Reproduced with Permission from *Journal of Materials Chemistry*, 21, 10094-10101, 2011 by J. L. Schaefer, S. S. Moganty, D. A. Yanga, and L. A. Archer.

#### **Abstract**

Oligomer-suspended  $\text{SiO}_2$ -polyethylene glycol nanoparticles are studied as porous media electrolytes. At  $\text{SiO}_2$  volume fractions,  $\phi$ , bracketing a critical value  $\phi_y = 0.29$ , the suspensions jam and their mechanical modulus increase by more than seven orders. For  $\phi > \phi_y$ , the mean pore diameter is close to the anion size, yet the ionic conductivity remains surprisingly high and can be understood, at all  $\phi$ , using a simple effective medium model proposed by Maxwell.  $\text{SiO}_2$ -polyethylene glycol hybrid electrolytes are also reported to manifest attractive electrochemical stability windows (0.3–6.3 V) and to reach a steady-state interfacial impedance when in contact with metallic lithium.

#### **Introduction**

Lithium ions are the active charge carrying species in the most energy dense secondary batteries of today, those used in electronics and hybrid electric transportation. Currently commercialized lithiated anode materials such as  $\text{LiC}_6$  and  $\text{Li}_4\text{Ti}_5\text{O}_{12}$  have relatively low theoretical energy capacities (360 mA h g<sup>-1</sup> and 175 mA h g<sup>-1</sup>, respectively). Advanced secondary battery systems employing electrodes such as  $\text{LiCoPO}_4$ , <sup>[1]</sup> lithium, <sup>[2–5]</sup> or sulfur<sup>[6]</sup> require electrolytes with

specific properties such as wide electrochemical stability windows, high mechanical strength, and/or inertness or non-solvency towards the electrode materials and their intercalation products. Next-generation lithium ion batteries should also employ electrolytes that are non-flammable, nonvolatile, non-leakable, and non-toxic, making them safer both in use and after disposal. In pursuit of such materials, several classes of electrolytes have been studied as replacements for conventional liquid electrolytes: polymers,<sup>[7–11]</sup> polymer composites,<sup>[12–15]</sup> hybrids,<sup>[16–18]</sup> gels,<sup>[19,20]</sup> ionic liquids,<sup>[21]</sup> and ceramics.<sup>[22]</sup> In many cases, mechanical integrity of the electrolyte comes at a cost: namely, a large loss in ionic conductivity, which places undesirable limits on the charge/discharge rate of the cell. Liquid and particulate plasticizers have been used with some success in circumventing this constraint in composite and gel polymer electrolytes.<sup>[4,15,19,23]</sup> With a mechanically strong framework in place such as a polymer or ceramic, the liquid plasticizer serves as a freely diffusing ionic conduction medium that provides ionic conductivities near that of a pure liquid electrolyte. If a liquid plasticizer with good thermal and electrochemical properties is utilized, safety concerns are reduced. In the case of particulate plasticizers, of either nano- or micron-scale, the particles have been shown to decrease crystallization of the surrounding matrix, thereby enhancing segmental motion of the host polymer and increasing conduction. While nanoparticles have been shown most successful in this area, in typical polymer composites particle aggregation occurs; this reduces the effectiveness of the individual particles in inhibiting crystallization but allows for formation of a percolated particulate network that aids in bulk mechanical strength.

Recently, we reported on the synthesis and characterization of novel metal oxide–ionic liquid (IL)<sup>[24]</sup> and metal oxide–polyethylene glycol (PEG) hybrid electrolytes based on self-suspended

nanoscale organic hybrid materials (NOHMs).<sup>[25]</sup> Because they are self-suspended, these electrolytes are homogeneous fluids, where the tethered units (ILs or PEG oligomers) simultaneously serve as the suspending medium for the nanoparticle cores and as an ion conducting network for lithium ion transport. These electrolytes have uniformly dispersed nanoparticle cores, unlike the typical composite electrolytes. By manipulating the volume fraction and average size of dispersed particles, it should be possible to design electrolytes that yield and flow under conditions of battery assembly/manufacturing, but which exist as porous ion-conducting “solids” during normal battery operation.

In this article we report on mechanical properties, conductivity, and electrochemical stability of a family of hybrid electrolytes based on concentrated suspensions of SiO<sub>2</sub> nanoparticles in oligomeric PEG. In order to create homogeneous suspensions at high silica volume fraction  $\phi$ , the SiO<sub>2</sub> nanoparticles are sterically stabilized by covalently tethering a dense brush of oligo-PEG chains to each particle (Fig. 5.1(B)). This approach allows for the creation of suspension electrolytes with a wide range of nanoparticle filler fraction and yet uniformly dispersed, non-percolated, ceramic cores.

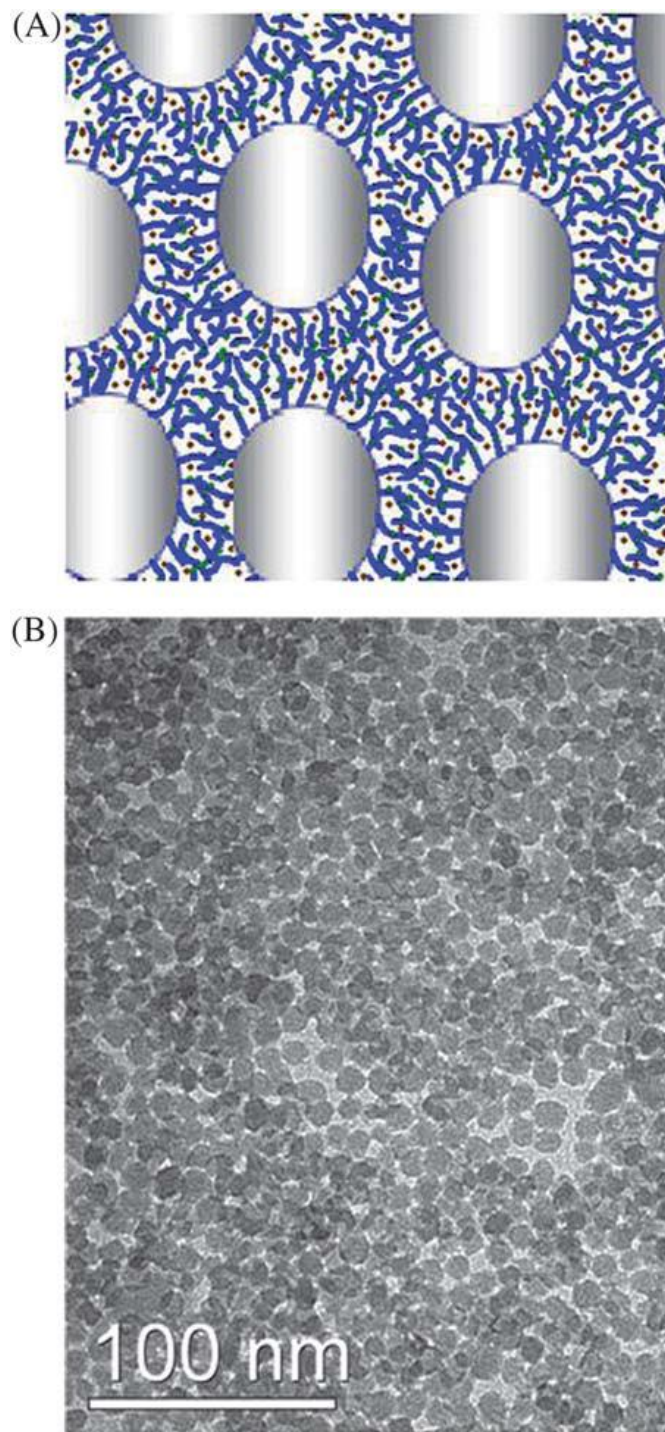


**Figure 5.1** Hydraulically interconnected framework: (A) schematic – grey circles represent impermeable particles; green and brown dots represent the lithium cations and TFSI anions, respectively. (B) TEM micrograph of a PEGDME 250-SiO<sub>2</sub> hybrid electrolyte with  $\phi \approx 0.3$ .

## **Experimental**

### *Synthesis*

Silica nanoparticles were densely grafted,  $\Sigma \approx 1.1$  chains nm<sup>-2</sup>, with a polyethylene glycol methyl ether corona (Fig. 2(A)), using our previously reported method,<sup>[25,26]</sup> and purified rigorously by repeated precipitation in ethanol. Electrolytes were prepared ranging from 0–100 wt% NOHMs in PEGDME, polyethylene glycol dimethyl ether ( $M_n = 250$ , Aldrich) and doped with lithium salt. PEGDME was chosen because it is a low-cost, nonvolatile material known to exhibit excellent lithium ion conductivity.

A solution of lithium bis(trifluoromethanesulfone imide) (LiTFSI, Aldrich) was prepared in dry methanol (Aldrich) in an Argon-filled glove box (MBraun Labmaster) before use. The lithium salt solution was added to the NOHMs/PEGDME blends at a concentration of 1 M in the organic phase for all samples. After mixing, samples were dried in the convection oven at 50°C overnight and for at least 24 hours under high vacuum.

### *Characterization*

The tethered PEG brush on the purified SiO<sub>2</sub> particles was characterized by several methods. Dynamic light scattering (DLS) was performed on a Malvern Instruments Zetasizer Nano-ZS at 25°C. Intrinsic viscosity of the particles in a low molecular weight polyethylene glycol dimethyl ether host was determined from dilute solution viscosity measurements at 35°C using a Rheometrics Scientific ARES rheometer outfitted with 50 mm parallel plate fixtures. The core particle weight fraction in the hybrids was determined by thermal gravimetric analysis (TGA); heating at 10°C min<sup>-1</sup> to 550°C.

The dynamic shear rheological properties of the electrolytes were studied using frequency- and strain-dependent oscillatory shear measurements on an ARES Rheometer and an Anton Paar MCR501. All experiments were performed at 35°C. Strain sweep measurements were executed at a fixed shear frequency,  $\omega = 10 \text{ rad s}^{-1}$ ; frequency sweep experiments were performed at a strain within the linear viscoelastic regime for the material—0.5% for the stiff hybrid electrolytes and 25% for the liquid-like materials. Glass transition temperatures of the electrolytes were determined with a TA Differential Scanning Calorimeter at a ramp rate of 10°C min<sup>-1</sup>.

#### *Electrochemical measurements*

The ionic conductivity and relaxation frequency of the electrolytes were measured as a function of temperature (-5 to 100°C) using a Novocontrol Broadband Dielectric Spectrometer. The DC conductivity at each temperature was determined from the plateau value of a plot of Re[conductivity] as a function of frequency, as described by Jonscher.<sup>[27]</sup> The segmental relaxation frequency was taken to be the frequency associated with the major peak in tan( $\delta$ ). Electrochemical stability window, lithium transference number, and interfacial impedance of the hybrid electrolytes were performed on a Solartron Electrochemical Impedance Spectrometer. For all experiments, electrolytes with a high fraction of hybrid were charged to a donut shaped Teflon ring, which prevented short circuiting of the two lithium metal electrodes in the Swagelok stainless steel—Teflon cells. Electrochemical stability windows were determined by linear scan voltammetry at a scan rate of 1 mV s<sup>-1</sup>, and taken to be the values at the change in slope of the current vs. voltage plot. The lithium transference number of the electrolytes was determined using the method proposed by Bruce<sup>[28]</sup> and Scrosati<sup>[29]</sup> where initial and steady state values of current are found for a symmetric lithium cell undergoing polarization,

with corrections from impedance measurements of the interfacial resistance both before and after polarization.

## Results and discussion

### *Characterization of nanoscale hybrids*

Dynamic light scattering (DLS) measurements in chloroform (Fig. 5.2(B)) indicate that the hybrids are comprised of a 2.4 nm PEG brush tethered to each SiO<sub>2</sub> nanoparticle core. Viscosity measurements (Fig. 5.2(C)) preformed on dilute suspensions of the SiO<sub>2</sub>–oligo PEG particles in polyethylene glycol dimethyl ether,  $M_n \approx 500$ , can be fitted using the Einstein formula,  $\eta = \mu_s (1 + [\eta] \phi)$ , to yield an intrinsic viscosity  $[\eta] \approx 11.1$  for the particles. Here,  $\eta$  is the suspension viscosity,  $\mu_s$  is the viscosity of the suspending medium (PEG-500), and  $\phi$  is the volume fraction of SiO<sub>2</sub> nanocores in the suspension. The measured intrinsic viscosity is evidently substantially larger than would be expected for a suspension of hard spheres, for which  $[\eta]_{HS} = 5/2$ ; the difference can be used to compute the apparent swelling  $\Delta \equiv 2h/d \approx 0.65$  of the particles using the expression,<sup>30</sup>  $[\eta]/[\eta]_{HS} = (1 + \Delta)^3$ , where the term on the right is a correction to the volume fraction  $\phi$  in Einstein's formula to account for the “extra” volume occupied by the tethered polymer chains;  $d \approx 7$  nm is the average diameter (Fig. 1(C)) of the un-functionalized SiO<sub>2</sub> particles; and  $h$  is the hydrodynamic thickness of the PEG brush tethered to the particle. Thus we find  $h \approx 2.3$  nm, which is satisfactorily close to the value deduced from DLS. The equilibrium radius of gyration of a PEG chain of average molar mass  $M_w$  can be estimated using the formula,<sup>31</sup>  $R_g = \frac{1}{\sqrt{6}} \left( C_\infty \frac{M_w}{m_0} l_m^2 \right)^{1/2} \approx 6.6 \times 10^{-2} M_w^{1/2}$  nm. Thus for the tethered PEG-trimethoxy silane chains with  $M_w = 660$  g mol<sup>-1</sup>,  $M_{w,PEG} \approx 540$  g mol<sup>-1</sup>,  $R_g \approx 1.5$  nm and  $h = 2R_g$

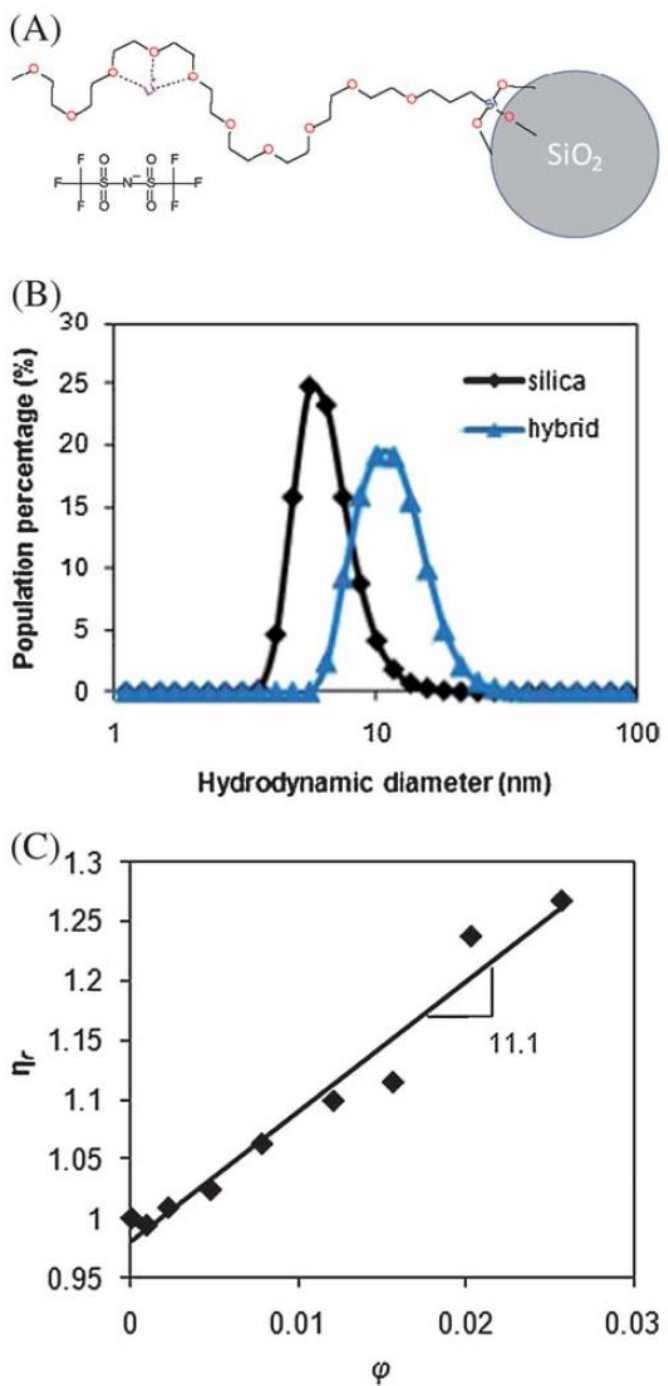


**Figure 5.2** SiO<sub>2</sub>-PEG NOHMs hybrids: (A) schematic of polymer chain bonded to silica core with associated ions. (B) Dynamic light scattering measurements of the base silica and purified hybrid. (C) Plot of relative viscosity vs.  $\phi$  used to determine the intrinsic viscosity of the hybrid units.

$\approx 3$  nm. Here  $C_\infty = 5.5$  is the characteristic stiffness ratio for PEG;  $l_m \approx 0.48$  nm is the size of a statistical segment; and  $m_0 = 44$  is the repeat unit molar mass for PEG. A more accurate estimate for the height of the tethered brush, which takes into account crowding and stretching of polymer chains in the brush, can be obtained using de Gennes' blob model for a neutral polymer grafted to a planar substrate modified to account for the spherical geometry of the substrate. This analysis yields  $h = \sum_i \frac{\xi_i}{g_i} \approx 3.6$  nm, which is larger than the brush height obtained using both experimental methods.

Here  $\xi$  is the correlation length and  $g$  is the number of monomers per correlation volume in each layer of correlation blobs. The fact that the brush height estimated from  $R_g$  is closer to the values derived from experiment, particularly for the small polymer chain lengths considered here, implies that the PEG chains assume a more collapsed (greater attraction) to the  $\text{SiO}_2$  substrate than expected for the neutral polymer assumed in the analysis.

#### *Characterization of electrolytes*

The transmission electron microscopy (TEM) image in Fig. 5.1(B) shows that the PEGDME 250– $\text{SiO}_2$  hybrid electrolytes are comprised of homogeneously dispersed nanoparticles in a suspending fluid, with no evidence of aggregation. This latter feature is remarkable for the notoriously “sticky”  $\text{SiO}_2$  nanocores; it attests to the effectiveness of the grafted PEG oligomers in imparting colloidal stability to  $\text{SiO}_2$  particles. Fig. 5.3(A) reports the dynamic shear elastic/storage,  $G'$ , and viscous/loss,  $G''$ , moduli of PEGDME 250– $\text{SiO}_2$  hybrid electrolytes at various  $\text{SiO}_2$  volume fractions and shear frequencies,  $\omega$ . In a typical elastic solid, motion of individual material elements is constrained by interactions with their neighbors and energy storage normal dominates viscous losses,  $G' \gg G''$ . In such a material the elastic modulus is set by interactions between neighboring material elements and generally will not change with shear

frequency. At the opposite extreme are hybrid electrolyte suspensions where the viscous, fluid stresses dominate and hence  $G'' > G'$ , and both are functions of  $\phi$ . Fig. 5.3(A) shows that for a PEGDME 250–SiO<sub>2</sub> hybrid with  $\phi = 0.19$ , the minimum spacing between the particles,  $d_{p-p} = [(\phi_m/\phi)^{1/3} - 1]d \approx 0.5d > h$ , and  $G'' \gg G'$ , indicative of a fluid-like suspension. At a moderately higher SiO<sub>2</sub> volume fraction,  $\phi = 0.29$ ;  $d_{p-p} \approx 0.3d \approx h$ , the storage modulus increases by more than four orders of magnitude, is greater than the loss modulus over the entire frequency range, and exhibits a much weaker dependence on frequency; indicative of a gel-like solid response. This observation confirms that the tethered PEG chains allow the jammed state to be accessed at lower f. Fig. 5.3(A) further shows that by  $\phi = 0.46$ ;  $d_{p-p} \approx 0.1d \ll h$ ,  $G' \gg G''$ , and the dynamic moduli are essentially independent of shear frequency. This means that the suspensions are completely jammed and the tethered polymer brush highly compressed at particle volume fractions well below  $\phi_m$ .

As pointed out in the Introduction, one advantage of a solid-like electrolyte created from a jammed suspension of particles is that, like its thermoplastic polymer host, it is processable. Specifically, at shear stresses above a critical value,  $\tau_y$ , the jammed suspension yields and flows, and as such can be shaped in a typical manufacturing process. Fig. 5.3(B) demonstrates this feature through the effect of shear strain on mechanical moduli. In the small-strain limit  $\gamma \rightarrow 0$ ,  $G'$  is independent of strain for all hybrids, which allows us to determine the apparent elastic modulus,  $G_e = G'_{\lim \gamma \rightarrow 0}$ , for all materials. At low volume fractions, e.g.  $\phi = 0.19$ , the condition  $G'' > G'$  is observed at all strains, confirming that the materials are essentially fluids.

Additionally, at shear strains order 2, the storage modulus is observed to decrease with increasing strain. Termed strain-softening,<sup>[30,32]</sup> this characteristic is commonplace for polymer liquids and is thought to reflect shear alignment of macromolecules in the fluid.<sup>[32]</sup> At the next

higher volume fraction,  $\phi \approx 0.24$ , the shear strain at the onset of softening is much lower, in fact more than an order of magnitude lower than for a typical polymer. Additionally, at strains above this value both moduli decrease with increasing strain, and the shear stress (not shown) manifests a noticeable slope change. All of these features are characteristics of yielding, and the shear strain and stress at which the slope change is observed are the yield strain,  $\gamma_y$ , and yield stress  $\tau_y$  at the conditions of the measurements. At even higher volume fractions,  $\phi \approx 0.29$ ,  $\gamma_y$  is essentially independent of  $f$  and the loss modulus,  $G''$ , manifests a pronounced maximum prior to the onset of strain-softening. This maximum is also a characteristic of yielding,<sup>[33,34]</sup> it is thought to reflect enhanced viscous dissipation as the cages that constrain motion of individual particles are broken down by the imposed shear. Significantly, back-to-back experiments reveal negligible changes in  $\tau_y$  and  $\gamma_y$ , and at shear strains beyond the yielding transition, a cross-over to liquid-like flow behaviors,  $G'' > G'$ , is observed; confirming that moderate shear stress/strain can be used to transform the jammed materials into a processable form, from which it rapidly recovers (becomes jammed again) upon removal of the stress/strain.

Fig. 3(C) reports the effect of SiO<sub>2</sub> volume fraction on  $G_e$ ,  $\tau_y$ , and  $G'$ . The figure shows that at a volume fraction  $\phi = \phi_y \approx 0.29$  a dramatic mechanical transformation is observed in which the storage modulus,  $G'$ , increases by over 4 orders of magnitude. These observations reflect a transition from a liquid-like state to a jammed, disordered solid-like material state. A similar transition is seen (Fig. 5.3(D)) when the low-frequency power-law indices,  $G' \approx \gamma^m$ ;  $G'' \approx \gamma^{m''}$ , are plotted against  $\phi$ , also indicative of a transition to a solid-like material at  $\phi \approx 0.29$ . In a suspension of hard spheres, the jamming transition is known to occur at  $\phi \approx 0.63$ . Extrapolation of this result to our hybrid system suggests that the inner 1.1 nm of tethered oligomers behave mechanically as part of the hard SiO<sub>2</sub> nanocore.

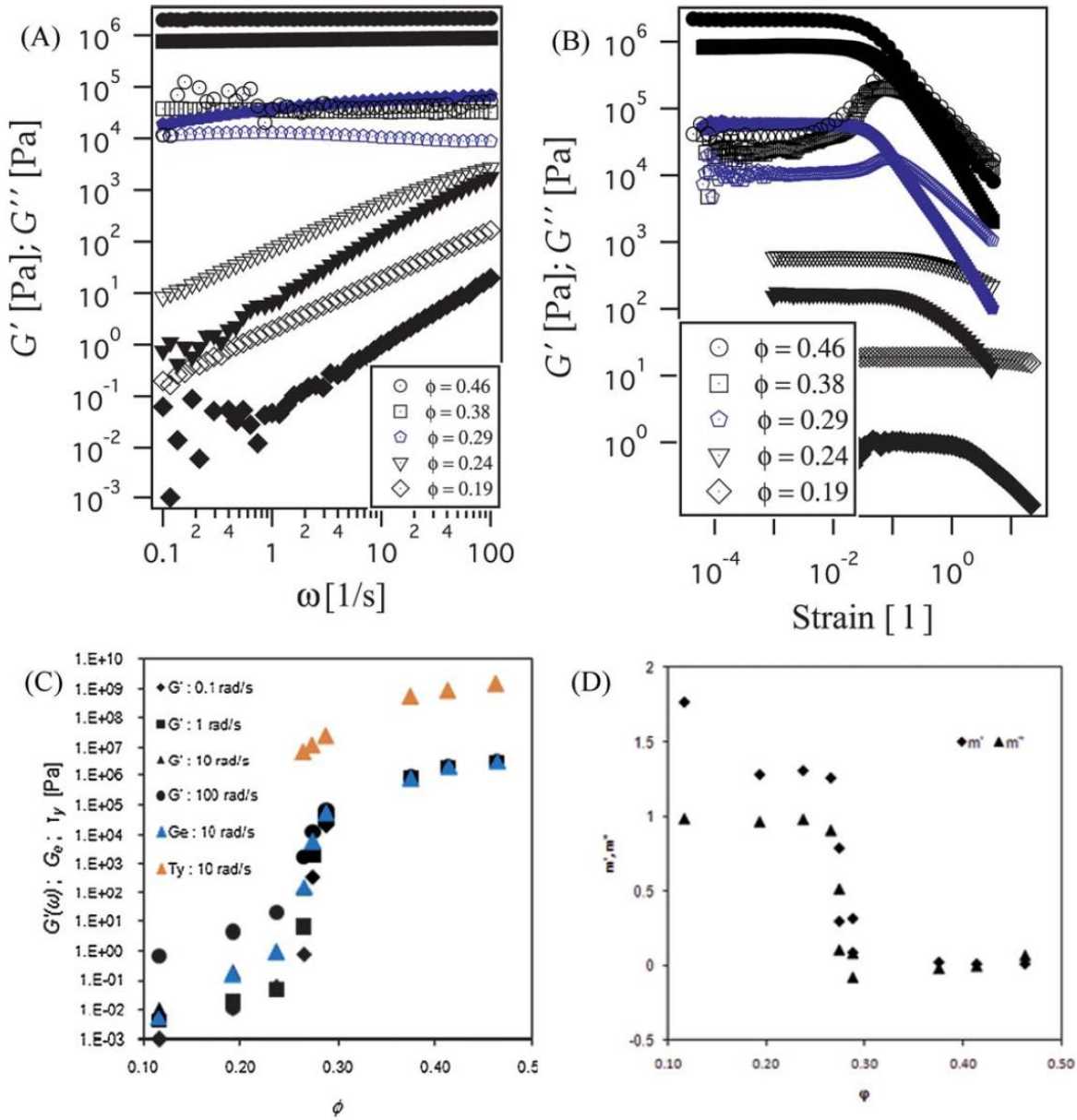


**Figure 5.3** Rheology: (A) Storage modulus,  $G'$ , (filled symbols) and loss modulus,  $G''$ , (open symbols) of PEGDME 250-SiO<sub>2</sub> hybrid electrolytes with varying  $\phi$ , as a function of shear frequency, (B)  $G'$  and  $G''$  of the electrolytes as a function of strain,  $\gamma$ . (C)  $G'$  as obtained from frequency sweep measurements in the linear viscoelastic regime;  $G_e$  and  $\tau_y$  as obtained from strain sweep measurements at  $\omega = 10 \text{ rad s}^{-1}$  as a function of  $\phi$ . (D) Slopes  $m'$  and  $m''$  of the power law dependence of  $G'$  and  $G''$  from frequency sweep measurements.

Temperature-dependent ionic conductivity for PEGDME 250–SiO<sub>2</sub> hybrid electrolytes at various  $\phi$  is reported in Fig. 4(A). The material with  $\phi = 0.55$  is the self-suspended/pure PEG–SiO<sub>2</sub> NOHMs, it contains no PEGDME 250. It is immediately evident from the plot that whether they are self- or oligomer-suspended, all hybrid electrolytes studied display Vogel–Thamann–Fulcher (VTF) temperature dependent conductivity,  $\sigma = A \exp(-B/(T - T_0))$ , over the entire temperature range. Here  $B$  is the pseudoactivation energy for coupled ion and local polymer segment motions/breathing modes;  $T$  and  $T_0$  are the measurement and reference temperatures, respectively; and  $A$  is a pre-exponential factor. This behavior implies that the materials undergo no melting/crystallization transitions in the temperature range studied; this conclusion is supported by differential scanning calorimetry (DSC) measurements, which are silent in the same temperature range. These observations mean that, consistent with previous studies of Li<sup>+</sup> diffusion in PEG, segmental motion of the host and tethered PEG chains is important for the conduction mechanism.

Table 5.1 summarizes the pseudoactivation energy  $B$  (from the VTF fits) and glass transition temperature  $T_g$  (from DSC) for the materials in Fig. 4(A). It is noteworthy that the pseudoactivation energy for conduction of the pure NOHMs electrolyte (i.e. fraction of tethered chains equal unity) is equivalent to that of the temperature fit of the frequency maximum in the tan( $\delta$ ) (see ESI†). This observation is significant because equivalent temperature dependence for these properties confirms that conduction occurs primarily by segmental motion of polymer chains. Considering the dramatic changes in mechanical properties reported in the last section as hybrids are taken through the jamming transition, one might anticipate as remarkable changes in ionic conductivity. Fig. 5.4(A) and Table 5.1 show that this is, remarkably, not the case for PEGDME 250–SiO<sub>2</sub> hybrid electrolytes. In particular, Fig. 5.4(A) shows that the transition from

liquid-like to a jammed physical state produces only a fractional decrease in conductivity at a chosen temperature value. The conductivity decreases noticeably, however, as  $f$  is increased beyond  $f_y$ , and most notably for the pure NOHMs electrolytes.

As a group, the hybrid electrolytes manifest the desirable attribute of maintaining both high conductivity and mechanical strength. For example, a material with  $\varphi = 0.38$ ;  $d_{p-p} \approx 0.2h = 1.3$  nm and mean pore size  $a = \frac{2(1-\varphi)}{3\varphi}d \approx 1.1d = 7.6$  nm displays a storage modulus close to 1 MPa and an ionic conductivity of  $3.5 \times 10^{-4}$  S cm<sup>-1</sup> at 35°C, and even a practical conductivity of  $1.0 \times 10^{-4}$  S cm<sup>-1</sup> at 10°C. Likewise, the pseudoactivation energy for conduction in the hybrid with  $\varphi = 0.38$  is around 80% higher than the value in the hybrid with the lowest SiO<sub>2</sub> content ( $\varphi = 0.11$ )), while the elastic modulus,  $G_e$ , is close to eight orders of magnitude larger! That remarkable changes in mechanical properties in the hybrids produce at most modest changes in ionic conductivity suggests that even in a solid-like electrolyte material, ion conduction occurs more or less unimpeded by the jammed structures that produce mechanical reinforcement. The radius of gyration of PEGDME 250 can be crudely estimated using the formula presented earlier,  $R_g \approx 1$  nm. The ionic radius of the bis(trifluoromethanesulfonyl imide) (TFSI) anion has been estimated using hole theory for transport to be 3.62 Å,<sup>[35]</sup> substantially larger than the radius of a lithium ion, 0.76 Å. The dielectric constant  $D$  for PEG of molecular weight 200 has been reported to be 18.43 at 30°C,<sup>[36]</sup> the Debye screening length is  $\lambda_D = (\varepsilon_0 DRT / 2000F^2 I)^{1/2} \approx 1.5$  Å at 30°C for a 1 M solution of LiTFSI in PEG. Here  $F$  is the faraday charge;  $\varepsilon_0$  is the vacuum permittivity; and  $I$  is the ionic strength of the electrolyte. Thus for the PEGDME 250–SiO<sub>2</sub> hybrid electrolyte with  $\varphi = 0.38$  discussed above, PEG chains are strongly confined and TFSI ions can move, at best in single-file, undisturbed by the smallest bottlenecks in the porous material. For the pure NOHMs electrolyte,  $\varphi = 0.55$ ;  $d_{p-p} \approx 0.05h = 3.2$  Å, even single-file passage of TFSI through the

bottleneck region is on average disallowed. However, the mean pore diameter,  $a \approx 0.55d = 3.8$  nm, in the “continuum” representation of the material is still large enough to allow bulk-like ion transport in the pores. If ion transport in PEG–SiO<sub>2</sub> suspension electrolytes occurs by the same mechanisms as in bulk PEG—segmental motion and diffusion—the ionic conductivity should be to leading order proportional to the “void fraction”,  $(1 - \phi)$ . This statement is explored in Fig. 5.4(B) where the conductivity is plotted against void fraction at various temperature distances from the glass transition,  $T_r = T - T_g$ . Surprisingly, the figure shows that with the possible exception of the pure NOHMs electrolyte, the ionic conductivity is in fact proportional to the void fraction over the entire range of particle volume fractions. The figure also shows that the proportionality constant increases with increasing  $T_r$ , and that the jamming transition has no effect on ionic conductivity. Thermal and ionic conductivity in particle suspensions have been studied by several groups,<sup>[37–39]</sup> using a framework proposed by Maxwell.<sup>40</sup> In this model, the effective conductivity,  $\sigma$ , of a homogeneous suspension of particles of conductivity,  $\sigma_p$ , volume fraction,  $f$ , dispersed in a medium of conductivity,  $\sigma_0$ , can be computed using a simple formula,  $\sigma/\sigma_0 = (1 - 2\alpha\phi)/(1 + \alpha\phi)$ , where  $\alpha = (\sigma_0 - \sigma_p)/(2\sigma_0 + \sigma_p)$  and  $\sigma/\sigma_0$  is the relative conductance at the specified temperature. In the limiting case where the particles are perfect insulators  $\alpha = 1/2$  and Maxwell’s formula becomes,  $\sigma/\sigma_0 = 2(1 - \phi)/(2 + \phi)$ .

Fig. 5.4(C) shows several important features of the ionic conductivity manifested by our hybrid electrolytes are consistent with this model. First, the strong temperature dependence seen in the main figure essentially disappears when the conductivity is expressed in terms of the relative conductivity at the same  $T_r$ . This means that the conduction mechanism in the hybrids is the same as in free PEG. Additionally, it means that the change in shape of the conductivity versus temperature plots in Fig. 5.4(A) originates from the effect of  $\phi$  on  $T_g$ . Second, the figure shows

that when plotted in the Maxwell form, assuming that  $\text{SiO}_2$  is an ionic insulator, the relative conductivity is a linear function of the abscissa variable for all values of  $\phi$ , including the pure (self-suspended) NOHMs electrolyte. This result is remarkable; it means that the simple physics in the Maxwell expression are applicable over the entire range of volume fraction of  $\text{SiO}_2$  in the hybrids. The uniform particle spacing produced by the tethered PEG chains allows for this favorable result, which varies from the properties expected of a system with a percolated non-conducting phase where conduction is markedly inhibited. It is important to point out, however, that the slope of the straight line in Fig. 5.4(C) is 3.5, compared to the theoretical value of 2. This difference implies that the  $\text{SiO}_2$  particles do make a non-negligible contribution to the ionic conductivity of the hybrids, likely because the tethered PEG chains are able to interact with  $\text{Li}^+$  which reduces its mobility. Based on findings from our previous study which show that changing the core particle chemistry from  $\text{SiO}_2$  to  $\text{TiO}_2$  has no effect on the conduction properties,<sup>[25]</sup> we believe that the dense functionalization of the nanoparticle surface with oligomers inhibits the anion adsorption effect reported in “soggy-sand” electrolytes.<sup>[41]</sup>

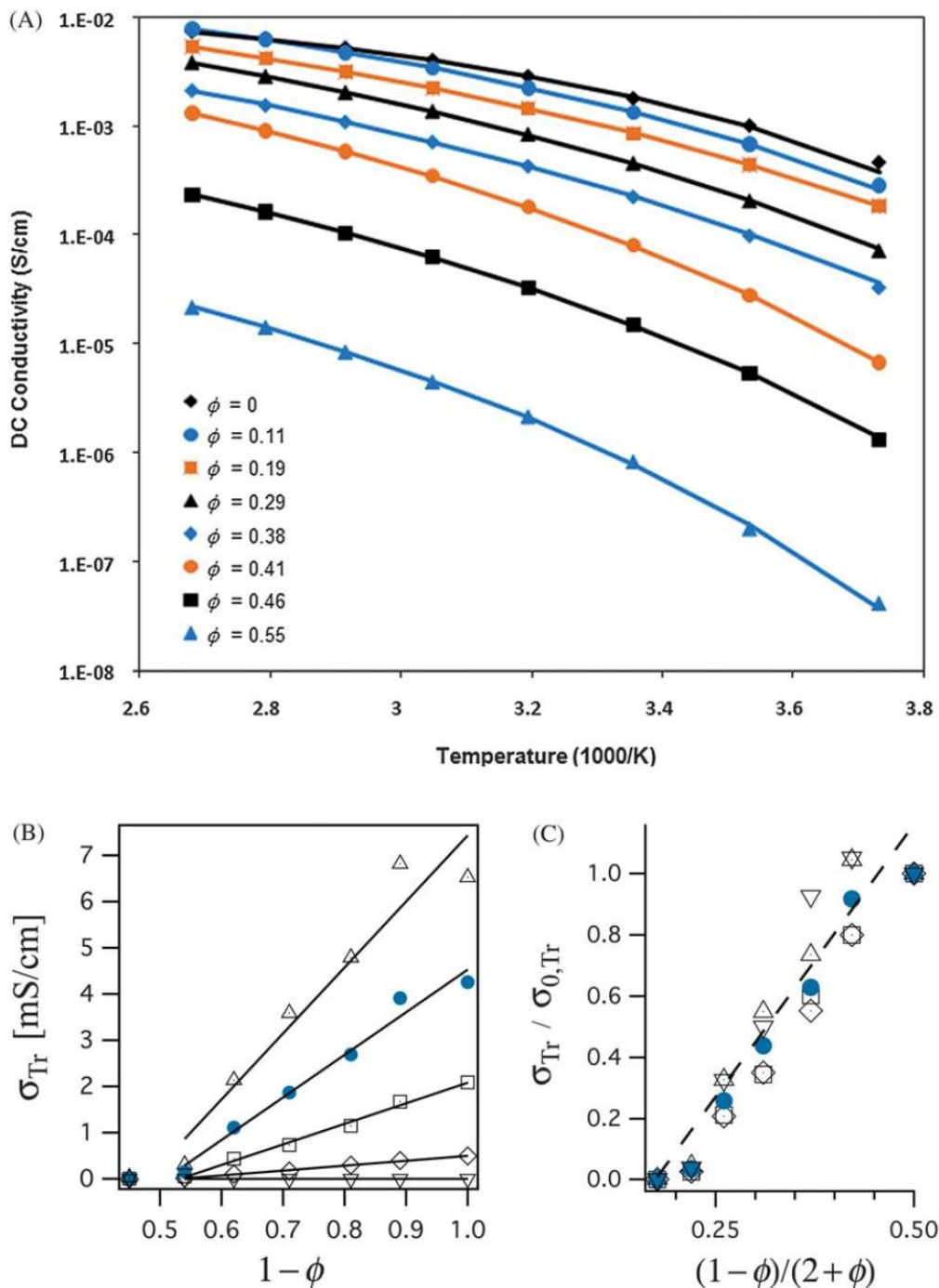


**Figure 5.4** Ionic conductivity: (A) full range of electrolyte from pure plasticizer to pure hybrid.

Points are the actual data and lines are the VTF fits. (B) Temperature reduced conductivity  $\sigma_{Tr}$ , where  $T_r = T - T_g$  for  $T_r = 75, 90, 120, 150, 180$  K. (C) Relative conductivity versus reduced core volume fraction.

**Table 5.1** Pseudoactivation energy,  $B$ , of ionic conduction and glass transition temperature,  $T_g$ , of electrolytes as a function of silica volume fraction,  $\phi$ .

$\phi$	$B/\text{K}$	$T_g/\text{K}$
0	$252 \pm 26$	181.5
0.11	$475 \pm 30$	184
0.19	$592 \pm 5$	186
0.29	$718 \pm 17$	189.5
0.38	$790 \pm 38$	194
0.46	$856 \pm 14$	206
0.55	$904 \pm 84$	213

Electrochemical stability measurements were conducted on a jammed suspension electrolyte,  $\varphi = 0.3$ , in a symmetric, lithium/electrolyte/lithium, configuration in Swagelok cells. Fig. 5.5(A) shows the impedance response at various intervals in time; the points are the data and lines are fits to the equivalent circuit model in the inset. This circuit model has been used previously to explain the impedance response of electrolytes in symmetric lithium cells,<sup>[42]</sup> where  $R_b$  is the bulk electrolyte resistance,  $R_{int1}$  and  $R_{int2}$  are interfacial resistances,  $Q_1$  and  $Q_2$  are the corresponding constant phase element capacitances, and  $W$  is the Warburg diffusion element. Fig. 5.5(B) summarizes the magnitude of the bulk and interfacial resistances, which near steady-state values over a 1000 hour evaluation period. Consistent interfacial resistances and impedance response means that a stable solid electrolyte interfacial (SEI) layer is formed with metallic lithium.

Fig. 5.5(C) shows the electrochemical stability window for both the jammed hybrid and pure PEGDME electrolytes in contact with lithium. Like most PEG/PEO based electrolytes, the cathodic stability is about 0.3 V; the anodic stability of this electrolyte is around 6.3 V. This wide electrochemical stability window allows for the potential use of this electrolyte with a range of electrode materials. Finally, the lithium transference number, the fraction of the ionic conductivity due to lithium transport, was determined by the Bruce/Scrosati method:<sup>[28,29]</sup>  $T_{Li+} = I_{ss}(\Delta V - I_0 R_0) / (I_0(\Delta V - I_{ss} R_{ss}))$  where  $I_0$  and  $I_{ss}$  are the initial and steady-state current of a cell undergoing a polarization potential of  $\Delta V$ , and  $R_0$  and  $R_{ss}$  and the interface charge transfer resistances before and after polarization. The transference number was determined to be less than unity, as expected for a PEG based system:  $T_{Li+} = 0.4 \pm 0.1$  when  $I_0$  was taken to be the actual measured initial current and  $T_{Li+} = 0.65 \pm 0.1$  when  $I_0$  is taken to be the initial current as estimated by fitting the transient current to a single exponential decay (see SI).

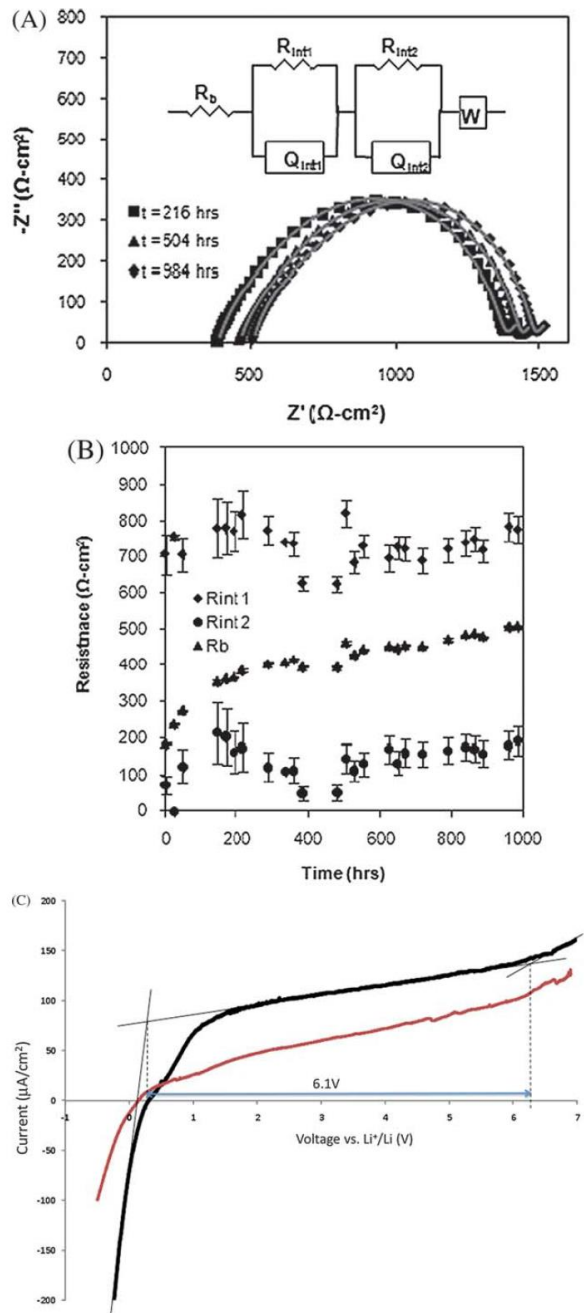


**Figure 5.5** Electrochemical characterization: (A) interfacial charge transfer resistance of an aging cell at discrete points in time. Lines are fits to the displayed equivalent circuit model. (B) Values of the resistances  $R_{int1}$ ,  $R_{int2}$ , and  $R_b$ , determined by circuit fitting, as a function of time. (C) Electrochemical stability windows of pure PEGDME electrolyte ( $\phi = 0$ ) in red, and plasticized NOHMs electrolyte ( $\phi = 0.3$ ) in black.

## Conclusions

We have shown in this work that mechanically tunable, processable, hybrid electrolytes can be created using jammed, homogeneous suspensions of SiO<sub>2</sub>–PEG hybrid particles dispersed in oligomeric PEG hosts. Notably, the jamming transition that yields marked—desirable—increases in mechanical moduli produces only modest changes in ionic conductivity. The effective medium model of Maxwell is used to show that even at SiO<sub>2</sub> core fractions where the inter-particle “throat” diameters in the jammed hybrids are close to the anion size, the conduction processes are largely unaffected by the porous, tortuous network of channels created by the SiO<sub>2</sub> network. Significantly, we also find that these hybrid electrolytes manifest reasonable lithium transference numbers and good electrochemical and interface stability in the presence of lithium. Together, these features make them promising candidates for application in advanced secondary lithium metal batteries; wherein the highly tortuous, nanometer-sized fluid pathways between the jammed SiO<sub>2</sub> particles are expected to frustrate/arrest lithium dendrite growth and proliferation after repeated charge/discharge cycles.

## References

1. F. Wang, J. Yang, Y. NuLi and J. Wang, *J. Power Sources*, 2010, 195, 6884.
2. J.-i. Yamaki, S.-i. Tobishima, K. Hayashi, K. Saito, Y. Nemoto and M. Arakawa, *J. Power Sources*, 1998, 74, 219.
3. R. Bhattacharyya, B. Key, H. Chen, A. S. Best, A. F. Hollenkamp and C. P. Grey, *Nat. Mater.*, 2010, 9, 504.
4. B. Scrosati and C. Vincent, *Mater. Res. Bull.*, 2000, 25, 28.
5. P. G. Bruce, B. Scrosati and J.-M. Tarascon, *Angew. Chem., Int. Ed.*, 2008, 47, 2930.

6. Y.-J. Choi, Y.-D. Chung, C.-Y. Baek and K.-W. Kim, *J. Power Sources*, 2008, 184, 548.
7. M. B. Armand, J. M. Chabagno and M. J. Duclot, *Fast Ion Transport in Solids*, North-Holland, New York, 1979, p. 131.
8. S. Sylla, J.-Y. Sanchez and M. Armand, *Electrochim. Acta*, 1992, 37, 1699.
9. P. Villano, M. Carewska, G. B. Appetecchi and S. Passerini, *J. Electrochem. Soc.*, 2002, 149, A1282.
10. M. Marzantowicz, J. R. Dygas, F. Krok, A. Tomaszevska, Z. Florjanczyk, E. Zygallo-Monikowska and G. Lapienis, *J. Power Sources*, 2009, 194, 51.
11. M. Singh, O. Odusanya, G. M. Wilmes, H. B. Eitouni, E. D. Gomez, A. J. Patel, V. L. Chen, M. J. Park, P. Fragouli, H. Iatrou, N. Hadjichristidis, D. Cookson and N. Balsara, *Macromolecules*, 2007, 40, 4578.
12. F. Croce, G. B. Appetecchi, L. Persi and B. Scrosati, *Nature*, 1998, 394, 456; F. Croce, R. Curini, A. Martinelli, L. Persi, F. Ronci, B. Scrosati and R. Caminiti, *J. Phys. Chem. B*, 1999, 103, 10632.
13. C. Capiglia, P. Mustarelli, E. Quartarone, C. Tomasi and A. Magistris, *Solid State Ionics*, 1999, 118, 73.
14. M. Reddy, P. Chu, J. Kumar and U. Rao, *J. Power Sources*, 2006, 161, 535.
15. H. J. Walls, M. W. Riley, R. R. Singhal, R. J. Spontak, P. S. Fedkiw and S. A. Khan, *Adv. Funct. Mater.*, 2003, 13, 710.
16. H.-M. Kao and C.-L. Chen, *Angew. Chem., Int. Ed.*, 2004, 43, 980.
17. H.-M. Xiong, D.-P. Liu, H. Zhang and J.-S. Chen, *J. Mater. Chem.*, 2004, 14, 2775.
18. P. Maitra and S. Wunder, *Chem. Mater.*, 2002, 14, 4494.

19. J.-M. Tarascon, A. S. Gozdz, C. Schmutz, F. Shokoohi and P. C. Warren, Solid State Ionics, 1996, 86–88, 49.
20. H. Ye, J. Huang, J. J. Xu, A. Khalfan and S. G. Greenbaum, J. Electrochem. Soc., 2007, 154, A1048.
21. S. Seki, Y. Ohno, Y. Kobayashi, H. Miyashiro, A. Usami, Y. Mita, H. Tokuda, M. Watanabe, K. Hayamizu, S. Tsuzuki, M. Hattori and N. Terada, J. Electrochem. Soc., 2007, 154, A173.
22. P. Birke, F. Salam, S. Doring and W. Weppner, Solid State Ionics, 1999, 118, 149.
23. D. K. Pradhan, R. N. P. Choudhary and B. K. Samantaray, Mater. Chem. Phys., 2009, 115, 557.
24. S. S. Moganty, N. Jayaprakash, J. L. Nugent, J. Shen and L. A. Archer, Angew. Chem., Int. Ed., 2010, 49, 9158.
25. J. L. Nugent, S. S. Moganty and L. A. Archer, Adv. Mater., 2010, 22, 3677.
26. Q. Zhang and L. A. Archer, Langmuir, 2002, 18, 10435.
27. A. K. Jonscher, Nature, 1977, 267, 673.
28. P. G. Bruce, J. Evans and C. A. Vincent, Solid State Ionics, 1988, 28–30, 918.
29. G. B. Appetecchi, G. Dautzenberg and B. Scrosati, J. Electrochem. Soc., 1996, 143, 6.
30. R. G. Larson, The Structure and Rheology of Complex Fluids, Oxford, New York, 1999.
31. M. Rubinstein and R. Colby, Polymer Physics, Oxford, New York, 2004.
32. M. Doi and S. F. Edwards, The Theory of Polymer Dynamics, Cambridge University Press, New York, 1980.
33. W. J. Frith, T. A. Strivens and J. Mewis, J. Colloid Interface Sci., 1990, 139, 55.
34. P. Agarwal, H. Qi and L. A. Archer, Nano Lett., 2010, 10, 111.
35. A. T. Abbott, ChemPhysChem, 2004, 5, 1242.

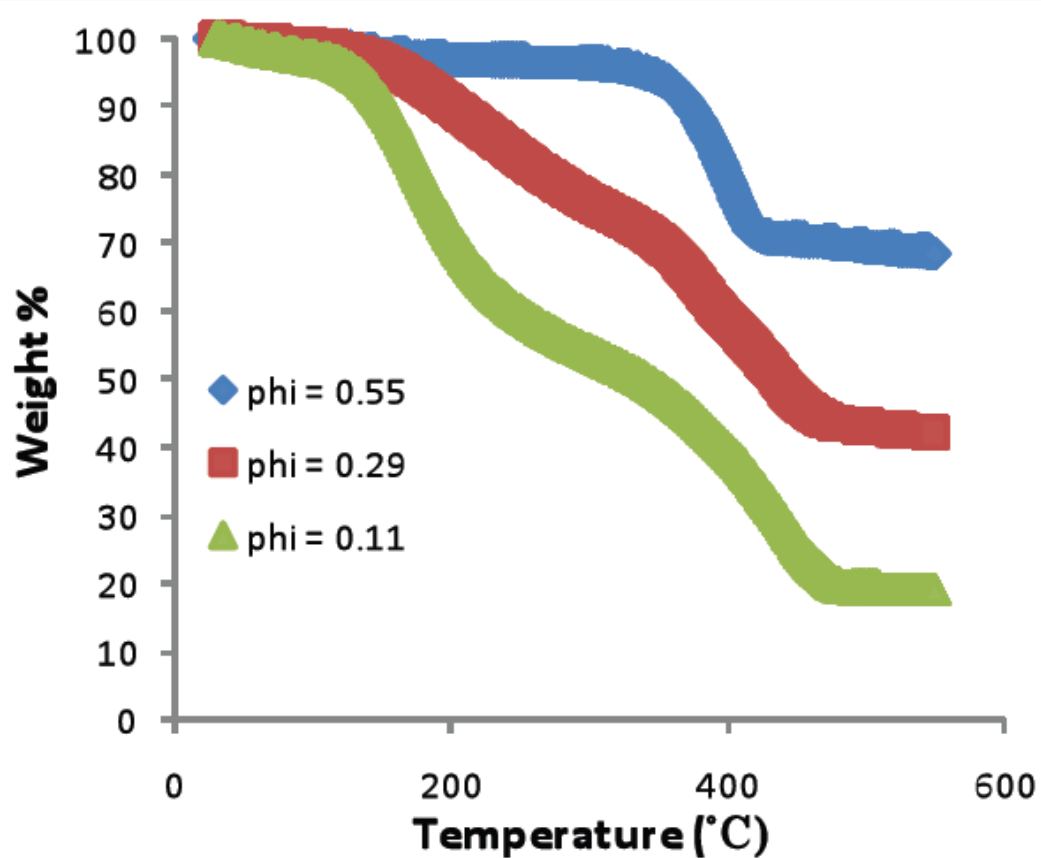
36. A. M. Awwad, H. Al-Dujaili and H. E. Salman, *J. Chem. Eng. Data*, 2002, 47, 421.
37. W. Yu and S. U. S. Choi, *J. Nanopart. Res.*, 2003, 5, 167.
38. M. Pavlin, T. Slivnik and D. Miklavcic, *IEEE Trans. Biomed. Eng.*, 2000, 49, 77.
39. H. Cheng and S. Torquato, *Proc. R. Soc. London, Ser. A*, 1997, 453, 145.
40. J. C. Maxwell, *Treatise on Electricity and Magnetism*, Oxford University Press, London, UK, 1873.
41. A. J. Bhattacharyya, M. Dolle and J. Maier, *Electrochem. Solid-State Lett.*, 2004, 7, A432.
42. S. Liu, N. Imanishi, T. Zhang, A. Hirano, Y. Takeda, O. Yamamoto and J. Yang, *J. Power Sources*, 2010, 195, 6847.

## **APPENDIX: SUPPORTING INFORMATION**

### *Synthesis*

An alkaline stabilized dispersion of silica nanoparticles, Ludox SM-30 (Aldrich), was diluted to 4 wt% particle fraction by the addition of potassium hydroxide solution, pH ~10. [Methoxy(polyethyleneoxy)propyl] trimethoxysilane, 90% (Gelest) at a ratio of 0.6g silane-PEG per 1.0 g silica was added dropwise, while stirring, in three aliquots each separated by heating at 100C in an oil bath for 1 hour followed by 10-15 minutes of sonication. Following the addition of the final aliquot of silane-PEG, the reaction solution was heated for 6 hours in an oil bath at 100C. The reaction solution was then poured into petri dishes and heated overnight in a convection oven at 70C to drive off remaining water and complete the silane reaction. The following day, the NOHMs were purified by washing with ethanol 3 times to remove any free silane-PEG, and resuspended in chloroform.

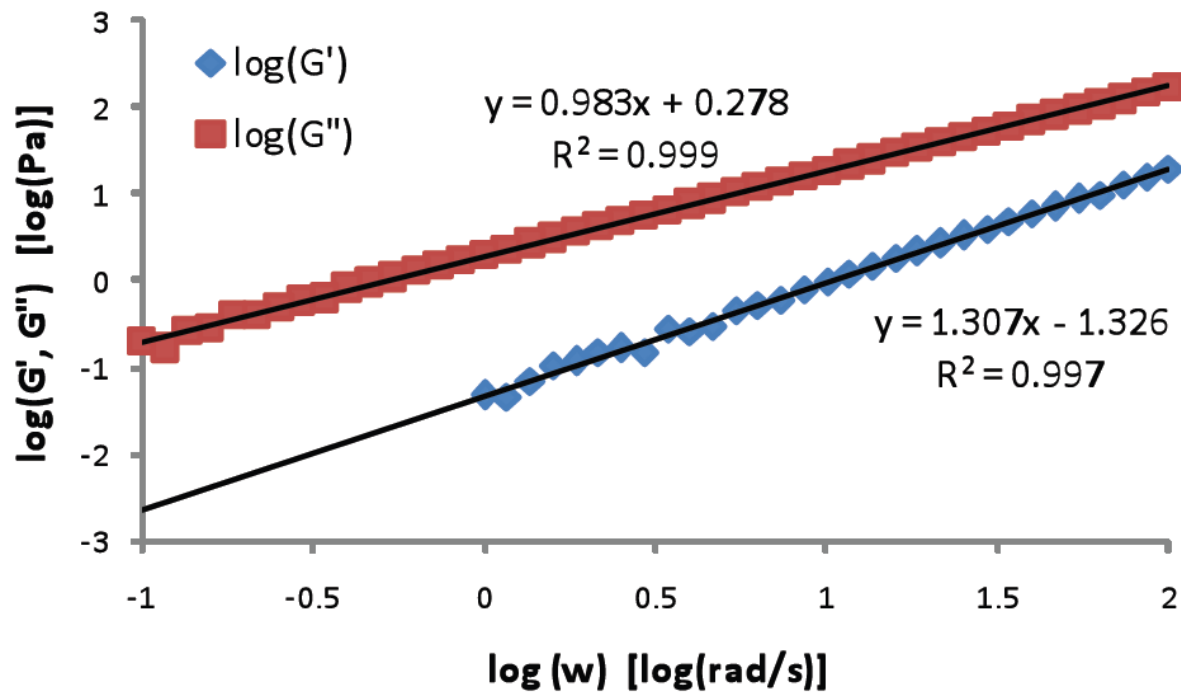
*Thermal Gravimetric Analysis*



**Supplementary Figure 5.1** Thermal gravimetric analysis (TGA) data of selected hybrid suspension electrolytes. The volume fraction,  $\phi$ , of silica in each sample was determined via this method.

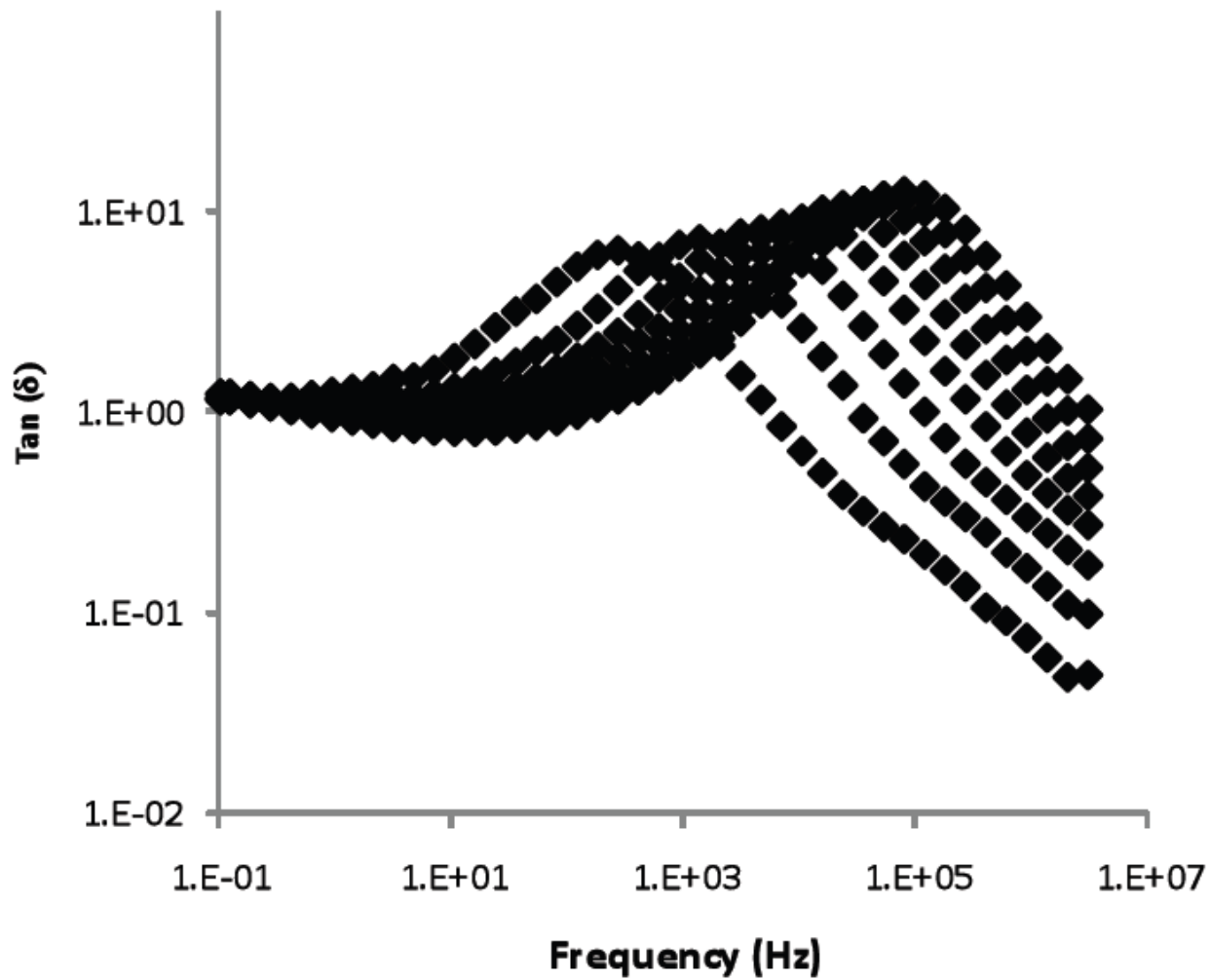
The pure NOHMs electrolyte is thermally stable to above 350°C. The plasticized electrolytes have reduced stability due to the decomposition of PEGDME 250.

*Power Law Frequency Dependence of the Moduli*

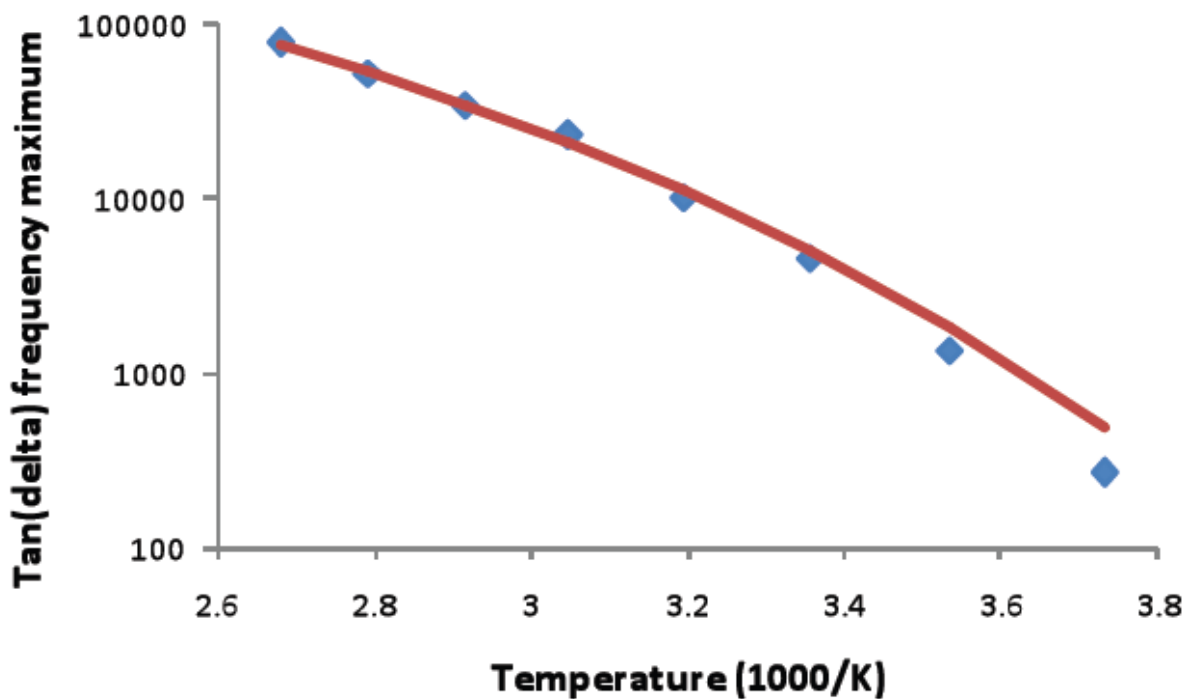


**Supplementary Figure 5.2** Example data analysis for a hybrid electrolyte with  $\phi = 0.24$ . For  $G', G'' \sim \omega^m$ ,  $m$  is the slope in the applicable fit equation.

$\tan(\delta)$  VTF fit



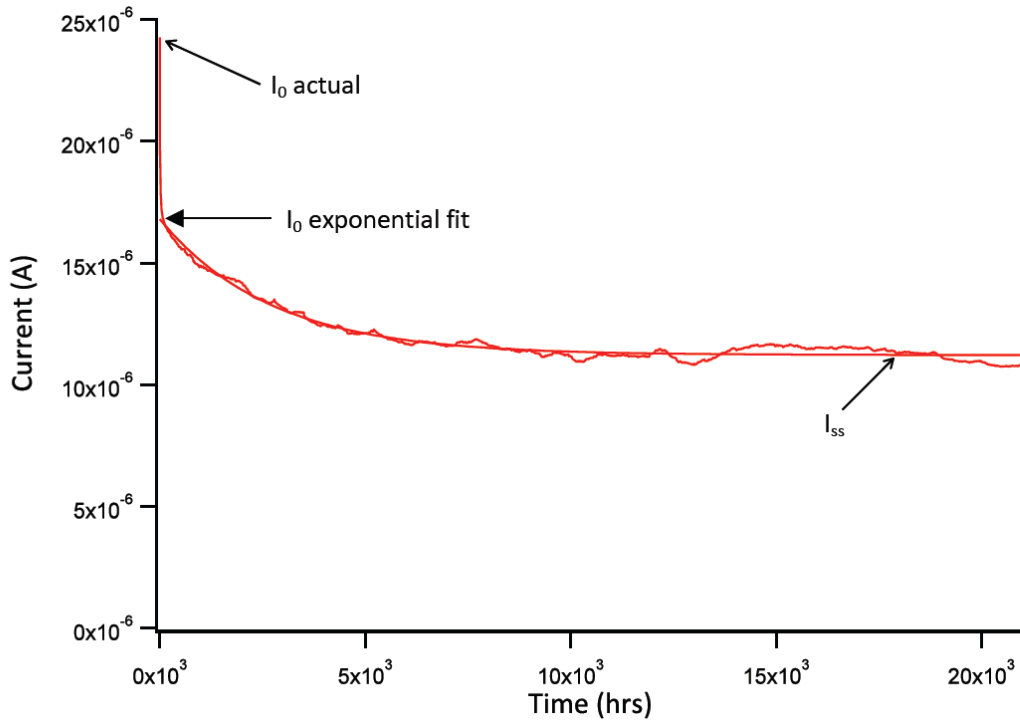
**Supplementary Figure 5.3** Data of  $\tan(\delta)$  vs. frequency at temperature -5 to 100°C in 15°C increments for the pure hybrid electrolyte ( $\phi = 0.55$ ) as obtained from dielectric spectroscopy. Values of the frequency maximum were recorded for fit to the VTF equation.



**Supplementary Figure 5.4** Data points for the frequency maximum of  $\tan(\delta)$  as obtained from SF 4.3. The fit to the VTF equation is the line in red. For the frequency VTF fit:  $B = -890 \pm 360$ . Similarly,  $B = -900 \pm 80$  for the ionic conductivity fit. This suggests that the mechanism for ionic conduction is through segmental motion of the polymer chains.

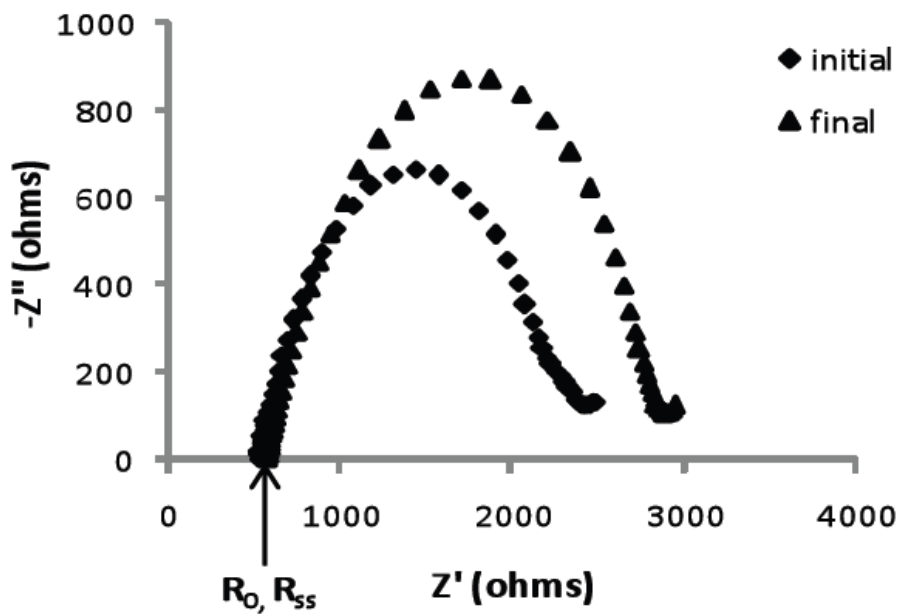
### Determination of the lithium transference number

Lithium transference measurements were performed on a Li / electrolyte,  $\phi = 0.30$  / Li cell using the method proposed by Bruce and Scrosati, where initial and steady state values of current are found for a symmetric lithium cell undergoing polarization, with corrections from impedance measurements of the bulk resistance both before and after polarization.

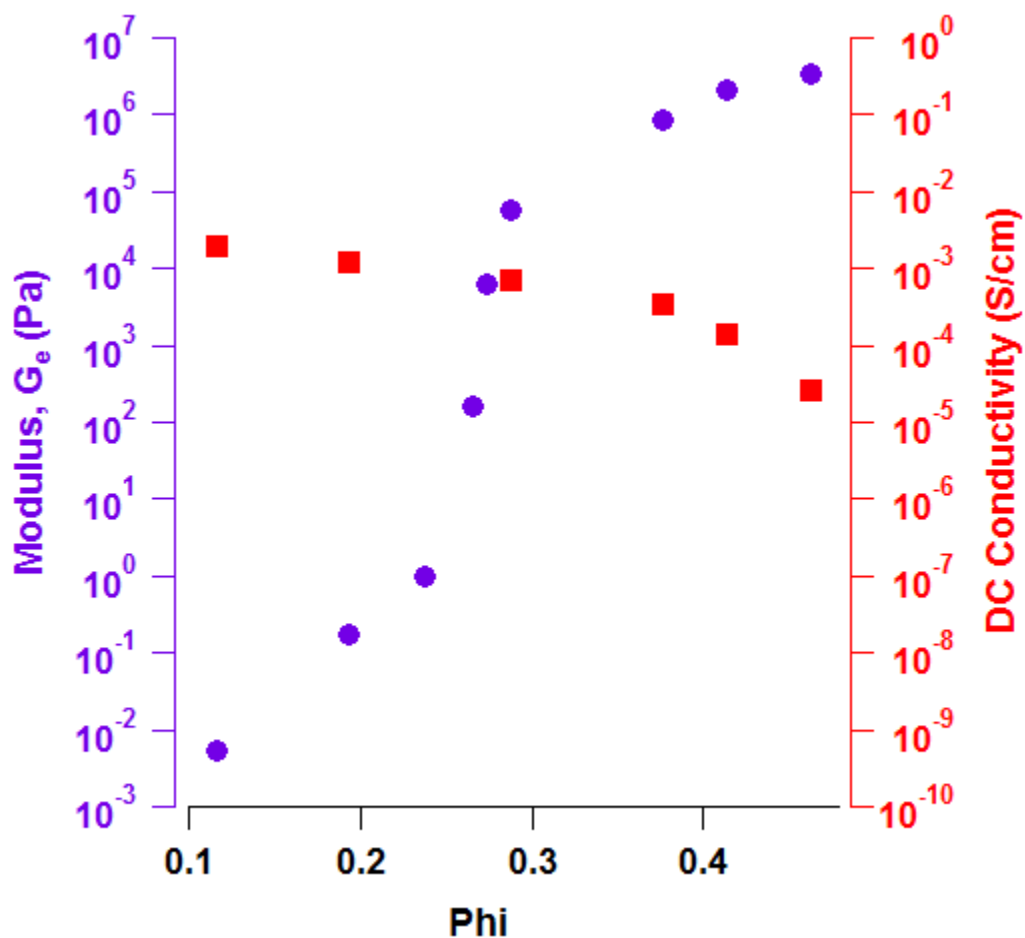


**Supplementary Figure 5.5** Current decay of a cell while undergoing a 50 mV polarization.

Calculations were performed with the actual  $I_0$  and  $I_0$  determined by fit to an exponential decay function;  $I_{ss}$  was determined by fit to an exponential decay function.



**Supplementary Figure 5.6** Impedance measurements from  $10^4$  to  $10^{-1}$  Hz, with a voltage amplitude of 10 mV before and after polarization, to determine bulk resistances  $R_0$  and  $R_{ss}$ .



**Supplementary Figure 5.7** Comparison of the storage modulus at low strain,  $G_e$ , and the DC conductivity of the hybrid electrolytes as a function of composition at 35°C.

## **CHAPTER 6:**

### **SHORT-CIRCUIT BEHAVIOR OF COIN CELLS CONTAINING TUNABLE NANOSCALE, HYBRID ELECTROLYTES**

Contributions by undergraduate researcher Brianna DeRooy to impedance, short-circuit, and lithium transference number testing.

#### **6.1 Introduction**

There are a limited number of published, quantitative studies of lithium metal battery lifetimes until short-circuit as a function of electrolyte properties. In this work, we investigate the lifetime of lithium metal batteries employing tunable, hybrid suspension electrolytes similar to those described in Chapter 5.

#### **6.2 Experimental**

Hybrid electrolytes were created from PEG-functionalized silica nanoparticles as described in Chapter 5, whereas the diameter of the silica nanocore was 7 nm (Ludox SM-30) or 18 nm (Ludox HS-40) and the volume fraction of silica was varied by the addition of the plasticizer tetraethylene glycol dimethyl ether (tetraglyme, Aldrich) or polyethylene glycol dimethyl ether (PEGDME, Mn  $\approx$  250, Aldrich). The electrolytes were doped with lithium salt LiTFSI to 1 M in the organic phase. Ionic conductivity of these electrolytes was measured as described in Chapter 5.

Symmetric lithium metal coin cells (size 2032, Hohsen) were prepared by charging a Teflon donut-shaped ring with an inner diameter of 6.35 mm and thickness of 0.030 inches with the

electrolyte and sandwiching this ring between two lithium metal electrodes. The lithium metal foil (Alfa Aesar) appeared a dull metallic color and clean before use; the foils were flattened until shiny by rolling with a clean, glass scintillation vial to remove the striations present from manufacturing. Impedance testing on these cells was performed as described in Chapter 3.

Lithium transference number testing was performed on symmetric lithium cells using the same method as described in Chapter 5 on a Solartron Electrochemical Impedance Spectrometer, the Bruce-Scrosati method, but with a slightly different test protocol. It was determined following the experiments reported in Chapter 5 and Chapter 8 that data points closer to the start of the constant voltage polarization step (first data point at 0.0003 s vs. 0.017 s) could be achieved by programming a rest step before the constant voltage polarization step. The schedule programmed into the Solartron for the polarization step was hence as follows:

Step 1 – Constant Voltage = 0 V for 5 minutes with a data point collected every 10 seconds

Step 2 – Constant Voltage = Polarization Voltage (ex. 50 mV) for 0.03 seconds with a data point collected every 1/10000 of a second

Step 3 – Constant Voltage = Polarization Voltage (ex. 50 mV) for 0.97 seconds with a data point collected every 1/1000 of a second

Step 4 – Constant Voltage = Polarization Voltage (ex. 50 mV) for 24 hours with a data point collected every 10 seconds

The measurement was manually stopped (prior to the finish of Step 4) when it was observed that a steady-state current had been obtained. This protocol resulted in determination of the lithium

transference number with a significantly improved reproducibility. Transference numbers are reported as a function of the applied polarization voltage. In the Ohmic regime where this method is suggested to be valid, measured transference number should be independent of polarization voltage.

Short-circuit testing was performed on Neware battery testers using the galvanostatic polarization method, whereas a constant current is applied until a sharp drop-off in the potential is observed, indicative of a short of the cell by a dendrite. In the cases where the cell recovered following the deviation in the potential, the first voltage drop is taken to be the short-circuit time,  $t_{sc}$ .

For temperature-dependent lithium transference and short-circuit testing, cells were contained in a VWR convection oven with wiring through the ceiling hole.

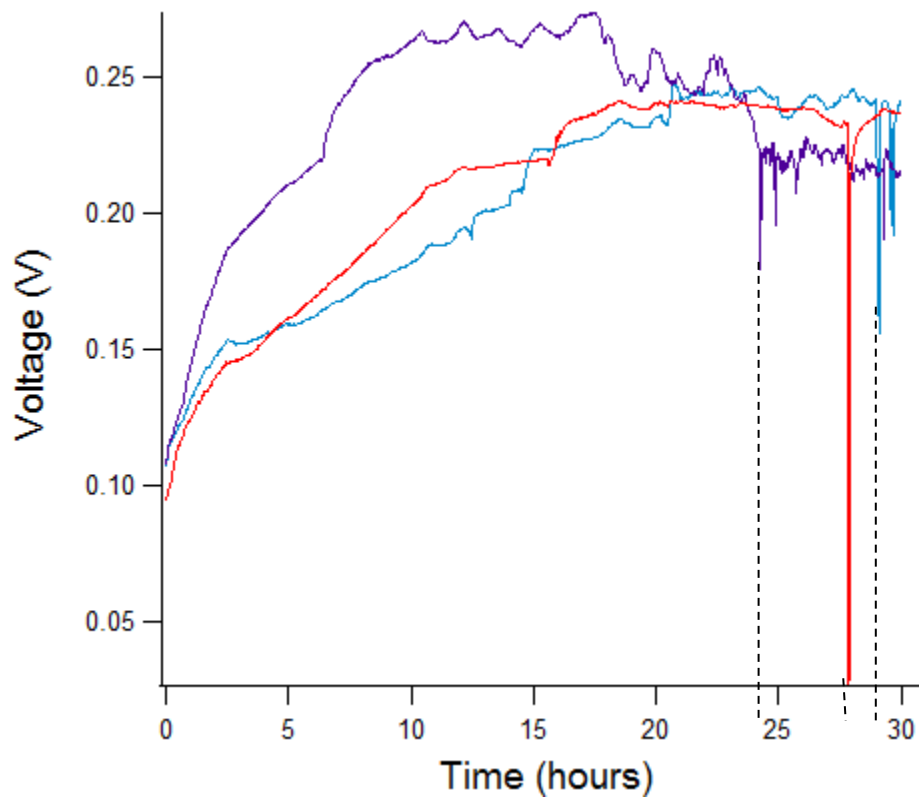
### 6.3 Results and Discussion

Table 6.1 summarizes the properties of the electrolytes employed in this study.

Figure 6.1 displays the voltage response of three different coin cells containing a hybrid electrolyte,  $\varphi = 0.32$ , undergoing galvanostatic polarization at room temperature at a current density,  $J$ , of  $0.158 \text{ mA/cm}^2$ . In every case, the potential of the cell rises from its initial value due to salt polarization within the electrolyte and the formation of the electrode-electrolyte interface. After some time, a drop-off in the potential is observed; the recorded short-circuit time is displayed by the dashed line in Figure 6.1. After the initial drop in the potential, where literature suggests that a short-circuit has occurred, all three coin cells recover to the steady-state voltage. Additional shorts appear to continue at a more frequent pace following the initial short. This phenomenon has been observed in the literature and is termed the thermal fuse effect.<sup>[1]</sup> It is

**Table 6.1** Properties of electrolytes under investigation

Liquid	SiO <sub>2</sub> -PEG, $\phi$	d (nm)	$d_{p-p}$ (nm)	$\sigma$ (S/cm)	C <sub>0</sub> (M)
Tetraglyme	0.30	7	2.0	$6.3 \times 10^{-4}$	0.70
Tetraglyme	0.32	7	1.8	$4.8 \times 10^{-4}$	0.68
Tetraglyme	0.37	7	1.4	$2.3 \times 10^{-4}$	0.63
Tetraglyme	0.40	7	1.2	$1.5 \times 10^{-4}$	0.60
Tetraglyme	0.40	18	3.0	$3.9 \times 10^{-4}$	0.60
Tetraglyme	0.43	18	2.5	$3.3 \times 10^{-4}$	0.57
Tetraglyme	0.46	18	2.1	$2.4 \times 10^{-4}$	0.54
Tetraglyme	0.50	18	1.5	$1.6 \times 10^{-4}$	0.50
PEGDME 250	0	---	---	$1.7 \times 10^{-3}$	1.0



**Figure 6.1** Representative voltage profiles for three different coin cells containing hybrid electrolyte sample #2 undergoing galvanostatic polarization at room temperature at  $J = 0.158 \text{ mA/cm}^2$ .

thought that the dissipation of energy through the dendrite at short-circuit can cause the dendrite to melt, thus eliminating the short and allowing continued operation of the cell. The mild fluctuations of the cell voltage throughout the polarization are likely due to changes in the ambient temperature of the laboratory.

The summary of the short-circuit times for coin cells containing a number of different hybrid electrolytes with gel-like mechanical properties and yield stress greater than gravity is displayed in Figure 6.2, along with data obtained for coin cells containing a pure plasticizer electrolyte with no hybrid particles and data previously published by Rosso, et. al obtained from coin cells operating at 90°C containing a high molecular weight polyethylene oxide electrolyte. Despite the scatter in the data, it is immediately apparent that regardless of electrolyte composition,  $t_{sc}$  follows a similar trend with  $J$ . Two different hypotheses that may explain this behavior are hereby explored.

Figure 6.3a displays the short-circuit times for cells containing three different hybrid electrolytes for which the obtained data sets were the most extensive as well as for cells containing the pure plasticizer-based electrolyte, along with the predicted  $t_{sc}$  from the Chazalviel model accounting for both the dendrite onset time and growth time:<sup>[2-4]</sup>

$$t_{sc} \approx \tau_s + t_g = \pi D \left( \frac{eC_0}{2Jt_a} \right)^2 + \frac{\sigma L}{\mu_a J} \quad \text{Equation 6.1}$$

As ion diffusivity and bulk ion concentration decrease with increasing hybrid particle content, the predicted  $t_{sc}$  decreases with increasing  $\phi$ . Equation 6.1 underpredicts the cell lifetime in the cases where the stiffest hybrid electrolyte of the series,  $\phi = 0.40$ , was employed. Likewise, Equation 6.1 overpredicts the cell lifetime when the electrolyte with no particle additives was used. This trend is more obvious in Figure 6.3b, where the experimental  $t_{sc}$  values are

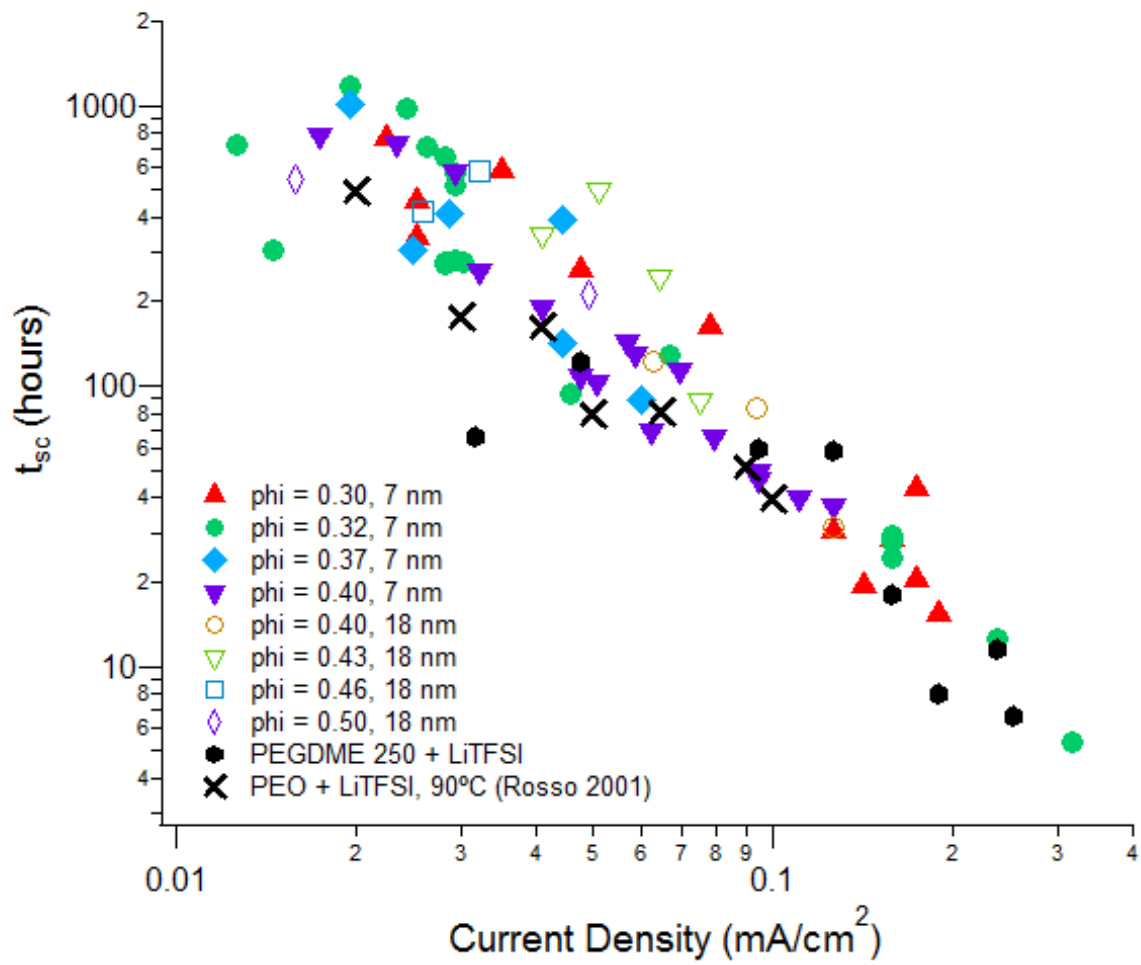


**Figure 6.2** Short-circuit times for coin cells undergoing galvanostatic polarization as a function of electrolyte composition and applied current density. Data on PEO + LiTFSI published by Rosso, et. al.<sup>[4]</sup>

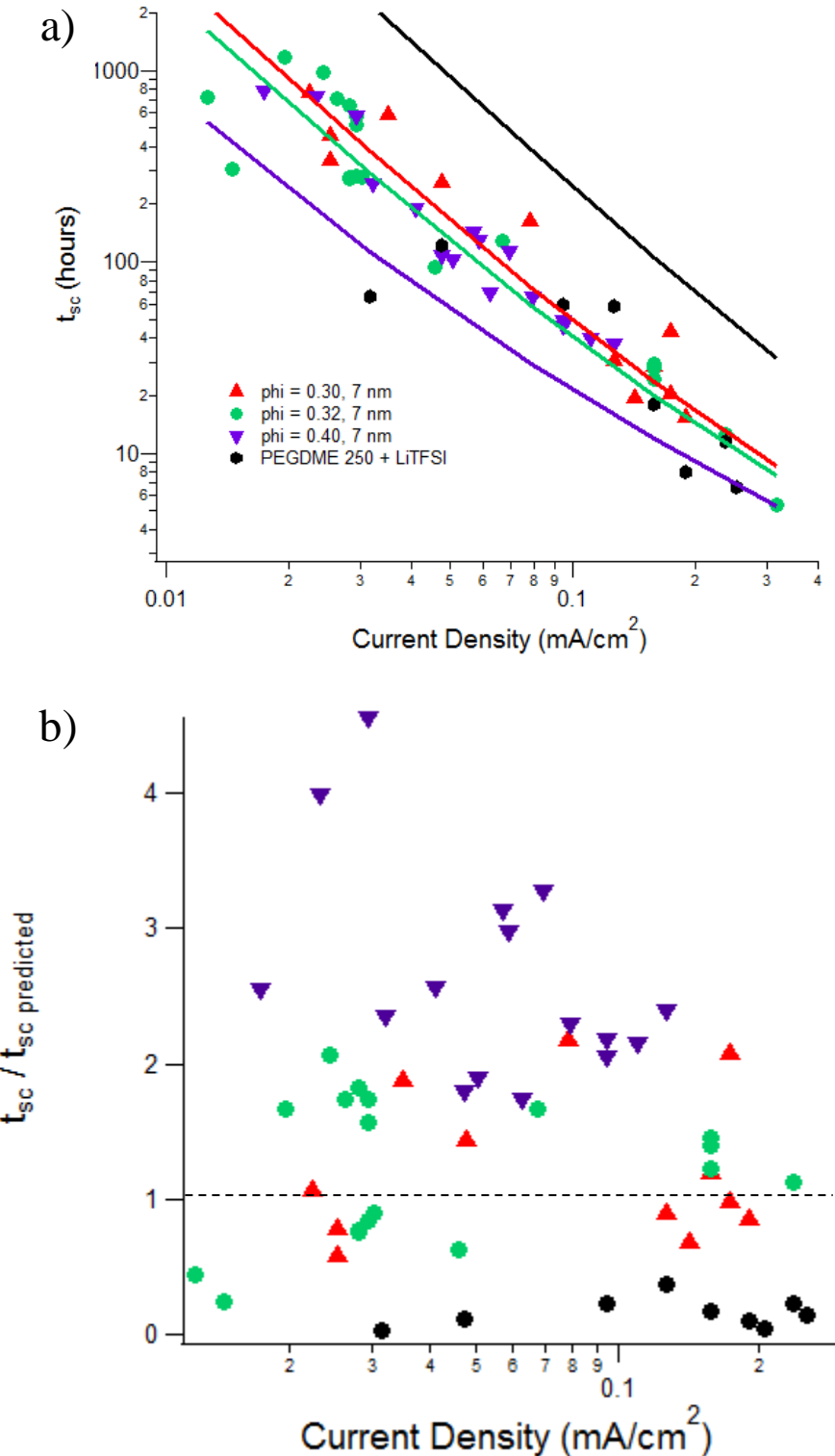


**Figure 6.3** a. Comparison of selected short-circuit data with the prediction by Equation 6.1 and b. Short-circuit data normalized by Equation 6.1.

normalized by the predicted  $t_{sc}$  values from Equation 6.1. Cells containing the stiffer hybrid electrolyte have lifetimes about 2-4 times that predicted by Equation 6.1, hence it could be possible that the mechanical properties of this electrolyte are enhancing cell lifetimes. However, cells containing the pure liquid electrolyte have lifetimes well below that of the predicted value, thus invalidating the theory that stiff electrolyte mechanics lead to a deviation from the Chazalviel prediction. It is clear that Equation 6.1 has predicted the correct relationship between short-circuit time and applied current density, but the effects of varying ambipolar diffusion coefficients are not observable in these experiments.

Published literature<sup>[5-7]</sup> suggests that reduced interfacial impedance may extend cell lifetimes of galvanostatically polarized lithium metal cells. Although the studied electrolytes containing varying amounts of functionalized particles, it is possible that similar composition and thus similar resistance to ion-transport exists at the electrode-electrolyte interface. If cells containing varying bulk electrolyte compositions had similar electrode-electrolyte interface composition, this characteristic should result in similar measured interfacial impedances. Figure 6.4 displays the impedance response of symmetric lithium coin cells containing electrolytes with selected compositions. Electrolytes with increased amounts of hybrid particles have higher interfacial impedance, where total interfacial impedance is taken to be the width of the impedance hemisphere. As increased interfacial impedance has previously been correlated with reduced short-circuit times, it is unlikely that the interfacial properties of cells containing the stiff electrolyte  $\varphi = 0.40$  with 7 nm nanocores results in the observed cell lifetimes that are similar to that obtained with electrolytes with lower filler loading.

The temperature dependent short-circuit times for cells containing selected hybrid electrolyte compositions are displayed in Figure 6.5. The observed short-circuit time decreases in nearly all

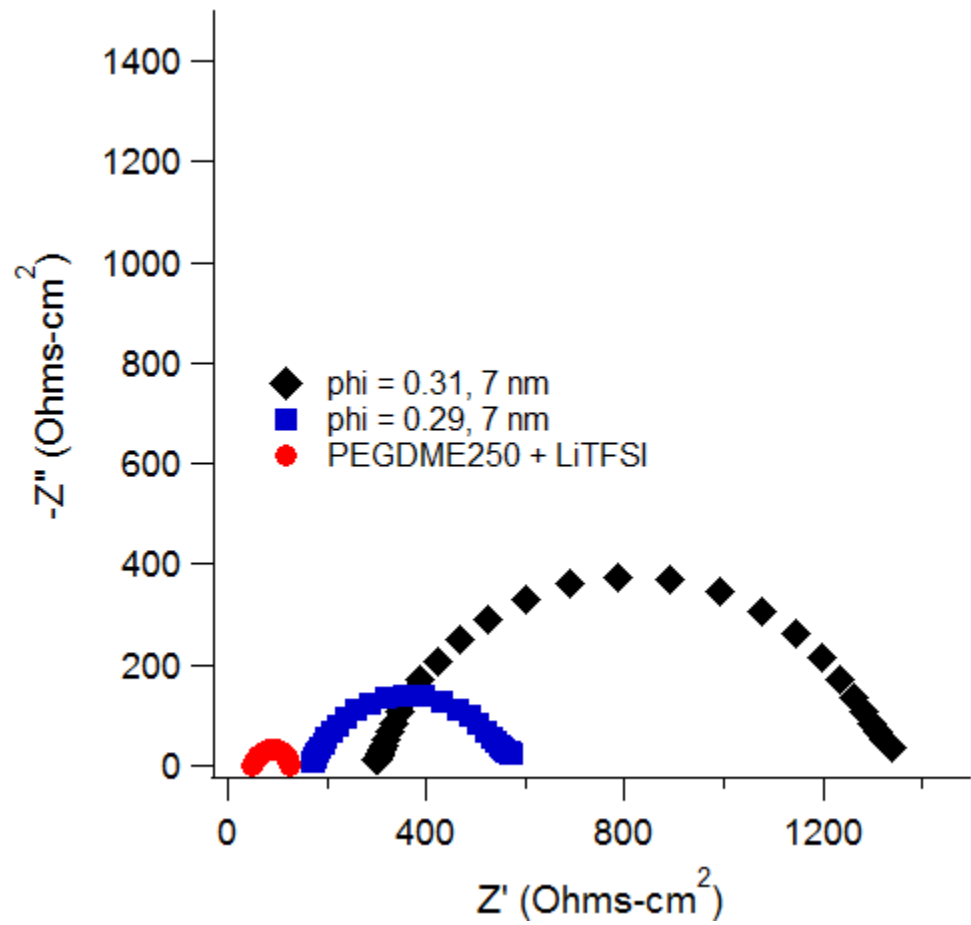


**Figure 6.4** Impedance responses of Li/electrolyte/Li cells at 20°C with varying electrolyte compositions.

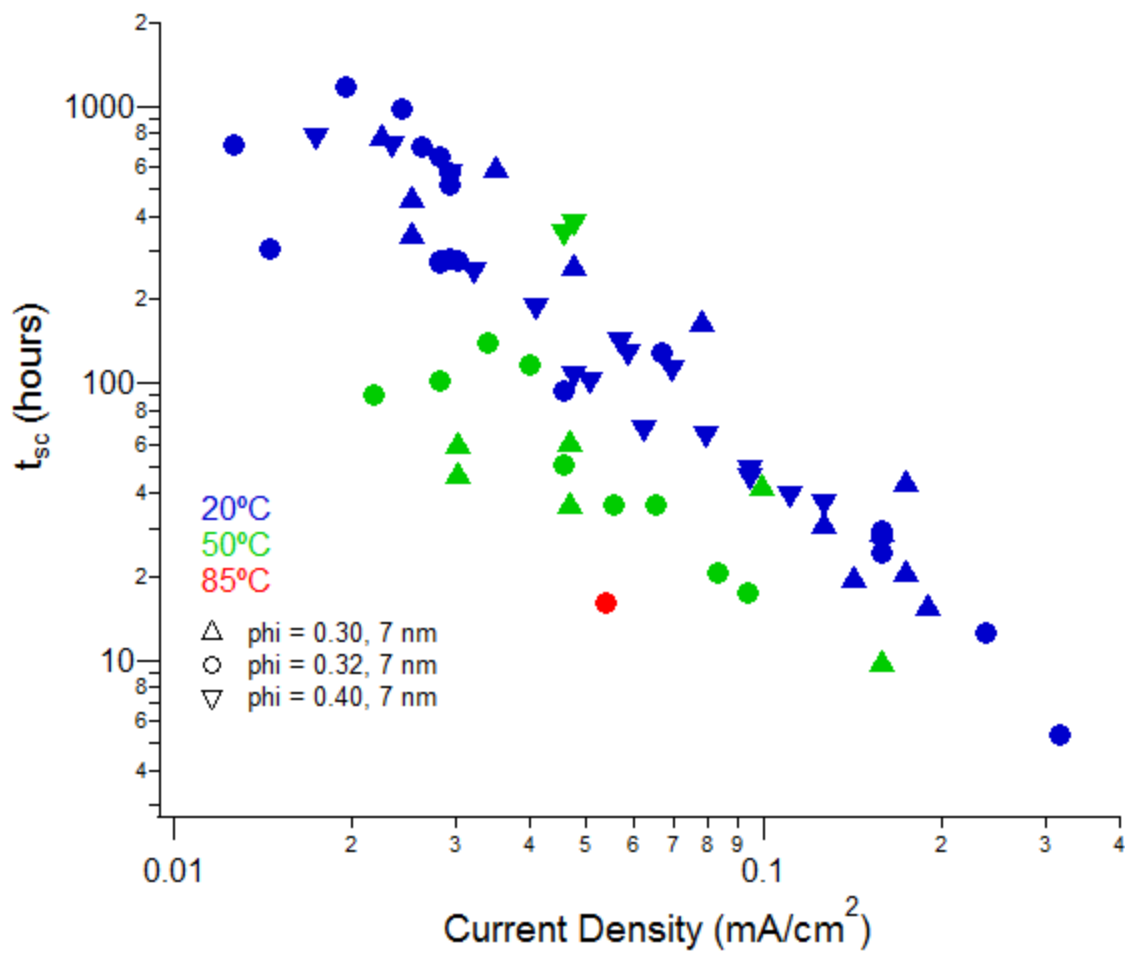


**Figure 6.5** Short-circuit times for coin cells undergoing galvanostatic polarization as a function of electrolyte composition, applied current density, and temperature.

cases with increasing temperature, but maintains a similar dependence on current density. The Chazalviel model predicts increased lifetimes due to increased ion diffusivity; however, it also predicts decreased lifetime with decreased lithium transference number.

As  $\text{Li}^+$  and  $\text{TFSI}^-$  diffusivities in PEG have been shown previously to have varying activation energies,<sup>[8]</sup> the lithium transference number of the investigated electrolytes was tested as a function of temperature using the Bruce-Scrosati method as discussed in the experimental section. Figure 6.6 displays the obtained transference numbers for hybrid electrolytes as a function of temperature and composition. The lithium transference number is a weak function of composition and is nearly temperature invariant over the studied range, so this parameter does not account for the observed discrepancy between the measured short-circuit time and the Chazalviel model.

Impedance spectra were measured to determine the effect of temperature on the interfacial resistance; representative plots are shown in Figure 6.7. At room temperature, the bulk and interfacial impedances of the electrolyte with a higher loading of hybrid particles is higher. However, the trend reverses at high temperatures, where the interfacial impedance of the electrolyte with a lower loading of particles is higher than that of the stiffer electrolyte. This may be explained by the decomposition of the plasticizer, tetraglyme, at elevated temperatures when in contact with the lithium metal electrode, as the electrolytes containing less hybrid particles have a higher loading of plasticizer. The increase in the interfacial impedance could alternatively be due to decomposition of an impurity, such as water. Furthermore, the impedance data explains the observed temperature-dependent short-circuit behavior as reported in Figure 6.5. Cells employing electrolytes containing fewer hybrid particles ( $\phi = 0.30, 0.32$ ) had reduced lifetimes at higher temperatures due to reaction of the plasticizer with the metal interface, while

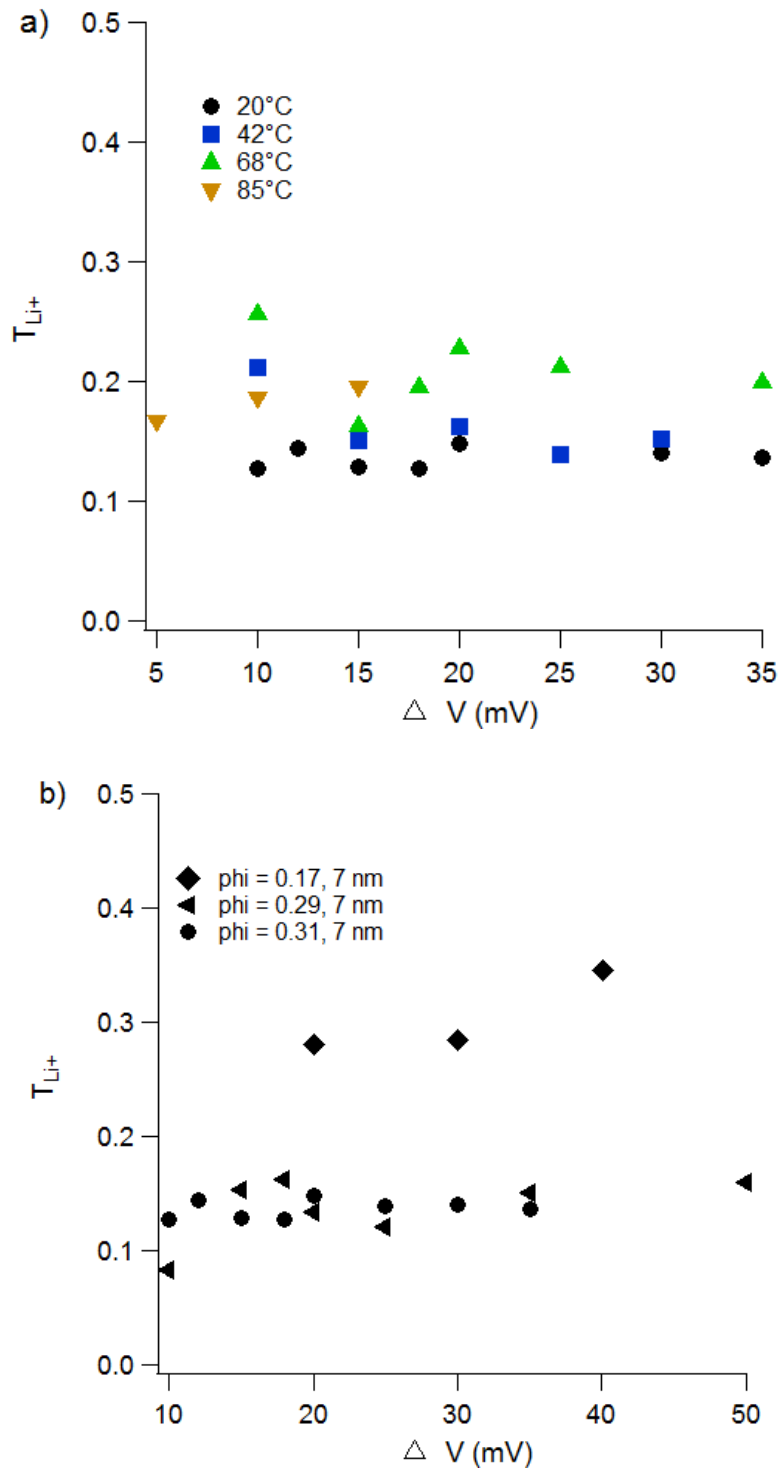


**Figure 6.6** Measured lithium transference number as a function of applied polarization voltage as a function of a) temperature for a hybrid electrolyte with  $\varphi = 0.31$  and b) hybrid electrolyte composition at  $20^\circ C$ .

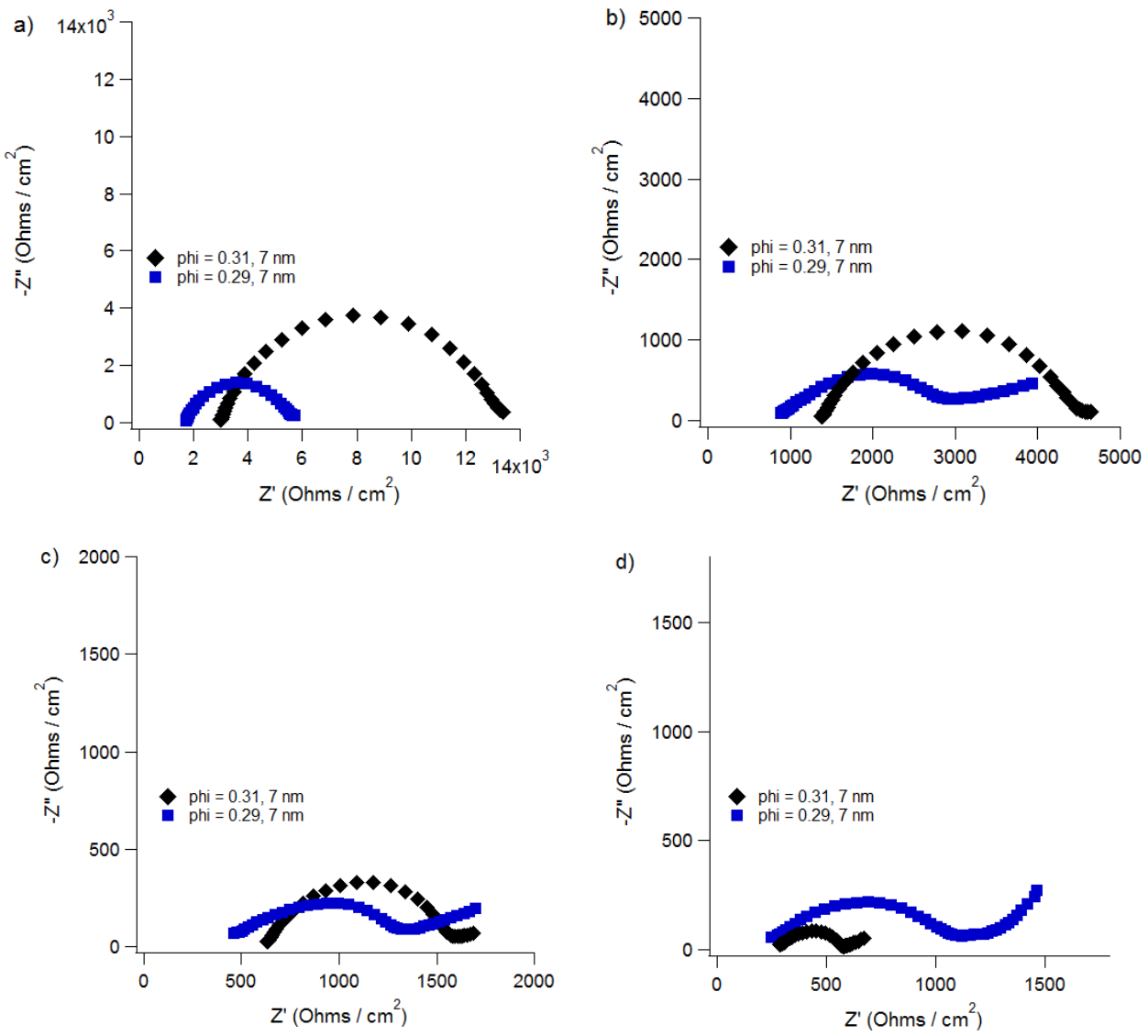


**Figure 6.7** Impedance spectra of hybrid electrolytes with varying composition as a function a temperature, at a) 20°C, b) 35°C, c) 55°C, and d) 85°C.

the electrolyte containing the least amount of plasticizer and most particles ( $\phi = 0.40$ ) actually had an increased lifetime with increasing temperature. This result suggests that chemical stability of electrolyte solvent with the lithium metal electrode strongly contributes to the absolute observed short-circuit time.

The conclusion that chemical or electrochemical stability of the electrolyte with the lithium metal electrolyte strongly effects short-circuit time is further supported by comparison of the data hereby discussed on studies with PEG-based electrolytes and that published by colleague Yingying Lu on studies with propylene carbonate (PC)-based electrolytes<sup>[9]</sup> using the same coin cell configuration and same salt type at 1 M concentration (Figure 6.8). It is accepted that carbonate electrolytes have a reduced stability than polyether electrolytes when in contact with lithium metal. It is clear from Figure 6.8 that the PEG-based electrolytes yield longer cell lifetimes in galvanostatic polarization testing than the PC-based electrolytes.

In summary, it is found that the polyether-based electrolytes under investigation result in similar cell lifetimes when employed in symmetric lithium cells undergoing galvanostatic polarization testing, regardless of the exact electrolyte composition (loading of hybrid particles). The lifetimes of cells containing these polyether electrolytes were found to substantially exceed that previously published on propylene carbonate electrolytes. Thus, it is concluded that the stability of the electrolyte with lithium metal is a crucial parameter effecting lithium dendrite formation. Over the range of electrolytes tested,  $G' < 5 \text{ MPa}$ , the mechanical properties of the electrolyte were not found to measureable effect cell lifetime until failure by dendrite short-circuit.

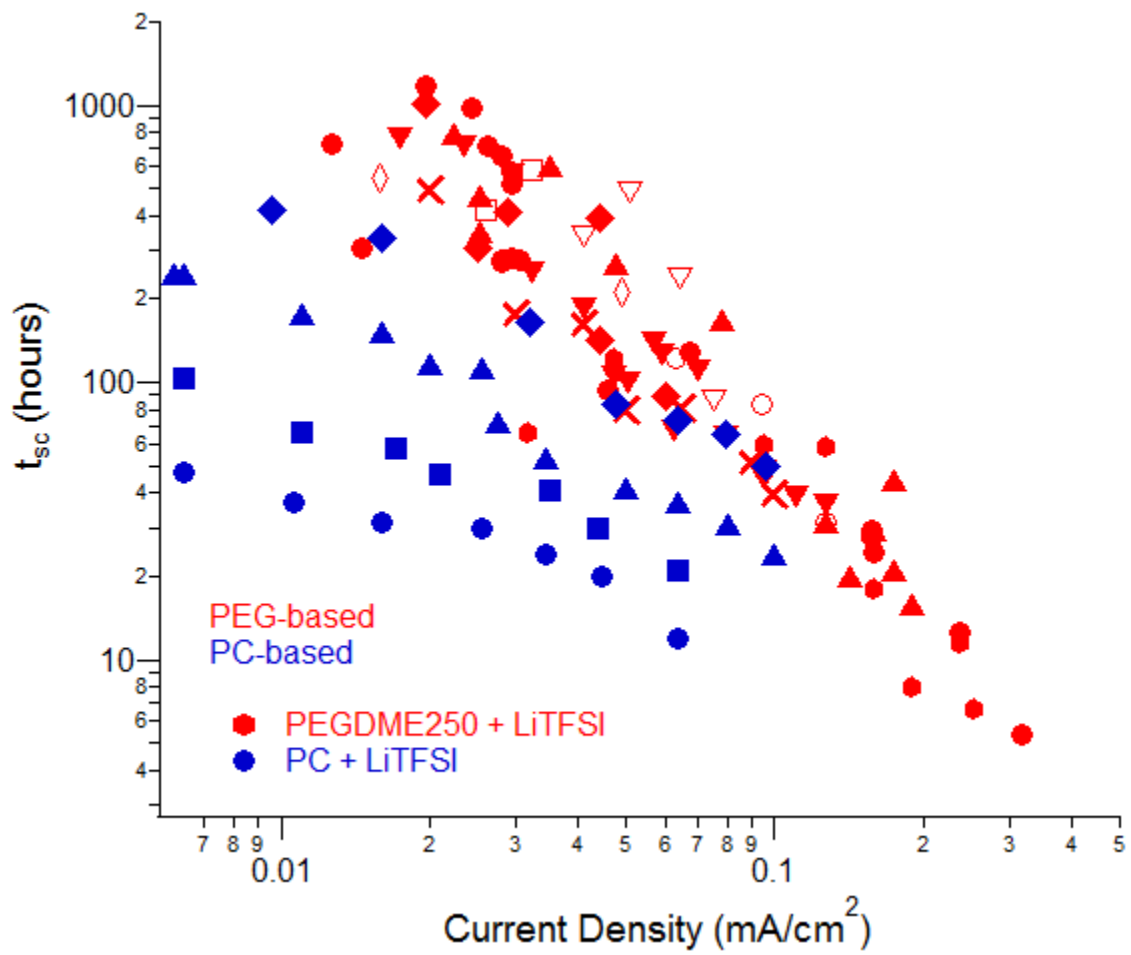


**Figure 6.8** Comparison of short-circuit times for coin cells undergoing galvanostatic polarization with PEG-based and PC-based electrolytes. Data for PC-based electrolytes published by Y. Lu, et.al.<sup>[9]</sup>

## References

- [1] M. Rosso, C. Brissot, A. Teyssot, M. Dolle, L. Sannier, J.-M. Tarascon, R. Bouchet, S. Lascaud, *Electrochimica Acta* 2006, 51, 5334.
- [2] J.-N. Chazalviel, *Physical Review A* 1990, 42, 7355.
- [3] C. Brissot, M. Rosso, J.-N. Chazalviel, S. Lascaud, *Journal of Power Sources* 1999, 81-82, 925.
- [4] M. Rosso, T. Gobron, C. Brissot, J.-N. Chazalviel, S. Lascaud, *Journal of Power Sources* 2001, 97-98, 804.
- [5] S. Liu, H. Wang, N. Imanishi, T. Zhang, A. Hirano, Y. Takeda, O. Yamamoto, J. Yang, *Journal of Power Sources* 2011, 196, 7681.
- [6] S. Liu, N. Imanishi, T. Zhang, A. Hirano, Y. Takeda, O. Yamamoto, J. Yang, *Journal of The Electrochemical Society* 2010, 157, A1092.
- [7] S. Liu, N. Imanishi, T. Zhang, A. Hirano, Y. Takeda, O. Yamamoto, J. Yang, *Journal of Power Sources* 2010, 195, 6847.
- [8] A. Johansson, A. Gogoll, J. Tegenfeldt, *Polymer* 1996, 37, 1387.
- [9] Y. Y. Lu, S. K. Das, S. S. Moganty, L. A. Archer, *Advanced Materials* 2012, 24, 4430.

## CHAPTER 7:

### STUDIES ON CROSSLINKED COPOLYMER ELECTROLYTES

In collaboration with Professor Geoffrey W. Coates and Rachna Khurana.

#### **7.1 Introduction**

Copolymers are an electrolyte platform that has garnered significant interest for use in lithium metal batteries, as previously discussed in Chapter 2. In this Chapter, I detail studies on a crosslinked copolymer electrolyte synthesized by Rachna Khurana of Professor Geoffrey Coate's research group of the Department of Chemistry and Chemical Biology of Cornell University.

All data reported here is my own work, unless otherwise noted.

The structure of the crosslinked copolymer electrolyte under investigation is shown schematically in Figure 7.1, drawing courtesy of Rachna Khurana and adapted by myself. The copolymer consists of polyethylene chains that are connected with polyethylene oxide crosslinkers. The copolymer electrolytes contain LiTFSI at a loading of 1:20 Li:EO units, and it is most likely that all of the salt resides near the polyethylene oxide chains within the electrolyte. The length of the polyethylene oxide crosslinker is varied, as well as the average spacing along the polyethylene chain between crosslinks. Some electrolyte variations also include polyethylene glycol dimethyl ether,  $M_n = 250$ , as a plasticizer in various loadings.

#### **7.2 Experimental**

The crosslinked polymer electrolyte films and a control polyethylene oxide electrolyte ( $M_n \approx 900,000$ , 1:20 LiTFSI:EO) film were cut into circular samples using a metal punch for testing.

Ionic conductivity of the electrolyte films and impedance testing of symmetric lithium coin cells was measured with a Novacontrol Dielectric spectrometer fitted with a Quatro temperature control system using gold plated electrodes from -5 to 100°C in increments of 15°C. Typically, two films (~ 200 $\mu$ m thick each) were sandwiched together for ionic conductivity measurements to improve the width of the plateau of  $\sigma'$  vs. frequency, as thinner samples underwent electrode polarization at a frequency near to that of the crossover frequency to power-law behavior of  $\sigma'$ . The resistance between the two films was found to be negligible.

Thermal transition properties of the electrolyte films were measured using differential scanning calorimetry (DSC) on a TA Instruments model Q2000.

The temperature-dependent mechanical properties of the electrolyte films were measured utilizing both dynamic mechanical analysis (DMA) in tensile film mode with a TA Instruments DMA Q800 and shear rheology with an Anton Paar MCR-301 rheometer equipped with 10 mm parallel plates. The rheometer gap was zeroed at 90°C, and the measurement gap distance was modified for each measurement to keep the normal force within an acceptable range (3-15 N).

Structure of the electrolyte films was studied by atomic force microscopy (AFM) in tapping mode with an Asylum Research MFP3D-Bio-AFM using a silicon cantilever and by Small angle X-Ray scattering (SAXS) measurements at beamline 12-ID-B, sector 12, Advanced Photon Source at Argonne National Laboratory. SAXS measurements were conducted using custom-built sample holder at 70°C using a point-collimated beam. The exposure times were limited to typically 0.5 seconds to minimize X-ray damage to the samples. SAXS measurements were conducted by Akanksha Agarwal, Rahul Mangal, and Yu Ho Wen. SAXS profiles obtained in

different locations of the same sample were identical, indicating that the profiles are representative of the entire sample

Symmetric lithium coin cells for short-circuit and impedance measurements were prepared in an argon filled MBraun glovebox using Hohsen components, size 2032, with 9.9 mm diameter lithium electrodes and a 12.7 mm diameter crosslinked electrolyte sample. The thickness of the crosslinked electrolytes was  $200 \pm 30 \mu\text{m}$ . Coin cell crimping was performed with a MTI electric crimping machine to ensure uniformity.

Galvanostatic polarization and galvanostatic cycling short-circuit measurements were performed using a Neware CT-3008 battery tester with wiring into (Fisher Scientific and VWR) convection ovens to maintain  $T \approx 90^\circ\text{C}$ , unless otherwise specified. Galvanostatic cycling test protocol was repeated three hour charge and three hour discharge at the reported current densities, with no rest periods. Galvanostatic polarization measurements were a continual charge at the specified current density until short-circuit.

Scanning electron microscopy (SEM) images of the lithium electrodes following short-circuit testing were obtained on a Zeiss LEO 1550 FE-SEM. The coin cells were opened post-battery testing in an argon glovebox and put into double sealed plastic bags. The harvested electrodes were transported to the SEM in these argon-filled bags, removed from the bags and placed on the sample holder, and then put into the imaging chamber and under vacuum. Transfer time in the air is estimated at less than 60 seconds maximum.

### 7.3 Results and Discussion

Table 7.1 summarizes the properties of the dry crosslinked electrolytes under investigation, and Table 7.2 summarizes properties of a set of plasticized crosslinked electrolytes. Composition

labeling is as follows:  $^a\text{PEOX}^{b,c}\text{PE}^d\text{PEG}$  (x:y:z), where a is the average number of ethylene oxide (EO) units in the crosslinker, b is the average number of ethylene units between crosslinks, c is the average theoretical length of the polyethylene chain backbone as computed from catalyst loading, d is the average number of EO units in the polyethylene glycol dimethyl ether plasticizer, x is the weight percentage of PEOX, y is the weight percentage of PE, and z is the weight percentage of PEG. In cases where the film does not contain plasticizer, d and z are omitted.

The ionic conductivity of a series of electrolytes with an average of 33 PE units between PEO crosslinkers of varied lengths is displayed in Figure 7.1. The data points are the measured data, and the lines are fits to Arrhenius and VFT temperature dependence at low and high temperatures, respectively. The known  $T_m$  values obtained from DSC, as displayed in Table 7.1, were used to determine appropriate temperature ranges to apply the two fits. An optimum crosslinker length exists in terms of ionic conductivity of the copolymer electrolytes. Relatively long crosslinkers lengths afford high conductivity at high temperatures, but low conductivity at ambient temperatures due to crystallization of the PEO. At very short crosslinker lengths, crystallinity is suppressed but ionic conductivity is reduced at all temperatures due to reduced segmental motion as a result of chain constraint. At the optimum crosslinker length, similar high conductivity is achieved at elevated temperatures and enhanced conductivity persists at ambient temperatures due to decreased crystallinity. This behavior is analogous for that reported in Chapter 4 for all-solid-state hybrid electrolytes with varying chain lengths, though the optimum PEO chain length is longer for the copolymer electrolytes due to constraint of the chain at both ends rather than just one. Furthermore, data from DSC shows that a melt transition does indeed

**Table 7.1** Composition and properties of unplasticized, crosslinked electrolytes

Composition	T <sub>g</sub> (°C)*	T <sub>m1</sub> (°C)*, <sup>a</sup>	T <sub>m2</sub> (°C)*, <sup>β</sup>	σ at 25°C (S/cm)	σ at 90°C (S/cm)
<sup>40</sup> PEOX <sup>17,16600</sup> PE (55:45)	-44	---	89	8.3 x 10 <sup>-6</sup>	3.1 x 10 <sup>-4</sup>
<sup>40</sup> PEOX <sup>23,14000</sup> PE (50:50)	-45	---	82	9.0 x 10 <sup>-6</sup>	3.6 x 10 <sup>-4</sup>
<sup>40</sup> PEOX <sup>33,10800</sup> PE (42:58)	-45	---	61	5.2 x 10 <sup>-6</sup>	1.9 x 10 <sup>-4</sup>
<sup>80</sup> PEOX <sup>17,31500</sup> PE (74:26)	-48	25	74	3.1 x 10 <sup>-5</sup>	7.3 x 10 <sup>-4</sup>
<sup>80</sup> PEOX <sup>23,24800</sup> PE (69:31)	-50	26	88	2.8 x 10 <sup>-5</sup>	8.7 x 10 <sup>-4</sup>
<sup>80</sup> PEOX <sup>33,18800</sup> PE (62:38)	-49	23	94	2.3 x 10 <sup>-5</sup>	7.0 x 10 <sup>-4</sup>
<sup>80</sup> PEOX <sup>33,8960</sup> PE (60:40)	-50	16	103	3.2 x 10 <sup>-5</sup>	5.0 x 10 <sup>-4</sup>
<sup>130</sup> PEOX <sup>17,27500</sup> PE (83:17)	-38	38	97	7.4 x 10 <sup>-6</sup>	7.8 x 10 <sup>-4</sup>
<sup>130</sup> PEOX <sup>23,37400</sup> PE (79:21)	-39	37	103	8.4 x 10 <sup>-6</sup>	7.7 x 10 <sup>-4</sup>
<sup>130</sup> PEOX <sup>33,49200</sup> PE (73:27)	-38	39	111	8.2 x 10 <sup>-6</sup>	8.7 x 10 <sup>-4</sup>

\* DSC measurements were performed by both J. L. Schaefer and R. Khurana

<sup>a</sup> T<sub>m</sub> of polyethylene oxide domain

<sup>β</sup> T<sub>m</sub> of polyethylene domain

**Table 7.2** Composition and properties of selected plasticized, crosslinked electrolytes

Sample	T <sub>g</sub> (°C)*	T <sub>m1</sub> (°C)*, <sup>a</sup>	T <sub>m2</sub> (°C) * <sup>,β</sup>	σ at 90°C (S/cm)	G' at 90°C (Pa)	R <sub>int</sub> at 90°C (Ω·cm <sup>2</sup> )
<sup>80</sup> PEOX <sup>33,89</sup> PE (60:40)	-50	16	103	5.0 x 10 <sup>-4</sup>	0.27	11.5
<sup>80</sup> PEOX <sup>33,89</sup> PE <sup>5</sup> PEG (50:33:17)	-54	15	91	9.6 x 10 <sup>-4</sup>	0.18	10.9
<sup>80</sup> PEOX <sup>33,88</sup> PE <sup>5</sup> PEG (45:30:25)	-57	16	97	1.0 x 10 <sup>-3</sup>	0.12	7.7
<sup>80</sup> PEOX <sup>33,88</sup> PE <sup>5</sup> PEG (41:27:32)	-61	18	95	1.9 x 10 <sup>-3</sup>	0.11	4.7
<sup>80</sup> PEOX <sup>33,96</sup> PE <sup>5</sup> PEG (36:24:40)	-65	14	96	2.1 x 10 <sup>-3</sup>	0.11	4.2

\* DSC measurements were performed by both J. L. Schaefer and R. Khurana

<sup>a</sup> T<sub>m</sub> of polyethylene oxide domain

<sup>β</sup> T<sub>m</sub> of polyethylene domain

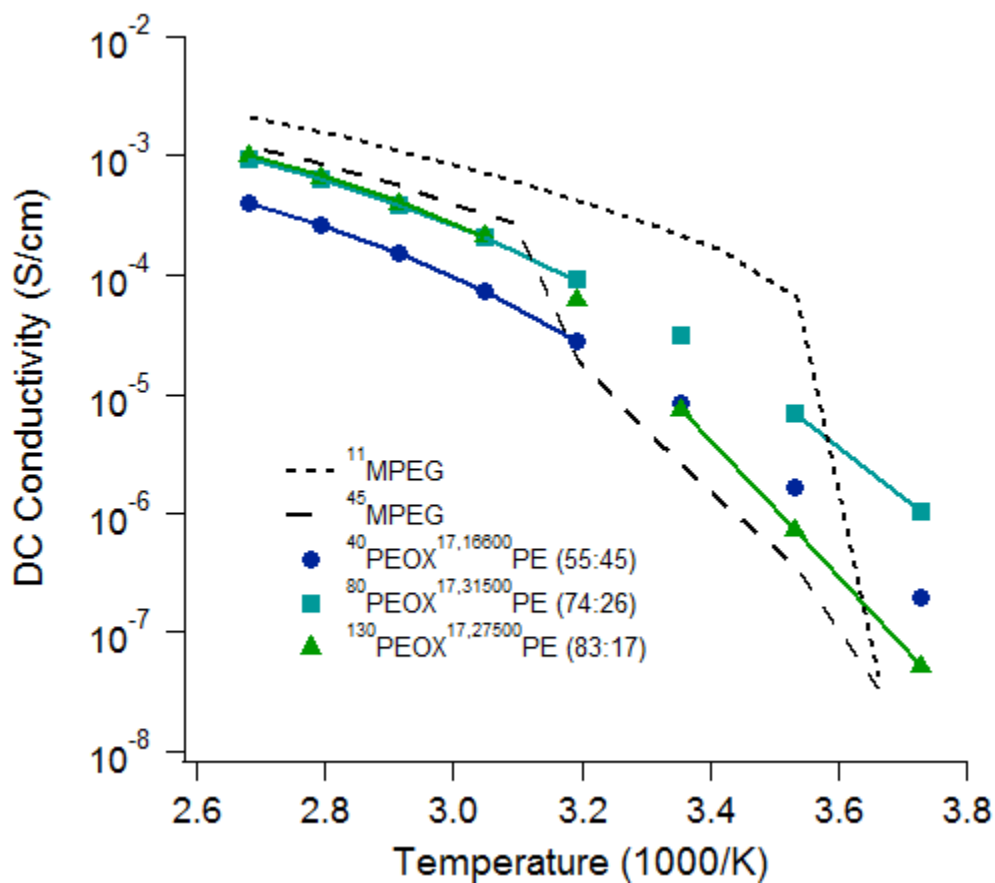


**Figure 7.1** Ionic conductivity of the crosslinked PE-EO electrolytes as a function of crosslinker length. Lines show fits to the VTF and Arrhenius temperature dependency models.

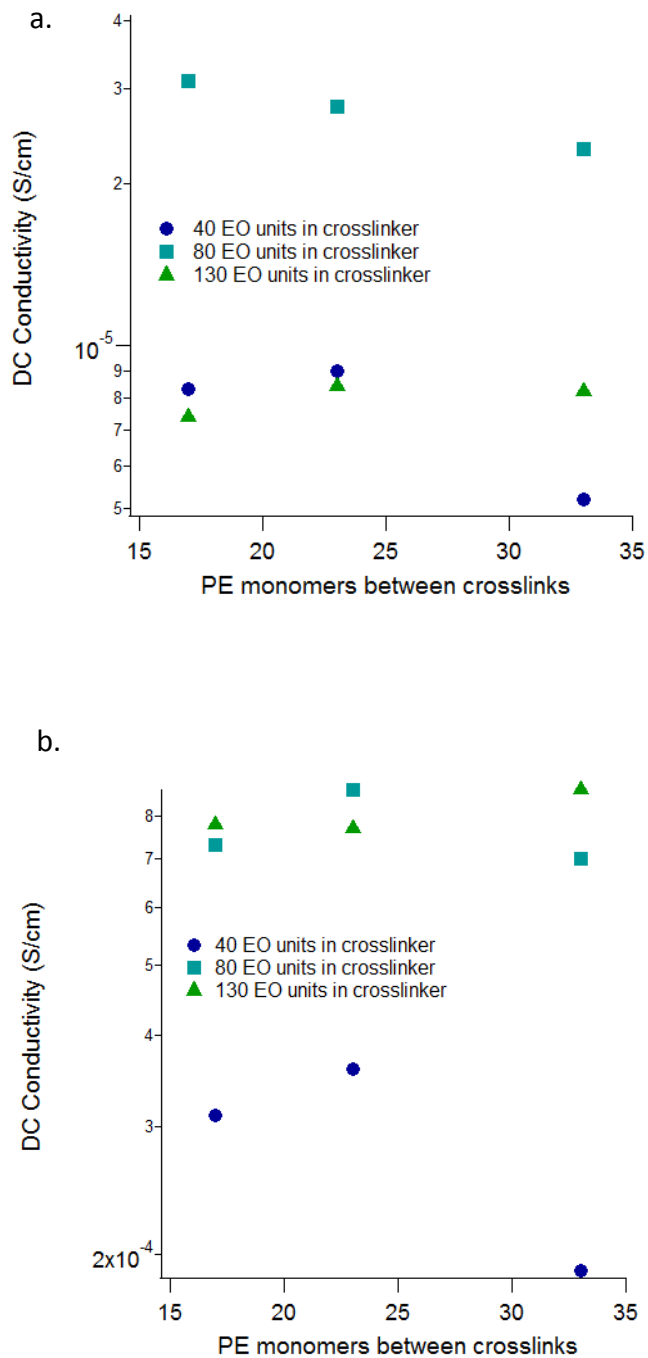


**Figure 7.2** Ionic conductivity of the dry crosslinked electrolytes as a function of PEO crosslinker length and number of PE units between crosslinks at a. 25°C and b. 90°C.

exist at 23°C for the  $^{80}\text{PEOX}^{33,18800}\text{PE}$  (62:38) electrolyte, but the activation energy of the Arrhenius ionic conductivity for this sample is much lower than for the  $^{130}\text{PEOX}^{33,49200}\text{PE}$  (73:27) electrolyte with the long crosslinker length. The relationship of crosslinker length to ionic conductivity persists with changes in the PE spacing between crosslinks, as displayed in Figure 7.2.

The thermal properties of the electrolytes were measured with differential scanning calorimetry. These properties are summarized in Table 7.1 for all of the studied samples. Figure 7.3 displays the glass transition temperatures of the dry crosslinked electrolytes as a function of composition. Electrolytes containing PEO crosslinkers of an optimum length for ionic conductivity, 80 monomers, have the lowest glass transition temperatures in comparison with electrolytes containing either longer or shorter PEO crosslinkers. The effect of spacing of the crosslinkers along the PE backbone has a relatively low effect on the glass transition temperature.

Increase in the conductivity of the crosslinked electrolytes may be facilely achieved with the addition of oligomeric plasticizer. Figure 7.4 shows the conductivity for the series of plasticized copolymer electrolytes defined in Table 2.

Mechanical properties of the copolymer electrolytes were studied using both DMA and rheology. DMA was an easier method for obtaining mechanical property information over a very wide temperature range, however, the low moduli of the films at the main temperature of the electrochemical testing (90°C) prevented accurate data collection at these elevated temperatures. Furthermore, DMA measurements were difficult to perform on the dry crosslinked films due to difficulty in clamping the samples. Rheological measurements proved more reliable at ambient to elevated temperatures than DMA, and results for the electrolytes defined in Table 2 are

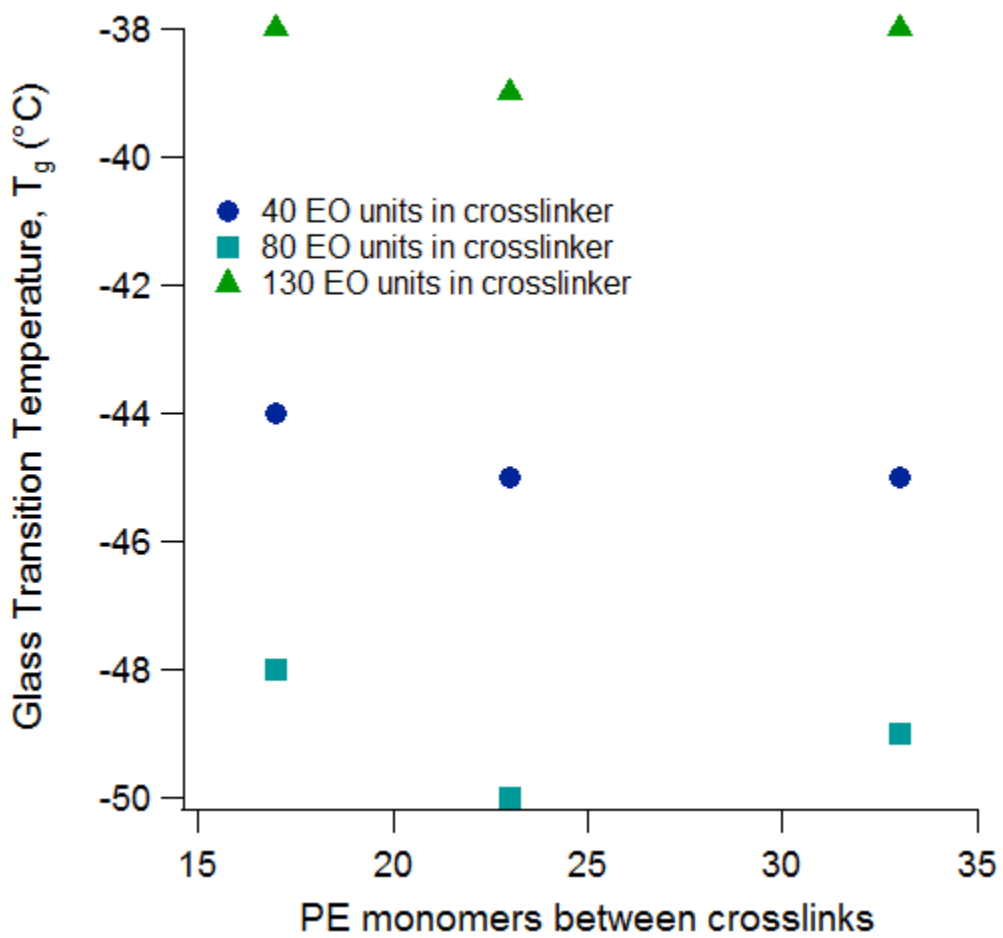


**Figure 7.3** Glass transition temperatures of the dry crosslinked electrolytes as a function of composition.

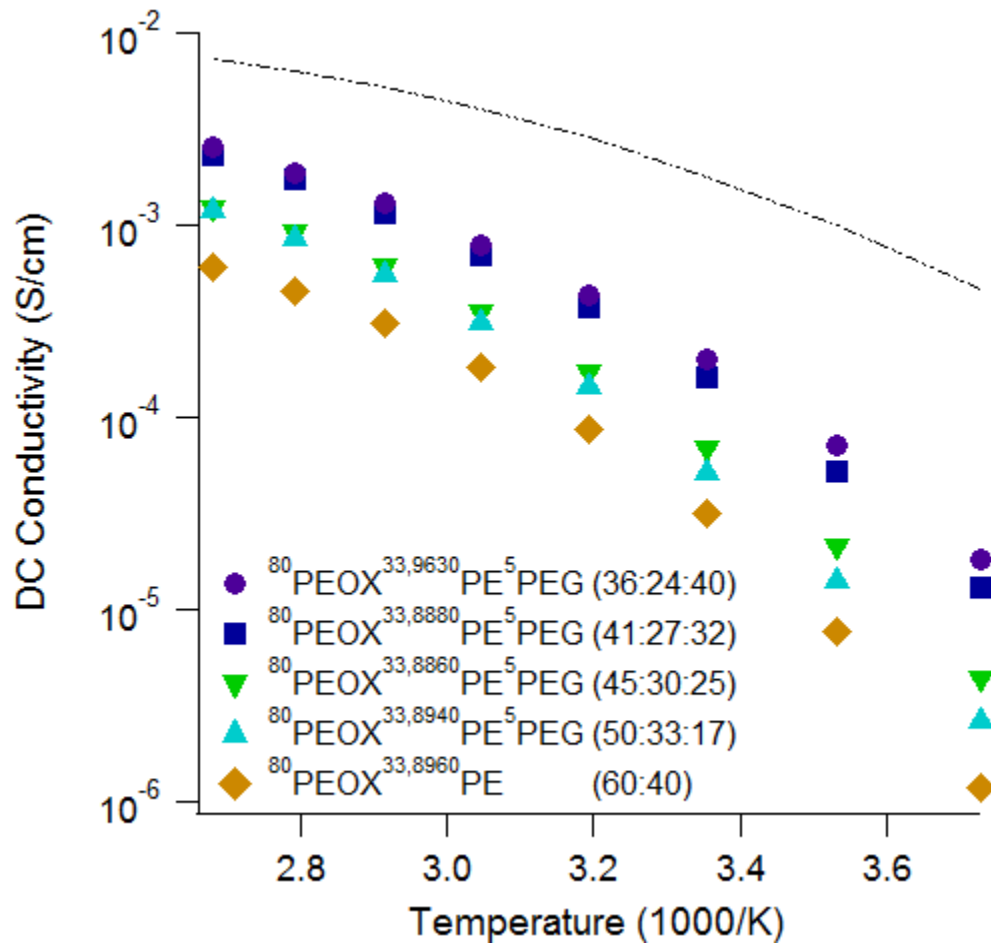


**Figure 7.4** Ionic conductivity of electrolytes with the  $^{80}\text{PEOX}^{33,8960}\text{PE}$  (60:40) crosslinked matrix and varying amounts of plasticizer. Dotted line shows the ionic conductivity of the pure plasticizer with LiTFSI for comparison.

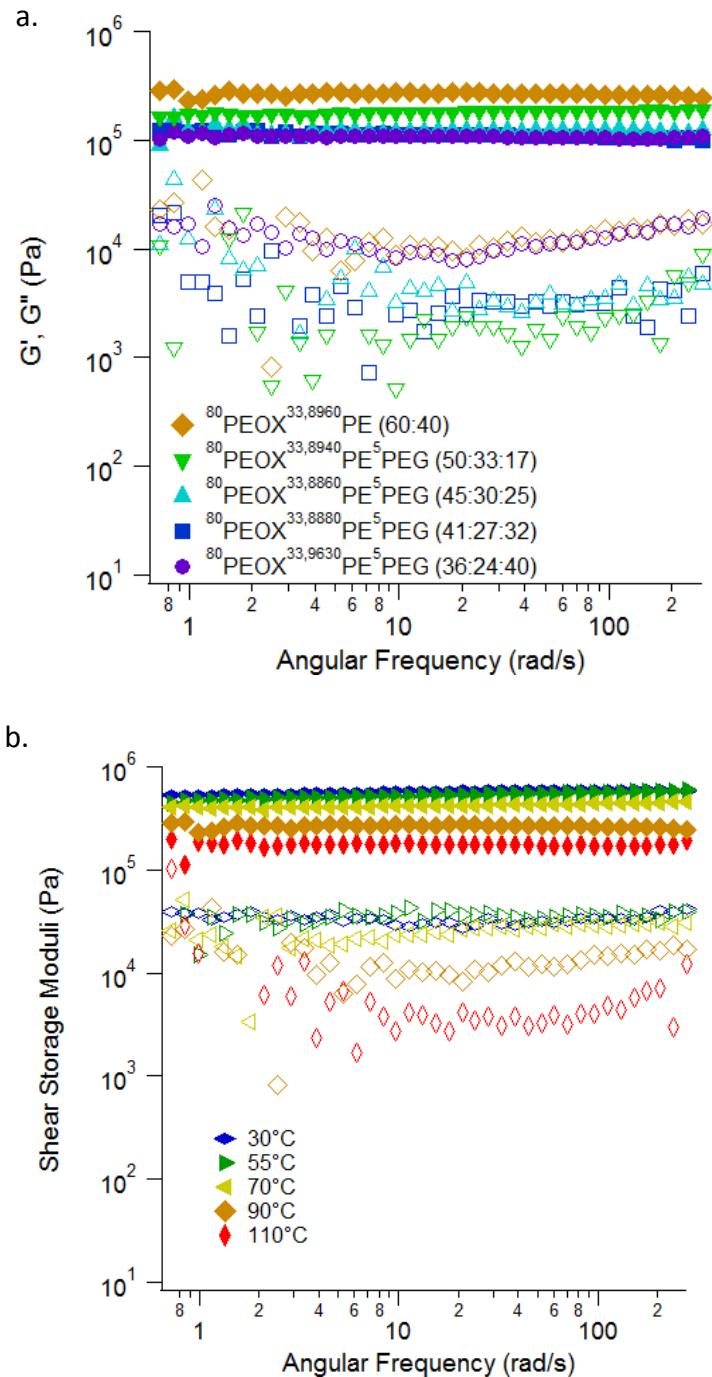


**Figure 7.5** Storage moduli,  $G'$  (closed symbols), and loss moduli,  $G''$  (open symbols), of the crosslinked electrolytes as determined by shear rheology at low strain (0.1%) as a function of frequency and a. as a function of composition at 90°C, b. as a function of temperature for sample  $^{80}\text{PEOX}^{33,8960}\text{PE}$  (60:40).

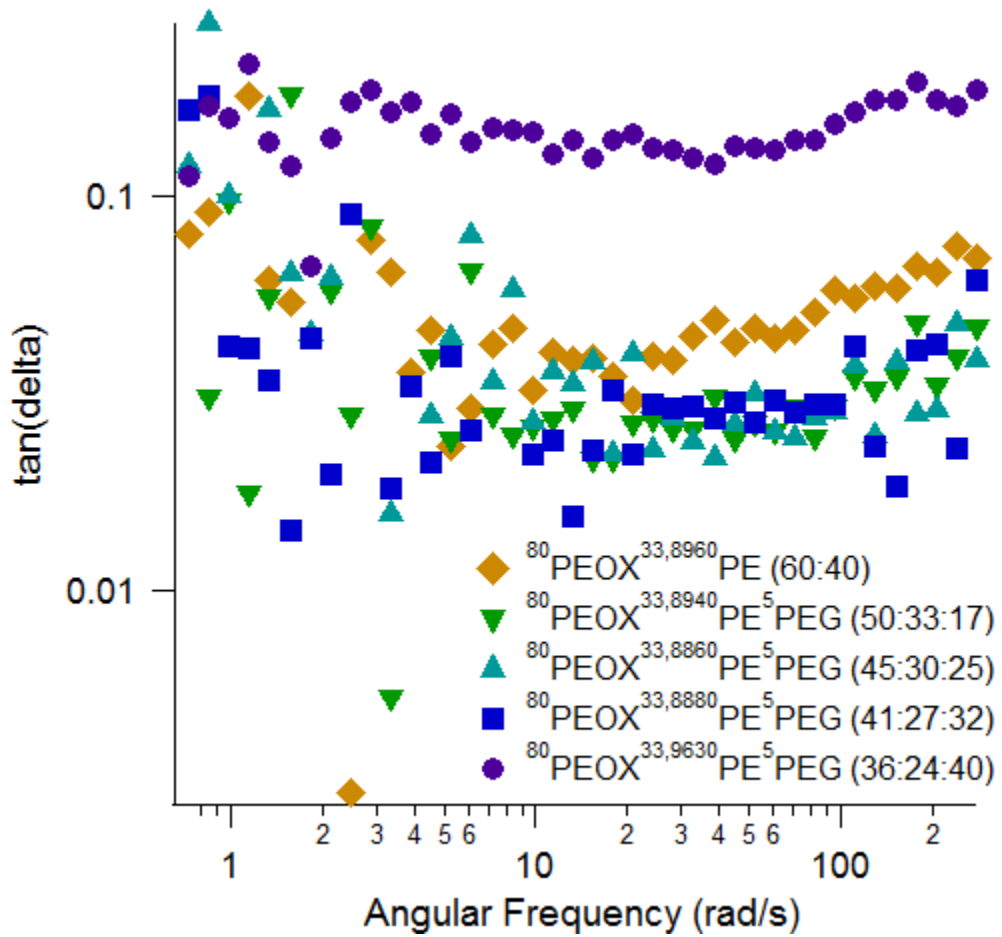


**Figure 7.6** The  $\tan(\delta) = G''/G'$  as determined by shear rheology as a function of frequency and composition at 90°C.

displayed in Figure 7.5. However, rheological measurements were difficult to perform on some compositions of the dry or moderately plasticized crosslinked films, likely due to a lack of tackiness and good adhesion between the sample and the fixture. At 90°C, the shear storage modulus G' of the tested crosslinked electrolytes fell in the range of 0.1 – 0.5 MPa. The function  $\tan(\delta) = G''/G'$  as determined from shear rheology is shown in Figure 7.6 as a function of composition; the magnitude of  $\tan(\delta)$  for the highly plasticized sample is markedly higher than the others. In the literature, low  $\tan(\delta)$  is related to higher crosslinking efficiency,<sup>[1]</sup> thus it is likely that the effectiveness of the crosslinking reaction was inhibited at plasticizer loadings of 40% and above.

The structure of the crosslinked copolymer films was studied via AFM and SAXS. Representative AFM images of electrolyte  $^{80}\text{PEOX}^{33,8960}\text{PE}$  (60:40) at four different sample locations are displayed in Figure 7.8. Most of the images contain a significant amount of noise, likely due to the cantilever tip sticking to the sample. However, it is obvious from comparison of the amplitude images (Fig. 7.8a-d) and phase images (Fig. 7.8e-h), that the electrolytes are phase segregated. This is expected, as two different melting temperatures were observable in DSC for this composition. Specifically, regions that are darker in the phase images, relating to a shorter lag time for the mechanical response, are most likely that of the PE domains whereas the remaining, continuous phase is that of PEO. SAXS was then utilized to obtain more comprehensive data on the electrolyte structure.

Figure 7.9 displays the scattering signal intensity versus wavevector ( $q$ ) profiles for the dry crosslinked electrolytes defined in Table 1 as obtained from SAXS. Between electrolytes with the same PEOX length and similar PE extent of polymerization, increases in the crosslinker

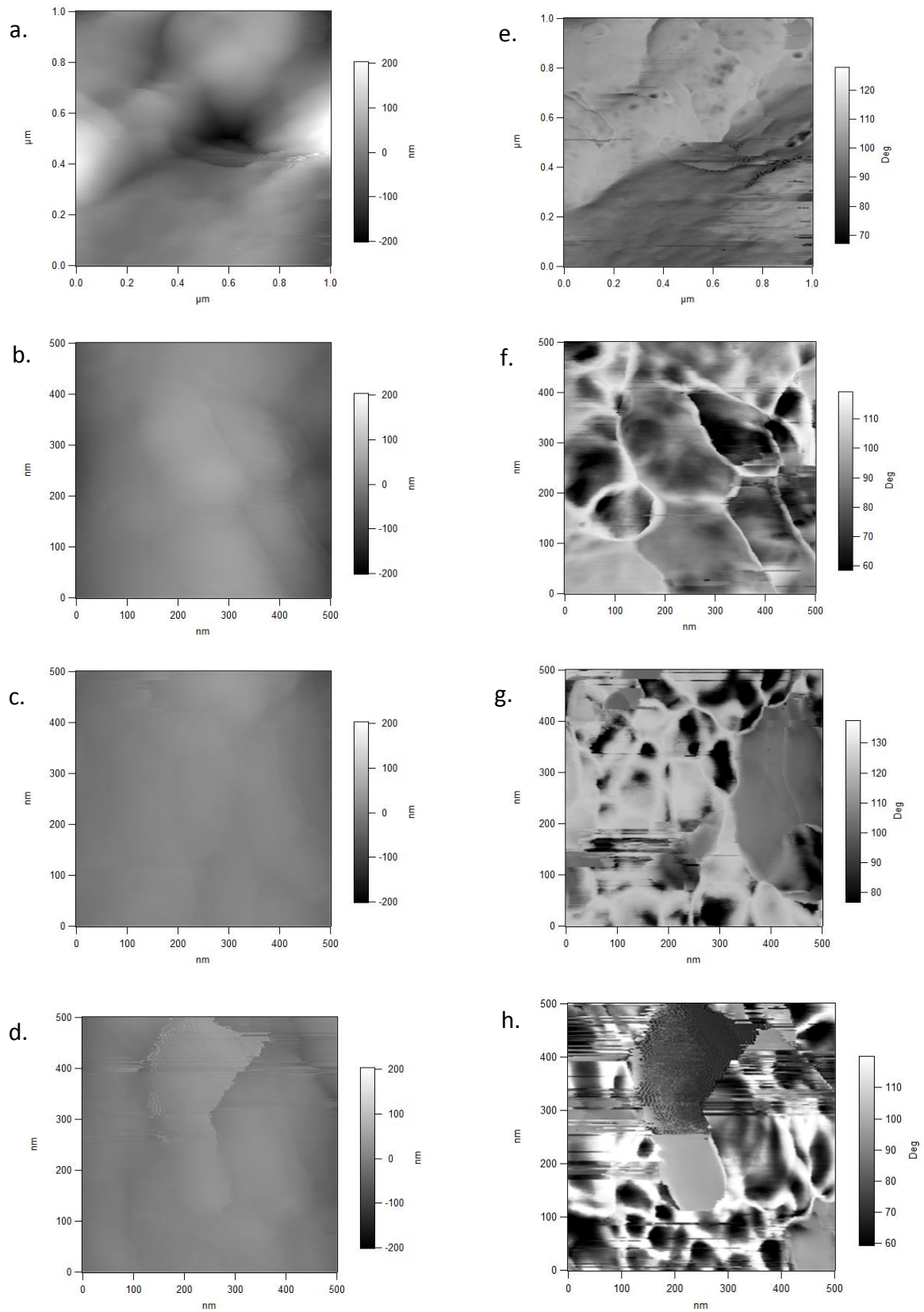


**Figure 7.8** AFM images of  $^{80}\text{PEO}X^{33,8960}\text{PE}$  (60:40) in locations 1-4: a. amplitude, b. phase.

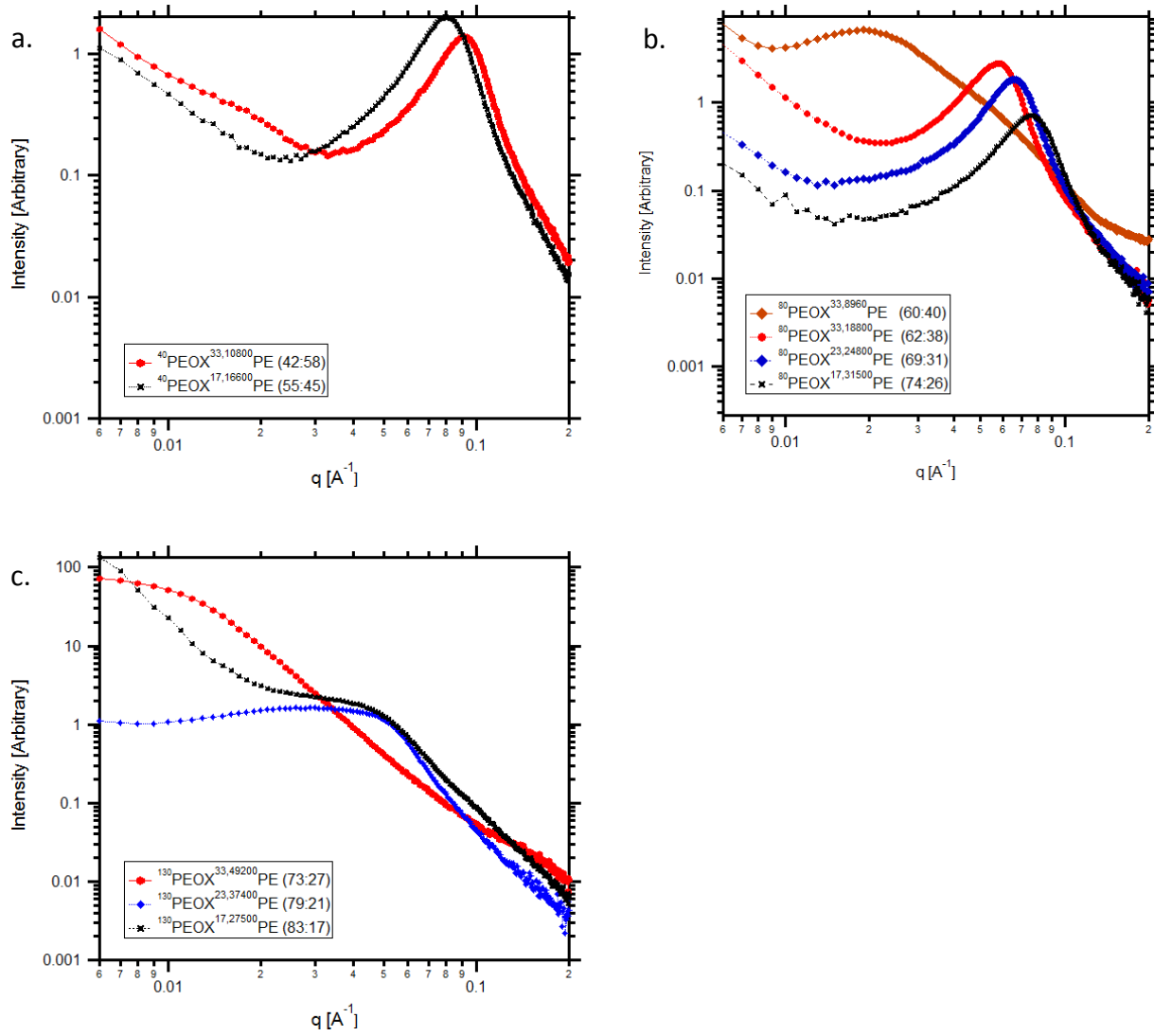


**Figure 7.9** Small Angle X-ray Scattering (SAXS) profiles of scattering single intensity as a function of wavevector ( $q$ ) for sample dry crosslinked electrolytes with PEO crosslinkers of a. 40, b. 80, and c. 130 monomers.

density (thus increase in the PEOX fraction and decrease in the PE length between crosslinks) led to a reduction in a characteristic length-scale related to the scatterer, as noted by the shift in the peak to higher wavevectors. It is most likely that this characteristic length scale is representative of the PE domain size. Notably, it is also apparent from Figure 7.9b that the extent of PE polymerization has a significant influence on the resulting membrane structure, as seen from comparison of data obtained from  $^{80}\text{PEOX}^{33,8960}$ PE (60:40) and  $^{80}\text{PEOX}^{33,18800}$ PE (62:38). Electrolyte  $^{80}\text{PEOX}^{33,8960}$ PE (60:40) has a very broad peak in the scattering profile, which is not surprising given the large distribution in domain sizes observed via AFM. In contrast, electrolyte  $^{80}\text{PEOX}^{33,18800}$ PE (62:38) provides a much narrower peak that is significantly shifted to larger wavevectors, or smaller size. The SAXS data obtained for the electrolytes defined in Table 7.2 in displayed in Figure 7.10. Increasing amounts of the EO-based plasticizer resulted in a narrower peak that is shifted to smaller sizes, indicating smaller, more uniform distribution of PE domains.

Impedance spectra of symmetric lithium coin cells containing the crosslinked electrolytes are displayed in Figure 7.11 as a function of electrolyte composition and temperature. Figure 7.12 provides a summary of the extracted bulk and overall interfacial resistances, where the bulk resistance was taken to be the first intercept at the x-axis, and the interfacial resistance was taken to be the width of the impedance hemisphere. Impedance values are acceptably low. Notably, the interfacial impedance in the cells is even lower than the bulk resistance at high temperatures.

Electrochemical stability of the crosslinked electrolytes when in contact with lithium metal was tested via cyclic voltammetry of a symmetric lithium coin cell containing the crosslinked electrolytes. Figure 7.13 shows a representative voltammogram, indicating that the electrolytes are stable from -0.1 to about 7 V vs.  $\text{Li}^+/\text{Li}$  when in contact with lithium metal.

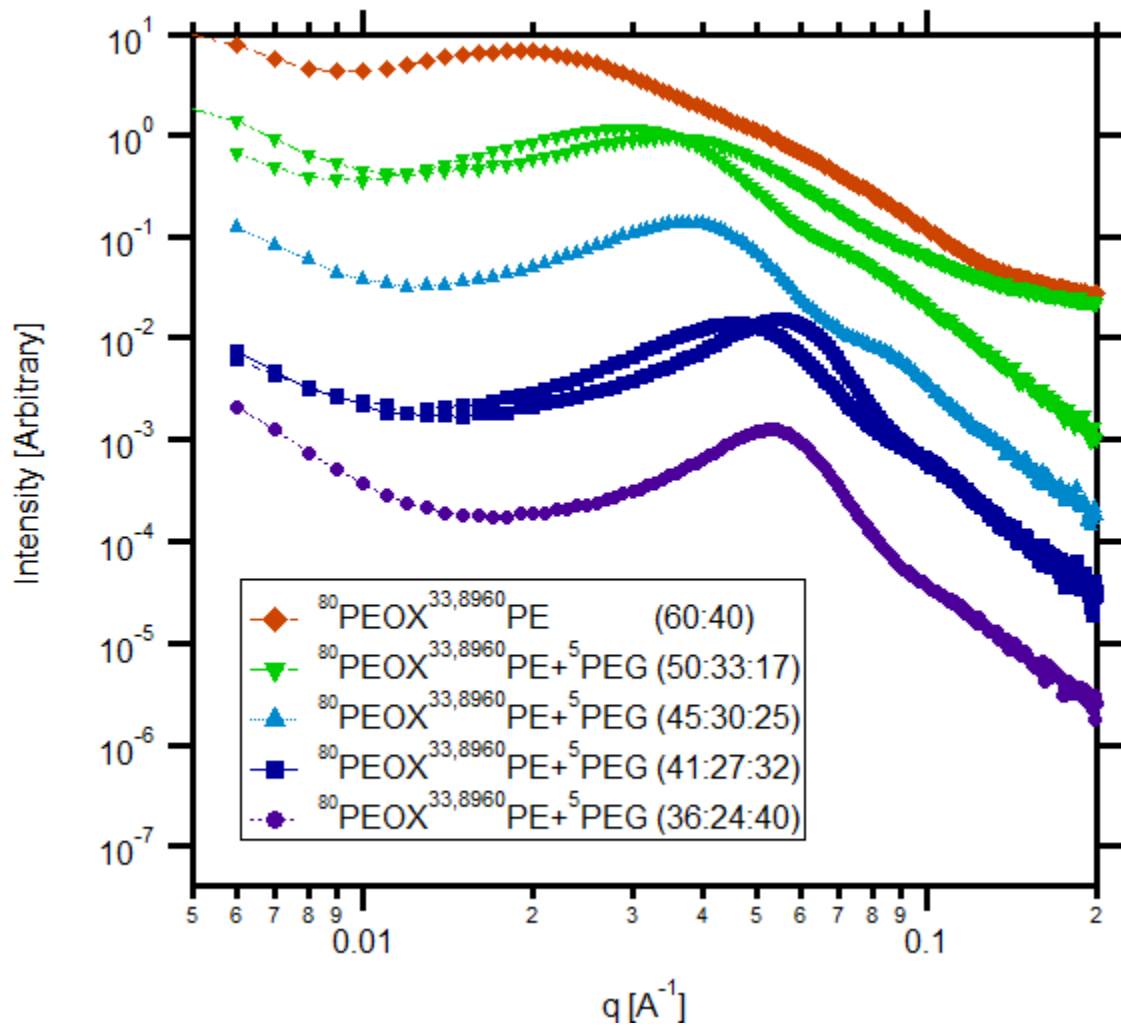


**Figure 7.10** Small Angle X-ray Scattering (SAXS) profiles of scattering single intensity as a function of wavevector ( $q$ ) for electrolyte  $^{80}\text{PEOX}^{33,8960}\text{PE}$  (60:40) and plasticized electrolytes with the same crosslinked matrix composition. In cases where multiple profiles are shown for a given composition, the samples tested were synthesized in different batches.

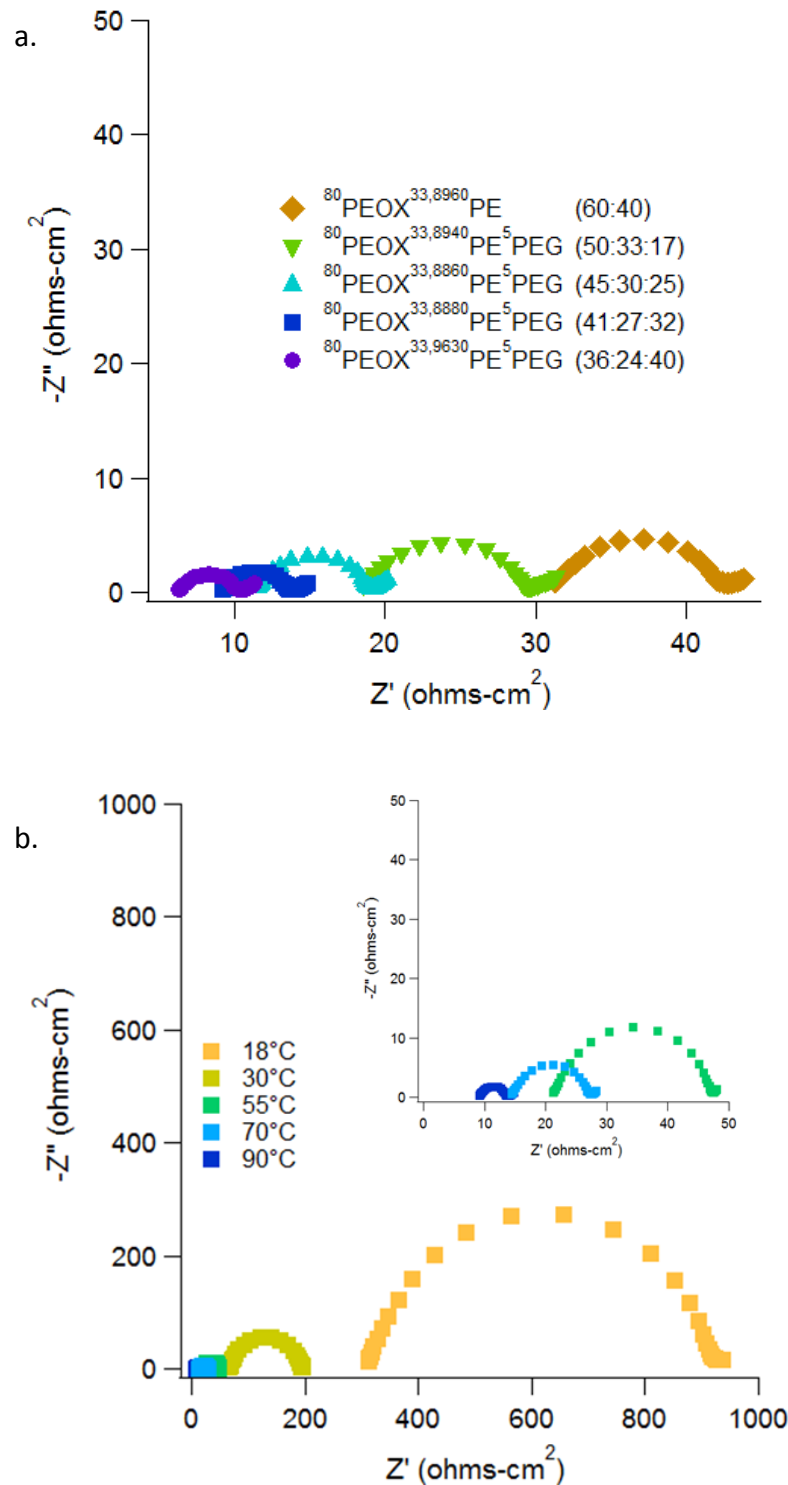


**Figure 7.11** Impedance of Li/crosslinked electrolyte/Li cells as a function of a. composition at 90°C and b. temperature with electrolyte composition  $^{80}\text{PEOX}^{33,8880}\text{PE}^5\text{PEG}$  (41:27:32).

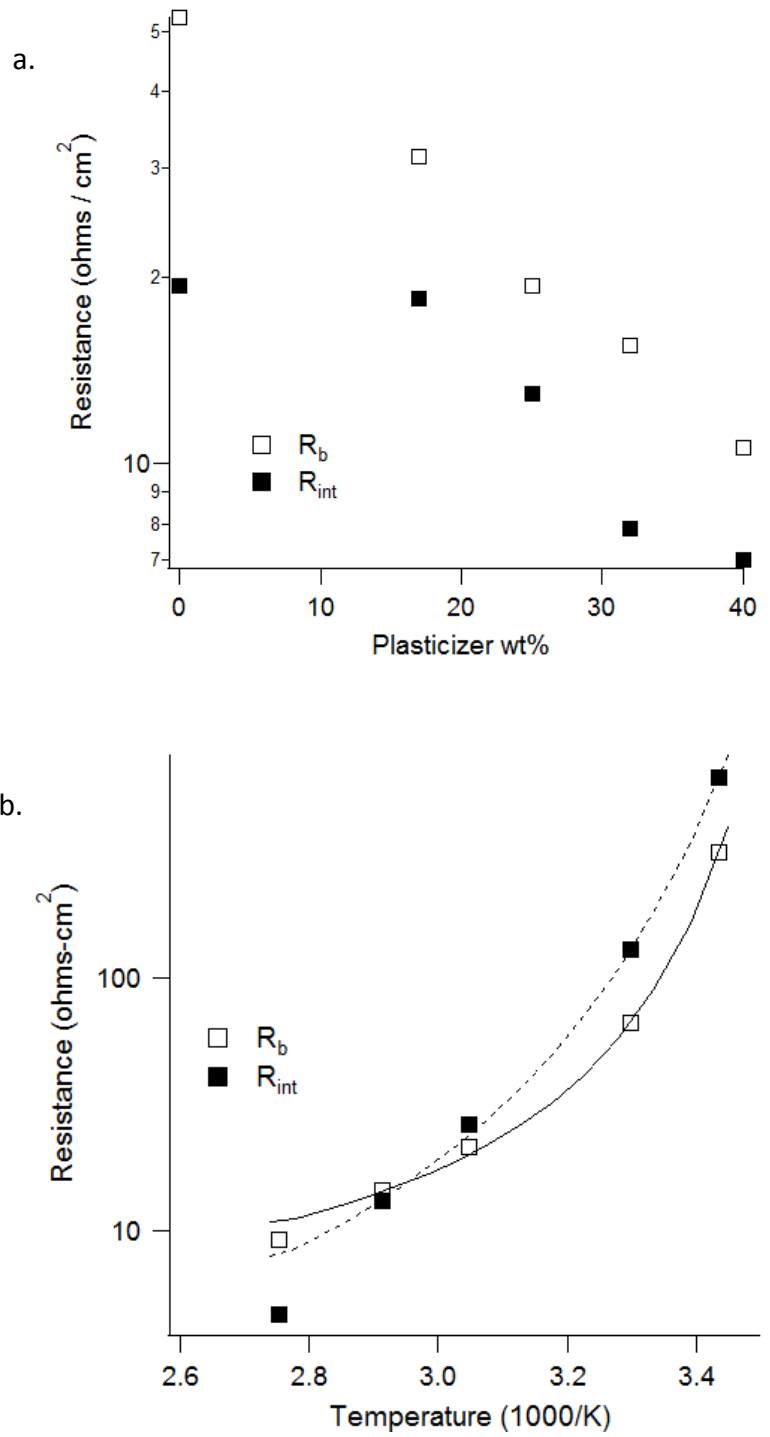


**Figure 7.12** Summary of the bulk and total interfacial resistances in the Li/crosslinked electrolyte/Li coin cells as a function of a. composition at 90°C and b. temperature with electrolyte composition  $^{80}\text{PEOX}^{33,8880}\text{PE}^5\text{PEG}$  (41:27:32). Lines are VTF fits to the data.

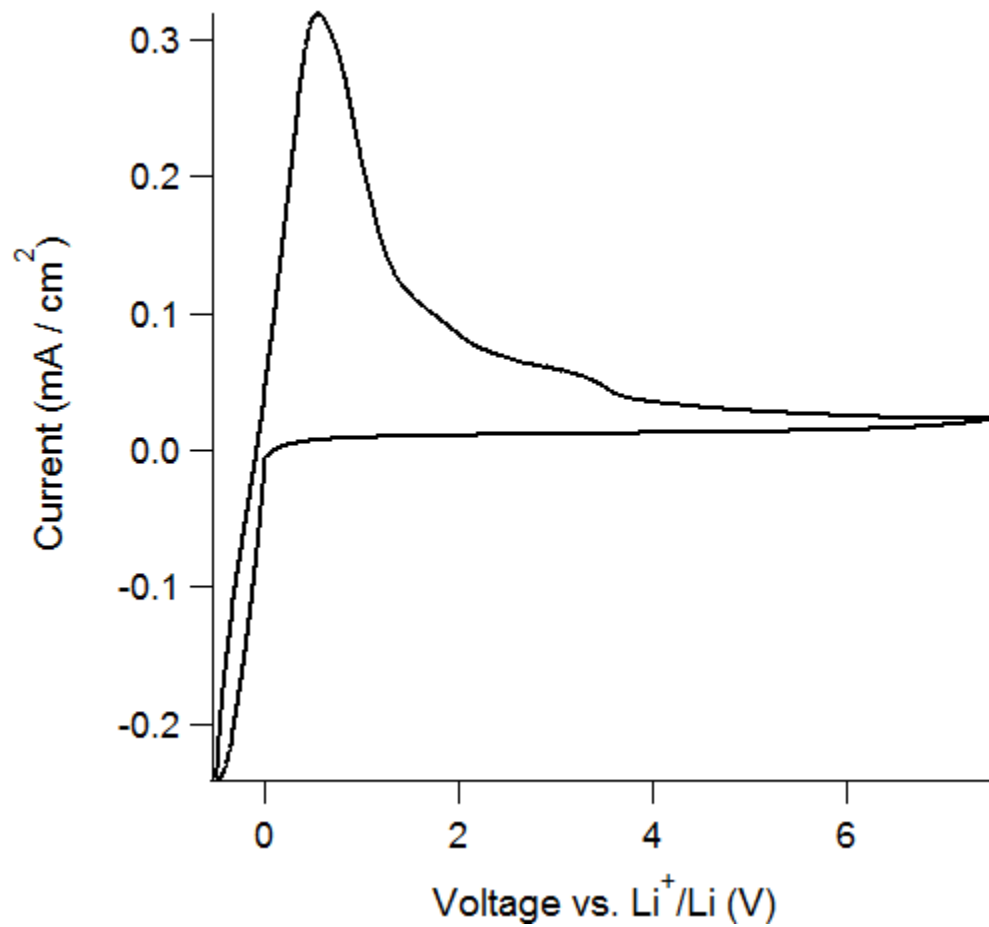


**Figure 7.13** Cyclic voltammetry of a Li/  $^{40}\text{PEOX}^{33,11000}\text{PE}^5\text{PEG}$  (28:40:32) /Li cell showing the electrochemical stability window (-0.1 V to 7 V) of the electrolyte when in contact with lithium metal.

The effectiveness of the electrolytes defined in Table 2 in uniformly plating lithium metal was tested via both the galvanostatic polarization and galvanostatic cycling methods. Upon galvanostatic polarization of a symmetric lithium coin cell containing a crosslinked electrolyte, a very stable potential was maintained. At long times, cell failure was observed by two different mechanisms displayed in Figure 7.14: a divergence in the potential as a result of running out of the source lithium electrode for plating (7.14a) or a sharp drop in the potential as a result of short-circuit by a dendrite (7.14b).

Nearly all cells galvanostatically polarized at  $0.26 \text{ mA/cm}^2$  ran out of lithium counter electrode, thus ceasing to function due to the first mechanism, when the typical Li electrode was used. Obtaining time-to-short-circuit ( $t_{sc}$ ) data points at this current density required layering of multiple foils to create a thicker Li electrode for stripping.

The time-to-short-circuit values for cells undergoing galvanostatic polarization over a range of current densities with crosslinked electrolytes containing varying amounts of plasticizer are displayed in Figure 7.15, along with results from a solid PEO electrolyte and the lifetime predictions from Equation 6.1 for cells containing selected electrolytes. In most cases the observed cell lifetime is an order of magnitude greater than the lifetimes predicted by Equation 6.1. In comparison, the lifetimes of cells containing the solid PEO electrolyte are low and more scattered. Testing of the dry crosslinked electrolyte was limited as the low threshold current density, due to the membrane's lower relative ionic conductivity. The dry crosslinked electrolyte still exhibited very long cell lifetime close to the maximum operating current density. In general, stiffer electrolytes containing less plasticizer resulted in longer cell lifetimes. This trend is not observable at the lowest measured current density,  $J = 0.26 \text{ mA/cm}^2$ , however, there

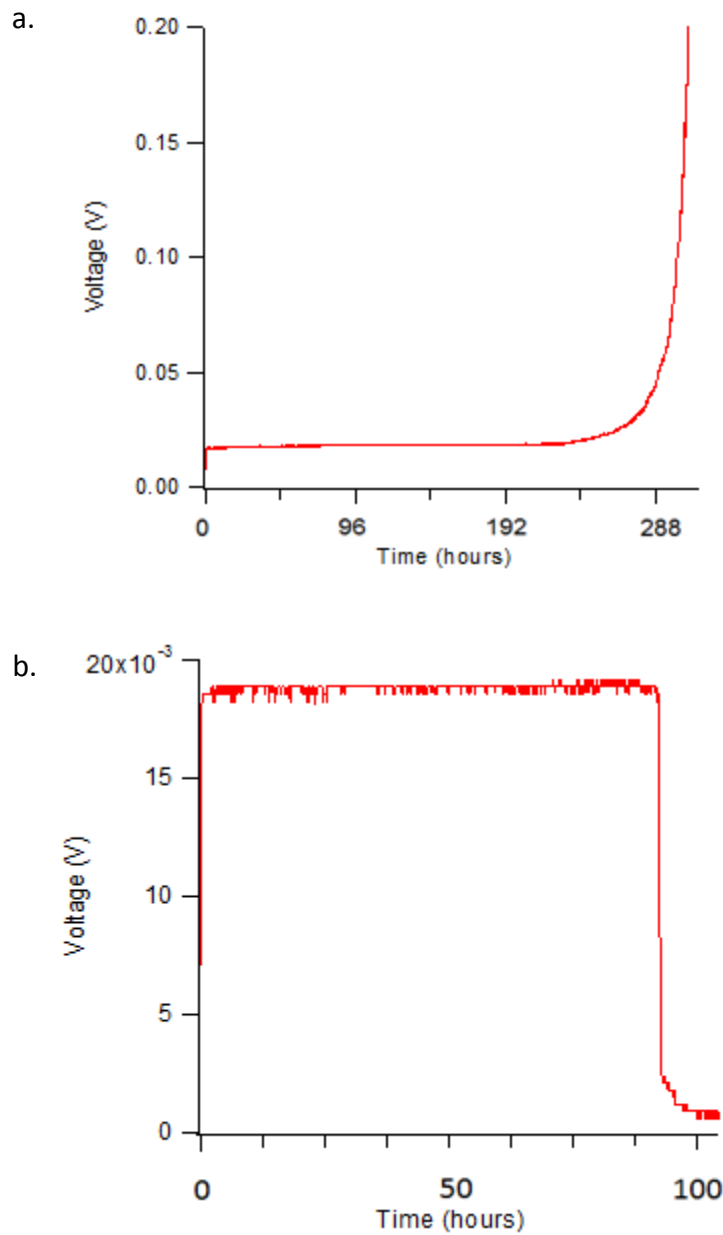


**Figure 7.14** Typical voltage profiles for Li/crosslinked electrolyte/Li cells undergoing galvanostatic polarization and failing due to a. plating entire Li counter-electrode or b. short-circuit.

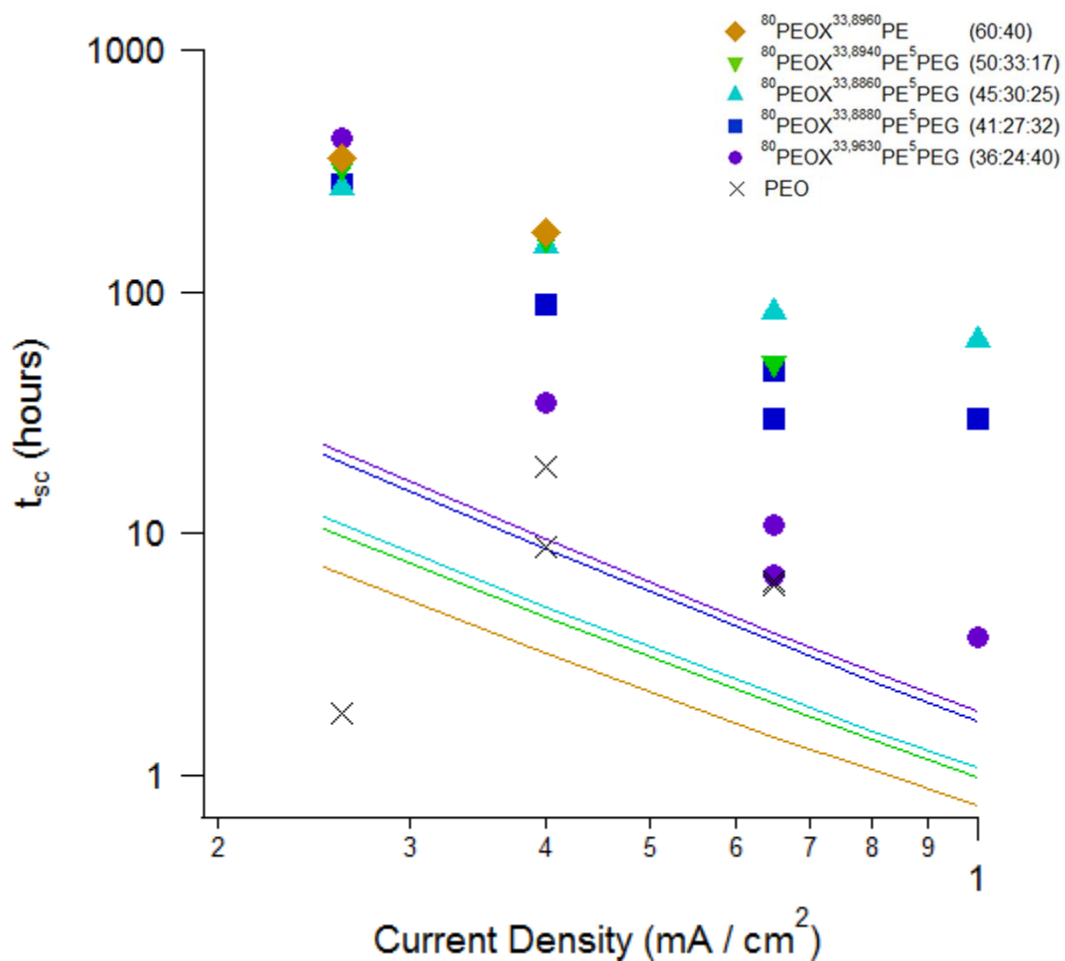


**Figure 7.15** Short-circuit times of Li/crosslinked electrolyte/Li cells undergoing galvanostatic polarization as a function of applied current density. The predicted lifetimes from Equation 6.1 are shown as lines, and for comparison, the short-circuit results for Li/PEO/Li cells.

may be larger scatter in the data at this current density as much thicker Li foils had to be utilized for the testing.

A typical voltage profile for the galvanostatic cycling tests is shown in Figure 7.15. As the lithium metal is shuttled back and forth between the two electrodes for this test, thickness of the electrodes was not a limitation. In comparison with the galvanostatic polarization tests, the galvanostatic cycling tests were much longer until completion. Figure 7.16 displays the total time until short-circuit ( $t_{sc}$ ) as well as the charge passed until short-circuit ( $C_d = t_{sc} \times J$ ) for galvanostatically cycled cells containing the crosslinked and standard PEO electrolytes as a function of applied current density. Use of the dry electrolyte resulted in increased lifetime in comparison with that of the plasticized electrolyte. In all of the testing, a single anomalous PEO cell also exhibited an enhanced lifetime.

Figure 7.16 also displays data published by Balsara, et al.<sup>2</sup> obtained by galvanostatically cycling using similar protocol on Li/block copolymer electrolyte/Li cells. In addition, Table 7.3 provides a comprehensive list of published short-circuit test results as a function of testing protocol (cell design, current density, temperature) and electrolyte composition, along with short-circuit data normalized to that obtained for a standard PEO electrolyte where reported. It is obvious that the cell lifetimes observed in this work well exceed those previously published, even though the moduli of these electrolytes are considerably lower than those under investigation by Balsara et. al. (0.1-0.5 MPa compared to 1-50 MPa). Hence, it is very unlikely that the mechanical properties of the crosslinked electrolytes are responsible for the long cell lifetimes. It is suspected that the structure of the electrolyte membranes may be very important for their performance. It is possible that higher fractions of PE in the membrane may promote more uniform  $\text{Li}^+$  deposition by reducing the translational freedom of  $\text{Li}^+$  parallel to the electrodes

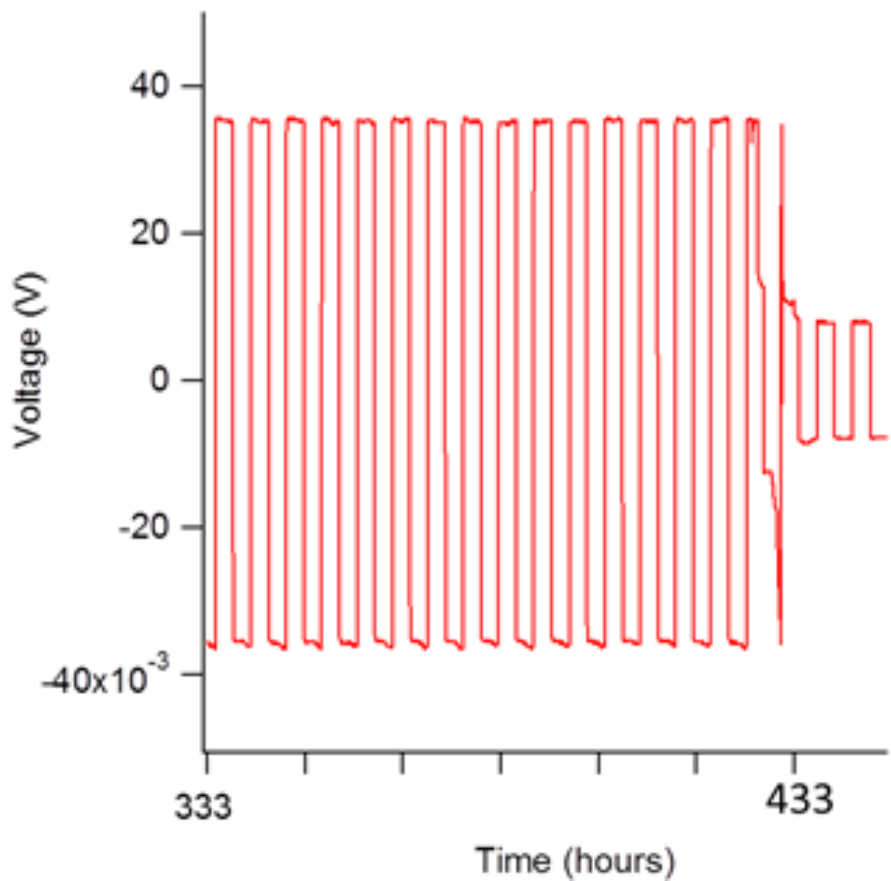


**Figure 7.15** A typical voltage profile for a Li/crosslinked electrolyte/Li cell undergoing galvanostatic cycling to short-circuit.

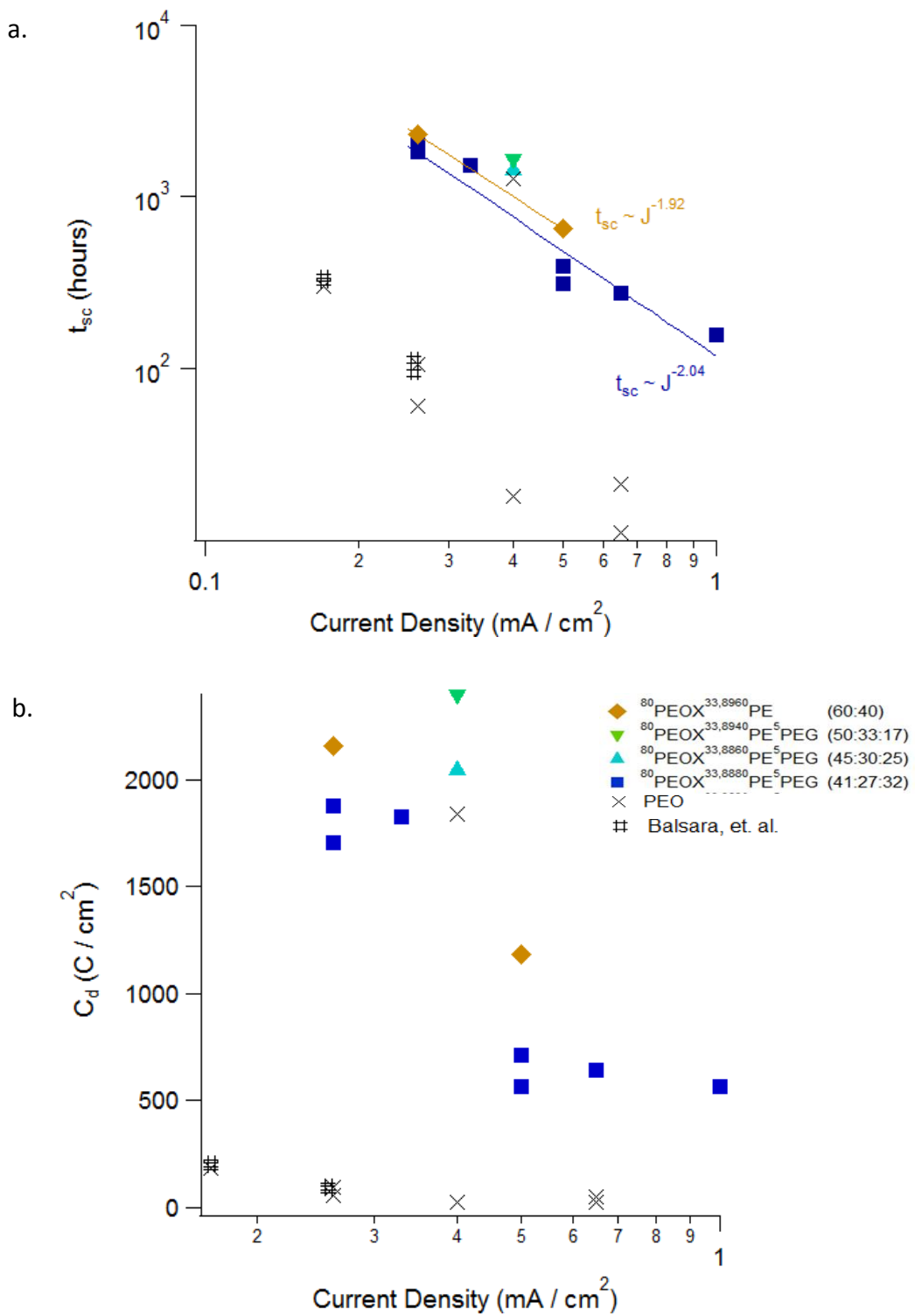


**Figure 7.16** Lifetimes of Li/crosslinked electrolyte/Li cells displayed in terms of a.  $t_{sc}$  and b.  $C_d$ . Shown for comparison are results from Li/PEO electrolyte/Li cells and results published by Balsara, et. al. on Li/block copolymer electrolyte/Li cells.<sup>2</sup>

**Table 7.3** Dendrite resistance for various electrolytes as a function of the test method with number of hours per half-cycle listed for cycling tests and cell type utilized: coin cell [CC] or visualization cell [VC], in terms of the time-to-short-circuit ( $t_{sc}$ ) as well as amount of charge passed until short-circuit ( $C_d$ ).

Electrolyte	Current Density (mA/cm <sup>2</sup> )	Test Method	Temperature (°C)	$t_{sc}$ (hours)	$C_d$ , electrolyte / $C_d$ , PEO	Ref.
EPTPA + EC/PC/1 M LiPF <sub>6</sub> + Al <sub>2</sub> O <sub>3</sub>	0.25	Cycling, 0.5 hrs. [CC]	25	23	---	3
PEG <sub>20</sub> LiTFSI (and + SiO <sub>2</sub> )	0.2 and 1.0	Cycling, 2 hrs. [VC]	25	> 66	---	4
PEO <sub>12</sub> LiTFSI	0.04 – 0.085	Cycling, 3 hrs. [CC]	90	242 - 31	1.0	2
Block Copolymer PS-PEO <sub>12</sub> LiTFSI	0.12–0.26	Cycling, 3 hrs. [CC]	90	> 2000 - 94	48 - 11	2
PEO <sub>20</sub> LiTFSI	0.17 – 0.65	Cycling, 3 hrs. [CC]	90	300 - 11	1.0	This work
PEO <sub>20</sub> LiTFSI**	0.4**	Cycling, 3 hrs. [CC]	90	> 1000**	---	This work
Crosslinked PE-PEO <sub>20</sub> LiTFSI	0.26 – 0.5	Cycling, 3 hrs. [CC]	90	2300 – 660	30	This work
PEO <sub>20-30</sub> LiTFSI	0.02 – 0.3	Polarization [CC]	90	500 - 1	1.0	5
PEG <sub>20</sub> LiTFSI	0.2 - 1.0	Polarization [VC]	25	21- 4	1.0	3
PEG <sub>20</sub> LiTFSI + SiO <sub>2</sub>	0.2 and 1.0	Polarization [VC]	25	108 - 19	1.8–5.1	3
PEO <sub>18</sub> LiTFSI	0.1–1.0	Polarization [VC]	60	225 - 15	1.0	6
PEO <sub>18</sub> LiTFSI + SiO <sub>2</sub>	0.1–1.0	Polarization [VC]	60	400 - 15	2.1 – 1.0	6
PEO <sub>18</sub> LiTFSI + ILs	0.1–1.0	Polarization [VC]	60	594 - 35	3.8 – 1.8	7
PEO <sub>18</sub> LiTFSI + SiO <sub>2</sub> + ILs	0.1–1.0	Polarization [VC]	60	672 – 37	4.2 – 2.2	8
PC/1 M LiTFSI + SiO <sub>2</sub> -IL	0.01 – 0.1	Polarization [CC]	20	420 - 50	---	9
PEG + SiO <sub>2</sub> -PEG-Li	0.03 – 0.065	Polarization [CC]	20	82 - 17	---	10
PEO <sub>20</sub> LiTFSI	0.26 – 0.65	Polarization [CC]	90	19 – 1.8	1.0	This work
Crosslinked PE-PEO <sub>20</sub> LiTFSI	0.26 - 0.4	Polarization [CC]	90	358 - 175	> 9.7	This work

\*\* 1 cell – anomalous result

EPTPA = UV-cured ethoxylated trimethylolpropane triacrylate

EC = ethylene carbonate

PC = propylene carbonate

PEG = polyethylene glycol dimethyl ether (low molecular weight polyethylene oxide)

PEO = polyethylene oxide

IL = ionic liquid

PS = polystyrene

PE = polyethylene

during transport. This would reduce the flux of Li<sup>+</sup> to a surface inhomogeneity, relative to the case of a 100% Li<sup>+</sup>-conducting matrix. To test this hypothesis, more detailed studies of the electrolyte membrane structure and cell lifetimes are required. Specifically, cryo-TEM may be utilized to more easily observe the segregation of the conducting (PEOX, PEG) and non-conducting (PE) domains. It would then be very useful to conduct cell lifetime studies using <sup>80</sup>PEOX<sup>33,18800</sup>PE (62:38) to compare with the results of <sup>80</sup>PEOX<sup>33,8960</sup>PE (60:40), as these electrolytes have very similar bulk properties but different structure, as is apparent from SAXS.

Figure 7.16 displays representative SEM images of the lithium electrodes post-deposition and short-circuiting. In general, the plated lithium electrode after the galvanostatic polarization tests was mostly flat; small areas were observed with finger-like dendrites as shown in Figure 7.16a. In contrast, the lithium electrodes post-galvanostatic cycling appeared to have a dense layer of mossy dendrites. This suggests that dendrites did not form immediately prior to short-circuit of the cycling cells, but likely grew through the electrolyte film over a period of multiple plating/stripping cycles.

In summary, the crosslinked copolymer electrolytes are found to be a useful platform for application in rechargeable lithium metal batteries. Constraint of the polyethylene oxide by crosslinking is found to be successful in decreasing the temperature dependence of the ionic conductivity. The electrolytes are also found to have wide electrochemical stability, below 0 V, and low interfacial impedance when in contact with lithium metal. Most importantly, the electrolytes extend lithium metal cell lifetime until short-circuit well beyond that reported for other electrolyte materials in the literature via both the galvanostatic polarization and galvanostatic cycling test methods. Given the low shear storage modulus of the electrolytes, it is suggested that the phase segregated structure of the electrolytes is most likely responsible for

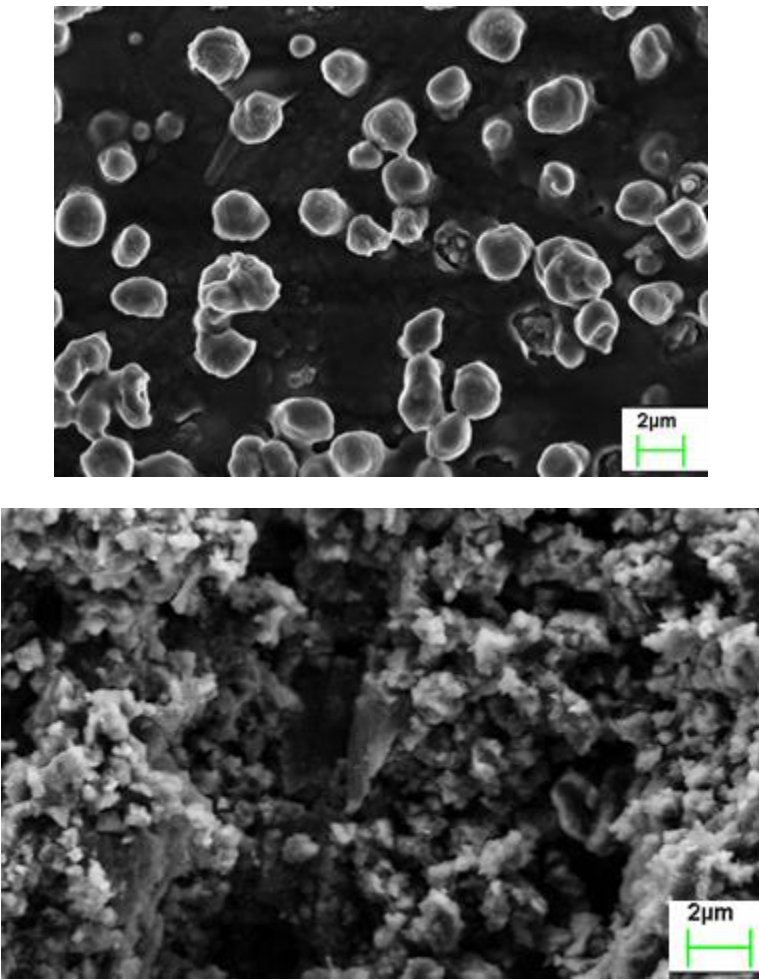


**Figure 7.17** Scanning electron micrographs of the plated lithium electrodes post-short-circuit from a. galvanostatic polarization and b. galvanostatic cycling.

their performance. It is possible that the electrolyte structure promotes more uniform Li<sup>+</sup> deposition across the electrode, hence delaying the onset of dendritic growth.

## References

- [1] M. Rubenstein and R. H. Colby, *Polymer Physics*, 2003, Oxford University Press.
- [2] G. M. Stone, S. A. Mullin, A. A. Teran, D. T. H. Jr., A. M. Minor, A. Hexemer, N. P. Balsara, *Journal of The Electrochemical Society* 2012, 159, A222.
- [3] S.-H. Kim, K.-H. Choi, S.-J. Cho, E.-H. Kil, and S.-Y. Lee, *Journal of Materials Chemistry A* 2013, 1, 4349-4355.
- [4] X.-W. Zhang, Y. Li, S. A. Khan, P. S. Fedkiw, *Journal of The Electrochemical Society* 2004, 151, A1257.
- [5] M. Rosso, T. Gobron, C. Brissot, J.-N. Chazalviel, S. Lascaud, *Journal of Power Sources* 2001, 97-98, 804.
- [6] S. Liu, N. Imanishi, T. Zhang, A. Hirano, Y. Takeda, O. Yamamoto, J. Yang, *Journal of Power Sources* 2010, 195, 6847.
- [7] S. Liu, N. Imanishi, T. Zhang, A. Hirano, Y. Takeda, O. Yamamoto, J. Yang, *Journal of The Electrochemical Society* 2010, 157, A1092.
- [8] S. Liu, H. Wang, N. Imanishi, T. Zhang, A. Hirano, Y. Takeda, O. Yamamoto, J. Yang, *Journal of Power Sources* 2011, 196, 7681.
- [9] Y. Y. Lu, S. K. Das, S. S. Moganty, L. A. Archer, *Advanced Materials* 2012, 24, 4430.
- [10] J. L. Schaefer, D. A. Yanga, L. A. Archer, *Chemistry of Materials* 2013, 25, 854.

**CHAPTER 8:**  
**HIGH LITHIUM TRANSFERENCE NUMBER ELECTROLYTES VIA CREATION OF**  
**3-DIMENSTIONAL, CHARGED, NANOPOROUS NETWORKS FROM DENSE**  
**FUNCTIONALIZED NANOPARTICLE COMPOSITES**

Reproduced with Permission from *Chemistry of Materials*, 25, 834-839, 2013 by J. L. Schaefer, D. A. Yanga, and L. A. Archer.

### **Abstract**

High lithium transference number,  $t_{Li+}$ , electrolytes are desired for use in both lithium-ion and lithium metal rechargeable battery technologies. Historically, low  $t_{Li+}$  electrolytes have hindered device performance by allowing ion concentration gradients within the cell, leading to high internal resistances that ultimately limit cell lifetime, charging rates, and energy density. Herein, we report on the synthesis and electrochemical features of electrolytes based on nanoparticle salts designed to provide high  $t_{Li+}$ . The salts are created by cofunctionalization of metal oxide nanoparticles with neutral organic ligands and tethered lithium salts. When dispersed in a conducting fluid such as tetraglyme, they spontaneously form a charged, nanoporous network of particles at moderate nanoparticle loadings. Modification of the tethered anion chemistry from  $-SO_3^-$  to  $-SO_3BF_3^-$  is shown to enhance ionic conductivity of the electrolytes by facilitating ion pair dissociation. At a particle volume fraction of 0.15, the electrolyte exists as a self-supported, nanoporous gel with an optimum ionic conductivity of  $10^{-4}$  S/cm at room temperature. Galvanostatic polarization measurements on symmetric lithium metal cells containing the electrolyte show that the cell short circuit time,  $t_{SC}$ , is inversely proportional to

the square of the applied current density  $t_{SC} : J^{-2}$ , consistent with previously predicted results for traditional polymer-in-salt electrolytes with low  $t_{Li+}$ . Our findings suggest that electrolytes with  $t_{Li+} \approx 1$  and good ion-pair dissociation delay lithium dendrite nucleation and may lead to improved lithium plating in rechargeable batteries with metallic lithium anodes.

## Introduction

Current lithium-ion battery electrolytes are composed of an aprotic organic solvent and dopant lithium salt, such as LiPF<sub>6</sub>. These electrolytes are highly combustible, may leak out of a battery, and are known to be incompatible with the lithium metal anodes currently under investigation due to their potential to increase battery energy density.<sup>1</sup> Mobile ions produced from the dopant lithium salt also lead to low lithium transference numbers,  $t_{Li+} < 0.5$ , thicker & more dense polymer build-up at the electrode-electrolyte interface, and ionic concentration gradients within the cell, which produce high internal and interfacial resistance. In concert with a lithium metal anode, an ion concentration gradient can also destabilize the electrode-electrolyte interface, leading to lithium dendrite formation. Thus, lithium battery electrolytes with  $t_{Li+}$  approaching unity are desired for application in advanced lithium-ion and lithium metal batteries that offer enhanced safety and energy storage capabilities.<sup>1-3</sup>

As an extreme example from nature, biological ion channels comprised of soft matter are able to completely and selectively screen ion transport based on subtle differences in ion size and charge.<sup>4</sup> It is generally understood that a delicate balance of excluded-volume, hydrophobic, and electrostatic forces achieved in these channels is responsible for this selectivity.<sup>5-6</sup> Artificial ion channels with highly charged walls (i.e. surface charge density greater than the charge density in a bulk electrolyte) and with pore dimensions comparable to the Debye screening length have

been shown to act as rectifiers for charge transport, whereby ions with the same charge as the channel walls are selectively screened from traversing the channels under a potential gradient.<sup>7</sup>

Application of this principle for efficient electromechanical energy conversion has been an area of steadily growing scientific and technological interest.<sup>8-9</sup>

Recently, we reported on the synthesis of hybrid nanoparticle-ionic liquid electrolytes<sup>10</sup> and hybrid nanoparticle-polymer electrolytes<sup>11,12</sup> that spontaneously jam above a critical particle loading<sup>13</sup> to form bulk, three-dimensional nanoporous media with high thermal and electrochemical stability. Some compositions of the electrolytes also display attractive ionic conductivity and mechanical tunability. These features are all desirable for improving safety and for accommodating growing interest in thin lithium batteries with unusual form factors.

Unfortunately, even at large nanoparticle loadings, where steric barriers should hinder transport - through the nanopore network formed by particles - of the bulky bis(trifluoromethanesulfonimide) TFSI counterion used for the electrolytes,  $t_{Li^+}$  does not approach unity; rather, it is consistently less than 0.5.

The large number of functional groups available on the nanoparticles provides an important path towards synthesis of nanoparticle-based lithium salts and charged, three-dimensional, nanoporous networks for hosting liquid electrolytes. The condition  $t_{Li^+} \approx 1$  can be reached in the former case because of the large difference in size, and thereby mobility, of the  $Li^+$  ion and its counterions (tethered to the nanoparticles). It can be achieved in the latter case, by internalizing charges introduced on the particle surfaces into the tortuous nanopores formed at particle salt concentrations above the jamming threshold.

Herein, we report on the physical properties of such a charged, 3-dimensional, nanoporous electrolyte and show that the condition  $t_{Li^+} \approx 1$  can be facilely achieved in these systems without

compromising conductivity. Shown in Figure 1, the nanoparticle lithium salt used in the current study is composed of a SiO<sub>2</sub> nanoparticle core co-functionalized with polyethylene glycol (PEG) ligands and a tethered –SO<sub>3</sub><sup>-</sup> or –SO<sub>3</sub>BF<sub>3</sub><sup>-</sup> anion coupled to Li<sup>+</sup>. Each 7 nm silica core is decorated with around 2.4 reactive sulfonic acid species per nm<sup>2</sup> of the bare particle surface. Complete reaction with amine PEG or LiOH would produce around 190 each of the tethered ions and PEG chains on a single nanoparticle. This means that at a particle volume fraction  $\phi \approx 0.25$ , the nominal Li<sup>+</sup> ion concentration in the electrolyte is 0.5M. By reducing the fraction of surface sites used to anchor PEG ligands, the Li<sup>+</sup> concentration can be increased at a fixed nanoparticle volume fraction. This must be balanced against the fact that the PEG ligands play multiple, important roles that impact electrolyte performance: they improve dissociation of Li<sup>+</sup> from the tethered anion, limit aggregation of the silica nanocores even at high particle loadings,<sup>11-13</sup> and they improve dissolution of the resultant nanoparticle salt into a chosen electrolyte media, tetraglyme in the case of the current study.

The molar mass per unit charge of the anionic nanoparticles is over 2200 g/mol/unit charge. This is roughly 8 times larger than the molar mass per unit charge ratio of the widely studied TFSI<sup>-</sup> anion. With straightforward modifications, the synthesis method can be adapted to produce nanoparticle-based lithium salts, and thus charged, 3-D nanoporous networks, with any of the typical anions used in lithium batteries tethered to nanoparticles of chosen size. At sufficiently high loadings and in high dielectric constant media, we anticipate designs of the materials for which even free anions in the electrolyte could be electrostatically excluded from the nanochannels between particles to enhance  $t_{Li^+}$ .

## Experimental Section

### Synthesis

The  $\text{SiO}_2\text{--SO}_3\text{Li}$  nanoparticle salts were synthesized in a two-step procedure that begins with condensation of a silane terminated sulfonic acid, (3-trihydroxysilyl)-propane sulfonic acid, with silica nanoparticles (Ludox SM-30, Aldrich) as described previously.<sup>11,13</sup> This step is followed by a rigorous dialysis process to remove unattached silane. In the second synthesis step, stoichiometric reaction of the purified sulfonic acid particles in aqueous suspension with an amine terminated polyethylene glycol methyl ether ( $M_n = 800$ , Polymer Source) and LiOH (Aldrich) is used to create the cofunctionalized particles. The resulting particles are dried, first at 80°C in a convection oven and then under vacuum at 0.015mbar overnight at room temperature. A sample of the intermediate, sulfonic acid functionalized nanoparticles in aqueous solution, was titrated against a strong base to determine the available number of acid sites, and thereby estimate of the maximum grafting density possible.  $\text{SiO}_2\text{--SO}_3\text{Li}$  electrolytes were prepared by dissolution of the dried nanoparticle salt in chloroform, followed by addition of an appropriate amount of tetraethylene glycol dimethyl ether (TEGDME, Aldrich), and finally by drying first in a convection oven at 50°C and then under vacuum at 0.015mbar at room temperature for 6 hours. The amount of TEGDME was varied to change the nanoparticle volume fraction  $\phi$ , and thereby the molarity, of the electrolytes. The  $\text{SiO}_2\text{--SO}_3\text{BF}_3\text{Li}$  electrolytes were prepared under an argon atmosphere via dissolution of the dried nanoparticle salt in chloroform, addition of trifluoroboron diethyl ether,  $\text{BF}_3\text{OEt}_2$  (Aldrich), in an amount stoichiometric to Li, and an appropriate amount of TEGDME, followed by drying at 50°C and then under vacuum at 0.015mbar at room temperature for 6 hours; a similar procedure has been employed by others<sup>14-15</sup> for modification

of related functional groups. No additional salt, other than the functionalized nanoparticles (Figure 8.1), was added to the electrolytes used in this study.

#### *Characterization*

NMR was performed on solutions of electrolytes,  $\phi = 0.15$ , in chloroform with varying amounts of  $\text{BF}_3\text{OEt}_2$  with an INOVA 600 spectrometer. Ionic conductivity was measured with a Novacontrol Dielectric spectrometer fitted with a Quatro temperature control system. Electrochemical measurements were performed using a Solartron CellTest model potentiostat. Impedance measurements were conducted using a Solartron Frequency Response Analyser (Model 1252) at frequencies ranging from 2 kHz to 900 mHz and at an amplitude of 10 mV. Galvanostatic polarization measurements were performed using a Neware CT-3008 battery tester. Symmetric lithium coin cells for electrochemical stability, impedance, and galvanostatic polarization measurements were prepared in an argon filled MBraun glovebox. Each coin cell contained a Teflon donut ring, I.D. = 0.25“ and thickness = 0.030“, that was charged with the gel electrolyte under investigation. All coin cell measurements were performed at room temperature (18°C).

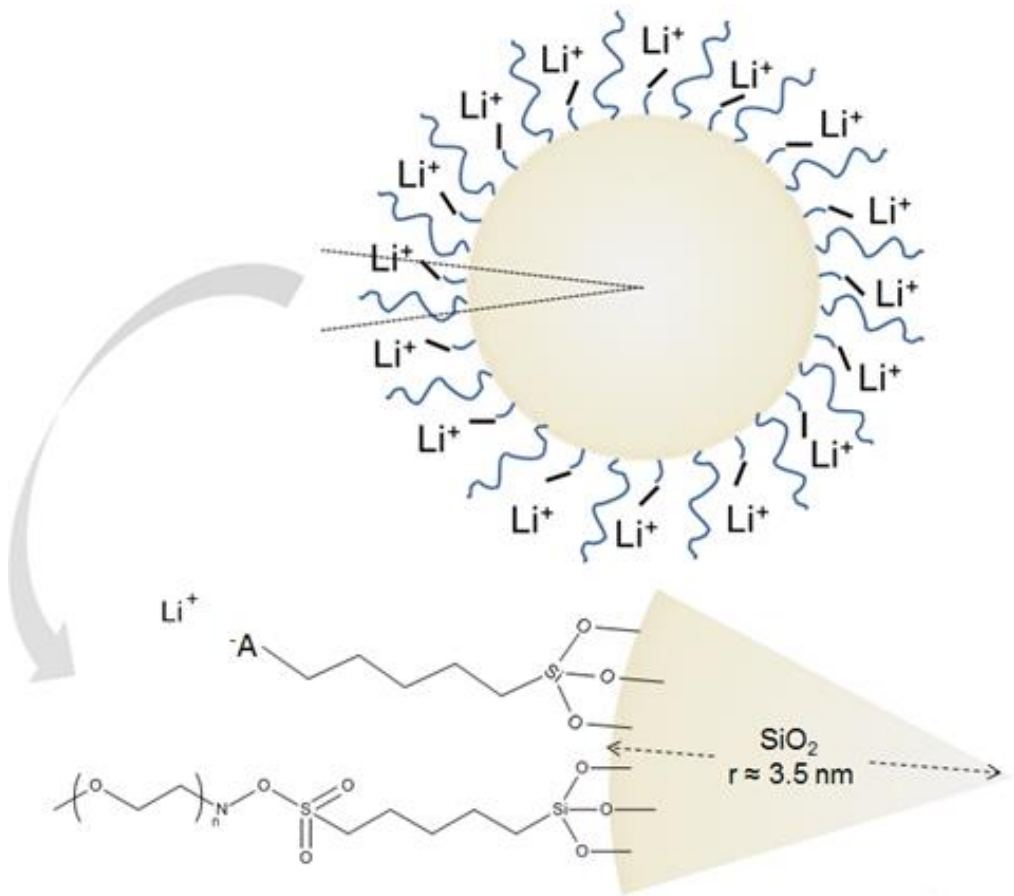


**Figure 8.1** Schematic of the nanometric lithium salt, where  $A^-$  is  $-SO_3^-$  or  $-SO_3BF_3^-$ . The total amount of  $Li^+$  ions is about 190 per nanoparticle.

## Results and Discussion

### $^{11}\text{B}$ and $^{19}\text{F}$ NMR

$^{11}\text{B}$  and  $^{19}\text{F}$  NMR confirm the chemical modification of  $\text{SiO}_2\text{--SO}_3\text{Li}$  to  $\text{SiO}_2\text{--SO}_3\text{BF}_3\text{Li}$ , as performed on solutions of electrolytes,  $\phi = 0.15$ , in chloroform with varying amounts of  $\text{BF}_3\text{OEt}_2$ , as shown in Figures 8.2(a) and 8.2(b). Systems 1 and 2 were synthesized from the  $\text{SiO}_2\text{--SO}_3\text{Li}$  salt with 50% and 100% stoichiometric equivalents, respectively, of  $\text{BF}_3\text{OEt}_2$  with respect to sulfonate anion number. System 3 was synthesized with 100% stoichiometric equivalents of  $\text{BF}_3\text{OEt}_2$  (to produce the  $\text{SiO}_2\text{--SO}_3\text{BF}_3\text{Li}$  salt) and additional 400% stoichiometric equivalents of  $\text{BF}_3\text{OEt}_2$  were added to the measurement solution. System 4 is only  $\text{BF}_3\text{OEt}_2$  in solution. As shown in Figures 8.2(a) and 8.2(b), only one peak is visible in systems containing only 50% and 100% stoichiometric amounts, no excess, of the additive.

In addition, all peaks in the  $^{19}\text{F}$ -NMR spectra are split 1:4, correlating with the natural abundancy of  $^{10}\text{B}:\text{ }^{11}\text{B}$ ,<sup>16</sup> indicating that all fluorine atoms remain bonded to boron. This knowledge, combined with chemical intuition of the chemistries involved, suggests that  $\text{BF}_3\text{OEt}_2$  has chemically combined with  $-\text{SO}_3^-$  to form  $-\text{SO}_3\text{BF}_3^-$  and  $\text{OEt}_2$  byproduct. The low molecular weight byproduct and any unreacted  $\text{BF}_3\text{OEt}_2$  is likely removed during vacuum drying, the final step in the electrolyte preparation process.

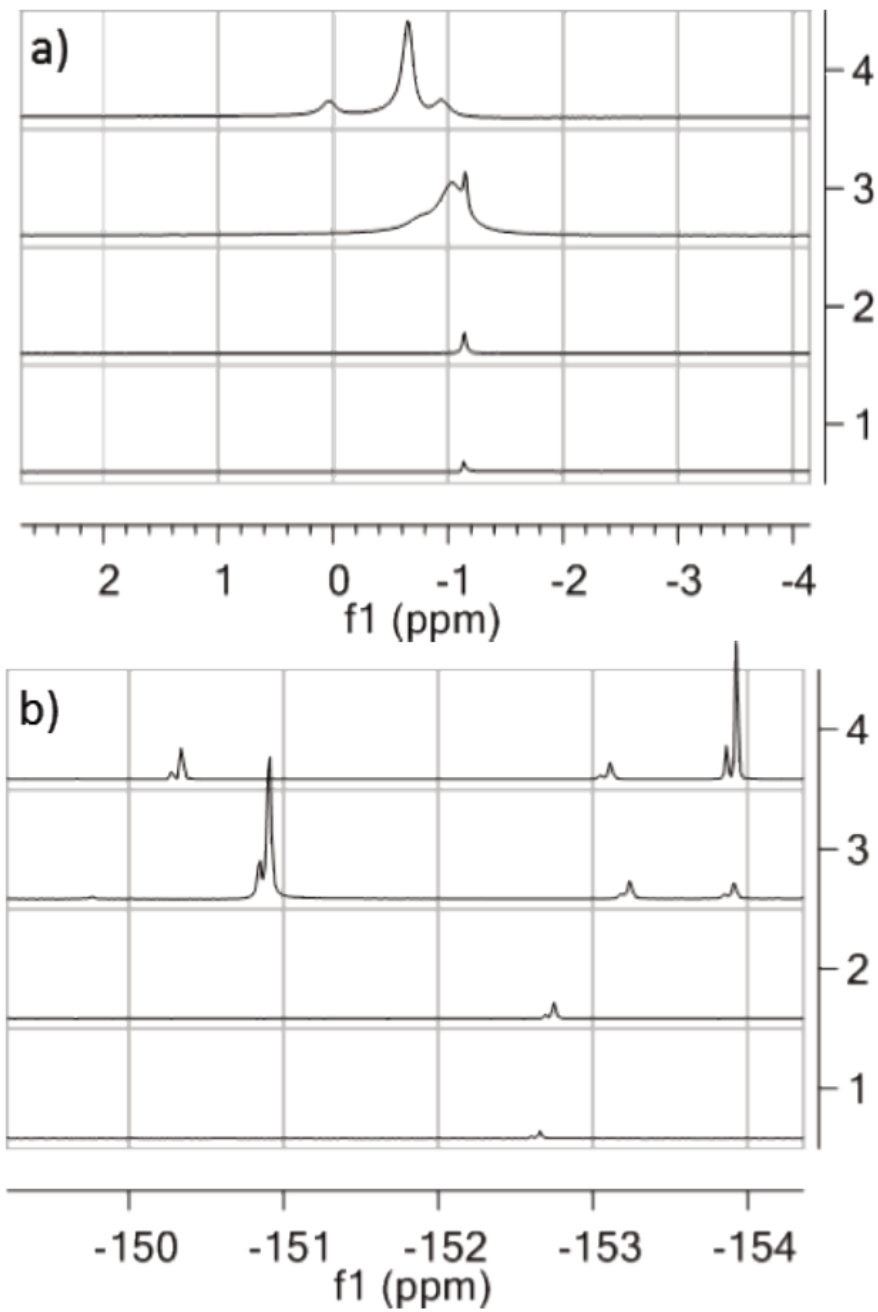


**Figure 8.2** a.  $^{11}\text{B}$ -NMR and b.  $^{19}\text{F}$ -NMR of samples in chloroform where samples 1 and 2 contain only the  $\text{SiO}_2\text{--SO}_3\text{BF}_3\text{Li}$  nanoparticle salt with varying levels of modification by  $\text{BF}_3\text{OEt}_2$ , sample 3 contains both  $\text{SiO}_2\text{--SO}_3\text{BF}_3\text{Li}$  and  $\text{BF}_3\text{OEt}_2$ , and sample 4 contains only  $\text{BF}_3\text{OEt}_2$ .

### *Ionic Conductivity*

Temperature-dependent ionic conductivity for electrolytes containing  $\text{SiO}_2\text{--SO}_3\text{Li}$  and  $\text{SiO}_2\text{--SO}_3\text{BF}_3\text{Li}$  at selected loadings is reported in Figure 3(a). The anion modified with  $\text{BF}_3\text{OEt}_2$  has improved ionic conductivity over the entire investigated temperature range. Interestingly, the effect of temperature on ionic conductivity of electrolytes containing the  $\text{SiO}_2\text{--SO}_3\text{BF}_3\text{Li}$  salt is reduced as shown by a reduction in the relative change in conductivity over a given temperature range. Ionic conductivity is nearly temperature invariant from 50–100°C in electrolytes with certain  $\text{SiO}_2\text{--SO}_3\text{BF}_3\text{Li}$  loadings. It is unclear to what temperature the  $\text{SiO}_2\text{--SO}_3\text{BF}_3\text{Li}$  salt is thermally stable, at sufficiently high temperatures, however, the complex is expected to decompose, releasing free  $\text{BF}_3$ . Figure 3(b) reports the ionic conductivity of electrolytes with varying nanoparticle concentrations, in terms of silica volume fraction,  $\phi$ , at selected isotherms. It is apparent from the results that there is an optimum composition for achieving electrolytes with improved ionic conductivity. This behavior is analogous to the optimum salt composition observed in conventional liquid electrolytes and reflects a balance between an increase in the mobile ion concentration that accompanies addition of more salt, and the reduced mobility of ions as ionic interactions reduce fluidity. The highest room temperature (25°C) ionic conductivity,  $\sigma = 1 \times 10^{-4} \text{ S/cm}$ , is observed for the electrolyte containing the  $\text{SiO}_2\text{--SO}_3\text{BF}_3\text{Li}$  salt at a loading of  $\phi \approx 0.15$ . At this composition, the charged nanoparticles strongly interact and the electrolyte exists as a gel with a yield stress greater than that of gravity.<sup>17,18</sup> The large majority of the ionic conductivity, therefore, is expected to be due to the mobility of  $\text{Li}^+$ .

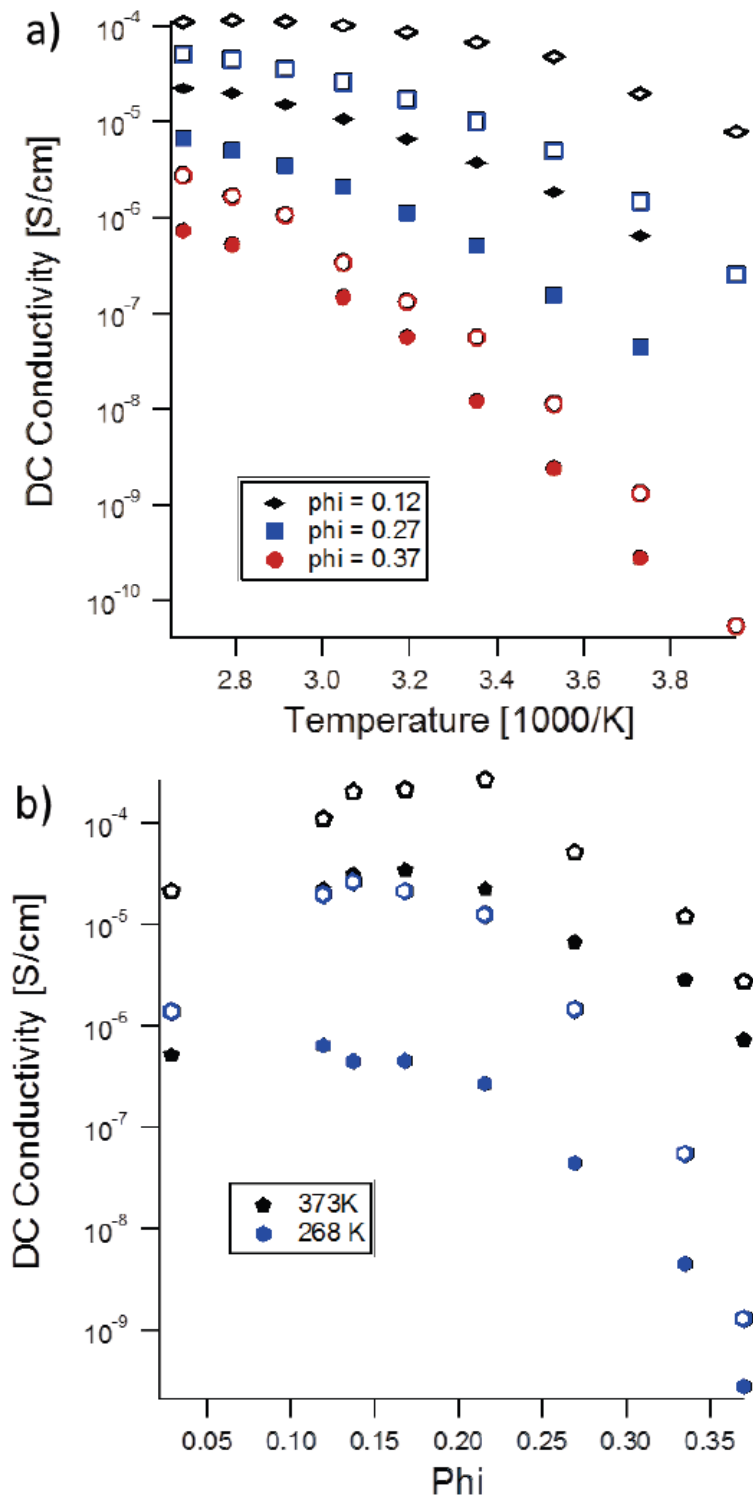


**Figure 8.3** DC conductivity for electrolytes containing nanometric  $\text{SiO}_2\text{-SO}_3\text{Li}$  salt [closed symbols] and  $\text{SiO}_2\text{-SO}_3\text{BF}_3\text{Li}$  salt [open symbols] in tetraglyme as a function of temperature, (a), and composition, (b).

### *Electrochemical Stability*

To characterize the electrochemical stability of the electrolytes, impedance spectroscopy was performed for a representative material with salt concentration  $\phi = 0.15$ , in a symmetric Li/electrolyte/Li coin-cell configuration. Figure 4(a) shows the impedance response at various intervals in time; the points are the data and lines are fits to the equivalent circuit model in the inset where  $R_b$  is the bulk electrolyte resistance,  $R_{int}$  is the interfacial resistance,  $Q_{int}$  is the corresponding constant phase element capacitance, and  $W$  is the Warburg diffusion element. Figure 4(b) summarizes the magnitude of the bulk and interfacial resistances, which approach steady-state values over a 1000-hour evaluation period. Consistent interfacial resistances and impedance response means that a stable solid electrolyte interfacial (SEI) layer is formed with metallic lithium. Electrolytes containing  $\text{SiO}_2\text{--SO}_3\text{BF}_3\text{Li}$  have both lower interfacial and bulk resistances. In contrast, electrolytes with  $\text{SiO}_2\text{--SO}_3\text{Li}$  have a wider electrochemical window, - 0.3 to over 6 V, versus 0.4 to 5.5 V for electrolytes containing  $\text{SiO}_2\text{--SO}_3\text{BF}_3\text{Li}$  (Figures 5(a) and 5(b)). As shown in our earlier work,<sup>10-12</sup> these wide electrochemical stability windows are characteristic of oligoglycol-based electrolytes.

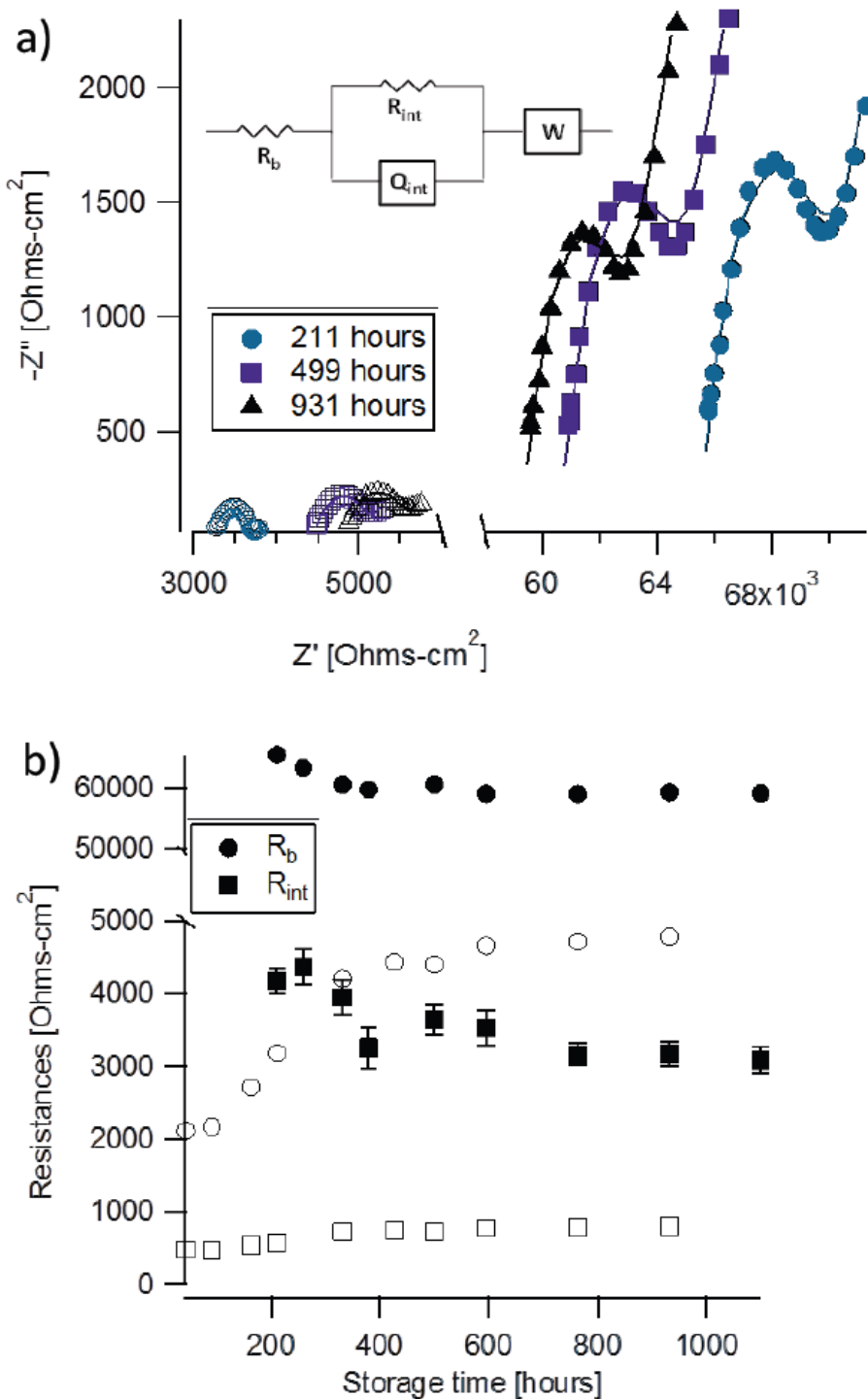


**Figure 8.4** (a) Impedance response of Li/electrolyte/Li cells containing nanometric  $\text{SiO}_2\text{--SO}_3\text{Li}$  salt [closed symbols] and  $\text{SiO}_2\text{--SO}_3\text{BF}_3\text{Li}$  salt [open symbols] as fit to an equivalent circuit model and (b) Resistances as a function of time as determined from the equivalent circuit model.

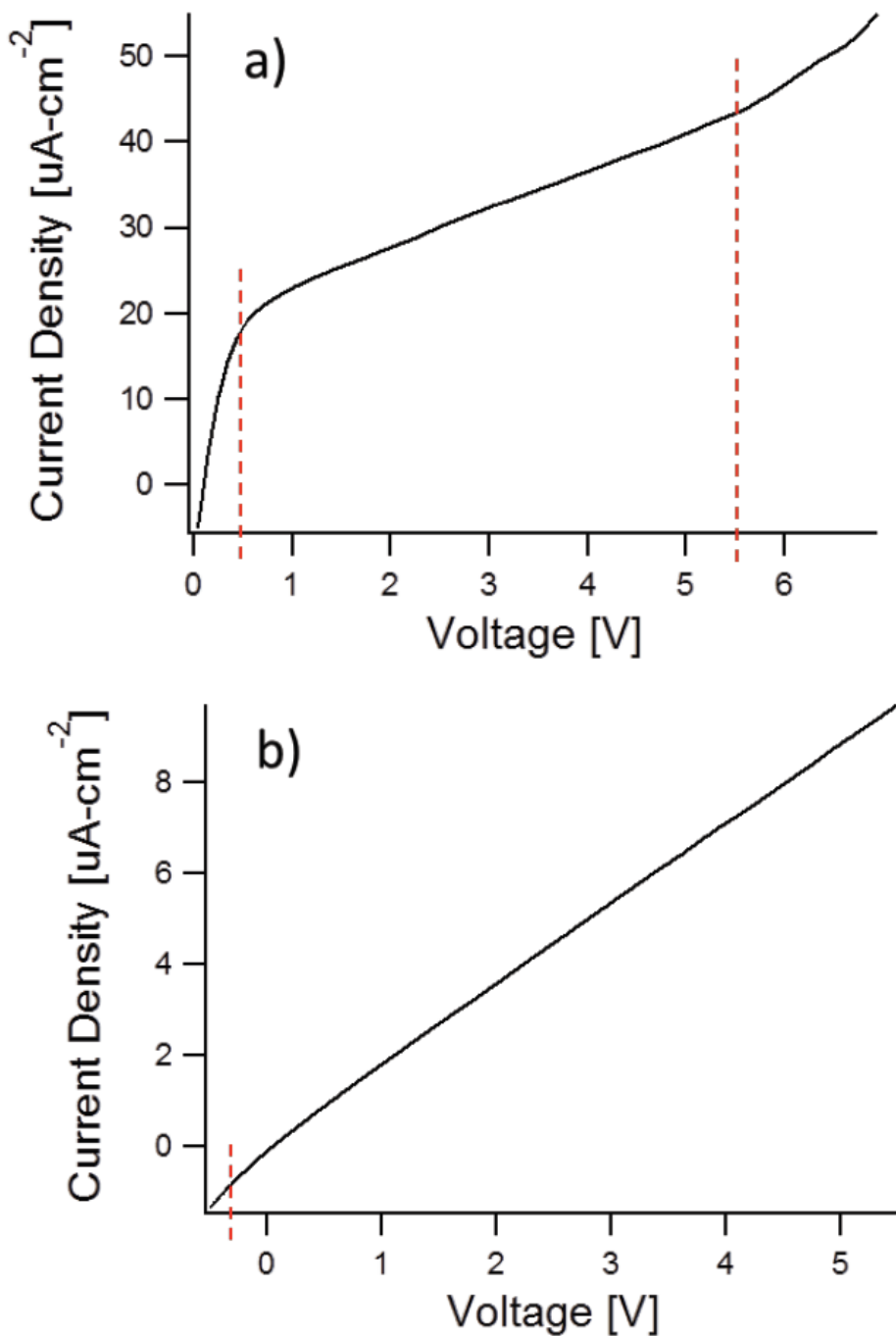


**Figure 8.5** Electrochemical stability windows of electrolyte containing nanometric (a)  $\text{SiO}_2-\text{SO}_3\text{BF}_3\text{Li}$  salt and (b)  $\text{SiO}_2-\text{SO}_3\text{Li}$  salt, as measured in a symmetric Li/electrolyte/Li coin cell configuration.

### *Mobile Ion Concentration*

The mobile ion concentration, or the fraction of Li<sup>+</sup> dissociated from the nanoparticle-tethered SiO<sub>2</sub>–SO<sub>3</sub>BF<sub>3</sub><sup>-</sup> anion, is an important characteristic of an electrolyte. It depends on the atomic make-up and molecular structure of ions in the salt and on the dielectric constant of the electrolyte medium. It is known that it can be enhanced by polymers such as PEG that have strong affinity for Li<sup>+</sup>.<sup>20-22</sup>

To estimate the mobile ion concentration we utilize dielectric spectroscopy and a recently reported model, which analyzes frequency-dependent electrode polarization in single-ion conductors of low conductivity.<sup>19</sup> For such conductors, the ratio of the dielectric loss to storage,  $\tan \delta = \epsilon''/\epsilon'$ , measured over a range of frequencies, , can be related to the mobile ion

concentration through the formula, 
$$\tan \delta = \frac{\omega \tau_{EP}}{1 + \omega^2 \tau_{EP}^2 / M}$$
 where  $\tau_{EP}$  is the electrode polarization relaxation time and  $M$  is the ratio of the sample thickness,  $L$ , to twice the Debye length. The mobile ion concentration,  $C_0 = \sigma_0 / q\mu$ , can be determined from the ion mobility,

$$\mu = \frac{qL^2}{4kTM\tau_{EP}}$$
, the measured DC conductivity,  $\sigma_0$  , and the  $\tau_{EP}$  and  $M$  values that yield the best fit of the  $\tan \delta$  data near  $\omega\tau_{EP} \approx 1$ . Here,  $q$  is the charge of the monovalent mobile Li<sup>+</sup> ion.

Figure 6(a) displays the frequency dependence of tanas obtained at 0°C; the fit to this data as obtained using the Origin® nonlinear curve fitting routine is displayed in blue. The fit is good near the maximum, but poor at frequencies bracketing the maximum value. We believe the large deviations at low frequencies are a consequence of multiple factors, including the high ionic conductivity of the electrolytes, which push the limits of validity of the electrode polarization model used to analyze the  $\tan \delta$  results. Fitting the region near the  $\tan \delta$  maximum provides an

estimate for  $\tau_{EP}$ , which can be used to deduce the mobile ion concentration. Figure 6(b) reports  $C_0$  as a function of temperature for electrolyte containing the  $\text{SiO}_2\text{-SO}_3\text{BF}_3\text{Li}$  salt at  $\phi = 0.15$ . The mobile ion concentration is seen to display Arrhenius temperature dependence above the phase transition temperature of the electrolyte ( $T_c = -18^\circ\text{C}$  by DSC measurements). The  $C_0$  values in Figure 6(b) are high in comparison to what has previously been determined for polymer electrolytes containing sulfoisophthalate anions.<sup>19</sup> This is not a surprising result, however, considering the relatively high ionic conductivity of the present electrolytes. The specific chemical and steric features of the  $\text{SiO}_2\text{-SO}_3\text{BF}_3^-$  linkage and the affinity of PEG for  $\text{Li}^+$  are both believed to play a role in this observation. Extrapolation of the mobile ion concentration in a single ion conductor to infinite temperature should yield the total ion concentration in the electrolyte.<sup>18</sup> Extrapolation of the Arrhenius fit in Fig 6 yields an intercept of  $1.4 \times 10^{27}$  ions/m<sup>3</sup>, which is approximately 9 times larger than the total concentration of  $\text{Li}^+$  ions ( $1.6 \times 10^{26}$  /m<sup>3</sup>) associated with the nanoparticle salts in the electrolyte. This finding most likely reflects the breakdown of the assumptions about electrolyte conductivity that leads to the simple relationship between  $\tan\delta$  and  $\tau_{EP}$  used to fit experimental data. It is also possible that the instability of the  $\text{SiO}_2\text{-SO}_3\text{BF}_3^-$  anion at elevated temperature may already be reflected in this result.

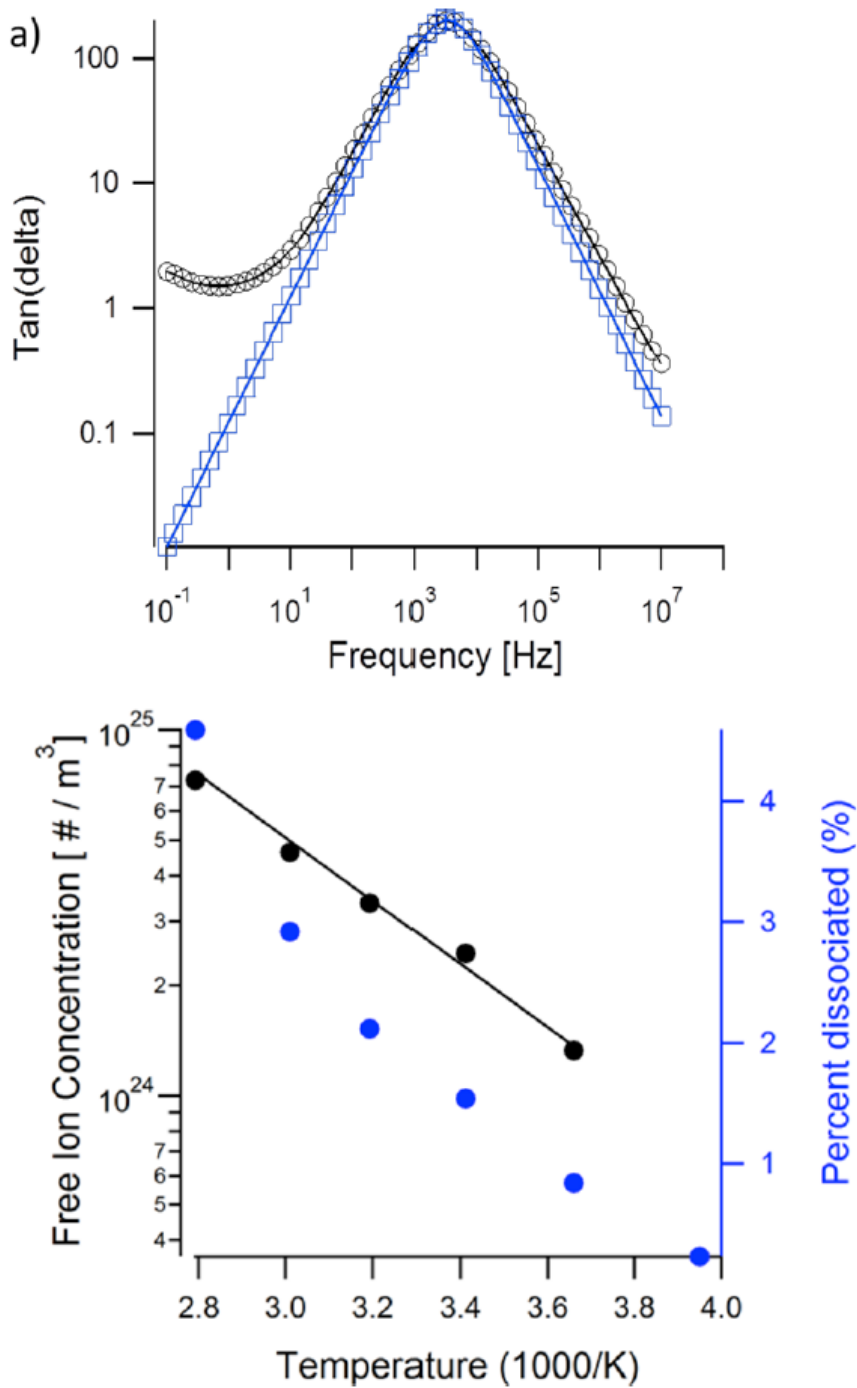


**Figure 8.6** (a) Frequency dependence of  $\tan\delta$  at  $0^\circ\text{C}$ , experimental [black] and fit [blue] and (b) calculated mobile ion concentration as a function of temperature for a  $\text{SiO}_2-\text{SO}_3\text{BF}_3\text{Li}$  electrolyte with  $\varphi = 0.15$ .

### *Lithium plating via galvanostatic polarization and determination of lithium transference number*

Galvanostatic polarization measurements were conducted to investigate the efficiency of lithium plating from the  $\text{SiO}_2\text{-SO}_3\text{BF}_3\text{Li}$  based electrolytes. Previous reports<sup>23,24</sup> find the short circuit time  $t_{SC}$  of symmetric lithium cells containing a polymer-in-salt electrolyte follows a simple universal relationship:  $t_{SC} \propto \tau_s \approx \pi D(eC_0 / 2Jt_a)^2$ . Here  $\tau_s$  is Sand's time, a function of the ambipolar diffusion coefficient  $D$ , mobile ion concentration,  $C_0$ , current density  $J$  and the anion transference number  $t_a$ . In an ideal single-ion conducting electrolyte,  $t_a \rightarrow 0$  and  $t_{SC}$  diverges. For non-zero values of  $t_a$  the time ( $\tau_g$ ) required for dendrites to grow across the cell should also be considered in analyzing empirical data for the short-circuit time. Previous optical measurements<sup>24</sup> indicate that dendrites grow at a speed  $v = \mu_a E$ , where  $\mu_a$  is the anion mobility, and electric field,  $E = J / \sigma$ , at moderate fields. The time required for dendrites to traverse the distance  $L$  between electrodes can therefore be approximated as  $\tau_g \approx L\sigma / \mu_a J$ .

Knowledge of the mobile ion concentration in conjunction with ionic conductivity data allows the ambipolar diffusion coefficient, , tp be calculated using the Nernst-Einstein equation:

$D = \sigma kT / C_0 q^2$ . Table 1 displays  $C_0$  and resulting diffusivity at 18°C for an electrolyte containing  $\text{SiO}_2\text{-SO}_3\text{BF}_3\text{Li}$  salt at  $\phi = 0.15$  for two limiting situations. In case 1, the mobile ion concentration is as calculated by the fit of the  $\tan \delta$  versus  $\omega$  data; in case 2, the mobile ion concentration is assumed to be the limiting value where complete ion dissociation exists and all  $\text{Li}^+$  ions are free. The magnitude of  $D$  is higher in case 1 than in an equivalent concentration of LiTFSI in TEGDME, where the Li salt is believed to be fully dissociated. This suggests that if the electrode polarization model is applicable to this system, diffusion of  $\text{Li}^+$  is by a different

mechanism, such as hopping between the anion sites available on the nanoparticles rather than diffusion in concert with the TEGDME molecules.

Table 8.1. Ambipolar diffusion coefficient,  $D$ , as a function of mobile ion concentration,  $C_o$ .

case	(#/m <sup>3</sup> )	(m <sup>2</sup> /s)
1	$9.4 \times 10^{23}$	$2.1 \times 10^{-9}$
2	$1.6 \times 10^{26}$	$1.2 \times 10^{-11}$

The short circuit time  $t_{sc}$  for symmetric lithium metal cells containing the SiO<sub>2</sub>–SO<sub>3</sub>BF<sub>3</sub>Li electrolyte,  $\varphi = 0.15$ , were determined from a sharp drop in potential vs. time diagrams (see Figure 7(a)). Figures 7(b) and 7(c) show the relationship between  $t_{sc}$  and current density at varying  $t_a$ . The lines in the figure are predicted values for  $\tau_s$  at the indicated  $t_a$ , for electrolytes with the same parameters as in case 1 and case 2, respectively. The data set is not extensive, but it is noticeable that  $t_{sc} : 1/J^2$ , as predicted. By substituting the relevant values for case 1 for the other variables in  $\tau_s$ , calculating  $t_a$ , using this value to determine  $\tau_g$ , modifying the value of  $\tau_s$ , and iterating until convergence, we find  $t_{Li+} \approx 0.96$  for this system. The converged values of  $\tau_s$  for case 1, after accounting for predicted  $\tau_g$  are displayed in Figure 7(b); the maximum error is less than 10%. The same approach was applied to case 2 and  $\tau_g$  was determined to be much higher under these conditions. After accounting for  $\tau_g$  in the first iteration,  $\tau_s$  was not proportional to  $1/J^2$ , and further iteration was not possible to refine the estimate for  $t_a$ . To a first approximation, the results yield  $t_{Li+} \approx 0.7$  for case 2. For comparison, voltastatic polarizations were also performed to determine  $t_{Li+}$ . These measurements yield  $t_{Li+}$  in the range 0.6 to 0.9. Figure 7(d) shows the asymptotic effect of  $t_a$  on  $t_{sc}$ , which makes it

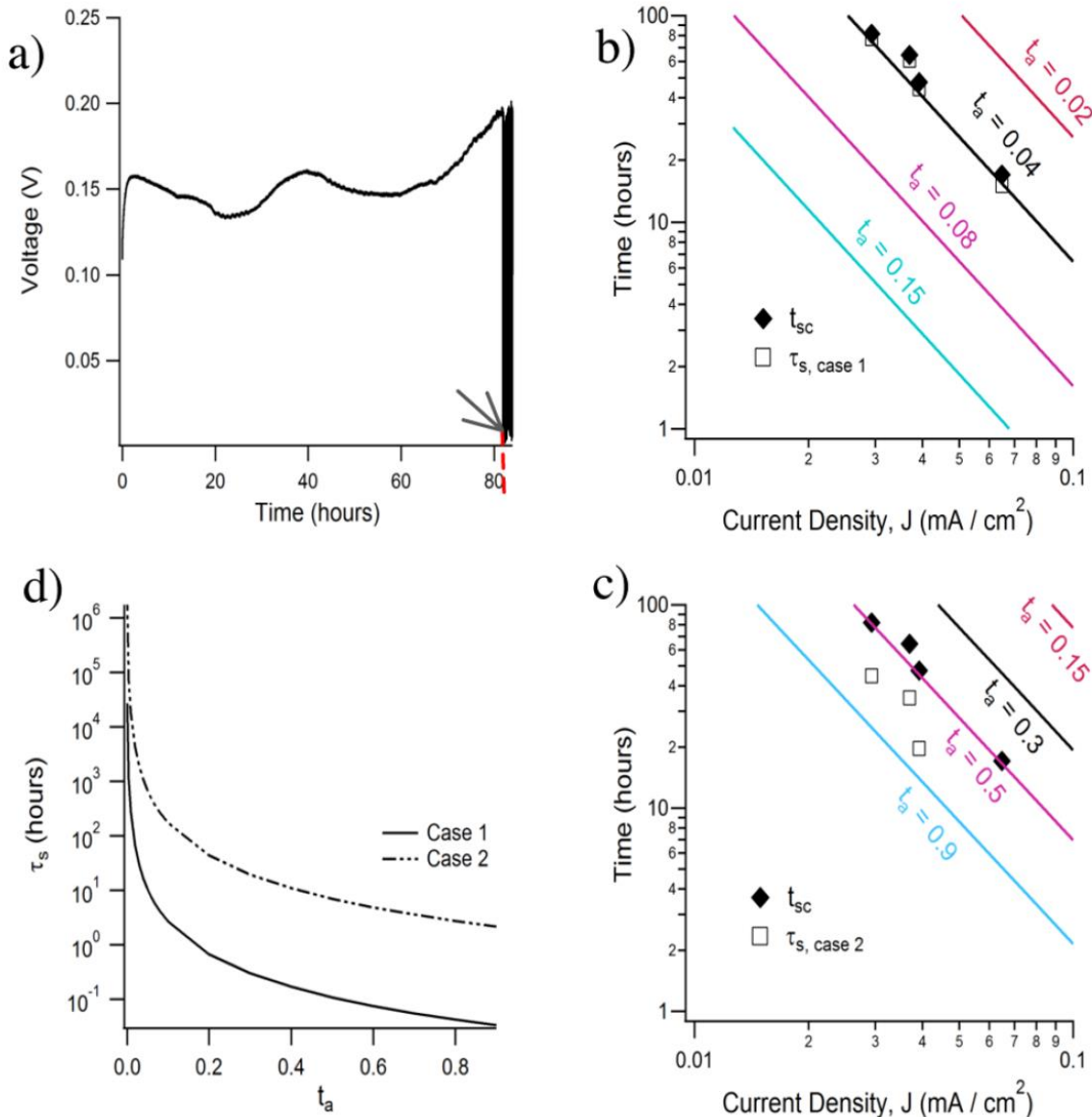


**Figure 8.7** a) Representative voltage-versus time profile from a polarization experiment using a  $\text{Li/SiO}_2\text{-SO}_3\text{BF}_3\text{Li}$  electrolyte,  $\varphi = 0.15$  /Li coin cell with  $J = 0.0294 \text{ mA/cm}^2$ , to determine the short-circuit time,  $t_{sc}$ . Measured  $t_{sc}$  versus  $J$  compared with the predicted under two scenarios: b) variables as in case 1 described in the text; c) as in case 2. d)  $\tau_s$  versus  $t_a$  for parameters in cases 1 and 2.

clear that to achieve electrolytes with substantially larger  $t_{SC}$  based on suppressing of  $t_a$  alone will require improvements in the salt and electrolyte chemistry to facilitate a combination of good ion pair dissociation, high ionic conductivity, and  $t_a$ .

## Conclusions

In summary, we report a facile route towards single-ion conducting electrolytes based on nanoparticle lithium salts. By tethering organic counteranions to nanoparticles, we show that it is possible to simultaneously achieve electrolytes with reasonable ionic conductivity ( $1 \times 10^4$  S/cm) at room temperature and high lithium transference number. Further improvements in the electrolytes are possible through use of liquid hosts with higher dielectric constants (e.g. propylene carbonate,  $\epsilon \approx 64$ ), than tetraethylene glycol dimethyl ether ( $\epsilon \approx 7.9$ ), to enhance ion pair dissociation and conductivity. Optimization of the nanoparticle physical characteristics (e.g. size, ratio of tethered anions to polymer, volume fraction in the host, diameter of the electrolyte network nanopores) and the counteranion chemistry also provide straightforward paths towards even higher  $t_{Li}$  and electrolyte conductivities.

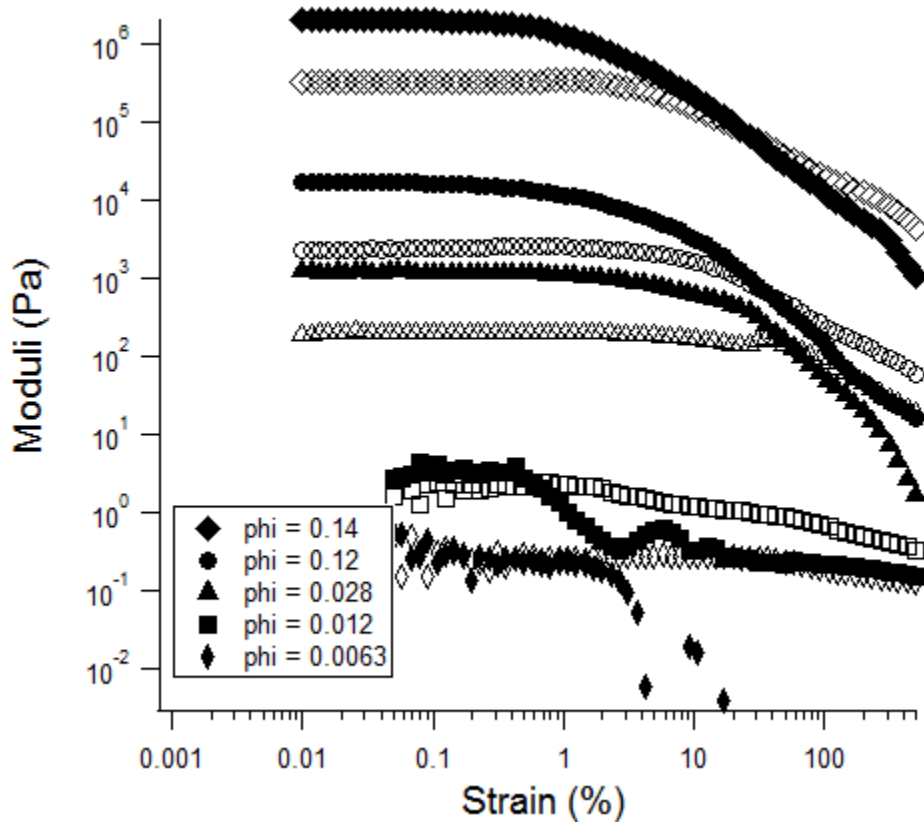
## References

1. Armand, M.; Tarascon, J.-M. *Nature* **2008**, *451*, 652-657.
2. Kerr, J. B. In *Lithium Batteries: Science and Technology*, (Eds.: Nazri, G.-A; Pistoia, G.), Springer, **2009**, pp. 574-615.
3. MacFarlane, D.; Huang, J.; Forsyth, M. *Nature* **1999**, *402*, 792-794.
4. Nishizawa, M.; Martin, C.R.; Menon, V.P. *Science* **1995**, *268*, 700–702.

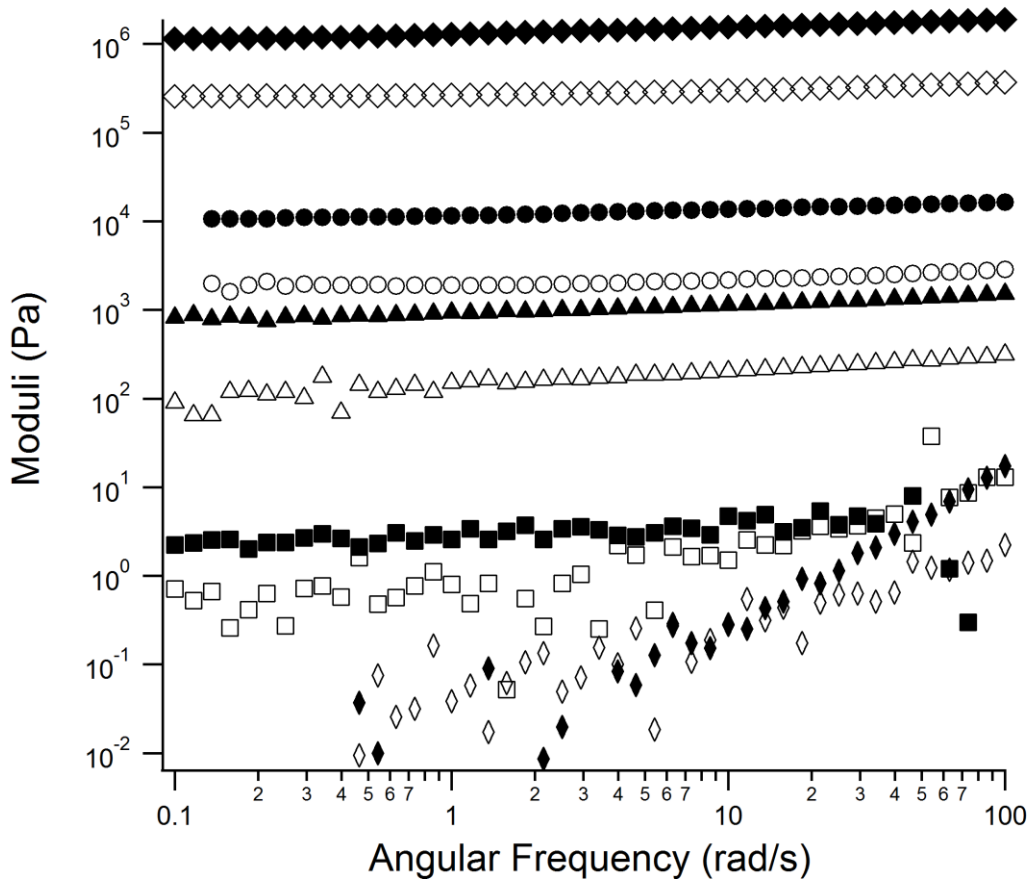
5. Siwy, Z.; Trofin, L.; Kohli, P.; Baker, L.; Trautmann, C.; Martin, C.R. *J. Am. Chem. Soc.* **2005**, *127*, 5000-5001.
6. Vlassiouk, I.; Siwy, Z. *Nano Lett.* **2007**, *7*, 552-556.
7. Vlassiouk, I.; Smirnov, S.; Siwy, Z. *Nano Lett.* **2008**, *7*, 1978-1985.
8. Daiguji, H.; Yang, P.; Szeri, A.J.; Majumdar, A. *Nano Lett.* **2004**, *4*, 2315-2321.
9. Gillespie, D. *Nano Lett.* **2012**, *12*, 1410-1416.
10. Moganty, S.S.; Jayaprakash, N.; Nugent; J.L.; Shen, J.; Archer, L.A. *Angewandte Chemie, Int. Ed.* **2010**, *48*, 9158-9161.
11. Nugent, J.L.; Moganty, S.S.; Archer, L.A. *Advanced Materials* **2010**, *22*, 3677-3680.
12. Schaefer, J.L.; Moganty, S.S.; Yanga, D.A.; Archer, L.A. *J. Mater. Chem.* **2011**, *21*, 10094-10101.
13. Agarwal, P.; Qi, H.; Archer, L.A. *Nano Lett.* **2010**, *10*, 111-115; Agarwal, P.; Srivastava, S.; Archer, L.A. *Phys. Rev. Lett.* **2011**, *107*, 268302.
14. Itoh, T.; Yoshikawa, M.; Uno, T.; Kubo, M. *Ionics* **2009**, *15*, 27-33.
15. Chinnam, P.R.; Wunder, S.L. *Chem. Mater.* **2011**, *23*, 5111-5121.
16. Lambert, J. B.; Shurvell, H. F.; Lightner, D. A.; Cooks, R. G. *Organic Structural Spectroscopy*, Prentice Hall, 2001.
17. Hong, B.; Chremos, A.; Panagiotopoulos, A. Z. *Faraday Discuss.* **2012**, *154*, 29-40.
18. Srivastava, S.; Shin, J. H.; Archer, L.A. *Soft Matter*, **2012**, *8*, 4097-4108.
19. Klein, R.; Zhang, S.; Dou, S.; Jones, B.; Colby, R.; Runt, J. *J. Chem. Phys.* **2006**, *124*, 144903-144910.
20. Hallac, B. B.; Geiculescu, O. E.; Rajagopal, R. V.; Creager, S. E.; DesMarteau, D. D. *Electrochim. Acta* **2008**, *53*, 5985-5991.

21. Tamura, T.; Hachida, T.; Yoshida, K.; Tachikawa, N.; Dokko, K.; Watanabe, M. *J. Power Sources* **2010**, *195*, 6095-6100.
22. Yanai, N.; Uemura, T.; Horike, S.; Shimomura, S.; Kitagawa, S. *Chem. Commun.* **2011**, *47*, 1722-1724.
23. Brissot, C.; Rosso, M.; Chazalviel, J.-N.; Lascaud, S. *J. Power Sources* **1999**, *81-82*, 925-929.
24. Rosso, M.; Gobron, T.; Brissot, C.; Chazalviel, J.-N.; Lascaud, S. *J. Power Sources* **2001**, *97-98*, 804-806.

## APPENDIX. Supporting Information for Chapter 8



**Supplementary figure 8.1** Storage moduli (closed symbols) and loss moduli (open symbols) as a function of applied strain at  $\omega = 10$  Hz for hybrid  $\text{SiO}_2\text{-SO}_3\text{BF}_3\text{Li}$  electrolytes with varying lithiated particle content. The small peak in the loss moduli at higher particle loadings is indicative of soft glassy behavior. The dominance of the storage moduli over that of the loss moduli at low strain at low particle loadings is indicative of large-scale network formation.



**Supplementary figure 8.2** Storage moduli (closed symbols) and loss moduli (open symbols) as a function of applied angular frequency at 0.1% strain for hybrid SiO<sub>2</sub>-SO<sub>3</sub>BF<sub>3</sub>Li electrolytes with varying lithiated particle content. The dominance of the storage moduli over that of the loss moduli at low particle loadings ( $\phi \geq 0.012$ ) is indicative of large-scale network formation.

## CHAPTER 9:

### COVALENTLY COFUNCTIONALIZED HYBRID NANOPARTICLE SALTS AND EFFECT OF SOLVENT TYPE ON ION DISSOCIATION

#### **Introduction**

During the review of the manuscript hereby republished as Chapter 8, it was suggested that the sulfonamide bond shown in Figure 8.1, schematic of the lithium nanoparticle salt, may not form under the conditions of which the synthesis was performed: reaction in aqueous solution without catalyst, followed by drying. Hence, it is possible that the true structure of these particles includes an ionic linkage: PEG-NH<sub>3</sub><sup>+</sup>-SO<sub>3</sub>-SiO<sub>2</sub>. This would allow for an additional mobile cation in the system other than Li<sup>+</sup>. This chapter provides details regarding the synthesis and characterization of covalently cofunctionalized nanoparticles salts as reported in Chapter 3, specifically in Table 3.1 and Figure 3.7. A schematic of the target nanoparticle salt is shown here as Figure 9.1.

#### **Experimental**

*Synthesis of covalently functionalized nanoparticle salts:* An alkaline, aqueous solution of silica nanoparticles (Ludox SM-30, Aldrich) was diluted to 4 wt% silica by the addition of deionized water. An aqueous solution of silane terminated sulfonic acid ((3-trihydroxysilyl)-propane sulfonic acid, 30-35wt%, Gelest), as received, was brought to an alkaline pH (~ 9) by the addition of sodium hydroxide pellets. While stirring vigorously, the silane-sodium sulfonate solution was added dropwise to the diluted silica particle solution followed by the dropwise addition of silane terminated polyethylene glycol methyl ether

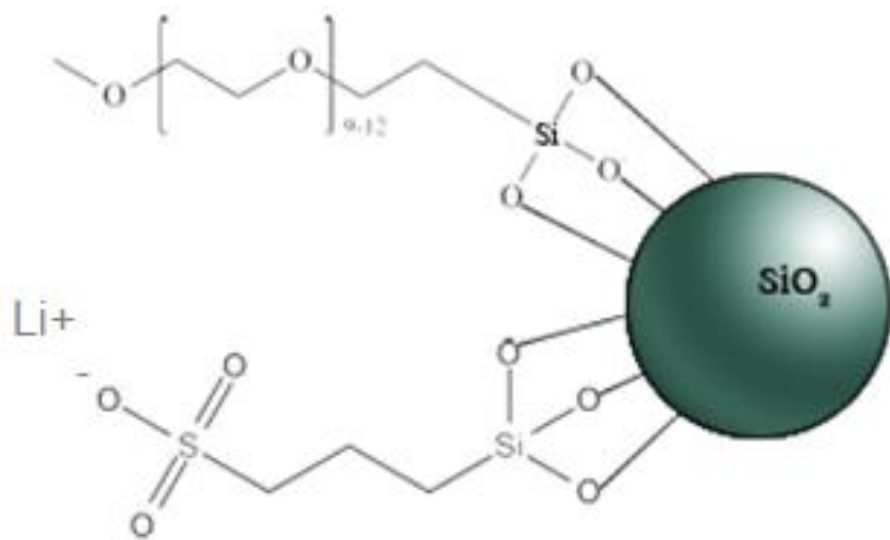


**Figure 9.1** Schematic of the covalently, cofunctionalized nanoparticle salt discussed in this Chapter.

(methoxy(polyethyleneoxy)propyl trimethoxysilane, 90%, Gelest) in a ratio of 4:3:3 by weight, silica:silane-sulfonic acid:silane-PEG. The bottle of the clear, colorless reaction solution was then placed in an oil bath at 100°C for 6-7 hours, stirring with the cap off. Next, the reaction solution was allowed to cool, and then transferred to dialysis membranes (7 kDa molecular weight cut-off, Thermo-Scientific Snakeskin). The reaction solution was dialyzed against deionized water for a minimum of four days with a minimum of eight water exchanges, where the ratio of the volume of the dialyzate to that of the deionized water was 1:10. Following dialysis, the purified reaction solution was ion-exchanged with a sodium-ion exchange resin (Dowex HCR-W2, Sigma-Aldrich) to replace any remaining Na<sup>+</sup> with H<sup>+</sup>. Ion-exchange led to a reduction in the pH of the purified reaction solution from > 4 to ~ 2.5. The solution was then titrated with lithium hydroxide (Aldrich) to a pH of just less than 6.00. The lithiated, cofunctionalized particle solution was then dried in a convection oven at 80°C to remove the majority of the water. Then, the lithiated particles were dried under vacuum at 100°C for 12 hours, where the particles were contained in a 100 mL round-bottom flask that was directly attached to a vacuum pump via tubing. Following the vacuum drying, the valve to the flask was closed, and the particles were immediately transferred to an argon glove-box.

*Electrolyte preparation:* Electrolytes were prepared of the lithiated particles in a number of varying battery-relevant solvents: dimethyl acetamide (DMA, Aldrich, anhydrous), dimethyl carbonate (DMC, Aldrich, anhydrous), dimethyl sulfoxide (DMSO, Aldrich, anhydrous), ethylene carbonate (EC, Aldrich, anhydrous), polyethylene glycol dimethyl ether Mn ~ 250 (PEGDME 250, Aldrich, dried under vacumm at 100°C for 24 hours), propylene carbonate (PC, Aldrich, anhydrous), and sulfolane (Aldrich). Properties of these solvents are given in Table 9.1.

**Table 9.1** Properties of solvents used in electrolytes

Name	Abbreviation	T <sub>m</sub> (°C)	T <sub>b</sub> (°C)	η (cP) at 25°C	ε at 25°C
Dimethyl acetamide	DMA	- 20	165	3.7	37.8
Dimethyl carbonate	DMC	3	90	0.59*	3.1
Dimethyl sulfoxide	DMSO	19	189	3.9	46.7
Ethylene carbonate	EC	35	261	1.9#	89.8
Polyethylene glycol dimethyl ether	PEGDME 250	-23	> 250	6.2	7
Propylene carbonate	PC	-49	242	2.5	64.9
Sulfolane	---	28	285	10.3	44

\* at 20°C

# at 35°C

First, the lithiated particles were dispersed in methanol, previously dried over molecular sieves in the glovebox, for 12 hours. The lithiated particles did not completely dissolve in the methanol, but the solvent appeared to wet and swell the particle aggregates, and the solution was stirred vigorously to break the particle aggregates into smaller pieces.

The dispersion of lithiated particles in methanol was combined with the following solvents of high thermal stability, such that the target loading of lithiated particles in the solvent was 25wt%: EC, PC, PEGDME 250, and sulfolane. The dispersion of lithiated particles in methanol was combined with a large excess of the following solvents of lower thermal stability: DMA and DMSO. Finally, with the intent of producing a sample of lithiated particles in a 50/50 volume mixture of EC/DMC, the dispersion of lithiated particles in methanol was combined with a large excess of DMC and the amount of EC necessary for 37.5wt% of the final electrolyte.

The vials containing the lithiated particles dispersed in methanol and the appropriate solvent(s) were transferred to a convection oven at 70°C to dry off the methanol. Following methanol evaporation, the samples of lithiated particles in high thermal stability solvents - EC, PC, PEGDME 250, and sulfolane – were transferred to the vacuum oven and heated under vacuum at 50°C for a minimum of 12 hours. Following vacuum drying, the samples containing only EC, PC, PEGDME 250, and sulfolane were then transferred to an argon-filled glovebox for storage. The samples of lithiated particles containing DMA, DMSO, and EC/DMC were also heated at 70°C to evaporate methanol, but continual addition of the solvent with low thermal stability was required. After transfer of the samples containing EC, PC, PEGDME 250, and sulfolane to the vacuum oven, samples of DMA, DMSO, and EC/DMC remained in the convection oven and the temperature was increased to 90°C. Over a time period of six hours, anhydrous solvent was continually added to prevent complete drying of the particles. Finally, the solvent level was

allowed to evaporate until the lithiated particle-based samples looked like a wet sand of similar viscosity to the 25wt% particle samples based on EC, PC, PEGDME 250, and sulfolane. The lithiated particle electrolytes containing DMA, DMSO, and EC/DMC were then transferred to an argon-filled glovebox for storage.

*Thermal Gravimetric Analysis:* Thermal gravimetric analysis (TGA) was performed using a TA Instruments TGA on the final samples to confirm the loading of the lithiated particles in the electrolytes.

*Dielectric Spectroscopy Measurements:* Dielectric spectroscopy was performed on the samples using a Novacontrol Dielectric spectrometer fitted with a Quatro temperature control system at the default applied voltage amplitude (1 V) and at temperatures from 10° to 85°C in increments of 15°C. The samples, which physically resembled wet sand or gel, were charged to a teflon ring (inner diameter = 5.0 mm, thickness = 1.8 mm) inside the Novocontrol liquid sample cell holder with gold-plated electrodes while inside the glovebox. Upon removal from the glovebox, the sample cell was immediately screwed into the sample holder and placed in the cryostat under nitrogen flow.

## **Results and Discussion**

TGA determined that the loading of lithiated particles in all of the electrolytes was 20-35wt%. This range is near that of the optimum particle loading for ionic conductivity as observed in the study reported in Chapter 8.

The ionic conductivity of the lithiated particle electrolytes as a function of solvent and temperature is shown in Figure 9.2. It is clear that the solvent type has a large impact on ionic conductivity; switching PEGDME 250 with another solvent led to increases in conductivity of up to more than two orders of magnitude. Comparison of Figure 9.2 with Table 1 reveals that conductivity is not a clear function of the solvent dielectric constant. It is typically assumed that solvents with higher dielectric constants allow for increased ion pair dissociation as the Bjerrum length, the length scale at which the electrostatic interaction between two elementary charges is comparable in magnitude to thermal energy, is inversely proportional to solvent dielectric constant as discussed in Chapter 2. Rather, it is likely that the specific chemistry of the solvent plays an important role in determining the extent of dissociation of the lithium sulfonate ion pair. The dielectric spectroscopy data was further analyzed in an attempt to determine mobile ion concentrations and ion mobilities. As discussed in Chapter 8, data obtained from dielectric spectroscopy may be fit to a previously proposed electrode polarization model:<sup>1</sup>

$$\tan \delta = \frac{\omega \tau_{EP}}{1 + \omega^2 \tau_{EP}^2 / M}$$

This model fits the magnitude and the frequency of the peak maximum in  $\tan \delta$ ,  $\tan \delta_{max}$  and  $f_{max}$ , to determine the diffusivity and number of conducting ions,<sup>2,3</sup> where

$$D = \frac{2\pi f_{max} L^2}{32(\tan \delta)_{max}^3} \text{ and } p_0 = \frac{\sigma kT}{Dq^2}.$$

Figure 9.3 displays  $f_{max}$  and  $\tan \delta_{max}$  for the  $\tan \delta$  spectra from the same dielectric spectroscopy measurements used to determine the ionic conductivity of the electrolytes as displayed in Figure 9.2. In all cases,  $f_{max}$  increases with increasing temperature, as expected; the relaxation time of the conducting ion is faster at increased temperature. However,  $\tan \delta_{max}$  is not a consistent function with temperature for all solvents. In most cases, when the solvent is in the melt state,  $\tan \delta_{max}$  is not a function of temperature.

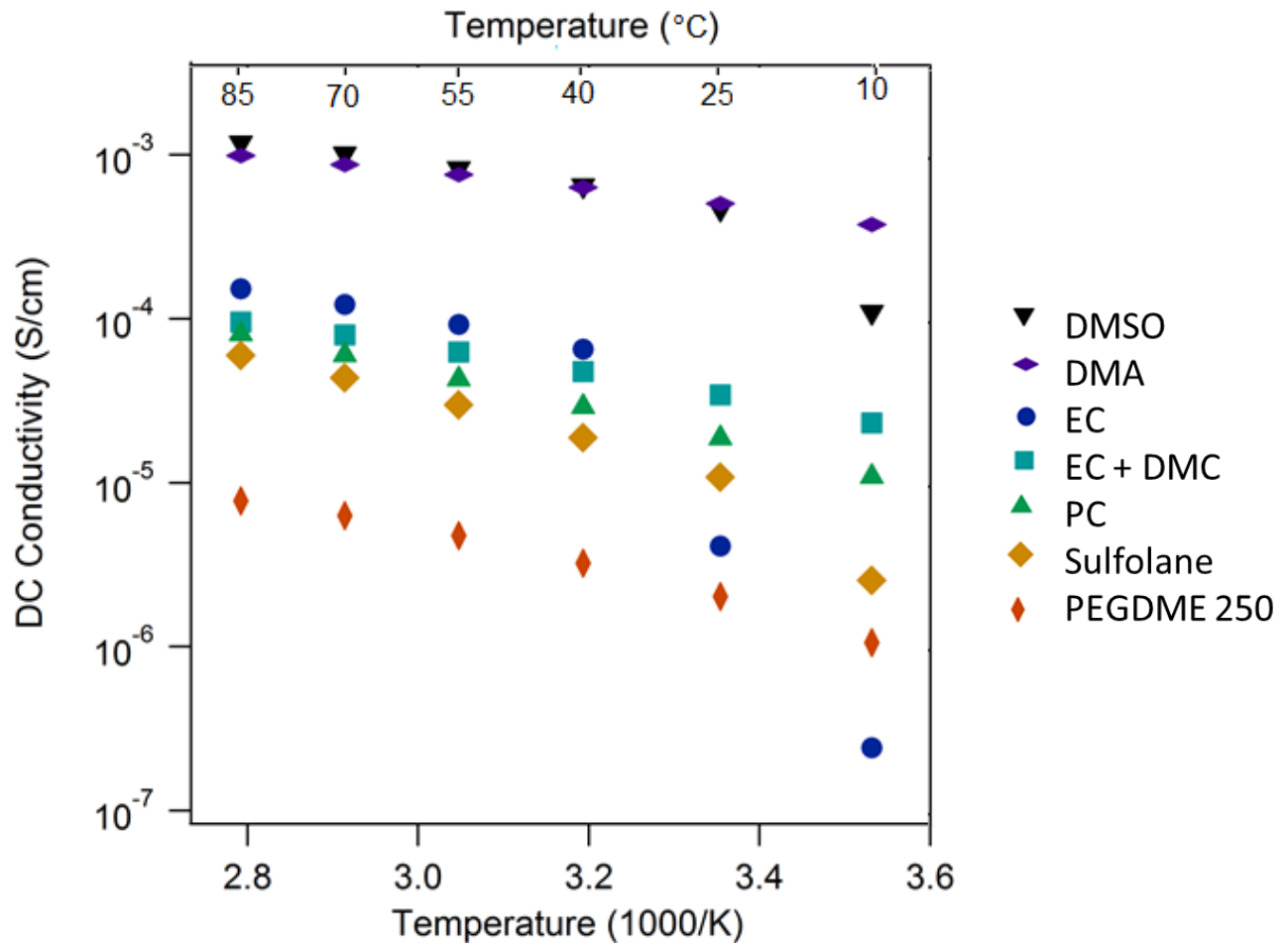


**Figure 9.2** DC ionic conductivity of electrolytes containing 20-35wt% of the nanoscale lithium salt as a function of temperature and the suspending fluid.

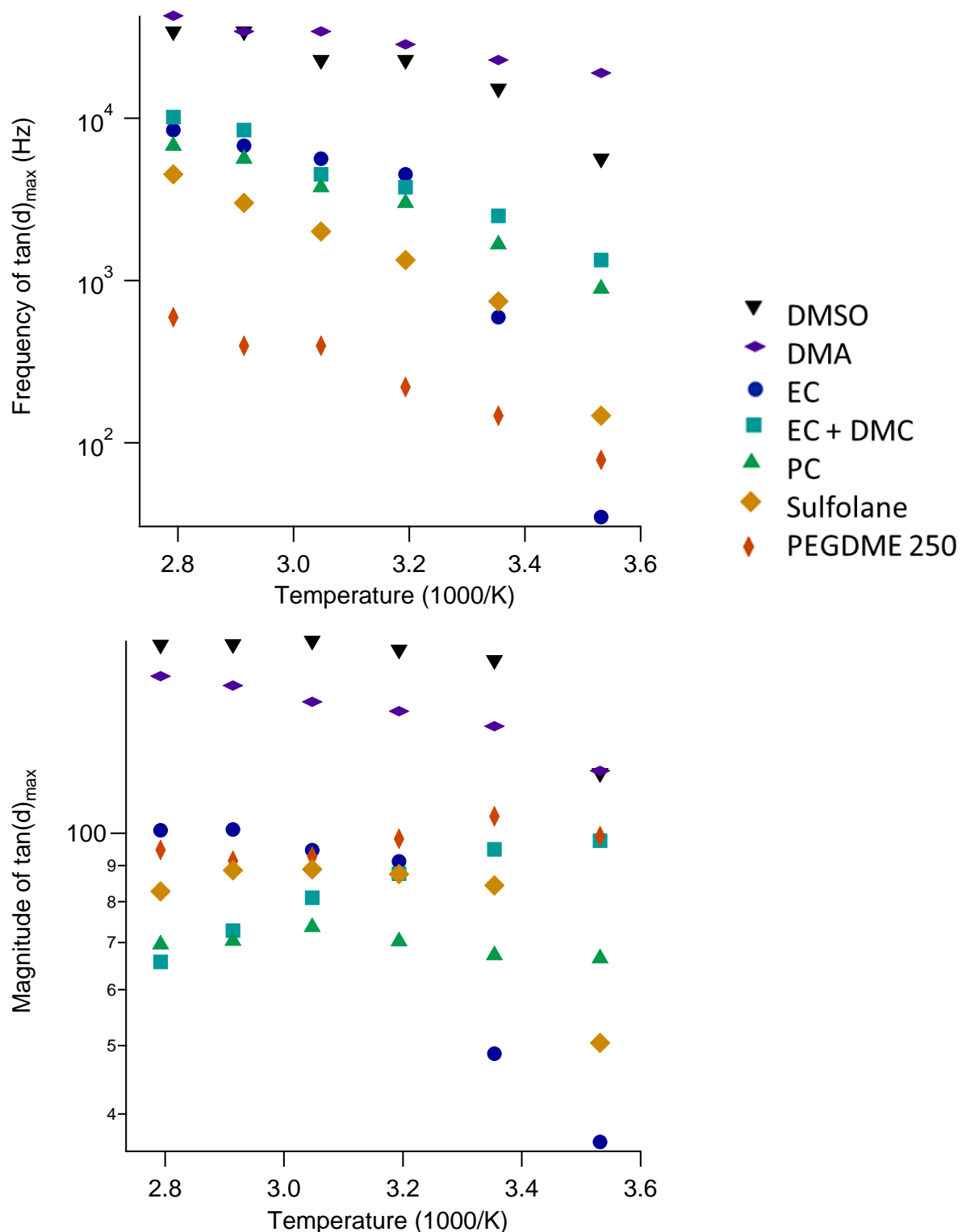


**Figure 9.3**  $f_{\max}$  and  $\tan\delta_{\max}$  obtained from dielectric spectroscopy for the lithiated particle electrolytes as a function of temperature and solvent type.

Figure 9.4 displays the calculated ion diffusivity and mobile ion concentration, as determined from  $f_{\max}$  and  $\tan\delta_{\max}$ . Both the predicted magnitude and temperature dependence of ion diffusivity are not as expected. The predicted ion diffusivities vary about four orders of magnitude at 85°C, though the viscosity of the solvents varies by about one order of magnitude. Even considering varying hydrodynamic radii of the conducting ions in various solvents, due to variations in solvent coordination, this amount of difference is not expected. Furthermore, in cases where the solvent undergoes a melting transition in the investigated temperature range, ion diffusivity is predicted to increase rather than decrease in the crystallized solvent relative to the liquid solvent. Given that the diffusivity of Li<sup>+</sup> in water is  $1 \times 10^{-9} \text{ m}^2/\text{s}$  at 25°C, the majority of the predicted ion diffusivities seem unphysical.

The predicted mobile ion concentrations vary by about six orders of magnitude for the electrolytes based on the different solvents. The solvent with the highest dielectric constant, EC, is predicted to have the highest mobile ion concentration while the solvent with the lowest dielectric constant, PEGDME 250, the lowest mobile ion concentration. In some cases (DMSO, DMA, PC), the mobile ion concentration is invariant with temperature; this behavior is expected in systems where the majority of ion pairs are dissociated.

In summary, particle-based electrolytes containing tethered lithium salts are found to have conductivities that are a strong function of suspending solvent chemistry. The predicted conducting ion diffusivities and mobile ion concentrations as determined from the electrode polarization model from dielectric spectroscopy are found to be unphysical. This conclusion agrees with findings recently published by Sokolov et. al.<sup>4</sup> that also suggest that this model predicts unrealistic magnitudes of ion diffusivities for simple salt-in-solvent electrolytes.

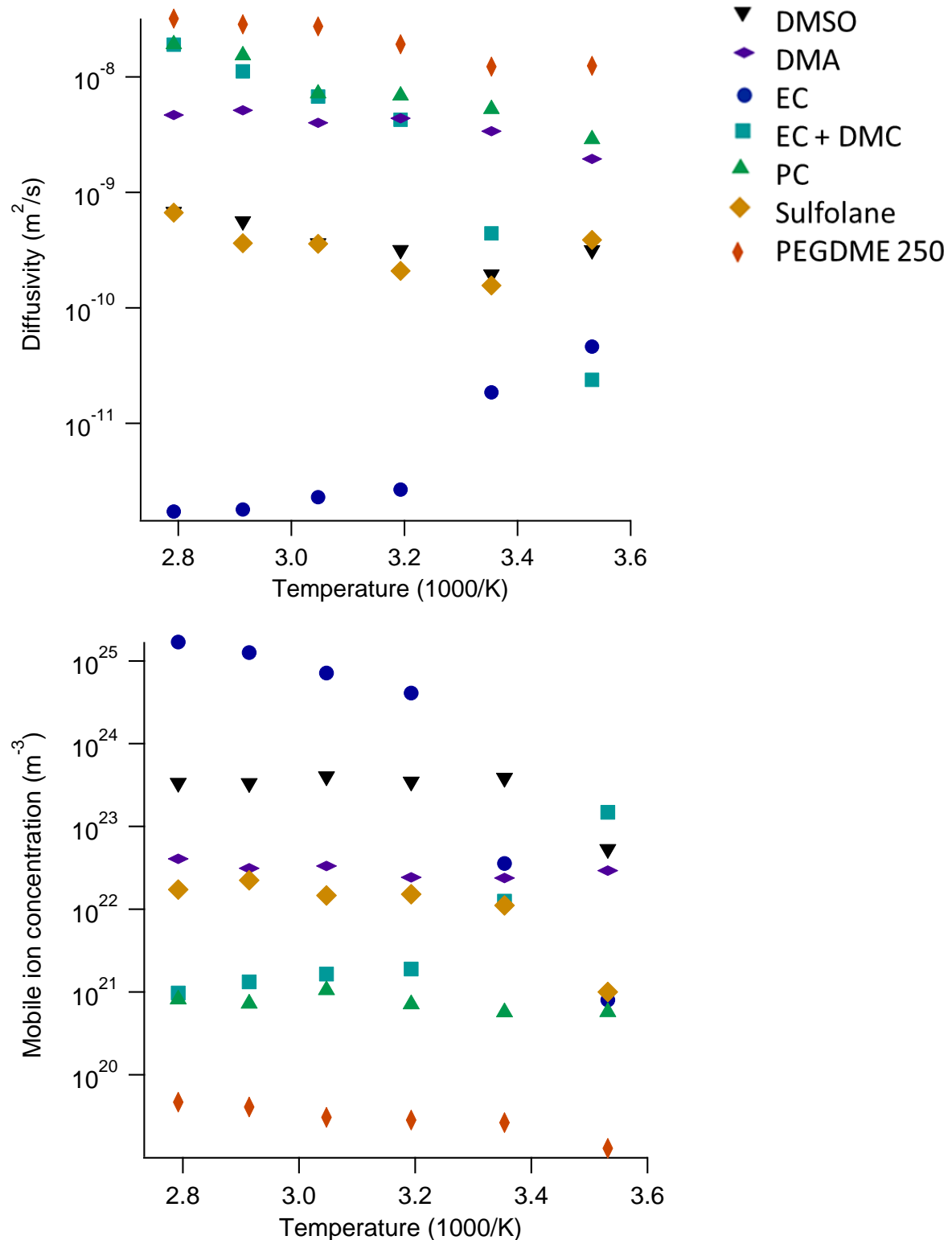


**Figure 9.4** Ion diffusivity and mobile ion concentrations as predicted from dielectric spectroscopy for the lithiated particle electrolytes as a function of temperature and solvent type.

## References

- [1] R. J. Klein, S. Zhang, S. Dou, B. H. Jones, R. H. Colby, J. Runt, *The Journal of Chemical Physics* 2006, 124, 144903.
- [2] T. Sorensen, V. Compan, J. Chen. *Soc. Faraday Trans.* 1995, 91, 4235.
- [3] A. Munar, A. Andrio, R. Iserte, V. Compan, *Journal of Non-Crystalline Solids* 2011, 357, 3064.
- [4] Y. Wang, C.-N. Sun, F. Fan, J. R. Sangoro, M. B. Berman, S. G. Greenbaum, T. A. Zawodzinski, A. Sokolov, *Physical Review E* 2013, 87, 0423081.